

# Structure tuning for enhanced properties in isotactic polypropylene

**Citation for published version (APA):**

Caelters, H. J. M. (2017). *Structure tuning for enhanced properties in isotactic polypropylene*. [Phd Thesis 1 (Research TU/e / Graduation TU/e), Mechanical Engineering]. Technische Universiteit Eindhoven.

**Document status and date:**

Published: 07/06/2017

**Document Version:**

Publisher's PDF, also known as Version of Record (includes final page, issue and volume numbers)

**Please check the document version of this publication:**

- A submitted manuscript is the version of the article upon submission and before peer-review. There can be important differences between the submitted version and the official published version of record. People interested in the research are advised to contact the author for the final version of the publication, or visit the DOI to the publisher's website.
- The final author version and the galley proof are versions of the publication after peer review.
- The final published version features the final layout of the paper including the volume, issue and page numbers.

[Link to publication](#)

**General rights**

Copyright and moral rights for the publications made accessible in the public portal are retained by the authors and/or other copyright owners and it is a condition of accessing publications that users recognise and abide by the legal requirements associated with these rights.

- Users may download and print one copy of any publication from the public portal for the purpose of private study or research.
- You may not further distribute the material or use it for any profit-making activity or commercial gain
- You may freely distribute the URL identifying the publication in the public portal.

If the publication is distributed under the terms of Article 25fa of the Dutch Copyright Act, indicated by the "Taverne" license above, please follow below link for the End User Agreement:

[www.tue.nl/taverne](http://www.tue.nl/taverne)

**Take down policy**

If you believe that this document breaches copyright please contact us at:

[openaccess@tue.nl](mailto:openaccess@tue.nl)

providing details and we will investigate your claim.

# **Structure Tuning for Enhanced Properties in isotactic Polypropylene**

Harm Caelers





Structure Tuning for Enhanced Properties in isotactic Polypropylene by Harm J.M. Caelers.  
Technische Universiteit Eindhoven, 2017.

A catalogue record is available from the Eindhoven University of Technology Library  
ISBN: 978-90-386-4290-1

Reproduction: University Press Facilities, Eindhoven, The Netherlands.  
Cover design: Frank Geurts (Design), Rudy Deblieck and Wilma Gijsbers (SEM image).  
Illustration: Image of a craze-like structure, visualized with scanning electron microscopy.

This work has been financially supported by SABIC, Geleen.

# Structure Tuning for Enhanced Properties in isotactic Polypropylene

PROEFSCHRIFT

ter verkrijging van de graad van doctor aan de Technische Universiteit  
Eindhoven, op gezag van de rector magnificus, prof.dr.ir. F.P.T. Baaijens,  
voor een commissie aangewezen door het College voor Promoties, in het  
openbaar te verdedigen op woensdag 7 juni 2017 om 16.00 uur

door

Henricus Johannes Maria Caelers

geboren te Venray

Dit proefschrift is goedgekeurd door de promotoren en de samenstelling van de promotiecommissie is als volgt:

voorzitter:	prof.dr. L.P.H. de Goey
1 <sup>e</sup> promotor:	prof.dr.ir. G.W.M. Peters
2 <sup>e</sup> promotor:	prof.dr.ir. L.E. Govaert
leden:	prof.dr. O. Lame (INSA Lyon)
	prof.dr. G. Strobl (ALU Freiburg)
	prof.dr.ir. T.A.Tervoort (ETH Zurich)
	dr.ir. J.A.W. van Dommelen
adviseur:(s)	dr. K. Remerie (SABIC)

*Het onderzoek of ontwerp dat in dit proefschrift wordt beschreven is uitgevoerd in overeenstemming met de TU/e Gedragscode Wetenschapsbeoefening.*

# Contents

<b>Summary</b>	<b>ix</b>
<b>1 Introduction</b>	<b>1</b>
1.1 Motivation .....	1
1.2 Processing-Structure-Properties Relations .....	2
1.3 Evolution of structure and properties .....	3
1.4 Scope and outline of this thesis .....	4
<b>2 The prediction of mechanical performance of iPP on the basis of processing conditions</b>	<b>7</b>
2.1 Introduction .....	8
2.2 Experimental .....	10
2.2.1 Materials .....	10
2.2.2 Sample preparation .....	10
2.2.3 X-ray .....	11
2.2.4 Mechanical testing .....	14
2.3 Background .....	15
2.3.1 Thermal analysis .....	15
2.3.2 Crystallization kinetics .....	17
2.3.3 Deformation kinetics .....	20
2.3.4 The relation between crystallization temperature and lamellar thickness .....	23
2.4 Results and discussion .....	26
2.4.1 Temperature predictions .....	26
2.4.2 X-ray analysis .....	27
2.4.3 Relation between $T_c$ and $l_c$ .....	29

---

2.4.4	Yield stress predictions .....	30
2.5	Conclusion .....	32
<b>3</b>	<b>Deformation and failure kinetics of iPP-polymorphs</b>	<b>35</b>
3.1	Introduction .....	36
3.2	Material and methods .....	38
3.2.1	Material .....	38
3.2.2	Sample preparation and X-ray characterization .....	38
3.2.3	DMTA .....	43
3.2.4	Mechanical testing .....	43
3.3	Results and discussion .....	44
3.3.1	DMTA results .....	44
3.3.2	Intrinsic material response .....	45
3.3.3	Yield kinetics .....	49
3.3.4	Failure kinetics .....	60
3.4	Conclusion .....	63
<b>4</b>	<b>Deformation-induced phase transitions in iPP polymorphs</b>	<b>67</b>
4.1	Introduction .....	68
4.2	Experimental .....	70
4.2.1	Material and sample preparation .....	70
4.2.2	Mechanical testing .....	71
4.2.3	X-ray techniques and analysis .....	73
4.3	Results .....	82
4.3.1	The mechanical response .....	82
4.3.2	WAXD analysis .....	86
4.3.3	SAXS analysis .....	95
4.4	Discussion and conclusion .....	102
<b>5</b>	<b>Long term failure predictions in polypropylenes</b>	<b>107</b>
5.1	Introduction .....	108
5.2	Experimental .....	110
5.2.1	Materials and sample preparation .....	110
5.2.2	Mechanical testing .....	110

---

5.2.3	X-ray analysis .....	111
5.2.4	Scanning electron microscopy.....	112
5.3	Results and discussion .....	112
5.3.1	Morphology and deformation kinetics of polypropylenes .....	113
5.3.2	Evolution of structure and properties .....	115
5.3.3	Life-time predictions .....	121
5.3.4	Lifetime improvement .....	126
5.4	Conclusion .....	130
<b>6</b>	<b>Conclusions and Recommendations</b>	<b>133</b>
6.1	Conclusions .....	133
6.2	Recommendations .....	136
	<b>Samenvatting</b>	<b>149</b>
	<b>Dankwoord</b>	<b>153</b>
	<b>Curriculum Vitae</b>	<b>155</b>
	<b>List of Publications</b>	<b>157</b>



# Summary

Isotactic polypropylene (iPP) is a low cost semi-crystalline polymer that is easy processable, has a wide variety in properties and, therefore, is used for many applications. Typically, parts are produced in processes like injection molding and extrusion. Independent of the technique used, the conditions applied during processing, i.e. temperature, cooling rate, pressure and flow impose a large footprint on the morphology created during solidification. These structural features, at the micro-, nano- or Å-scale level, are of utmost importance for the mechanical performance, e.g. yield and failure kinetics. Voids, forming under specific loading conditions are affecting the mechanical response. At the nanometer length scale lamellar thickness is of importance and the Å-scale is dictated by the crystal unit cell structures.

The goal of this project is to contribute to a methodology that enables direct evaluation of the mechanical performance of polymer products for isotactic polypropylene on the basis of morphological information obtained from process simulations. The complexity of this problem for the case of isotactic polypropylene results from the rich polymorphism and morphologies that the material displays. Depending on the conditions experienced during processing, these morphologies and the resulting mechanical properties can vary strongly in a product.

To demonstrate the idea of this approach, a simplified, but feasible, case is presented first. Only one crystal phase (monoclinic  $\alpha$ ) is considered and the influence of varying non-isothermal, non-homogeneous processing conditions is investigated. The resulting, heterogeneous morphology is predicted with a crystallization model previously developed within the Polymer Technology group. Structural features, such as the local distribution of lamellar thickness, are used to predict yield kinetics. Comparison with experimentally obtained results shows good agreement and, therefore, demonstrate the validity of this approach.

Due to the complexity of the problem the work focuses on a systematic investigation of well-defined sub-problems. A proper selection of the processing conditions facilitates the investigation of samples consisting of single polymorphs, and revealed the yield and failure kinetics. The mechanical response of the separate morphologies was successfully modeled, and the predicted time-to-failure as a function of loading conditions



is experimentally validated for  $\alpha$ -,  $\beta$ - and  $\gamma$ -iPP. Although the unit cell structures are very different, some remarkable similarities were found. The kinetics observed at temperatures above the  $\alpha_c$  relaxation temperature are similar for all polymorphs. Above this temperature the constrained amorphous domains could be rejuvenated with thermal treatments.

Next, the structural evolution taking place during mechanical loading was extensively investigated, mainly by combining time-resolved in-situ X-ray experiments (conducted at the European Synchrotron and Radiation Facility (ESRF) in Grenoble) with uniaxial tensile and compression experiments. Structural changes occurring in  $\alpha$ -,  $\beta$ - and  $\gamma$ -iPP were revealed. The evolution in terms of phase transitions, crystallinity and lamellar thickness, and finally void formation, is linked to the intrinsic material response obtained from compression experiments. At all stretching temperatures the crystallinity decreases upon deformation and, depending on the temperature, different new structures are formed. Stretching at low temperatures leads to crystal destruction and the formation of oriented mesophase, independent of the initial polymorph. At high temperatures, above  $T_{\alpha_c}$ , all polymorphs transform into oriented  $\alpha$ -iPP. Small quantities of the initial structures remain present in the material. The compression experiments, where localization phenomena are excluded, show that these transformations take place at similar strains for all polymorphs. The onset of void formation is observed prior to yielding and is the most intense for  $\beta$ -iPP.

The acquired knowledge of the morphology dependent intrinsic material behavior, the yield and failure kinetics and the structural evolution upon deformation are used to investigate a well known procedure to certify polymer products. Time dependent behaviour, typical for these materials, nourishes the need for certification data of particular products, subjected to loads. A currently used method to fulfill this need for life time predictions of plastic pipes, ISO 9080, is based on time temperature superposition, but lacks some important characteristics. The shortcomings of this method show that proper descriptions and estimations of time to failure require an extension of the procedure. Two separate types of structural evolution during service life time are revealed, and the insidious effects on the procedure are discussed. Furthermore it is demonstrated that the brittle failure mechanism is interpreted in the wrong way since it shows plastic like phenomena. This offers new insights in the structure property relations displayed in iPP, and the route towards enhanced properties via structure tuning.

### 1.1 Motivation

Failure of polymers under loading conditions, either static or dynamic, is a major concern in load-bearing objects. Irrespective of the applied conditions, failure will eventually always occur [1]. Therefore, being able to estimate the timespan at which this will take place is essential. Generally, failure is subdivided over three different regimes, see Figure (1.1) [2]: In regime I, plasticity controlled ductile failure takes place, resulting from the accumulation of a critical amount of plastic strain. To obtain estimations of lifespans in this regime, predictions are based on measurements using time-temperature superposition; i.e. temperature is used to speed up the failure kinetics. In regime II, fatigue crack growth controlled brittle failure is considered, where the initiation and growth of cracks dominates failure. This mode is typically found at larger time scales. When, in this regime, temperature induced acceleration is no longer sufficient, time-to-failure can be reduced with cyclic loading conditions, often encountered in real applications as well. Finally, in regime III, chemical degradation prevails. This failure mechanism is typically found at even longer timescales and can be postponed by the addition of stabilizers. This is no part of this project.

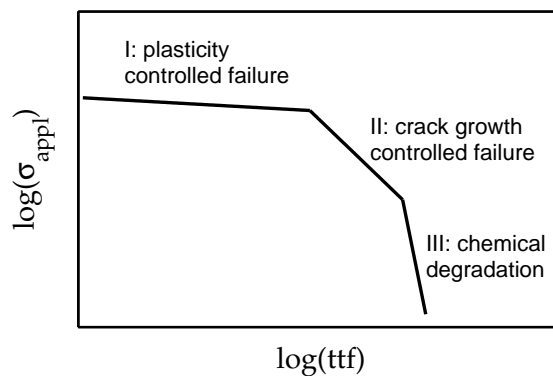


**Figure 1.1:** Schematic representation of the distinct failure mechanisms, typically present in iPP.

As pointed out before, the estimation of the lifespan is essential and, therefore, has been subject of considerable studies. These investigations, aiming at the development of predictive methods, have not only led to procedures that require shorter time spans for experimental completion, but also to the identification of characteristics, unique for the different failure mechanisms and, therefore, allowing to distinguish between them [3,4]. Moreover, these methods offer a valuable tool for quick material characterization in the search for enhanced long term properties.

## 1.2 Processing-Structure-Properties Relations

The issue of predicting lifetime is particularly complex in the case of semi-crystalline polymers like iPP. These materials are composed of crystalline and amorphous parts, present in an alternating sequence. The crystalline domains can be ordered in a highly anisotropic manner. This, as well as their size, is strongly dependent on molecular weight distribution, tacticity, comonomer content and, often more important, the conditions experienced during processing. Since the latter one can typically cause strong spatial variations throughout a product, the structural features exhibit very different characteristics [5,6].

In the particular case of iPP an additional structural feature comes into play, making the situation even more complicated. iPP exhibits several polymorphs, i.e. crystal forms of which the formation is enhanced, in a higher or lower extent, by different processing conditions [7–9]. For example, under moderate cooling conditions, high tacticity iPP crystallizes in the  $\alpha$  form, a monoclinic unit cell structure comprised of iPP chains in the ternary helical conformation, see Figure (1.2a). Fast cooling results in the formation of so called mesophase, a disordered crystalline form that shows long range order in the direction of the chain axis only. The addition of  $\beta$  specific nucleating agent, and/or flow, promotes the development of pseudo-hexagonal  $\beta$ -phase, see Figure (1.2b). Finally,  $\gamma$ -crystals can be formed when high pressure is applied during the crystallization process. This crystal modification is comprised of orthorhombic unit cell structures, and is rather special since the ternary helices are included in a crossed manner, see Figure (1.2c). The formation of the orthorhombic crystal structure is enhanced if low tacticity iPP or random comonomer is used [10–13].

In an industrial production process like injection molding these structures generally coexist. High cooling rates (at the wall of the mold), flow as a result of injecting the material (filling phase) and the application of large pressures (packing phase), to compensate for shrinkage in the cooling phase, are indispensable ingredients in this process. Due to the complicated mixture of structures resulting from processing, the improvement of properties is a complicated task, with many tuning parameters. This makes it a time-consuming and costly process of trial and error. However, a methodology that enables for direct evaluation of mechanical performance of processed objects, on

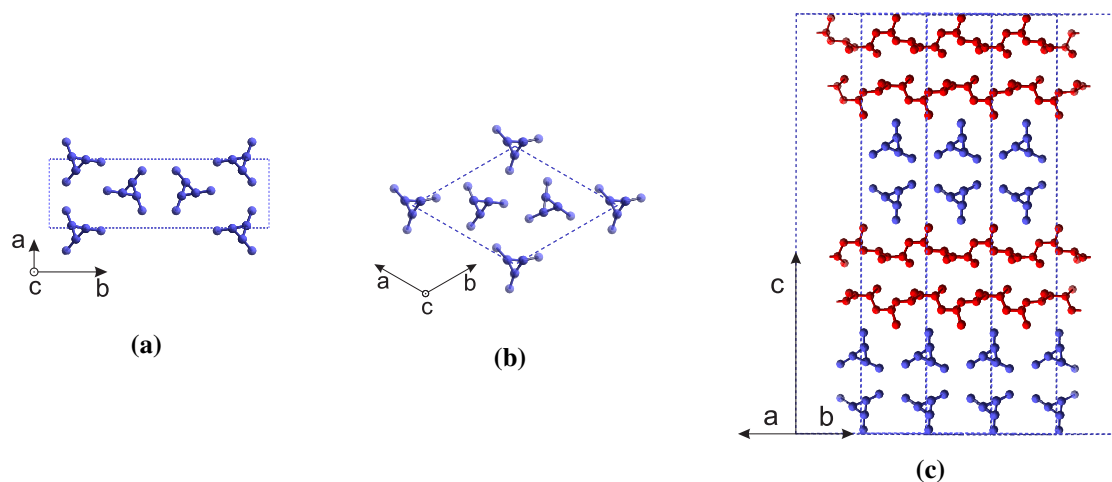


**Figure 1.2:** The crystallographic structures of the iPP-polymorphs. a) monoclinic  $\alpha$ -iPP, b) pseudo-hexagonal  $\beta$ -iPP and c) orthorhombic  $\gamma$ -iPP.

the basis of the morphology obtained from process simulations, would be a major step forward. To succeed in the development of such a methodology, the problem is divided in two main parts. First, the step from processing to structure has to be bridged by a crystallization model capable of predicting the formation kinetics of the individual phases, their dependence on cooling rate, pressure and flow induced molecular stretch and orientation. The research on this topic recently lead to a successful model framework, capable of predicting all the morphological characteristics [14, 15]. Second, the mechanical performance of the individual phases, as well as their dependence on these morphological parameters, has to be characterized and modeled. With respect to this latter part, some important parts of knowledge still have to be gained. This is the main topic of this thesis.

### 1.3 Evolution of structure and properties

The issue of lifetime predictions and the estimation of mechanical properties becomes even more complicated because of structural evolution. With respect to this evolution two cases can be distinguished: i) the evolution of structure as a function of deformation, and ii) temperature induced evolution as a function of time. Deformation is accompanied by deterioration of the structural integrity and, therewith, the features dominating the mechanical response. In the specific case of iPP, deterioration and subsequently the formation of new structures, is displayed by all polymorphs. Self-evidently, understanding of the processes involved, is required to understand the relation to the macroscopic mechanical response.

The evolution of structure and properties over time is unavoidable in long term applications of iPP. It is well known that at room temperature, as well as at elevated temperature, the yield stress increases over time [16, 17]. The evolution below and above the  $\alpha_c$ -relaxation temperature originates from different mechanisms and, consequently, displays different kinetics. Both evolutions affect the intrinsic mechanical response of iPP, and are dictated by a change in micro-structure, which is typically out of equilibrium. As a result, the properties depend on the thermodynamic state. This can, particularly in the case of time temperature superposition, corrupt the life time predictions severely.

## 1.4 Scope and outline of this thesis

This thesis aims to identify the morphological features that determine the mechanical properties of iPP products, with a special focus on polymorphism. The work is intended to contribute to the ultimate goal, i.e. gaining complete understanding of processing-structure-property relations in iPP. The development of predictive models for iPP performance, allowing for the evaluation of long term properties of objects on the basis of processing conditions, requires not only a sophisticated crystallization model, but also the identification of the key structural features determining the mechanical properties. Furthermore, the evolution of properties as a function of deformation and temperature over time, is of vital importance to correctly predict the performance of iPP, and needs to be quantified.

In **Chapter 2** it is demonstrated, for a simplified but feasible case, that a direct evaluation and prediction of mechanical properties on the basis of processing conditions can be done. The processing conditions are chosen such, that only the monoclinic  $\alpha$ -phase is formed. For this specific situation, a successful pathway to predict the relevant spatially variable morphological features resulting from compression molding of iPP sheets, is shown. The structural information obtained from the model turned out to be sufficient to calculate the corresponding average yield stress over the sheet thickness.

With knowledge about the crystallization kinetics, and through proper selection of processing conditions and additives, isotropic samples consisting of solely  $\alpha$ -,  $\beta$ - and  $\gamma$ -iPP, were prepared in **Chapter 3**. Mechanical analysis performed on these samples revealed the intrinsic material behavior, as well as the yield and failure kinetics of the different iPP polymorphs. Similarities and differences observed in DMTA and compression experiments are discussed extensively, and the effect of thermal rejuvenation of the constrained amorphous phase is established.

A more detailed investigation into the relation between polymorphism and intrinsic material behavior is performed in **Chapter 4**, where the intrinsic material behavior is linked to structural evolution upon deformation. Transitions taking place at large

deformations were monitored with in situ tensile deformation. Due to the negative hydrostatic stresses present in this loading geometry, the process of voiding could be monitored using advanced in-situ X-ray scattering methods. Additionally, in situ compression experiments allowed for a direct coupling of transitions taking place at true strains lower than 80%, and true intrinsic material behavior.

In **Chapter 5**, structural evolution taking place during generation of certification data is investigated. It is demonstrated that different types of structural evolution can take place, causing significantly changing mechanical properties. As a consequence, life time predictions based on extrapolation can be corrupted. The difficulties and concerns coming along with this evolution, and the effect on life-time predictions, are discussed in detail.

Finally, at the end of the thesis in **Chapter 6**, the most important general conclusions and recommendations for future research are summarized.



---

# The prediction of mechanical performance of isotactic polypropylene on the basis of processing conditions

Chapter 2

## Abstract

A strategy is presented to predict the yield kinetics following from different thermomechanical histories experienced during processing in non-isothermal quiescent conditions. This strategy deals with three main parts, i.e. processing, structure and properties. In the first part the applied cooling conditions are combined with the crystallization kinetics and the cooling history of the material is calculated. From this history the lamellar thickness distributions are predicted in the second part. Finally, in the third part these distributions are used to predict yield stresses. Experimental validation is carried out for all the different parts of the strategy. In situ temperature measurements, lamellar thickness distributions from SAXS experiments and yield stresses measured in uni-axial tensile deformation are performed for validation purposes. The versatility is investigated by applying this procedure on two different iPP grades. The yield stress predictions show good agreement with the experimentally obtained results in two separate deformation mechanisms, and only a few parameters are dependent on the specific iPP grades that were used here. Moreover, it is shown that the average lamellar thickness is sufficient to predict the yield stress, and that the width of lamellar thickness distributions does not have to be taken into account.

---

Reproduced from: H.J.M. Caelers, L.E. Govaert, G.W.M. Peters. The prediction of mechanical performance of isotactic polypropylene on the basis of processing conditions. *Polymer*, 83, 116–128 (2016)



## 2.1 Introduction

Polymers are used in a wide spectrum of applications ranging from packaging to structural engineering. Polyolefins, specifically polyethylene and polypropylene, form a substantial part of the synthetic polymers used because of their low costs, ease of manufacturing and versatility. To illustrate, these materials are used in extrusion processes (pipes), film blowing processes (packaging) and injection molding processes (structural applications). Within this specific class of materials multiple variants of polypropylene exist, e.g. isotactic-, syndiotactic-, atactic polypropylene and many copolymers. Their properties are related to the chemical structure, in particular the presence of regularity [18], since it allows polypropylene (iPP and sPP) to partially crystallize upon cooling. Due to the ability to crystallize the solidification takes place at higher temperatures as compared to aPP, largely affecting the mechanical properties. Other important aspects dominating the morphology and thereby the mechanical properties, are the processing conditions. Flow and cooling conditions are known to largely affect the morphology and therewith the yield kinetics and overall mechanical response [19, 20]. Since changes of these processing conditions throughout a product may therefore result in strong spatial variations of mechanical performance [21], an undesired consequence is that weak spots are typically present. In this work a first attempt is made to relate the mechanical properties to the morphology resulting from well-defined processing conditions.

The solid crystalline parts, present in iPP, are connected by chains surpassing the amorphous regions [22, 23]. Some general findings on the relation between the crystals and the mechanical properties follow from several studies performed in the past. First, the Young's modulus increases with the degree of crystallinity, whereas the impact performance and the toughness decrease [24, 25]. Furthermore, the yield stress appears to be strongly correlated to lamellar thickness [26–31]. This relation was rationally based on the nucleation and propagation of screw dislocations [29] in the crystalline lamellae and thus on the lamellar thickness.

Besides the variations in the thickness of the crystalline domains (lamellae), multiple crystallographic structures can be present. In iPP, monoclinic  $\alpha$ , pseudo-hexagonal  $\beta$ , orthorhombic  $\gamma$  and mesomorphic unit cell structures [8, 32] can be formed with alternating amorphous and rigid amorphous regions in between [33], affecting the mechanical properties as well. The presence of these regions together with the polymorphism makes it complicated to reveal the relationship between mechanical properties observed on a macroscopic scale to morphologies present at a microscopic or even smaller nanometer scale [34].

The crystallization process is kinetically controlled and therefore local thermo-mechanical conditions experienced by the polymer during processing can have pronounced effects on the lamellar morphology that forms, as well as on the polymorphism within the crystals [21, 35–37]. Structure development under processing conditions has been subject of substantial research carried out in the past [38–40]. When we focus on conditions imposed during a compression molding process, i.e. moderate non-isothermal quiescent

conditions, it is found that in the case of neat iPP typically  $\alpha$ -crystals develop [41]. Depending on the applied cooling rate, the crystallinity as well as the number and size of spherulites varies. Furthermore, this unavoidably results in variations of the lateral size of the crystal sheet-like domains, but more important for the yield kinetics, differences in the thickness will appear. The lamellar thickness is determined by the undercooling during the crystallization process [42] and, therefore, directly related to the cooling rate. Van Erp et al. [20] specified this effect of cooling rate to investigate the structure property relation for iPP. On the other hand, several studies have been devoted to the development of model frameworks capable of quantitatively predicting the processing dependent crystal structures as a result of processing [41, 43–46].

The main aim of this work was to make a coupling between the processing-structure and structure-property relation in a predictive way. The strategy chosen to accomplish this goal is schematically shown in Figure (2.1) and is divided into three main blocks. Different processing histories are obtained in terms of variable cooling rates. In the first block the processing dependent crystallization kinetics are predicted as a function of time and temperature. The time-temperature history follows from the heat equation, which is used in combination with the crystallization model proposed by van Drongelen et al. [41] to account for latent heat release. Temperature and pressure dependent growth rate and nucleation density are the most important parameters governing the crystallization process, whereas the boundary conditions together with the thermal contact resistance determine the temperature evolution. In the second block the obtained evolution of crystal volume as a function of temperature is used in combination with the Lauritzen-Hoffman equation [42] to determine the lamellar thickness distributions resulting from the different cooling rates. Also the dependency of the molecular features of the iPP chain on the crystallization temperature and lamellar thickness is determined. Finally, in block three, the lamellar thickness is used to get the yield kinetics by making use of an empirical relation reported by van Erp et al. [20].

In the present study we will first give more detailed background information on 1) the crystallization model and the simplifications that are used, 2) the coupling to a structural feature, in this case lamellar thickness and 3) the relation between the lamellar thickness and the yield kinetics. Subsequently these three distinct parts are coupled and used to predict yield stresses resulting from well defined thermo-mechanical histories. The validity of this approach is experimentally shown for two iPP grades.

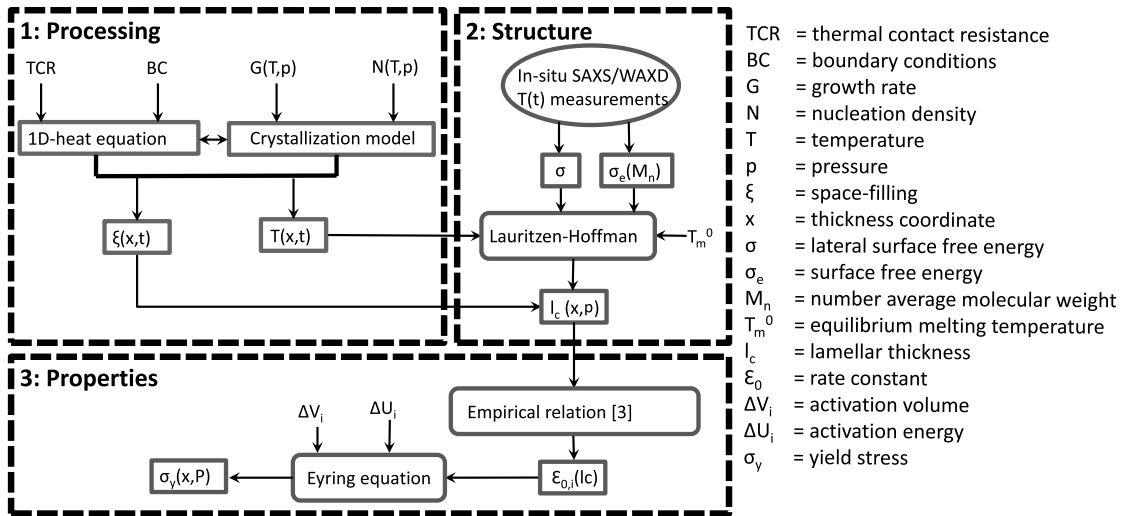


Figure 2.1: Strategy to predict the yield stress directly from processing conditions

## 2.2 Experimental

### 2.2.1 Materials

Two isotactic polypropylene homopolymer grades were used: iPP-1 (Borealis HD234CF) with a weight averaged molar weight  $M_w=310$  kg/mol and a polydispersity  $M_w/M_n=3.4$ , and iPP-2 (Borealis HD601CF) with  $M_w=365$  kg/mol and  $M_w/M_n=5.4$ . These two materials were chosen because they were used in several other crystallization studies in our group [6, 41].

### 2.2.2 Sample preparation

To obtain samples with different thermal histories, sheet material with a thickness of 1 mm was compression molded from both the iPP-1 and iPP-2 grade. A mold, sample surface area of 100 cm<sup>2</sup>, was sandwiched in between stainless steel sheets (0.5mm) and placed in a hot press, see Figure (2.2). The stack was subsequently heated to 230°C and a force of 100 kN was applied stepwise. The sheets were kept under these conditions for 3 minutes to erase previous thermo-mechanical history. The solidification was induced by putting the stack in a cold press for 3 minutes, at temperatures varying from 20°C to 90°C (steps of 10 °C). To monitor the temperature during solidification, a small calibrated thermocouple was embedded in the polymer. A fast acquisition data logger (National Instruments Hi-speed USB 9162, sampling frequency 10 Hz) was used to record the temperature in-situ.

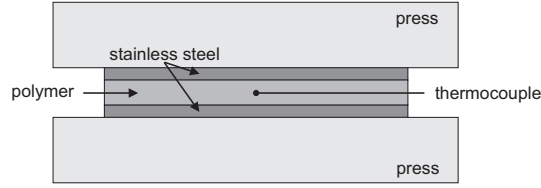


**Figure 2.2:** Schematic representation of the compression moulding process

### 2.2.3 X-ray

Small angle X-ray scattering (SAXS) and wide angle X-ray diffraction (WAXD) experiments were performed at the Dutch-Belgian (DUBBLE) beamline BM26 [47] of the European Synchrotron and Radiation Facility (Grenoble, France). Quasi-isothermal crystallization experiments were performed with a custom modified JHT-350 Linkam stage equipped with a pneumatically actuated temperature jump-stage [48]. The cold stage was set at temperatures of 100, 110 and 120°C respectively. To monitor the temperature and quasi-isothermal crystallization in time, a small thermocouple was embedded in the polymer. In-situ WAXD and SAXS patterns were recorded with acquisition rates of 20 frames per second. A wavelength of  $\lambda = 1.04\text{\AA}$  was used. The 2D SAXS patterns were recorded with a Pilatus 1M detector and the WAXD patterns with a Pilatus 300K detector, both with pixel size of  $172 \times 172 \mu\text{m}^2$ , placed at approximately 1.42 and 0.30 meter respectively.

Single shots were obtained ex-situ from the compression molded samples with the different cooling histories, with an acquisition time of 10 seconds. All the acquired images were corrected for beam intensity and scattering of the empty sample cell.

### WAXD

The obtained intensity profiles were plotted versus the scattering angle  $2\theta$ . The weight fraction of the crystallinity  $\chi_w$  was determined with eq. (2.1):

$$\chi_w = \frac{C_{tot} - C_a}{C_{tot}} \quad (2.1)$$

where  $C_{tot}$  is the total scattered intensity and  $C_a$  is the scattered intensity of an amorphous halo. The amorphous halo is measured on a quenched low tacticity polypropylene sample with negligible crystallinity, and scaled with the minimum between the  $(110)_\alpha$  and  $(040)_\alpha$  diffraction peaks [49]. The volume fraction of the crystallinity is given by [26]:

$$\chi = \frac{\frac{\chi_w}{\rho_c}}{\frac{\chi_w}{\rho_c} + \frac{1-\chi_w}{\rho_a}} \quad (2.2)$$

where  $\rho_a$  and  $\rho_c$  are the density of the amorphous and crystalline phase respectively, taken from [50].

## SAXS

The scattered intensity was obtained as a function of the scattering vector  $q$  which is given by:

$$q = \frac{4\pi}{\lambda} \sin(\theta) \quad (2.3)$$

where  $\theta$  is half of the scattering angle. In case of an isotropic system with a randomly oriented lamellar morphology the measured scattering intensity can be transposed into the 1D scattering intensity using Lorentz correction:

$$I_1(q) = I(q)q^2 \quad (2.4)$$

Once this correction is performed and the electron density differences in one direction are known, the average lamellar thickness  $l_c$  can be obtained from:

$$l_c = \frac{2\pi}{q_{I_1, max}} \chi \quad (2.5)$$

where  $q_{I_1, max}$  is the value for the magnitude of the scattering vector  $q$ , corresponding to the maximum of the Lorentz corrected scattering intensity, and  $\chi$  is the crystalline volume fraction. This method provides an average lamellar thickness. Information about lamellar thickness distributions was obtained using the interface distribution function (IDF) which is the second derivative of the 1D-correlation function  $\gamma_1(r)$  (eq. (2.7)) [51, 52], and is defined as:

$$g_1(r) = \frac{\delta^2 \gamma_1(r)}{\delta r^2} = -\frac{1}{Q} \int_{q_0}^{q_\infty} I_1(q) q^2 \cos(qr) dq \quad (2.6)$$

with

$$\gamma_1(r) = \frac{1}{Q} \int_{q_0}^{q_\infty} I_1(q) \cos(qr) dq \quad (2.7)$$

where  $Q$  is the invariant and  $r$  is the real space. The interface distribution function  $g_1(r)$  can also be obtained by taking the inverse Fourier transform of the interference function  $G_1(q)$  [53]

$$g_1(r) = \int_{q_0}^{q_\infty} G_1(q) \cos(qr) dq \quad (2.8)$$

in which

$$G_1(q) = \lim_{q \rightarrow \infty} I_1(q)q^2 - I_1(q)q^2. \quad (2.9)$$

Since the Fourier transform requires integration from  $q=0$  to infinite, the experimentally accessible  $q$  range has to be extrapolated. The triangle rule is used to extrapolate to zero  $q$ , whereas the Porod law is used to extrapolate to infinite  $q$ . In an ideal two-phase system with sharp boundaries the Porod law predicts a decay in scattered intensity proportional to  $q^{-4}$  at large angles. In reality the intensity often deviates from such an ideal system because of electron density fluctuations and finite interfaces between the crystalline and the amorphous layers. When taking these deviations into account, the adapted Porod law is given by [54]:

$$\lim_{q \rightarrow \infty} I_{obs}(q) = I_b(q) + \frac{K_p}{q^4} \exp(-\sigma^2 q^2) \quad (2.10)$$

where  $\sigma$  is related to the interface thickness,  $K_p$  is the Porod constant and  $I_b$  the scattering resulting from electron density fluctuations. The determination of the parameters required to correct for non-ideality is a sensitive process which can be rather difficult in case of a noisy signal. For this reason an approach proposed by Hsiao et al. [55] is used, where constraints are used to find the parameters required for the intensity corrections. This fit is based on two properties that have to be fulfilled by the interference function. First, the difference between the asymptote at large values of  $q$ , following from the Porod law, and the ideal scattered intensity should become zero. Moreover, as a second constraint, the

interface distribution function should start from the origin and as a result the total area of  $G_1(q)$  versus  $q$  should be zero. Minimization of eq. (2.11), which is only valid in the Porod region, and eq. (2.12) gives the values for the Porod constant, the interface thickness and the liquid-like scattering.

$$\lim_{q \rightarrow \infty} G_1(q) = \lim_{q \rightarrow \infty} [K_p - [I_{obs}(q) - I_b(q)]q^4 \exp(\sigma^2 q^2)] = 0 \quad (2.11)$$

$$\int_{q_0}^{q_\infty} G_1(q) dq = \int_{q_0}^{q_\infty} [K_p - (I_{obs}(q) - I_b(q))q^4 \exp(\sigma^2 q^2)] dq = 0 \quad (2.12)$$

The background intensity following from the electron density fluctuation or liquid like scattering is expressed by

$$I_b(q) = a + bq^2 + cq^4 + dq^6 \quad (2.13)$$

The most reliable average value and the distribution of the lamellar thickness, the long spacing and the amorphous regions can be obtained by deconvolution of the interface distance distribution function  $g_1(r)$ . Long spacings obtained by Bragg's law are typically considerably larger than the true values, especially when distributions are broad [56]. This will irrefutably result in erroneous lamellar thicknesses found with the method of combining WAXD and SAXS measurements eq. (2.5).

## 2.2.4 Mechanical testing

A punch was used to cut typical dog-bone shaped tensile test samples (according to ASTM D1708) from the different compression molded polymer sheets. A Zwick Z010 universal tensile tester equipped with a 2.5 kN load cell and a thermostatically controlled oven was used to perform the tensile tests at strain rates of  $10^{-3} s^{-1}$ . The tests were performed at 23°C and 80°C. In advance of the measurements at elevated temperatures, the tensile specimen was kept at the test temperature for 5 minutes (which is sufficient to achieve thermal equilibrium) before a pre-load of 0.2 MPa was applied. All tests were carried out at least in duplicate. Tensile tests were performed immediately after sample preparation (within minutes) to avoid effects of aging at room temperature [16, 57, 58].

## 2.3 Background

### 2.3.1 Thermal analysis

Cooling rate affects the crystallization process of iPP, but conversely, the cooling rate is influenced by the crystallization process because latent heat releases. This mutual influence of the cooling and crystallization process is elaborated in terms of a 1D conduction problem. In all the experimental test cases performed in this work the polymer layer is positioned in between layers of stainless steel. These are included in the model in order to get the boundary conditions right.

#### The heat balance

To predict the temperature profile in the polymer, the 1D heat equation for conduction is used:

$$\rho(P, \xi, T) \cdot C_p(\xi, T) \cdot \frac{\partial T}{\partial t} = \frac{\partial}{\partial x} \left( \lambda(\xi, T) \cdot \frac{\partial T}{\partial x} \right) + \rho(P, \xi, T) \cdot \Delta H \cdot \dot{\xi} \quad (2.14)$$

In this equation the specific heat  $C_p$  [J/kgK], the density  $\rho$  [kg/m<sup>3</sup>] and the thermal conductivity  $\lambda$  [W/mK] are all functions of temperature and crystallinity. The effect of pressure on the density is not taken into account. The last term of eq. (2.14) is the source term, representing the latent heat release due to crystallization [59]. The time derivative of the space filling,  $\dot{\xi}$ , follows directly from the crystallization model described in section 2.3.2 and  $\Delta H$  [J/kg] is the total enthalpy of transformation. To capture the phase dependent thermal properties a simple mixing rule, eq. (2.15), is used which is similar for heat capacity, density and thermal conductivity.

$$C_p(\xi, T) = \xi C_{p_{sc}}(T) + (1 - \xi) C_{p_a}(T) \quad (2.15)$$

The heat capacity and the thermal conductivity are linearly proportional to the temperature, whereas the density is proportional to the reciprocal temperature [50]. Subscripts  $a$  and  $sc$  refer to the amorphous and semi-crystalline phase, respectively. Heat transfer in the aluminum and steel layers of the experimental setup is again described with the 1D heat equation. However, in that case the thermal properties are assumed to be constant and the source term disappears. Therefore eq. (2.14) reduces to:

$$\rho C_p \frac{\partial T}{\partial t} = \lambda \left( \frac{\partial^2 T}{\partial x^2} \right) \quad (2.16)$$



The parameters that were used in the heat equation are given in Table (2.1).

**Table 2.1:** List of constants

	$\rho$ [kg/m <sup>3</sup> ]	$C_p$ [J/kgK]	$\lambda$ [W/mK]
Stainless steel	7930	502	17

### Thermal contact resistance

The experimental setup consists of a stack of polymer-, and stainless steel layers. As a result of surface roughness or interstitial materials, a pressure dependent thermal contact resistance is present between the layers. Moreover, the state of the polymer, melt or solid, influences the thermal contact behavior.

This contact behavior is included in the model using eq. (2.17). No data is available on pressure and state dependency, so the thermal contact resistance is assumed to be constant. It follows that the heat flux through the interface is given by:

$$\varphi_{int}(t) = \frac{T_{surf1} - T_{surf2}}{TCR} \quad (2.17)$$

where  $\varphi_{int}(t)$  [W/m<sup>2</sup>] is the heat flux from surface  $T_{surf1}$  [K] to surface  $T_{surf2}$  [K], and  $TCR$  [m<sup>2</sup>K/W] the thermal contact resistance. The ingoing heat flux (conduction) equals the flux through the interface, and the outgoing heat flux:

$$\varphi_{in}(t) = \varphi_{int}(t) = \varphi_{out}(t) \quad (2.18)$$

This results in:

$$\lambda_A \frac{dT}{dx} \Big|_{left} = \varphi_{int}(t) = \lambda_B \frac{dT}{dx} \Big|_{right} \quad (2.19)$$

were  $\lambda_A$  and  $\lambda_B$  are the thermal conductivities that belong to material  $A$  and  $B$  respectively. This is approximated by using the temperature gradient over the neighboring grid points:

$$\lambda_A \frac{\Delta T}{\Delta x} \Big|_{left} = \frac{T_{surf1} - T_{surf2}}{TCR} = \lambda_B \frac{\Delta T}{\Delta x} \Big|_{right} \quad (2.20)$$

After discretization using a finite difference method, the heat equation is solved using an implicit Euler scheme. The thermal contact resistance is determined by using the initial slope of the cooling curve for the fastest cooling rate. The parameter values used in the model for the thermal contact resistance are given in Table (2.2). For both iPP grades the same temperature dependent relations for density, specific heat and thermal conductivity are used [50] which explains why the fitted thermal contact resistance between the polymer and the stainless steel is different.

**Table 2.2:** List of parameter values

TCR in [ $m^2 K/W$ ]	Press iPP-1	Press iPP-2
Stainless steel - stainless steel	$3 \cdot 10^{-4}$	$3 \cdot 10^{-4}$
Stainless steel - polymer	$4.1 \cdot 10^{-4}$	$6 \cdot 10^{-4}$

### 2.3.2 Crystallization kinetics

Crystallization of iPP is influenced by the chain architecture. Isotacticity and comonomer content are key parameters with significant effects on crystallinity, polymorphism [12] and crystallization temperature [60]. Molecular weight affects the crystallization temperature [61]. Besides these chain architectural features the thermo mechanical history experienced during processing is of significant importance. In the absence of flow and shear, the arising morphology and the crystallographic structures present therein are determined by the cooling rate [62] and pressure [35]. In this work we focus on the relationship between processing and structure, which has been subject to substantial research, and is captured in multiple crystallization models, many of them lacking structural details. A validated model to describe the temperature and pressure dependent crystallization behavior of iPP in detail, i.e. local nucleation density, spherulite size etc., was proposed by van Drongelen et al. [41]. This model framework is capable of predicting multiphase structure development in quiescent non-isothermal isobaric conditions. In this work a simplified version of this model is used which only allows monoclinic alpha phase formation. From WAXD measurements it is shown later that the model is applicable for the thermo-mechanical histories assessed in this study.

#### The crystallization model

Crystallization is dominated by nucleation and growth. In quiescent conditions the nuclei grow radially until they finally impinge and reach complete space-filling. This can be described with the Kolmogoroff equation [63], which gives the space-filling as a result of nucleation and growth in an unconfined 3-dimensional space according to:

$$\xi(t) = \frac{\chi(t)}{\chi_\infty} = 1 - \exp(-\phi_0(t)) \quad (2.21)$$

where  $\chi(t)$  is the crystallized volume fraction at time  $t$  and  $\chi_\infty$  is the crystallinity when equilibrium is reached. The expected crystallized volume fraction if no impingement would occur  $\phi_0(t)$  is given by [63]:

$$\phi_0(t) = \frac{4\pi}{3} \int_{-\infty}^t dt' \alpha(t') \left[ \int_{-\infty}^t du G(u) \right]^3 \quad (2.22)$$

In this equation  $\alpha(t) = \alpha(T(t), p(t))$  and  $G(u) = G(T(u), p(u))$  are the (spherulitical) nucleation and growth rate respectively, both functions of temperature and pressure. In the special case of isothermal isobaric crystallization where growth rate and nucleation density (i.e. heterogeneous nucleation) are constants, the space filling in time  $\xi(t)$  reduces to

$$\xi(t) = 1 - \exp\left(-\frac{4\pi}{3} NG^3 t^3\right) \quad (2.23)$$

which is known as the classical Avrami equation [64, 65]. However, in this work non-isothermal crystallization is considered. Therefore, we start from the Kolmogoroff equation (2.22). To solve non-isothermal crystallization problems it is much easier to work with the Schneider rate equations which are basically a transform of this integral into a more suitable configuration. Now,  $\phi_0(t)$  follows from the rate equations [66]:

$$\begin{aligned} \dot{\phi}_3 &= 8\pi \dot{N} & (\phi_3 &= 8\pi N) \\ \dot{\phi}_2 &= G\phi_3 & (\phi_2 &= 8\pi R_{tot}) \\ \dot{\phi}_1 &= G\phi_2 & (\phi_1 &= S_{tot}) \\ \dot{\phi}_0 &= G\phi_1 & (\phi_0 &= V_{tot}) \end{aligned} \quad (2.24)$$

where  $N$  is the number of nuclei (heterogeneous nucleation density),  $\dot{N}$  is the nucleation rate,  $G$  is the spherulitic growth rate,  $R_{tot}$  is the sum of the spherulite radii,  $S_{tot}$  is the total surface of the spherulites and their total volume is given by  $V_{tot}$ . These structural features can be obtained since the nucleation and growth calculated via these equations, depend on the thermal history. The solution of these equations in isothermal conditions, and with a constant nucleation and growth rate, again results in eq. (2.23). In this work the number

of nuclei and the growth rate are temperature and pressure dependent and described by the expressions (2.25) and (2.26) respectively,

$$N(T, p) = N_{ref} \exp(-c_n(T(t) - T_{Nref}(p))) \quad (2.25)$$

$$G(T, p) = G_{max}(p) \exp(-c_g(T(t) - T_{Gref}(p))^2) \quad (2.26)$$

where  $N_{ref}$  is the reference number of nuclei at the reference temperature  $T_{Nref}$ .  $G_{max}$  is the maximum growth rate at the reference temperature  $T_{Gref}$ ,  $p$  is the pressure and  $c_n$  and  $c_g$  are constants. The effect of pressure on the nucleation density is incorporated by a shift in the reference temperature, and for the growth rate a shift of the reference temperature and a change in the maximum growth rate parameter  $G_{max}$  is included, according to the following equations,

$$T_{k,ref} = T_{k,ref}^0 + \zeta (p - p_0) \cdot 10^{-5} \quad (2.27)$$

$$G_{max} = G_{max}^0 \exp(a(p - p_0) + b(p - p_0)^2) \quad (2.28)$$

Where  $T_{k,ref}^0$  and  $G_{max}^0$  are the reference temperature and growth rate at atmospheric pressure  $p_0$  in bar, and  $a, b$  and  $\zeta$  are constants. The index  $k$  represents the growth ( $G$ ) and nucleation ( $N$ ).

In Figure (2.3) it is schematically shown how the effect of pressure shifts the nucleation density and the growthrate respectively.

Finally, when the nucleation density and the growth rate are adapted for the applied pressure and non-isothermal conditions, the space filling in time  $\xi$  follows from:

$$\dot{\xi} = (1 - \xi) \dot{\phi}_0 \quad (2.29)$$

An explicit Euler scheme is used to solve the crystallization model. The parameters required to describe the crystallization process are adopted from the work of van Drongelen et al. [41]. An overview is given in Table (2.3)

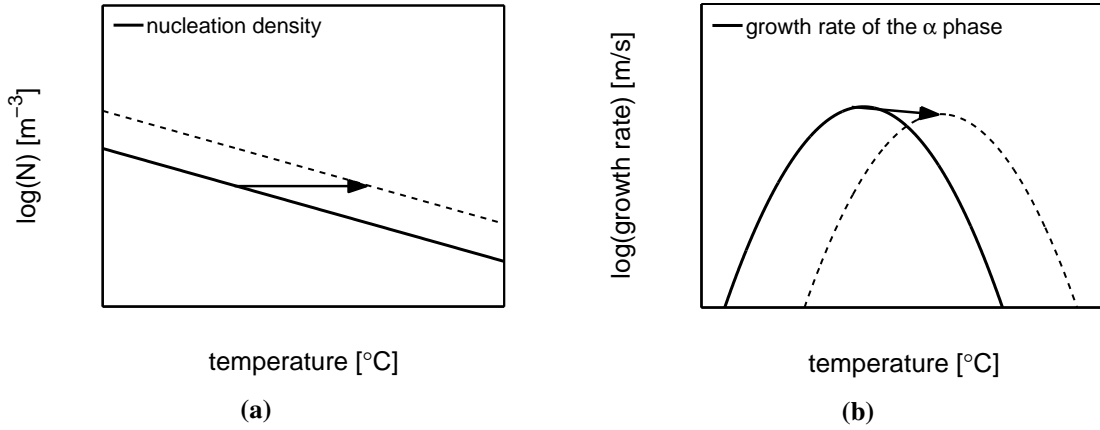


**Figure 2.3:** a) Shift in the nucleation density as a result of pressure ,b) Shift of the growth rate as a result of pressure. Adopted from [41]

**Table 2.3:** Model parameters.

Parameter	iPP-1	iPP-2	Unit
$N_{ref}$	$2.7 \cdot 10^{14}$	$1.2 \cdot 10^{14}$	$[m^{-3}]$
$T_{Nref}$	383	383	$[K]$
$c_n$	0.181	0.219	$[K^{-1}]$
$G_{max}^0$	$4.5 \cdot 10^{-6}$	$4.81 \cdot 10^{-6}$	$[ms^{-1}]$
$T_{Gref}^0$	363	363	$[K]$
$c_g$	$2.3 \cdot 10^{-3}$	$2.3 \cdot 10^{-3}$	$[K^{-2}]$
$a$	$1.60 \cdot 10^{-9}$	$1.60 \cdot 10^{-9}$	$[Pa^{-1}]$
$b$	0	0	$[Pa^{-2}]$
$\zeta$	0.0275	0.0275	$[bar^{-1}]$

### 2.3.3 Deformation kinetics

#### Yield kinetics

To predict yield stresses resulting from well defined processing conditions we first look at the phenomena related to deformation kinetics. The behavior typically displayed by isotactic polypropylene is shown in Figure (2.4a). At low strains the stress increases linearly. With further increasing strain, the stress and the molecular mobility within the polymer increase as well. Ultimately, in the yield point, the molecular mobility is so high that the material deforms plastically at a rate equal to the applied strain rate. The stress associated with this point is defined as the maximum in the stress-strain response and called the yield stress. With increasing strain-rates higher molecular mobility is required for yielding. This is achieved by a higher stress level, explaining the rate dependency

of the yield stress typically observed for polymers. Another way to induce mobility is raising the temperature. In the mechanical response this leads to decreasing yield stresses. After yielding strain softening takes place, leading to strain localization and subsequently necking.

The yield kinetics, i.e. the yield stresses over a broad range of temperatures and strain rates are shown in Figure (2.4b). From this figure it can directly be observed that the rate dependency at 23°C is stronger than at 110°C. At an intermediate temperature, for example at 80°C, we can distinguish the two slopes for different ranges of deformation rate, see Figure (2.5a). These different slopes originate from the fact that two separate deformation mechanisms are present, schematically represented in Figure (2.5b). At high temperatures or low strain rates, only the process of crystal slip or intra-lamellar deformation determines the yield stress [67]. At lower temperatures, crystal slip or inter-lamellar deformation starts to actively contribute to the observed yield stresses [68].

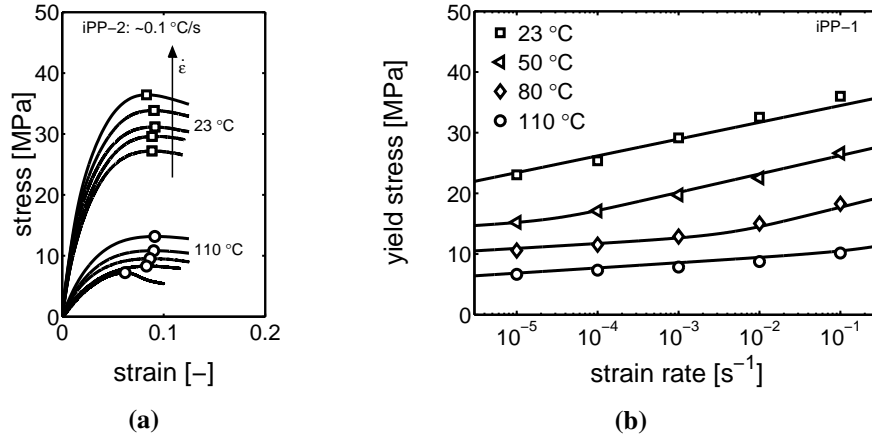


**Figure 2.4:** a) The stress-strain response of iPP as a function of strain rate and temperature, and b) The yield kinetics of iPP

Since the deformation processes act in parallel (stress additive), the observed kinetics can be described by taking the sum of the two separate processes. In this work this is done with the modified Ree-Eyring equation:

$$\sigma_{total} = \sum_{i=I,II} \sigma_i = \sum_{i=I,II} \frac{kT}{V_i^*} \sinh^{-1} \left( \frac{\dot{\epsilon}}{\dot{\epsilon}_{0,i} \exp(-\Delta U_i/RT)} \right) \quad (2.30)$$

In this equation  $k$  is the Boltzmann constant,  $T$  is the temperature in  $[K]$ ,  $\dot{\epsilon}$  is the applied strain rate,  $V_i^*$  is the activation volume of deformation mechanism  $i$ ,  $\Delta U_i$  is the activation energy of mechanism  $i$  and  $\dot{\epsilon}_{0,i}$  is the rate constant. The temperature and strain rate are specified in the experimental section.

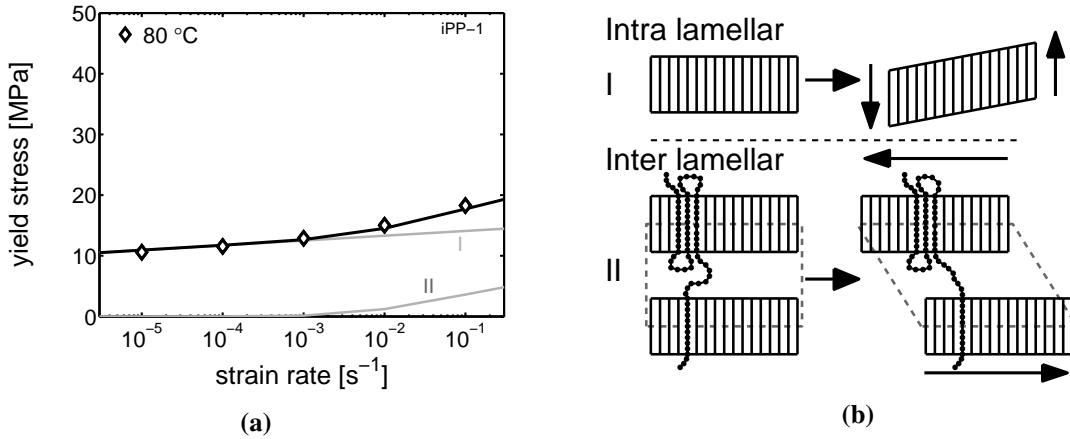


**Figure 2.5:** a): Yield data measured on iPP-1 at a temperature of  $80^{\circ}\text{C}$ . Two slopes corresponding to separate deformation mechanisms are indicated with I and II. b) Schematic representation of the intra- and interlamellar deformation mechanism

### The effect of processing

When we restrict ourselves to the influence of the cooling history a decrease in crystallinity and lamellar thickness is found upon increasing cooling rates. The effect of these structural features on the mechanical properties and in particular the yield stress was investigated in [20], and it was found that the resistance against yield becomes stronger with lower cooling rates. Furthermore it was found (by van Erp et al. [20]) that the activation volume and energy in the Ree-Eyring equation are independent of cooling rate,  $\alpha$ -nucleating agent or copolymer content. Moreover, the yield kinetics of multiple iPP grades including the ones used in this study, could be described perfectly with the same parameters. The only processing dependent variables in non-isothermal quiescent conditions were found to be the rate constants. Values for  $V_i^*$  and  $\Delta U_i$  are taken from van Erp et al. [20], and listed in Table (2.4).

**Table 2.4:** List of parameter values

	$V_i^* [nm^3]$	$\Delta U_i [kJ \cdot mol^{-1}]$
Mechanism I	14.20	503.7
Mechanism II	4.44	158.0

### Relation between structural features and yield kinetics

The only remaining Eyring parameters to be identified are the rate constants  $\dot{\epsilon}_{0,i}$ . The results of van Erp et al. [20] can straightforwardly be translated to obtain the relation

between the logarithm of the rate constant and the lamellar thickness, shown in Figure (2.6).

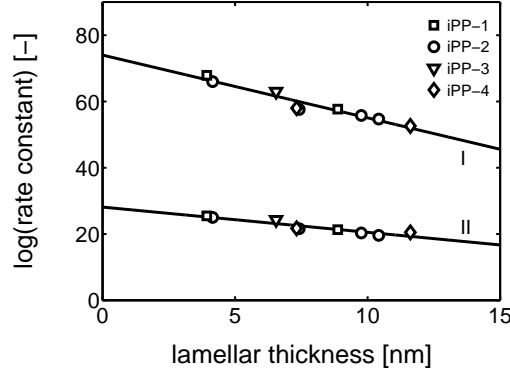


**Figure 2.6:** The relation between lamellar thickness and the rate constants, deduced from [20]

The relations associated to the lines depicted in Figure (2.6) are given by:

$$\begin{aligned} \log(\dot{\epsilon}_{0,I}) &= -1.90 \frac{l_c}{l_{c0}} + 74.01 \\ \log(\dot{\epsilon}_{0,II}) &= -0.76 \frac{l_c}{l_{c0}} + 28.12 \end{aligned} \quad (2.31)$$

with  $l_{c0} = 1\text{nm}$ . Making use of this empirical relation, which holds for multiple iPP grades enables us to predict yield kinetics once the lamellar thickness is known. Although the amount of imperfections present within the crystalline domains is cooling rate dependent, a relation between lamellar thickness and rate constant is sufficient to describe the data measured by van Erp et al. [20] under the processing conditions applied in his work.

### 2.3.4 The relation between crystallization temperature and lamellar thickness

The lamellar thickness of crystals that grow at a certain temperature  $T_c$  is inversely proportional to the undercooling according to [42]

$$l_c = \frac{2\sigma_e T_m^0}{\Delta h_f (T_m^0 - T_c)} + \delta l, \quad (2.32)$$

where  $\sigma_e$  is the surface free energy,  $\Delta h_f$  is the enthalpy of fusion and  $T_c$  is the crystallization temperature.  $T_m^0$  is the equilibrium melting temperature, i.e. the melting



temperature of a crystal with extremely large lamellar thickness. Here, the equilibrium crystallization temperature is not made pressure dependent since the pressures during the crystallization process are not far from atmospheric pressure as a result of shrinkage due to crystal formation. This first term in eq. (2.32) represents a stable condition where the increasing surface energy  $2\sigma_e$  equals the reduction in free energy obtained [69]. It should be emphasized that  $l_c$  is the lamellar thickness prior to thickening. The last term in eq. (2.32),  $\delta l$ , is related to the tendency of the polymer to maximize the crystal growth and basically is a quantity arising from the kinetic nature of crystal growth, given by [42]:

$$\delta l = \frac{kT_c}{2b_0\sigma} \left[ \frac{a_0\Delta h_f\Delta T + 4\sigma T_c^0}{a_0\Delta h_f\Delta T + 2\sigma T_c^0} \right] \quad (2.33)$$

where  $k$  is the Boltzmann constant,  $\sigma$  is the lateral surface free energy,  $b_0$  is the thickness of the surface layer and  $a_0$  is the width of the molecule. At low and moderate cooling rates  $\delta$  may be approximated by [70]:

$$\delta l \cong \frac{kT_c}{b_0\sigma} \quad (2.34)$$

The relation between lamellar thickness and crystallization temperature has been subject of many studies in the past, and an overview of some of these results is given in Figure (2.7). For example, Cheng et al. examined iPP with different degrees of stereo defects but similar molecular weight, and determined the lamellar thickness for samples crystallized isothermally at different temperatures [60]. The conclusion that can be drawn from these results is that a unique relation between  $T_c$  and  $l_c$  exists, independent of the degree of stereo defects. Iijima et al. used two iPP grades with similar isotacticity, but different molecular weights [71]. They found a relationship  $T_c$  versus  $l_c$  that holds for both their isotactic polypropylenes, independent of molecular weight. On the other hand, Lu et al. [61] used two isotactic polypropylenes with a much bigger difference in molecular weight. They found that as a result of increasing molecular weights, the surface free energy  $\sigma_e$  increases, and thus a shift in  $T_c$  versus  $l_c$ . This was interpreted as that for the lower molecular weight samples a relatively high amount of extended-chain crystallites are formed, whereas in case of higher molecular weight samples folded chain configurations are preferable. Experiments of Devoy et al. support this interpretation [72]. The  $T_m^0$  on the other hand was found to be unaffected, which is different from what Yamada et al. [73] found in their study. Lu et al. could reasonably resolve this latter disagreement by a crystallization theory proposed by Strobl [74] where the crystallization and melting are non-reversible processes. Based on the findings presented above the important conclusion is drawn that due to different molecular features present in specific iPP grades, deviations in the relation between crystallization temperature and lamellar thickness are found. Therefore this relation is determined for the iPP grades used in this

study. The assumption is made that the only variable parameter in eq. (2.32) is the surface free energy  $\sigma_e$ . In agreement with Angeloz et al. [39] and Iijima et al. [71] the equilibrium melting temperature  $T_m^0$  is chosen at 193°C, and used to describe the experimental data sets shown in Figure (2.7). An important note that should be emphasized is that the values found for lamellar thickness from X-ray experiments (partly) depend on the techniques used [56]. The interface distribution function as for example used by Iijima et al. gives the most probable value for the lamellar thickness, whereas the correlation function as for example used by Cheng et al. gives the mean value. Finally the relation of  $T_c$  versus  $l_c$  can be determined with DSC as well, as demonstrated by for example Wlochowicz et al. [75]. Another important note is that in case of extremely narrow molecular weight distributions trends will most likely be different, and only using  $\sigma_e$  to fit the relation is insufficient. The data found for the iPP grades in this work will be described using the same set of parameters, adopted from Xu et al. [76], and are given in Table (2.5).

**Table 2.5:** Model parameters.

Parameter	value
$\sigma_e [J \cdot nm^{-2}]$	$146 \cdot 10^{-21}$
$T_m^0 [K]$	466
$\Delta h_f [J \cdot nm^{-3}]$	$207 \cdot 938 \cdot 10^{-24}$
$b_0 [nm]$	0.626
$\sigma [J \cdot nm^{-2}]$	$11.95 \cdot 10^{-21}$

In Figure (2.7) it can be seen that experimental data of several authors can be described using this set of parameters, and only varying the value of the surface free energy  $\sigma_e$ . In Table (2.6) the values of this parameter are given.

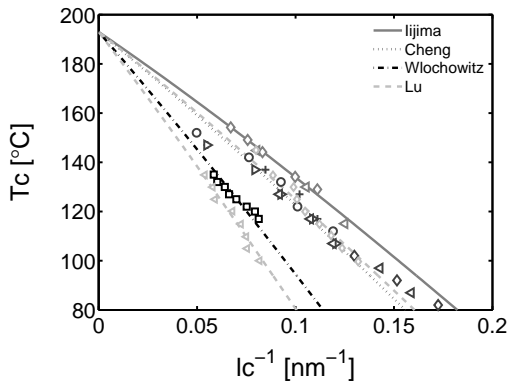


**Figure 2.7:** The relation between lamellar thickness and crystallization temperature. Lines are fitted using an equilibrium melting temperature of 193°C. Data are reproduced from [60, 61, 71, 75].

**Table 2.6:** surface free energy

Author	$\sigma_e [J \cdot nm^{-2}]$
Iijima	$113.88 \cdot 10^{-21}$
Lu (Mn=12kg/mol)	$131.40 \cdot 10^{-21}$
Cheng	$135.78 \cdot 10^{-21}$
Wlochowicz	$191.26 \cdot 10^{-21}$
Lu (Mn=340kg/mol)	$219.00 \cdot 10^{-21}$

The relation between  $T_c$  and  $l_c$  is determined for isothermal crystallization. For the non-isothermal experiments the temperature-time profiles are divided into discrete temperature steps and for each time step  $\Delta t$  a crystal volume:

$$\Delta V = \Delta t \cdot \dot{\xi} \quad (2.35)$$

is formed with an associated lamellar thickness obtained from eq. (2.32). The additional space-filling  $\dot{\xi}$ , achieved during that specific time step follows from eq. (2.29). As a result of the non-isothermal crystallization we predict lamellar thickness distributions.

## 2.4 Results and discussion

### 2.4.1 Temperature predictions

Crystallization from the melt begins with the formation of point-like nuclei that subsequently grow into spherulites. Due to the kinetics of the crystallization process different morphologies will arise when cooling rates are varied. In this study this was achieved by adjusting the temperature of the cold press, ranging from 20°C to 90°C. These temperatures act as boundary conditions in the thermal analysis. The melt was cooled from 220°C before it was placed in the cold press. In Figure (2.8a) a calculated cooling history of a 1 mm thick sheet in a 20°C cold press is shown, as a function of time and position. The cooling rates are the highest close to the wall and the lowest in the center. The effect of the latent heat release can be recognized in the center since the decrease in temperature is followed by an increase. Subsequently the temperature decreases again.

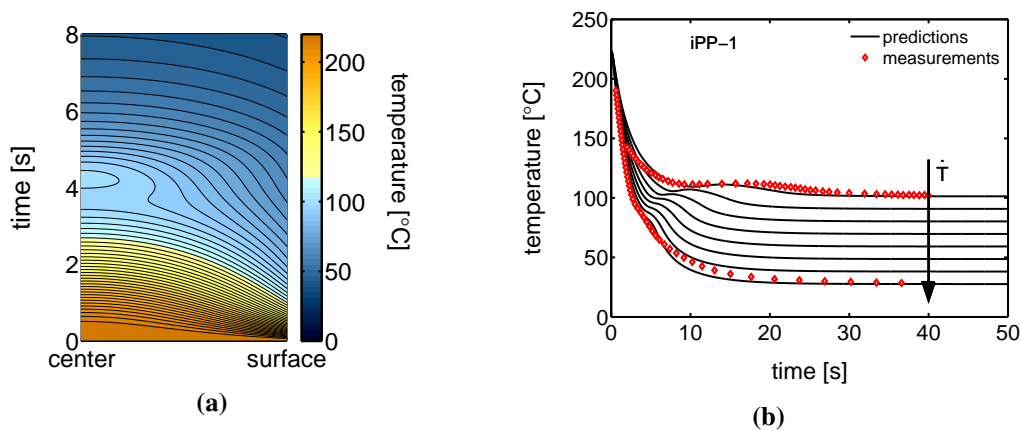


**Figure 2.8:** An example of the predicted temperature profile as a function of time and position. iPP-1 with the cold press set at 20°C (left) and the average time-temperature history of iPP-1 samples prepared with different cold press temperatures.

To validate the predicted temperature profiles, in-situ time-temperature measurements were performed in case of the slowest and the fastest cooling rates assessed in this work. The small thermocouple with a thickness of approximately 0.4 mm was embedded in the polymer material to record the temperature. Since the thermocouple is relatively thick compared to the polymer sheet, an average temperature over the sheet thickness is measured and, therefore, a comparison is made with the calculated average time-temperature profile, shown in Figure (2.8b). The position of the latent heat release contributions, featured by a plateau in the time-temperature profile, reveal that the crystallization temperatures decrease with increasing cooling rates. Moreover, it can be seen that the predictions are in good agreement with the experimental results, and that discrepancies arise mainly after the solidification. This can be explained by an increasing thermal contact resistance in the experiments, which is not included in the model. After solidification the material shrinks and as a result the contact pressure reduces. Therefore, the predicted cooling rate is higher than the measured temperature decrease after crystallization.

## 2.4.2 X-ray analysis

It is assumed that, under the moderate cooling conditions applied here, only monoclinic alpha phase will be formed and that, therefore, the crystallization model could be simplified to the form presented in section 2.3.2. To justify this assumption the wide angle X-ray patterns measured on iPP-1 for all eight cooling rates are depicted in Figure (2.9a). The crystallinities were all within  $64 \pm 5\%$  and, as expected, the characteristic  $\beta$  and  $\gamma$  peak are negligible with respect to the  $\alpha$  peak present at a scattering angle of  $2\theta \cong 12.5^\circ$ . Similar results are found for iPP-2.

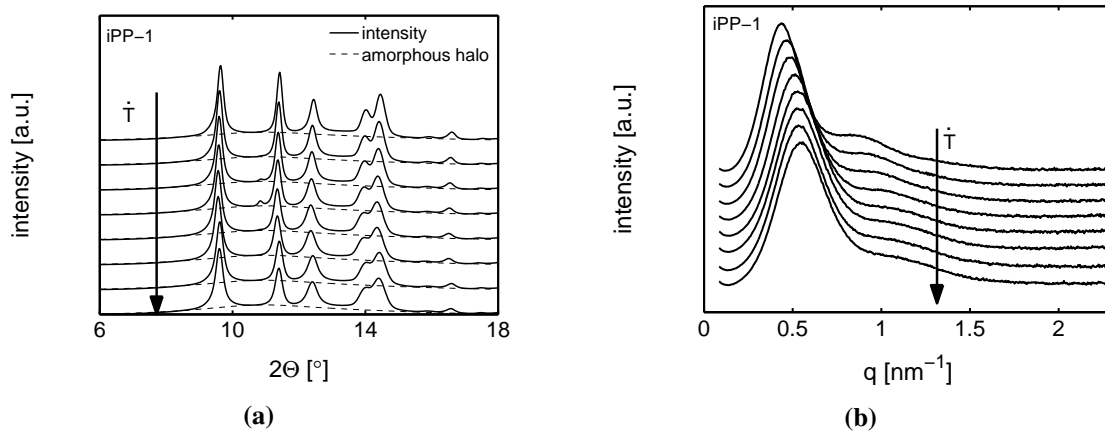


**Figure 2.9:** WAXD patterns (left) and SAXS patterns (right) measured on iPP-1 prepared with different cooling rates by adjusting the cold press temperature.

From Bragg's law the long spacing is obtained and via eq. (2.5) this gives the lamellar thickness. The SAXS data of the isothermal experiments, Figure (2.9b), is also used to

determine the interface distribution function. The corrections are explained in section 2.2.3, and a corrected 1D intensity pattern is visualised in Figure (2.10a). Also the interference function is depicted in Figure (2.10a) and is used to calculate the interface distance distribution function using eq. (2.8). A typical result is shown in Figure (2.10b) where the IDF of iPP-1 measured at 120°C is shown. Gaussians are used for deconvolution purposes. First, the most probable long spacing which is corresponding to the first minimum in  $g_1(r)$ , is fixed. Then, by using the crystallinity obtained via WAXD,  $\pm 5\%$  the ratio between the most probable lamellar thickness and amorphous layer thickness is determined and Gaussians are fitted to obtain the thickness distributions of both the crystalline and amorphous domains. The first maximum in  $g_1(r)$  corresponds to  $\alpha$  cross hatched structures and is fitted on the resulting part of the IDF [77]. The Gaussian distributions found via this deconvolution procedure are plotted in Figure (2.10b) as well.

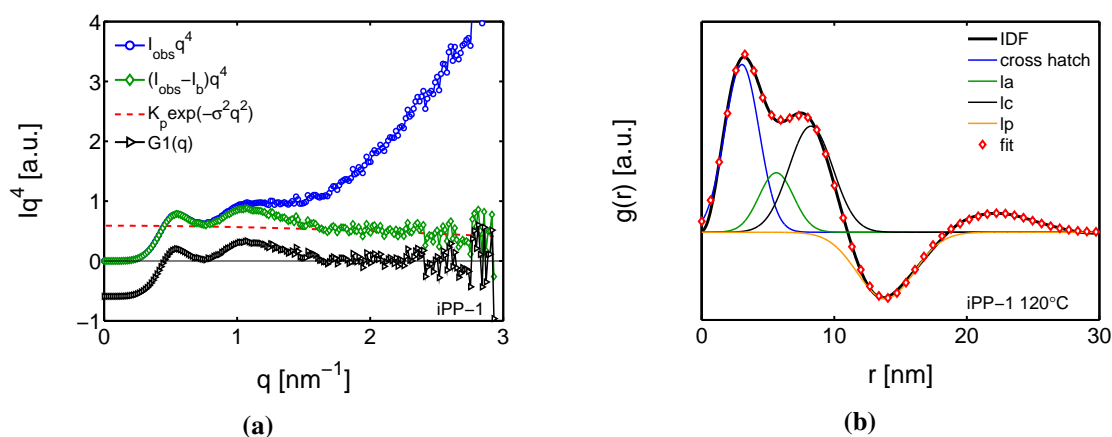


**Figure 2.10:** Correction of the observed intensity for electron density fluctuations and diffuse phase boundaries (left) and an interface distance distribution function obtained from a quasi-isothermal crystallization experiment on iPP-1 (right). The Gaussians obtained from deconvolution indicate the cross-hatch distance distribution (line), the amorphous layer thickness distribution (dashed line), the lamellar thickness distribution (dots) and the long period distribution (dash-dotted).

An important observation is that, although the quasi-isothermal crystallization would result in nearly uniform lamellar thickness according to eq. (2.32), we find distributions. The full width half maximum (FWHM) of the Gaussians is on average 3.25 for the isothermal crystallization experiments conducted on the two iPP grades. Consequently, this lamellar thickness distribution is also included in the predictions. At every time step and corresponding crystallization temperature step, a lamellar thickness distribution is formed with this FWHM. In this work the lamellar thickness obtained from the IDF was used since it gives the most probable value for the lamellar thickness [56]. Additionally, the lamellar thickness obtained from the combination of SAXS and WAXD experiments eq. (2.5) provides an estimation of the error made using the latter approach. The results are shown in Figure (2.11) and they are used in the following part by changing the

parameters in eq. (2.31) into the corrected ones given by:

$$\begin{aligned} \log(\dot{\epsilon}_{0,I}) &= -2.72 \frac{l_{c, IDF}}{l_{c0}} + 78.88 \\ \log(\dot{\epsilon}_{0,II}) &= -1.09 \frac{l_{c, IDF}}{l_{c0}} + 30.09 \end{aligned} \quad (2.36)$$

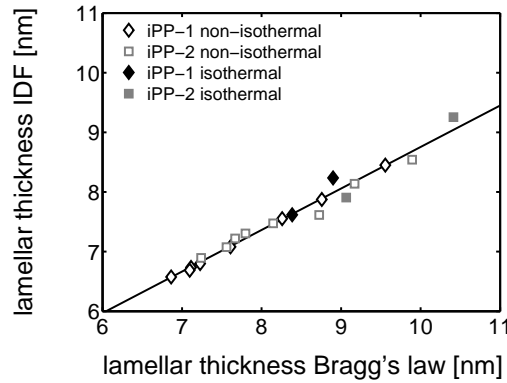


**Figure 2.11:** The lamellar thickness obtained from the interface distance distribution function (IDF) as a function of the lamellar thickness obtained from Bragg's law. Filled markers are from isothermal crystallization experiments and open markers are obtained from non-isothermal crystallization experiments

### 2.4.3 Relation between $T_c$ and $l_c$

As explained in 2.3.4 experimental data of several authors could be described using eq. (2.32) with an equilibrium crystallization temperature of 193°C and a variable surface free energy. Although different experimental methods for lamellar thickness determination yield differences in the values found, all presented data on the relation between crystallization temperature and lamellar thickness can be described accurately using the parameters given in Table (2.5) and a specific value for  $\sigma_e$  for each data set. To obtain the  $\sigma_e$  values for the two iPP grades used in this study, quasi-isothermal cooling experiments were conducted. In-situ temperature measurements demonstrate that the crystallization took place at conditions close to isothermal, see Figure (2.12a). These temperatures were plotted as a function of the lamellar thickness obtained from the IDF. From Figure (2.12b) it can be seen that using a surface free energy which is higher for the iPP with the highest molecular weight (iPP-2,  $\sigma_e = 155.5 \cdot 10^{-21} \text{ J/nm}^3$ ) and lower for the one with the low molecular weight (iPP-1,  $\sigma_e = 134.3 \cdot 10^{-21} \text{ J/nm}^3$ ) gives good descriptions for the lamellar thickness as a function of the crystallization temperature. Although the value of  $\sigma_e$  is determined on a small number of experimental data points, it seems reasonable with respect to the data reported by other authors.

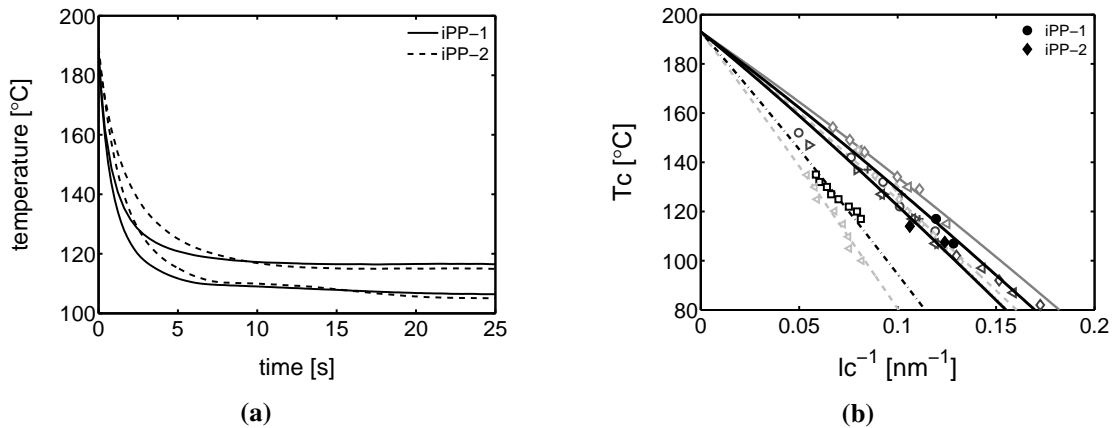


**Figure 2.12:** Temperature measurements in isothermal crystallization experiments (left), and the relation between the lamellar thickness and the crystallization temperature (right). Markers represent experimental data and lines are best fits. Filled markers are obtained from the isothermal experiments conducted on iPP-1 and iPP-2.

This fits the the expectations based on Lu et al. [61], even though the differences in molecular weight are so small that it is highly unlikely that this is the only molecular feature causing this difference. From the time-temperature history within the polymer sheet, combined with eq. (2.32) and the FWHM of 3.25, the lamellar thickness can be calculated. Summation of the distributions obtained at the different increments during the non-isothermal crystallization process gives the lamellar thickness distribution as a function of the position within the polymer sheet. In Figure (2.13a) an example of such a calculated lamellar thickness distribution profile is shown. In the center where the cooling rate was the lowest, the formed lamellae have the largest average thickness. Furthermore it can be seen that the width of the distribution is similar, independent of the position with respect to the walls of the compression molding machine. Typically the non-isothermal history adds 0.04 to the FWHM of the lamellar thickness distribution. To compare the predicted average lamellar thickness distributions with the experimentally obtained ones, they are plotted in Figure (2.13b) for the different cooling rates. The agreement between predictions and experiments is good for both grades (only results for iPP-1 are shown). The most probable lamellar thickness, as well as the corresponding width of the distributions fit the experimental data quite well, and differences of the average  $l_c$  are within 5%.

#### 2.4.4 Yield stress predictions

The lamellar thickness distributions obtained are used to predict the yield stress. Either the average lamellar thickness, or the lamellar thickness distribution can be used as an input for the relation between lamellar thickness and rate constant, see eq. (2.31). When lamellae of all thicknesses contribute equally to the resistance against yielding there is

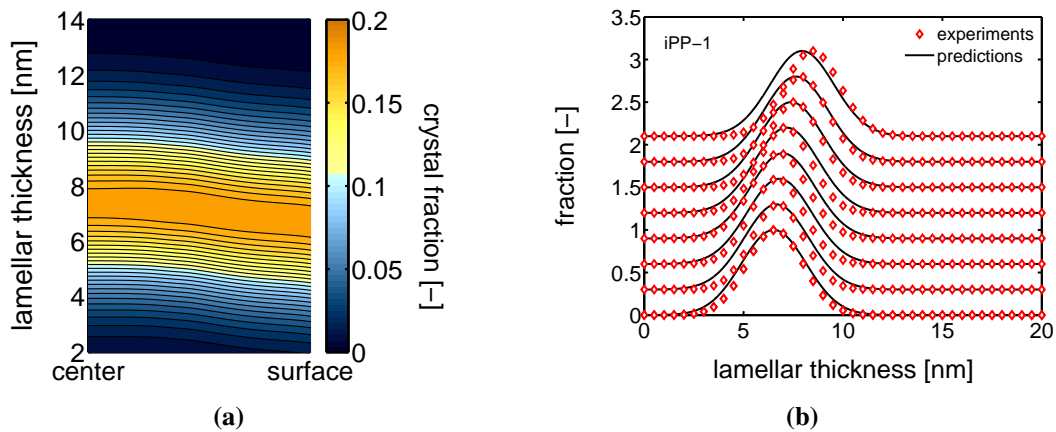


**Figure 2.13:** Predictions of the lamellar thickness distribution as a function of the position with respect to the walls of the mold in an iPP-1 sheet, cooled in a cold press set at 20°C (left). Predicted (lines) and measured (markers) average lamellar thickness distributions for different cooling rates.

actually no difference between the two procedures. To validate the yield stress predictions, experiments at room temperature and at 80°C at a strain rate of  $10^{-3} s^{-1}$  are carried out. At room temperature, both deformation mechanisms contribute to the yield stress whereas at 80°C only the contribution of the intra lamellar deformation process contributes to the yield stress. In Figure (2.14) it is shown that quantitative agreement is found for both mold temperatures. The differences in yield stress that can be seen between the two grades are in quantitative agreement with the predictions.

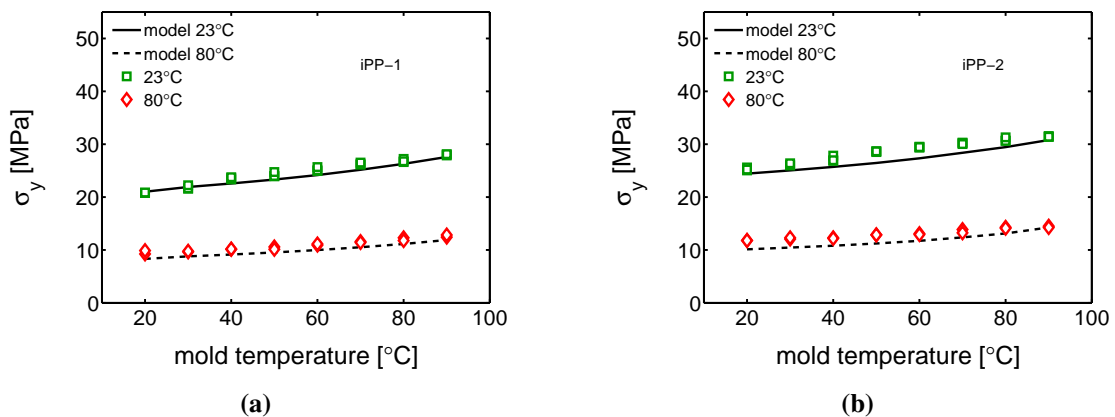


**Figure 2.14:** Yield stress of iPP-1 (left) and iPP-2 (right) at a strain rate of  $10^{-3}$  and temperatures of 23°C and 80°C. Lines are model predictions and markers are experimentally obtained data.



Although the two iPP grades used in this study are relatively similar in terms of molecular weight and polydispersity some clear differences can be observed in the level of the yield stress. These differences are first of all reflected in the crystallization model. The nucleation density as a function of temperature and pressure is different for the two grades and can be expected to be unique for every material. The maximum growth rate of the alpha crystals is slightly different for the two materials and as a result of these differences in the crystallization kinetics the range of crystallization temperatures in a non-isothermal cooling process is different. To relate crystallization kinetics and accompanying crystallization temperature to the formation of structural features like, in this case, the lamellar thickness, a material specific relation between these quantities had to be determined. In this work the inequalities were attributed to the differences in molecular chain architecture, and captured by varying the value for the surface free energy  $\sigma_e$ . The relation between lamellar thickness and yield stress contains the same parameters for both the materials, except for the rate constant which follows directly from the average lamellar thickness.

## 2.5 Conclusion

The 1D heat balance was successfully combined with a crystallization model capable of predicting the kinetics in non-isothermal pressure dependent quiescent conditions, and enabled us to predict the time-temperature history of two different iPP grades cooled in a compression molding machine at different rates. Besides the nucleation density as a function of temperature and the maximum growth rate of the  $\alpha$ -crystals all parameters in the crystallization model were the same for the two grades used in this work. The temperature predictions were experimentally validated using in-situ temperature measurements. The amount of crystal volume as a function of time and temperature followed from the model framework as well, and was used in combination with the Lauritzen Hoffman equation to predict the lamellar thickness distributions formed during the different cooling histories. By only varying the surface free energy, which is known to be molecular weight dependent, experimentally obtained data from multiple authors could be described. Therefore it was chosen to find a description of the lamellar thickness as a function of the crystallization temperature by fitting the surface free energy on data measured in-situ during an isothermal crystallization experiment. From this relation lamellar thickness distributions were predicted that were experimentally validated using the interface distribution function. Good agreement was found for both the iPP grades, not only in terms of the average lamellar thickness, but also in terms of the FWHM of the distribution. This confirms that under the cooling conditions applied in this study the Lauritzen-Hoffman equation can be used, despite the absence of isothermal conditions in time and position. Finally, the lamellar thickness distributions were used together with a corrected empirical relation between lamellar thickness and rate constant, eq. (2.36), reported in the work of van Erp et al. This enabled us to predict the yield stress directly after processing at all loading conditions, i.e. strain rate and temperature.

---

Predictions were made for a strain rate of  $10^{-3} \text{ s}^{-1}$  and temperatures of  $23^{\circ}\text{C}$  and  $80^{\circ}\text{C}$ . Tensile tests were carried out for validation and the predicted yield stresses of both the iPP grades showed good agreement with the experimentally obtained data at all loading conditions. This work shows that making the connection between processing and mechanical properties is feasible. Extension to flow and multiple crystallographic structures is part of future work.



---

# Deformation and failure kinetics of iPP-polymorphs

---

## Chapter 3

### Abstract

In this study the mechanical performance of the different polymorphs of isotactic polypropylene, typically present in iPP crystallized under industrial processing conditions, are assessed. Different preparation strategies were used to obtain samples consisting of almost solely  $\alpha$ -,  $\beta$ - or  $\gamma$ -crystals. X-ray measurements were used to validate that the desired phase was obtained. The intrinsic true stress-true strain response of all individual phases was measured in uniaxial compression at several strain rates (deformation kinetics). Moreover, measurements were performed over a wide temperature range, covering the window in between the glass transition and the melting temperature. The relation between obtained yield stress and the strain rate is described with a modification of the Ree-Eyring model. Differences and similarities in the deformation kinetics of the different phases are presented and discussed. Furthermore the presence of three deformation processes, acting in parallel, is revealed. The Ree-Eyring equation enables life time prediction for given thermal and mechanical conditions. These predictions were experimentally validated using constant load tests in uniaxial compression.

### 3.1 Introduction

Properties of isotactic polypropylene (iPP) result from a complex interplay between molecular architecture, strongly influenced by the polymerization method, additives, such as nucleating agents, and the morphological structure, which depends strongly on the thermo-mechanical history experienced during the solidification procedure. These "tools" create flexibility in tuning all kind of properties, which is the main reason that iPP shows such a broad application range. One can for example tune the transparency by the addition of nucleating agent, which leads to smaller spherulites [78, 79]. Toughness can be enhanced by the addition of a beta nucleation agent [80], or the incorporation of a copolymer [81], whereas elasticity and stiffness can be tuned with isotacticity [82]. A growing demand of iPP is currently found in structural applications, where temperature resistance and durability are key issues. The thermal stability can, for example, be improved by the addition of nanoparticles [83] and the long term properties in the ductile failure regime improve with decreasing cooling rate [20]. For this demand of a variety of properties for all kind of products, a detailed understanding of the underlying relations between structure and properties is of vital importance. When focusing at a fixed molecular architecture, in this case that of high tacticity iPP, one can still obtain huge differences in terms of crystal lattices and morphologies and, therewith, variation in physical and mechanical properties. Optimization of the properties by tuning the morphology with the applied conditions during the production process is a novel route towards improved performance, but this requires first of all knowledge about the structure property relations. In this study emphasis has been put on the effect of the crystallographic structure on the intrinsic mechanical response and the yield and failure kinetics. For isotactic polypropylene it is common knowledge that, depending on the applied conditions during the crystallization process, multiple crystallographic structures can be formed [8, 32]. If the isotacticity is sufficiently high, atmospheric pressure and moderate cooling conditions result in the formation of monoclinic  $\alpha$ -crystals, schematically shown in Figure (3.1a). Low isotacticity, comonomer like ethylene, or very high pressures result in orthorhombic  $\gamma$ -crystals (Figure (3.1c)) [10, 32, 35, 84], and the addition of  $\beta$  specific nucleation agent or the application of high shear rates gives pseudo-hexagonal  $\beta$  unit cell structures; Figure (3.1b) [8, 85, 86]. Moreover, quenching iPP at high cooling rates leads to mesophase formation. This is enhanced with increasing stereoregularity [87] or propene/ethylene random copolymer content [88]. This mesomorphic form of iPP is a disordered crystalline form that shows long range order only in the direction of the chain axis due to the ternary helical conformation. The cooling rates required to obtain almost solely mesophase in a high tacticity iPP are in the order of 200°C/s. From a practical point of view, these conditions are difficult to fulfill, and would result in large thermal and structural gradients when preparing samples for mechanical testing. Hence, the dimensions of tensile bars and of cylindrical samples used in tensile and compression experiments respectively, have typically dimensions in the order of millimeters. Therefore, this form is not considered in this work.

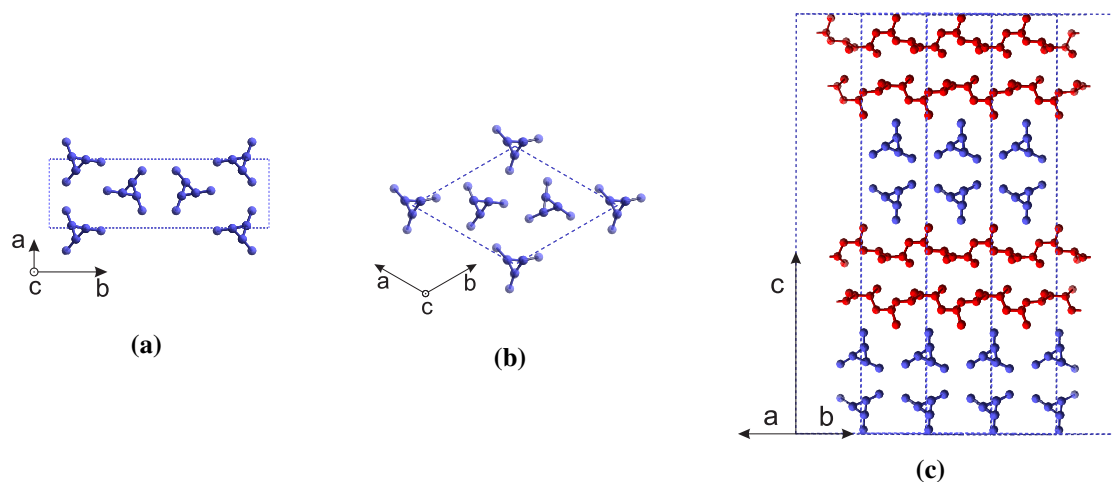


**Figure 3.1:** The crystallographic structures of the iPP-polymorphs. a) monoclinic  $\alpha$ -iPP, b) pseudo-hexagonal  $\beta$ -iPP and c) orthorhombic  $\gamma$ -iPP.

The macroscopic behavior of iPP containing these structures has already been investigated extensively. For example Van Erp et al. investigated the yield and failure kinetics of iPP materials containing either the dense  $\alpha$ -phase or the less dense mesomorphic phase in uni-axial tensile deformation. Combinations of the two, in various compositions, were investigated and some remarkable similarities were found. The activation-energy and volume, required to describe the yield kinetics were the same for all compositions [20]. Lezak et al. studied the plastic deformation behavior in  $\beta$ -iPP at different temperatures in plane-strain compression [89, 90] and made a comparison with  $\alpha$ -iPP. The initial rate of strain hardening was found to be higher for the  $\beta$ -iPP. The explanation for this is that chain slip and plastic deformation is relatively easy in  $\beta$ -crystals since no interlocking structures or cross hatches are present, whereas they typically are, in the case of  $\alpha$ -iPP. As a result the hardening due to molecular and crystalline orientation takes place at lower strains [91]. The  $\gamma$ -iPP phase was also investigated by means of plane strain compression by Lezak et al. [36, 37]. It was found that the Young's modulus and the yield stress were much higher compared to the  $\alpha$ -crystals. Similar results were found in tensile deformation where the  $\gamma$ -form displays elastic behavior in a relatively large range of deformation [92, 93]. These improved elastic properties in high tacticity iPP are thought to mainly originate from the fact that  $\gamma$ -iPP has a high fraction of tie chains (compared to  $\alpha$ -iPP) that connect the crystalline domains and thus behave as stress transmitters [94]. Although the mechanical response of these crystal structures has been topic of many studies, an extensive investigation in which the focus is on both the yield kinetics and the failure kinetics, is still lacking. Moreover, according to the knowledge of the authors, similarities and differences in the kinetics measured over a broad range of temperatures and strain rates have not been reported so far.

The present study focuses on this topic and compares samples containing one of the individual crystal phases. The different protocols used to prepare the samples containing

either  $\alpha$ -,  $\beta$ - or  $\gamma$ -crystals will be discussed first. The results of the sample preparation are analyzed by means of X-ray. These samples are then used to reveal the intrinsic material response obtained from uni-axial compression experiments. The yield kinetics and the creep behavior are determined by performing experiments over a wide range of loading conditions. The findings are discussed separately and a model is presented that captures the results over the whole range of experimental conditions.

## 3.2 Material and methods

### 3.2.1 Material

In this work an isotactic polypropylene homopolymer from Sabic is used. The weight averaged molar mass  $M_w$  of this injection molding grade is 320 kg/mole with a polydispersity index  $M_w/M_n$  of 5.4. This iPP grade is synthesized with Ziegler-Natta catalyst and has a high tacticity.

### 3.2.2 Sample preparation and X-ray characterization

In order to investigate the mechanical behaviour of iPP containing almost solely one of the distinct crystal phases, different sample preparation procedures were used. X-ray scattering is used to determine the degree of crystallinity and the lamellar thickness, which were measured by wide- and small-angle X-ray scattering (WAXD and SAXS) at the Dutch-Belgian (DUBBLE) beamline BM26 of the European Synchrotron and Radiation Facility in Grenoble (France) [47] using a Pilatus 300K and a Pilatus 1M detectors, respectively. The pixel size of both the detectors was  $172 \times 172 \mu m^2$ . In the case of the WAXD experiments the detector was placed at a distance of approximately 210 mm from the sample, whereas in case of the SAXS experiments this distance was approximately 6470 mm. The wavelength of the X-ray beam was  $\lambda = 1.033 \text{ \AA}$ . The exposure time was 30 seconds. All WAXD and SAXS data were background subtracted and integrated with the software package FIT2D. The intensity was plotted as a function of the scattering angle  $2\Theta$  and the weight percentage of crystallinity followed from:

$$\chi_w = \frac{C_{tot} - C_a}{C_{tot}} \quad (3.1)$$

Where  $C_{tot}$  is the total intensity (integrated area) and  $C_a$  is the integrated area of the scaled amorphous halo (determined on quenched low tacticity iPP with negligible crystallinity). The volume percentage of the crystallinity follows via

$$\chi = \frac{\frac{\chi_w}{\rho_c}}{\frac{\chi_w}{\rho_c} + \frac{1-\chi_w}{\rho_a}} \quad (3.2)$$

with  $\rho_c$  and  $\rho_a$  the density of the crystal phase and the amorphous phase respectively. The WAXD pattern was then used to determine the phase content of the desired crystal structures by means of fitting of the diffraction peaks using Voigt functions. To determine the long period from the SAXS data, the Lorentz corrected intensity was plotted as a function of the scattering vector  $q$ , given by:

$$q = \frac{4\pi}{\lambda} \sin(\theta) \quad (3.3)$$

Where  $\lambda$  is the wavelength and  $\Theta$  is half the scattering angle. For an isotropic system with a randomly oriented lamellar morphology the scattered intensity can be transposed to a 1D intensity using the Lorentz correction:

$$I_1(q) = I(q)q^2 \quad (3.4)$$

After the correction the long period and lamellar thickness can be obtained from:

$$l_c = l_p \cdot \chi = \frac{2\pi}{q_{I_1, max}} \chi \quad (3.5)$$

Where  $q_{I_1, max}$  is the value for the magnitude of the scattering vector, corresponding to the maximum of the Lorentz corrected intensity.

### **$\alpha$ -crystals**

Plates with a thickness of 6mm containing  $\alpha$ -iPP were prepared using compression moulding. The mould was placed in between a stack of aluminum foil (0.2 mm) and stainless steel plates (3mm), and subsequently placed in a hot press at a temperature of 230°C. Once the polymer was in the melt, pressure was applied stepwise until it reached a final value of about 10MPa. The sample was kept at this temperature for 5 minutes, erasing thermal history, and subsequently placed in a cold press at 20°C. After solidification the sample was removed from the mould. Cylindrically shaped compression specimens with a diameter and a height of  $\text{Ø}4 \times 4 \text{ mm}^2$  were machined from the plates, stored at room temperature and used in uni-axial compression experiments about 1 month after sample preparation. Sample characterization was done by means of WAXD and SAXS experiments. In Figure (3.2a) the result of a radial integration on the  $\alpha$ -iPP pattern is shown. The characteristic  $\alpha$  reflection at  $d = 4.78\text{Å}$  ( $2\Theta = 12.4^\circ$ ) is marked. The reflections of  $\beta$ - and  $\gamma$ -crystals are very small and can be found at  $d = 5.50\text{Å}$  ( $2\Theta = 10.83^\circ$ ) and  $d = 4.38\text{Å}$  ( $2\Theta = 13.31^\circ$ ), respectively. After fitting the amorphous halo, the volume percentage of crystals  $\chi$  was determined via (eq. (3.2)) to be 60%. Further fitting of the X-ray signal allows us to calculate the percentage of  $\alpha$ -crystals in the sample according to:



$$\chi_{\alpha} = \frac{A_{\alpha}}{A_{\alpha} + A_{\beta} + A_{\gamma}} \quad (3.6)$$

where  $\chi_{\alpha}$  is the volume fraction of  $\alpha$ -crystals and  $A_i$  is the area of the Voigt function that was used for fitting, corresponding to the different crystal structures. From this it was found that a successful procedure was used to prepare samples containing mainly the  $\alpha$ -phase with a volume percentage of approximately 94%. The lamellar thickness is obtained from the Lorentz corrected radially integrated SAXS experiments, shown in Figure (3.2b), and the WAXD data using (eq. (3.5)). The average lamellar thickness  $L_c$  is found to be 8.2 nm.

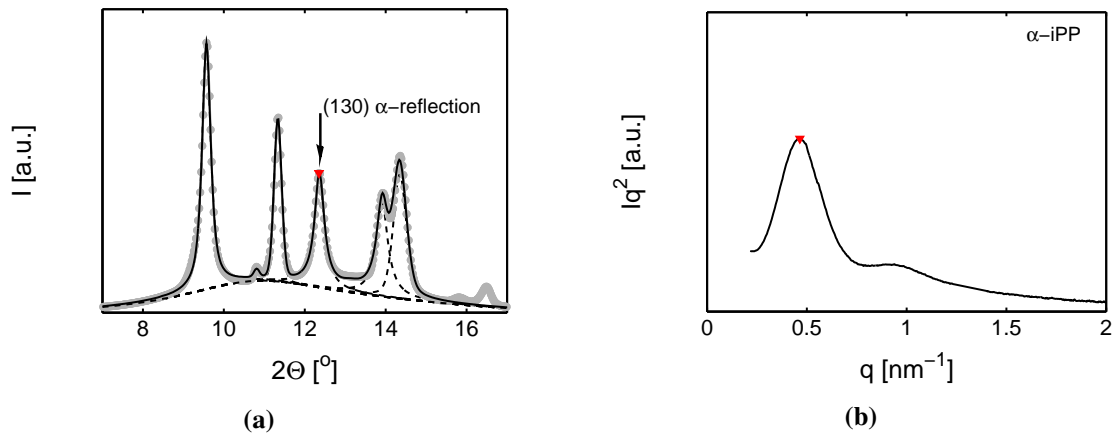


**Figure 3.2:** a) Radially integrated intensity as a function of the scattering angle  $2\theta$  (WAXD) and b), the corresponding Lorentz corrected scattering intensity as function of the scattering vector  $q$  (SAXS), for the  $\alpha$ -samples. The WAXD pattern is fitted using Voigt functions. The marker represents the characteristic reflection.

### $\beta$ -crystals

To study the deformation and failure kinetics of the  $\beta$ -phase iPP, a specific nucleating agent, NJSTAR NU100 (New Japan Chemical Group), was added with a weight percentage of 0.1% using a twin screw extruder. The  $\beta$  nucleated iPP pellets were compression molded in a mold of 8mm thickness. The procedure of the melting, the stepwise application of the pressure and the solidification was the same as for the  $\alpha$ -iPP. The diameter and height of the cylindrical samples for the uni-axial compression experiments were  $\text{\O}6 \times 6$  mm $^2$ .

The fitting of the integrated WAXD pattern, see Figure (3.3a), was again done with Voigt functions after subtraction of the amorphous halo. The crystallinity of the  $\beta$ -iPP was determined at 64 volume % of which 95% was the actual pseudo-hexagonal  $\beta$ -phase. The long period and the lamellar thickness are larger than in case of the  $\alpha$ -iPP (20.8 and 13.3

nm respectively). This follows directly from the SAXS result since the crystallinity is about the same, Figure (3.3b).

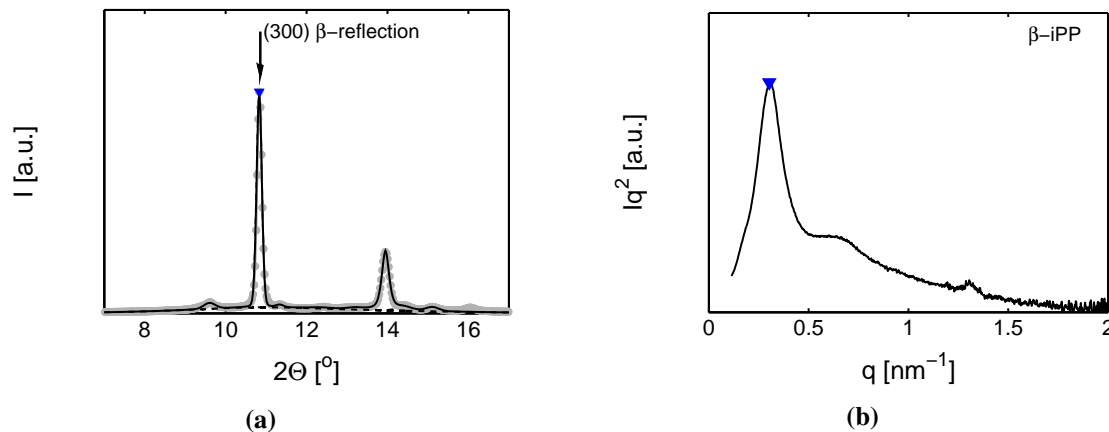


**Figure 3.3:** a) Radially integrated intensity as a function of the scattering angle  $2\theta$  (WAXD) and b), the corresponding Lorentz corrected scattering intensity as function of the scattering vector  $q$  (SAXS), for the  $\beta$ -samples. The WAXD pattern is fitted using Voigt functions. The marker represents the characteristic reflection.

### $\gamma$ -crystals

To prepare iPP containing mainly  $\gamma$ -crystals, a device is required that enables us to apply pressures high enough for the formation of orthorhombic structures. From Mezghani et al. [35] it is known that isothermal crystallization of high isotacticity iPP, like the one used in this work, requires a pressure of 180 MPa and a crystallization temperature around 180°C. This isothermal crystallization under these conditions predominantly results in the formation of  $\gamma$ -crystals. For this reason, a special tool was designed, enabling us to apply these conditions during solidification.

In Figure (3.4) a schematic of the pressure cell and a picture of the setup is shown. The device basically consists of a hollow cylinder containing cooling channels and heating elements. From bottom and top two plungers with a diameter of 60 mm, sealed with teflon plates, are used to apply pressure on the polymer. With the integrated cooling channels the applicable cooling rate is maximized and, therefore, the required time to reach the isothermal crystallization conditions is reduced. To control the temperature, thermocouples and heating elements are placed not only in the cylinder, but also in both the plungers, as close to the sample as possible. The pressure is controlled manually using a jack. The sample preparation procedure is designed on the basis of the work of Mezghani et al. [35], and shown in Figure (3.4c), where the applied thermo-mechanical history is shown as a function of time. The temperature is first increased to melt the iPP granulate. After erasing thermo-mechanical history and removing the trapped air, a pressure of 180 MPa is applied. Next, the sample is kept under isothermal conditions

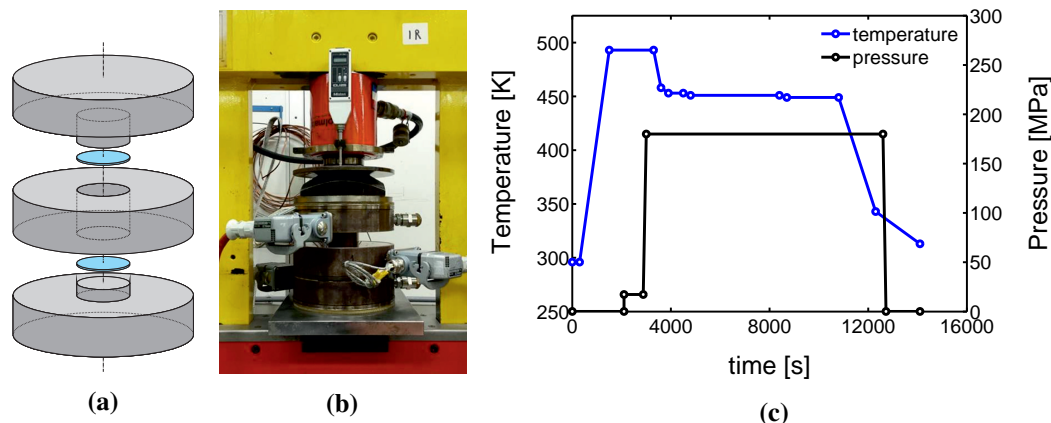


**Figure 3.4:** a) Schematic of the tool that is used to apply pressures for the preparation of iPP with  $\gamma$ -crystals. The blue disks are teflon plates for sealing. b) A picture of the experimental setup. c) The pressure-temperature protocol to prepare  $\gamma$ -iPP.

at 178°C, which is sufficiently low to crystallize the material (The melting temperature increases approximately 30°C when the pressure is increased 100 MPa, and with that also the under-cooling [41]). Finally, when the crystallization process has finished, the sample is cooled to room temperature by blowing compressed air through the cooling channels. After reaching room temperature the pressure is released and cylindrical disks containing  $\gamma$ -iPP are obtained. As a result, multiple compression samples of  $\text{\O}6 \times 6 \text{ mm}^2$  can be machined from 1 crystallization cycle. The WAXD pattern of the  $\gamma$ -iPP is shown in Figure (3.5a). With fitting, the  $\gamma$  phase content is found to be 99% of the total crystal fraction  $\chi$ , determined at 67%, meaning that the used procedure resulted in almost solely  $\gamma$ -crystals with an average lamellar thickness  $L_c$  of 10.0 nm. The SAXS pattern is shown in Figure (3.5b) and a summary of the sample characteristics is given in Table (3.1).

**Table 3.1:** Sample preparation and resulting crystallinity ( $\chi_w$  and  $\chi$ ), long period  $L_p$ , lamellar thickness  $L_c$  and amorphous layer thickness  $L_a$

	$\alpha - iPP$	$\beta - iPP$	$\gamma - iPP$
$\chi_w$ weight %	63	66	69
$\chi$ volume %	60	64	67
$L_p$ [nm]	13.5	20.8	14.9
$L_c$ [nm]	8.2	13.3	10.0
$L_a$ [nm]	5.3	7.5	4.9

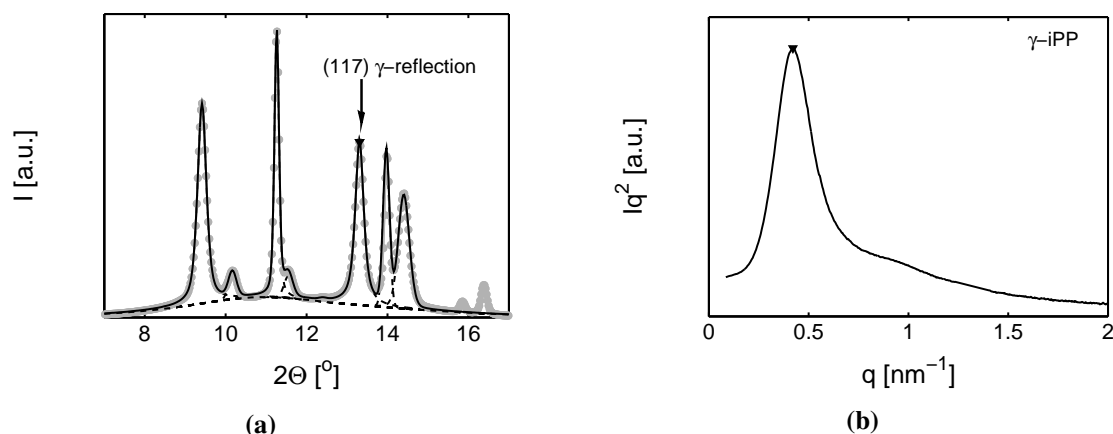


**Figure 3.5:** Radially integrated intensity as a function of the scattering angle  $2\theta$  (WAXD) and b), the corresponding Lorentz corrected scattering intensity as function of the scattering vector  $q$  (SAXS), for the  $\gamma$ -samples. The WAXD pattern is fitted using Voigt functions. The marker represents the characteristic reflection.

### 3.2.3 DMTA

DMTA measurements were performed on a TA Instruments Q800. Rectangular samples of 1mm x 4.5mm x 30mm (t x w x l), containing  $\alpha$ ,  $\beta$  and  $\gamma$ -crystals were machined from the polymer sheets. A frequency of 1Hz in a strain controlled experiment with an amplitude of 5  $\mu\text{m}/\text{mm}$  was applied. The storage and loss modulus were measured in a temperature window ranging from  $-80^\circ\text{C}$  to  $150^\circ\text{C}$ .

### 3.2.4 Mechanical testing

The mechanical characterization was done with uniaxial compression experiments performed on a Zwick 1475, equipped with a load cell of 100kN and a temperature chamber. Contact resistance between the cylindrically shaped specimens and the compression setup was reduced as far as possible with PTFE tape (3M 5480) on the flat side of the cylinder. Additionally, the contacts between the tape and the compression plates were lubricated with PTFE spray (Griffon TF89). Constant true strain-rate experiments were performed at rates of  $10^{-5}$  to  $10^{-1} \text{ s}^{-1}$  and temperatures from  $-10^\circ\text{C}$  to  $110^\circ\text{C}$  in true strain control. In addition the time to failure was measured using creep experiments in which constant true stress was applied. In both the type of experiments a correction was made in the true strain calculation to account for the stiffness of the experimental setup. Before starting the compression tests the samples were stored at the test temperature for 10 minutes to obtain thermal equilibrium between the sample and the thermally controlled environment in the oven.

### 3.3 Results and discussion

First, the mechanical behavior is compared in terms of DMTA measurements. Next, the intrinsic material behavior of iPP containing almost solely  $\alpha$ ,  $\beta$  or  $\gamma$ -crystals is discussed and compared by looking at the true stress - true strain response following from uniaxial compression experiments at room temperature and a strain rate of  $10^{-3} \text{ s}^{-1}$ . Finally the comparison is extended to the yield and failure kinetics, i.e. the yield and failure behavior over a broad range of temperatures and strain rates.

#### 3.3.1 DMTA results

The storage ( $E'$ ) and loss ( $E''$ ) moduli measured on the three iPP-samples are given in Figure (3.6a). Both the elastic and viscous moduli show qualitatively similar behavior in the lower temperature range. However, at temperatures between  $40^\circ\text{C}$  and  $120^\circ\text{C}$  the  $\beta$ -iPP shows a clear discrepancy when comparing with the other two samples. This is reflected in the DMTA experiments performed on these samples, as is shown in Figure (3.6b), where the relaxation mechanism in  $\beta$ -iPP appears less pronounced. Here, the  $\tan(\delta)$  and the dynamic modulus  $E_d$  as a function of temperature are shown. In the  $\tan(\delta)$  curve characteristic material behavior can be recognized and interpreted.

From the classical work performed by Boyd [68] it is known that when going from high to low temperatures the first peak, the  $\alpha_c$  relaxation, can be found around  $90^\circ\text{C}$ . This mechanism is related to rearrangements of/on the crystal surface due to translational movement of the stems. These movements can lead to redistributions of tight and loose folds and the inter-crystalline links and, therefore, softening of the inter lamellar material. The second peak, around a temperature of  $15^\circ\text{C}$ , is assigned to the  $\beta$  relaxation or the  $\alpha_a$  relaxation. The relaxation mechanism is linked to the loss of mobility in the (bulk) amorphous phase and is similar to the glass transition in an amorphous polymer. Finally, the last peak at a temperature of about  $-40^\circ\text{C}$  can be attributed to the  $\gamma$  relaxation. This relaxation mechanism is linked to the loss of segmental mobility in the (bulk) amorphous phase. All iPP-samples exhibit the expected response, but in the case of  $\beta$ -iPP, the  $\alpha_c$  transition is smeared out over a much broader temperature range than for the other two samples. The peak position of the  $\alpha_a$  relaxation is about the same for all iPP-samples. The dynamic moduli, also shown in Figure (3.6b), reveal that the  $\gamma$ -iPP displays the highest modulus over almost the entire temperature range. At low temperatures the  $\alpha$ -iPP has a much lower modulus.

An important observation for the case of iPP, is that the moduli in the  $\alpha_a$  and the  $\alpha_c$ -relaxation regions are not a unique function of the crystallinity [68]. The variation of the moduli with the crystallinity depends on how the crystals have been created. Furthermore, the  $\alpha_a$ -relaxation is related to the mobile amorphous fraction (MAF) in iPP, which can change upon storage at room temperature [58], see also sec. 3.3.3. In DMTA experiments, the amount of MAF is reflected in the area of the  $\alpha_a$  relaxation peak [95]. With an increasing fraction of MAF, the peak area increases. Simultaneously, the area underneath the  $\alpha_c$ -relaxation peak reflects the amount of rigid amorphous fraction (RAF).

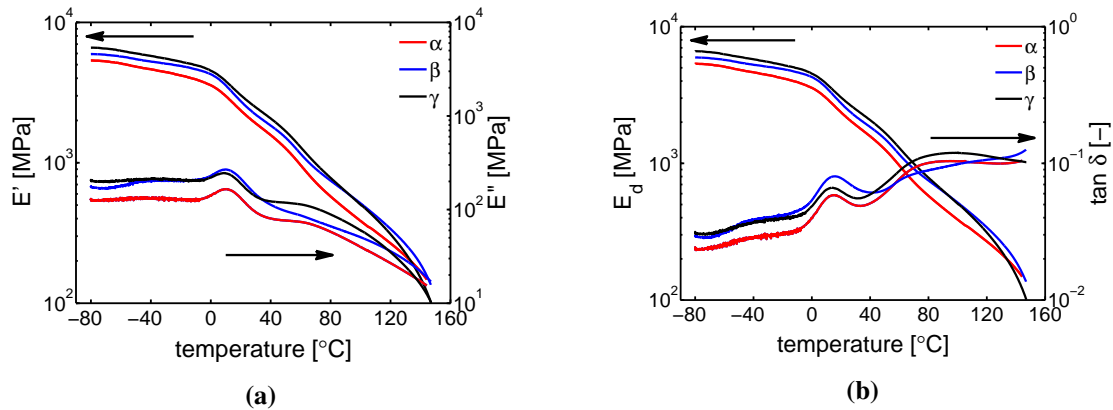


**Figure 3.6:** a) The elastic and storage modulus of the iPP-polymorphs as a function of temperature, and b) The dynamic modulus and the  $\tan(\delta)$  as a function of the temperature. The dynamic modulus  $E_d$  is the lowest for  $\alpha$ -iPP and the highest for  $\gamma$ -iPP in almost the entire temperature window. The  $\alpha_c$  relaxation of  $\beta$ -iPP is smeared out over a much broader transition range compared to  $\alpha$ -iPP and  $\gamma$ -iPP.

In a qualitative way, it can immediately be observed that the  $\beta$ -iPP displays a different response, particularly in the temperature window of the  $\alpha_c$ -relaxation, indicating that the amount of RAF is much smaller than in the case of the  $\alpha$  and  $\gamma$ -iPP. The amount MAF on the other hand is the largest for  $\beta$ -iPP (hence the logarithmic scale). This observation is confirmed by the work of Policianova et al. [96], where solid state NMR was used to investigate the molecular mobility in the amorphous and crystalline domains of  $\alpha$  and  $\beta$ -iPP. Compared to  $\beta$ -crystals, the  $\alpha$ -crystals exhibit larger restrictions on the chain mobility in the crystals, as well as in the constrained amorphous domains. Based on the DMTA results it is expected that the RAF in  $\gamma$ -iPP is even more constrained.

### 3.3.2 Intrinsic material response

To investigate the intrinsic stress-strain response, i.e. the material behavior in homogeneous deformation (to eliminate effects of sample geometry), the mechanical behavior is studied by means of uni-axial compression experiments. A typical example of results obtained from such experiments is shown in Figure (3.7), where the response, measured at room temperature and a strain rate of  $10^{-3} \text{ s}^{-1}$ , of  $\alpha$ -,  $\beta$ - and  $\gamma$ -iPP is shown. Initially linear elastic behavior is displayed but with increasing strain, and consequently increasing stress, a growing deviation from this behavior can be observed. The increasing stress makes the system more mobile, and thereby facilitates plastic deformation. At the yield stress, the mobility has become that high that the plastic deformation rate equals the applied strain rate. A higher applied strain rate requires a higher stress to achieve this balance for yielding, giving rise to the rate dependency of the yield stress. Mobility is also facilitated by temperature, making plastic flow more easy at elevated temperatures. After yielding, softening can be observed, subsequently followed by hardening. Obviously,

these mechanical characteristics are strongly connected to the morphology and structure on a microscopic scale. In the following sections we elaborate on the structural features that are of importance for these properties, and make a comparison between the different crystal structures.

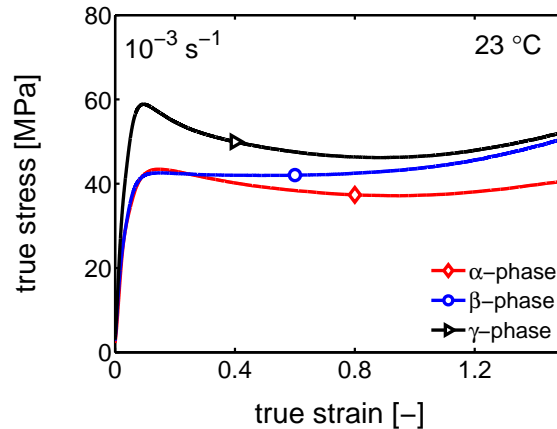


**Figure 3.7:** Intrinsic stress-strain response in uniaxial compression experiments, measured at room temperature and a strain rate of  $10^{-3} \text{ s}^{-1}$ .

### Elastic modulus

The elastic modulus is taken from the slope of the stress-strain response in the region where the behavior is linear elastic. The moduli show a strong temperature, see Figure (3.8), and rate dependence, originating from the time-dependent nature of polymeric materials. Determination of the modulus between true strains of 0.4 % and 1% reveals that the value of the modulus is the highest for the  $\gamma$ -crystals and the lowest for the  $\alpha$ -crystals. As expected, this is correlated to the crystallinity of the samples, Table (3.1). However, another contributing factor to the Young's modulus is the part of the amorphous phase that is in the glassy state at a given temperature. Besides crystallinity, the constraints imposed by the different crystallographic structures also affect the elastic modulus. The trend is in good agreement with the complex modulus measured with DMTA and plotted in Figure (3.6b).

### Yield stress

The yield stress of polymers depends strongly on loading conditions and, in the case of semi-crystalline polymers, it depends on structural features like crystallinity or lamellar thickness as well [20]. Furthermore, imperfections in the crystal lattices can have a pronounced effect [97]. It is difficult to draw clear conclusions on the effect of these distinct structural features, since it is hard to vary single features without affecting others. The crystallinity of the  $\alpha$ ,  $\beta$  and  $\gamma$ -iPP studied in this work is quite similar, but differences

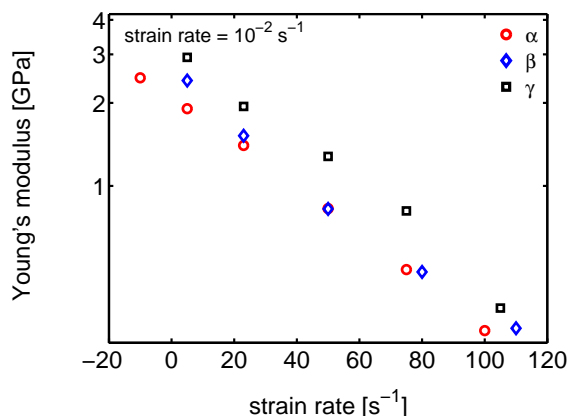


**Figure 3.8:** The Young's moduli obtained from uniaxial compression experiments at a strain rate of  $10^{-2} \text{ s}^{-1}$  at different temperatures for the three iPP-polymorphs.

are present in, for example, the lamellar thickness. Moreover, the amount of imperfections in the crystals can not be easily quantified. Although the crystallinities are comparable, the  $\gamma$ -samples show a much higher yield stress than  $\beta$  and  $\alpha$ -iPP, see Figure (3.7). The lamellar thickness of  $\alpha$ -iPP is much smaller than the lamellar thickness of  $\beta$ -iPP, but the yield stress is similar. This illustrates the before mentioned difficulties. For a given crystal phase the yield stress is correlated to the lamellar thickness; an increase of about 2 [nm] in the lamellar thickness of  $\alpha$ -iPP yields an increase of approximately 8 [MPa] in the yield stress [98]. This gives rise to the presumption that an additional feature like the crystal unit cell structure or the accompanying amount of imperfections affects the level of the yield stress as well. In section 3.3.3 we give a possible explanation for the large differences in the yield stress of the  $\gamma$ -phase compared to  $\alpha$  and  $\beta$ -iPP, based on the fact that in deformation at least half of the chains in the  $\gamma$ -crystals is loaded under an angle. The amorphous layer thickness and the constraints applied by the crystals on the amorphous domains most likely affects the level of the yield stress.

### Strain softening

In the amorphous phase, physical aging results in an increase in the yield stress. Upon deformation the stress decreases and, therefore, mechanically rejuvenates the sample. This process is called softening and is also observed in  $\alpha$  and  $\gamma$ -iPP (Figure (3.7)). The glass transition temperature  $T_g$  of bulk amorphous iPP is about  $-10^\circ\text{C}$  and is therefore lower than the temperature employed in the experiments. However, the transition from crystalline towards amorphous domains is not sharp. In the vicinity of the crystals the amorphous phase is constrained and thus less mobile. This leads to a gradient in the glass transition temperature. As a result, parts of the amorphous domains can be in the glassy state, even at temperatures far above the bulk amorphous  $T_g$ . For example, at room temperature, in the specific case of iPP, a distinction can be made between



mobile amorphous domains and rigid glassy amorphous domains. These domains are possible contributors to the softening behavior observed in the true stress-true strain response, depending on the temperature. Moreover, the amount of softening varies with the thermodynamic state and the fraction of the rigid amorphous phase. Besides the amorphous contribution to softening, there can also be a crystalline contribution. Yielding or plastic flow induces the destruction of crystals at low temperatures or phase transitions at elevated temperatures. Especially the destruction of crystals is generally accompanied by a decrease in the resistance against deformation (softening) and, therefore, a reduction of the stress in a constant rate experiment. The level of destruction is governed by the mobility of the chains within the crystallographic structure which is connected to the density. A comparison between the softening of  $\alpha$ -,  $\beta$ - and  $\gamma$ -iPP, Figure (3.7), reveals tremendous differences. Where the  $\beta$ -crystals don't show softening in their stress-strain response, the  $\gamma$ -crystals display a yield drop of about 15 MPa and the  $\alpha$ -crystals are in between.

### Strain hardening

In Figure (3.7) it can be seen that  $\beta$ -iPP shows much stronger strain hardening than  $\alpha$ -iPP. The hardening of  $\gamma$ -iPP samples is slightly stronger than that of  $\alpha$ -iPP. In general the level of hardening is assigned to the network density, which is high for  $\gamma$ -iPP [99]. In the case of semi-crystalline polymers this density consists out of entanglements and tie-molecules, since both can act as stress transmitters.

The entanglement density is related to the chain stiffness. Since in this work all samples are prepared with the same polymer this can not explain the large differences observed in the experiments. From Schrauwen et al. [26] it is known that within the exact same polymer, different hardening moduli can be found. This observation was attributed to reeling in; rearrangement of polymer chains that are folded into the crystals. In the case of  $\beta$ -iPP, nucleating agent is used and therefore the crystallization kinetics are very fast, reducing this phenomenon [100]. The  $\gamma$ -iPP on the other hand is isothermally crystallized, allowing in theory for chains reeling in and thus more disentanglement of the amorphous phase. Observing significant differences in the hardening modulus caused by reeling in requires much larger differences in crystallization times. Indeed, the time scales used by Schrauwen et al. to investigate reeling-in were much higher than the time scales required for the sample preparation in this work, taking this effect as an explanation for differences between the hardening of  $\alpha$ -,  $\beta$ - and  $\gamma$ -iPP into question. However, he investigated reeling in after the crystallization process, which is different from reeling in during crystallization where the crystallization rate dominates.

After yielding and plastic flow, chains can move through the crystals and therefore tie molecules loose their ability to act as a stress transmitter. However, it is known that upon deformation the solid state phase transitions take place into either meso-phase or other crystal structures [36,37,89,90,92,101–103]. This means that the structural integrity is at least partially maintained, and the destruction, transformation or reformation of crystals upon the application of strain can in that perspective no longer be neglected. To reveal

the exact role of the different mechanisms and find out whether they explain the large differences in hardening, further research is required.

### 3.3.3 Yield kinetics

The intrinsic yield kinetics are investigated by means of compression tests of which the results are shown in Figure (3.9), where the true stress as a function of the true strain is plotted for some of these experiments. The markers indicate the yield stress, defined as the maximum. Occasionally, in the case of  $\beta$ -iPP, a well defined yield point is missing. In these cases the yield stress was defined as the true stress corresponding to a true strain of 0.16 [-], which is chosen since this is a strain at which yielding typically occurs.

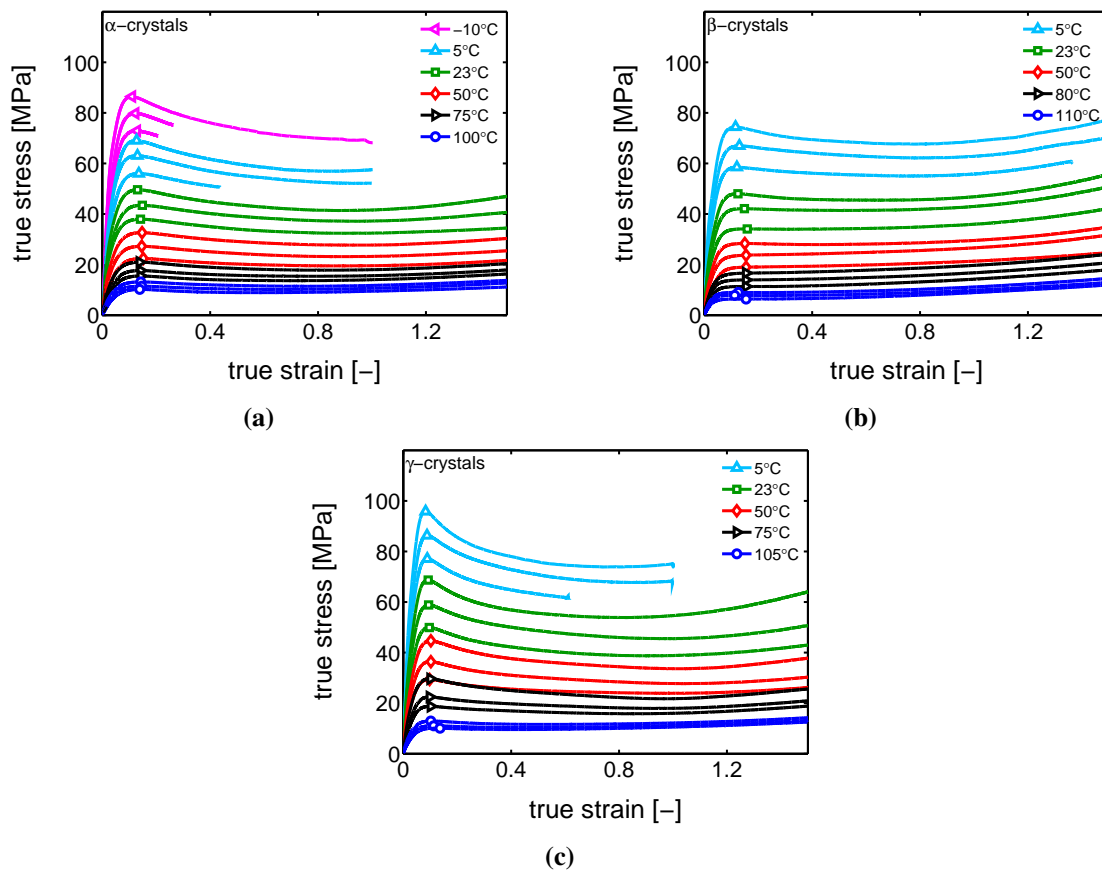


**Figure 3.9:** a) The stress-strain response of  $\alpha$ -iPP for different strain rates and temperatures. The temperature range varies between a minimum temperature around the glass transition and a maximum well below the melting temperature of the crystals. The strain rates shown in the graphs are  $10^{-4}$ ,  $10^{-3}$  and  $10^{-2}$  from bottom to top. b) The stress-strain response of  $\beta$ -iPP and c), The stress-strain response of  $\gamma$ -iPP. The markers represent the yield stress.

First we will focus on the yield kinetics of  $\alpha$ -iPP to discuss the typical behavior and the dependence on the loading conditions, i.e. temperature and strain rate. When plotting the yield stress as a function of the applied strain rate (Figure (3.10a)), it can be observed that at room temperature the rate dependency is much stronger than at elevated temperatures. This typical behavior is observed for many polymeric systems, either amorphous [104] or semi-crystalline [105] and the presence of multiple rate dependencies is related to the different deformation mechanisms that are active.

A successful way to describe this behavior was proposed by Ree and Eyring [106], who modeled the different rate dependencies by two stress activated deformation processes acting in parallel according to eq. (3.7):

$$\sigma_{total} = \sum_i \sigma_i = \sum_i \frac{kT}{V_i^*} \sinh^{-1} \left( \frac{\dot{\epsilon}}{\dot{\epsilon}_{0,i} \exp(-\Delta U_i / RT)} \right) \quad (3.7)$$

where  $k$  is the Boltzmann constant,  $R$  the universal gas constant,  $T$  is the temperature in  $[K]$ ,  $\dot{\epsilon}$  is the applied strain rate,  $V_i^*$  is the activation volume of deformation mechanism  $i$ ,  $\Delta U_i$  is the activation energy of mechanism  $i$  and  $\dot{\epsilon}_{0,i}$  is the rate constant. In this study, however, the experimentally assessed temperature window is extended so that a third deformation mechanism is required to adequately describe the yield kinetics.

Using this equation to fit the experimentally obtained yield stress for  $\alpha$ -iPP results in the description shown in Figure (3.10a).

The same fits are made for  $\beta$ - and  $\gamma$ -iPP shown in Figure (3.10c) and (3.10e) respectively. At room temperature the rate dependence of the  $\gamma$ -iPP is clearly the strongest and the yield stress is about 20% higher than in case of the  $\alpha$  or  $\beta$ -iPP. This is partly due to the fact that for  $\gamma$ -iPP, the contribution of the third rate dependency can already be observed in the response at room temperature (this is more clear in Figures (3.10b), (3.10d) and (3.10f)).

In the case of  $\alpha$ -iPP the appearance of a third slope is less obvious than in the case of  $\gamma$ -iPP, when only looking at the rate dependency. For this reason the yield data are presented in a different way, see Figures (3.10b), (3.10d) and (3.10f), where the yield stress is plotted as a function of the temperature for different strain rates. From this figure it is very obvious that the temperature dependency displays three different regions, each with their own slope.

The parameters used to describe the yield data are given in Table (3.2) for all crystallographic structures and the three deformation mechanisms. The activation volume is a measure for the rate dependency, whereas the activation energy is directly related to the temperature dependence. The rate constants are state parameters and depend on for example the lamellar thickness or physical age of the rigid amorphous domains [20]. Variations in the rate constants are only meaningful if the activation energy and volume are kept constant. For that reason they are not discussed further in this section, where the values of the Eyring parameters (for the different crystal structures) are compared.

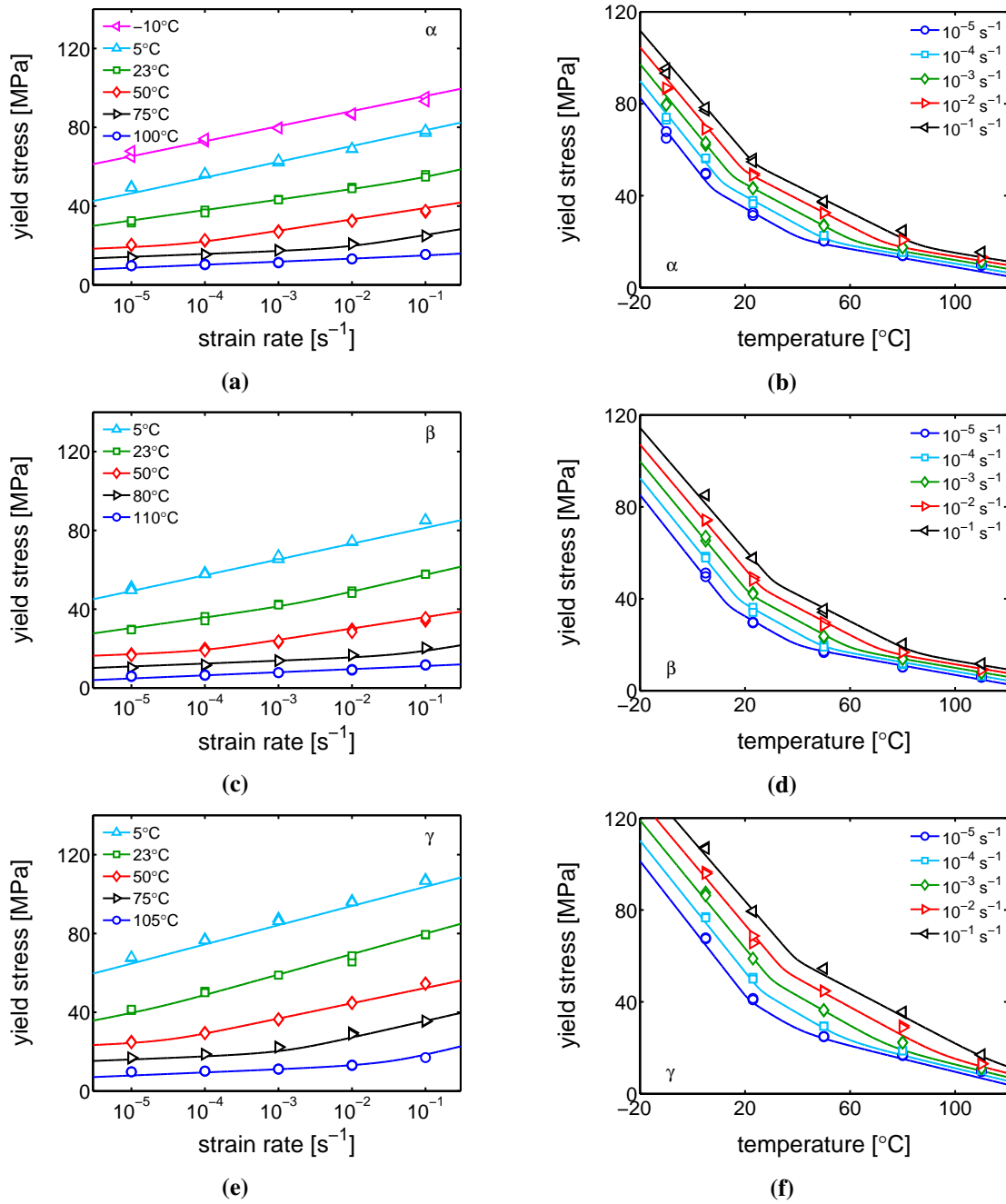


**Figure 3.10:** The yield kinetics of a)  $\alpha$ -iPP, c)  $\beta$ -iPP and e)  $\gamma$ -iPP. Markers represent the yield stress found with uniaxial compression experiments and lines are best fits of eq. (3.7). The yield kinetics of b)  $\alpha$ -iPP, d)  $\beta$ -iPP and f)  $\gamma$ -iPP presented as a function of temperature. Again lines are descriptions using the Eyring theory and markers represent the experimentally obtained yield stress.

**Table 3.2:** List of parameter values

	$V_i^* [m^3]$	$\Delta U_i [J \cdot mol^{-1}]$	$\dot{\epsilon}_{0,i} [s^{-1}]$
<b><math>\alpha</math>-crystals</b>			
Mechanism <i>I</i>	$7.70 \cdot 10^{-27}$	$3.84 \cdot 10^5$	$2.0 \cdot 10^{43}$
Mechanism <i>II</i>	$2.31 \cdot 10^{-27}$	$1.95 \cdot 10^5$	$4.1 \cdot 10^{27}$
Mechanism <i>III</i>	$2.89 \cdot 10^{-27}$	$3.95 \cdot 10^5$	$6.5 \cdot 10^{68}$
<b><math>\beta</math>-crystals</b>			
Mechanism <i>I</i>	$7.70 \cdot 10^{-27}$	$3.84 \cdot 10^5$	$4.2 \cdot 10^{44}$
Mechanism <i>II</i>	$2.31 \cdot 10^{-27}$	$1.95 \cdot 10^5$	$5.9 \cdot 10^{27}$
Mechanism <i>III</i>	$2.89 \cdot 10^{-27}$	$3.95 \cdot 10^5$	$1.6 \cdot 10^{67}$
<b><math>\gamma</math>-crystals</b>			
Mechanism <i>I</i>	$7.70 \cdot 10^{-27}$	$5.30 \cdot 10^5$	$2.0 \cdot 10^{63}$
Mechanism <i>II</i>	$1.59 \cdot 10^{-27}$	$1.25 \cdot 10^5$	$9.6 \cdot 10^{15}$
Mechanism <i>III</i>	$2.89 \cdot 10^{-27}$	$3.95 \cdot 10^5$	$2.0 \cdot 10^{65}$

The presence of the additional third deformation mechanism has already been observed before [107–109], and for the interpretation we start from Figure (3.10). Here, it can be clearly observed that for all three polymorphs the yield stress contribution of process 2 becomes negligible at a temperature of 80°C and a strain rate in the order of  $10^{-2}$ - $10^{-3} s^{-1}$ . This implies that, at higher temperature or lower strain rates, there is sufficient thermal mobility to facilitate the molecular deformation process without the requirement of substantial stress activation. The DMTA results in Figure (3.6) indicate that this "fade-out" region of the deformation mechanism II contribution coincides well with the onset of the so-called  $\alpha_c$ -relaxation. This transition finds its origin in the migration of conformational defects within the crystalline phase, causing a translational mobility of chains throughout the crystal lattice (chain diffusion) [68, 110]. This chain mobility releases the constraint on the inter lamellar amorphous region, allowing it to relax and deform. This creates the peculiar situation that the relaxation strength of the  $\alpha_c$ -transition is linked to the interlamellar amorphous regions, whereas the mobility undoubtedly originates within the crystalline phase [68]. In the case of the  $\alpha$  and  $\beta$ -polymorphs, the activation energy for process II, 195 kJ/mol, is well within the range of 163-222 kJ/mol reported for  $\alpha_c$ -relaxation in literature [111, 112]. It seems therefore appropriate to assign process II to deformation of the inter lamellar amorphous regions. Remarkably, the value for the  $\gamma$ -polymorph is considerably lower with only 125 kJ/mol. To our knowledge, however, there are no previous reports for  $\alpha_c$ -relaxation in  $\gamma$ -iPP. A hypothesis for the large differences observed between  $\gamma$ -iPP and the other crystal structures is given later in this section.

Concerning the high temperature/low strain rate process I, plastic deformation of the crystalline lamellae through a crystallographic slip mechanism was previously proposed as the underlying mechanism [4, 29, 67, 97]. Remarkably, however, the results presented here for the different polymorphs seem to disagree with this interpretation. As presented in Figure (3.1), the crystalline unit cells are considerably different for the three polymorphs, and, consequently, it is difficult to imagine that the slip kinetics of the polymorphs would be comparable. Nevertheless, the deformation kinetics (in terms of activation volume and thus stress dependence) are nearly identical for all three crystallographic structures. An explanation for this observation can possibly be found in the fact that the only structural similarity between the three crystallographic structures is the presence of isotactic chains in a ternary helical conformation. Since, above the  $\alpha_c$ -relaxation temperature, or at appropriate time scales, these chains will have obtained translational mobility, the origin of the plastic deformation of the lamellae might be found in a collective diffusive mobility of the chains from which the crystal is comprised. This collective translational mobility renders the crystal "fluid-like", giving rise to a diffuse type of deformation that is quite distinct from crystallographic slip [113].

The third process, appearing at low temperatures or high strain rate appears to be linked to the low temperature transition observed in DMTA, generally assigned to the glass transition of the unconstrained amorphous phase. For all three crystallographic structures the activation energy and activation volume of this  $\alpha_a$ -relaxation (or  $\beta$ -relaxation) is identical. The yield kinetics in the low temperature region are not influenced by the crystals and as expected, the Eyring parameters are similar, independent of the crystal structures. A schematic interpretation of these three different mechanisms follows from the classical work of Boyd [68], and is depicted in Figure (3.11).

Considering this schematic representation, combined with the observations made for the intra-lamellar deformation mechanism I, a discussion is triggered to find an explanation for the difference in activation energy between  $\gamma$ -iPP and the other two polymorphs. First of all, this mechanism is interpreted as a diffuse type of deformation, rather than the slip of planes within the crystallographic structure itself. Therefore it is suggested that the mobility of the helix is the dominant factor to determine the stress and temperature dependence of this process. However, as mentioned before, the activation energy for the  $\alpha$  and  $\beta$ -iPP can be chosen the same, whereas the activation energy of  $\gamma$ -iPP is distinctly higher. This activation energy of the intra-lamellar deformation mechanism is not related to the amount of imperfections in the crystals or the lamellar thickness, since both can be modeled successfully by only varying the rate constant, as is shown by Pepels et al. [97] and van Erp et al. [20] respectively. Therefore this can not be an explanation for the huge difference in activation energy observed for  $\gamma$ -iPP. On the other hand, it is known that  $\gamma$ -crystals display a crossed stacking of the chains within the lamellae, see Figure (3.12). This might possibly be at the origin of the high activation energy and yield stress. Due to the chain packing within the crystal lattice, stresses arising upon deformation always act under an angle since chains are stretched perpendicular to the lamellae (also lamellar stacks with a different orientation will at some point rotate perpendicular to the

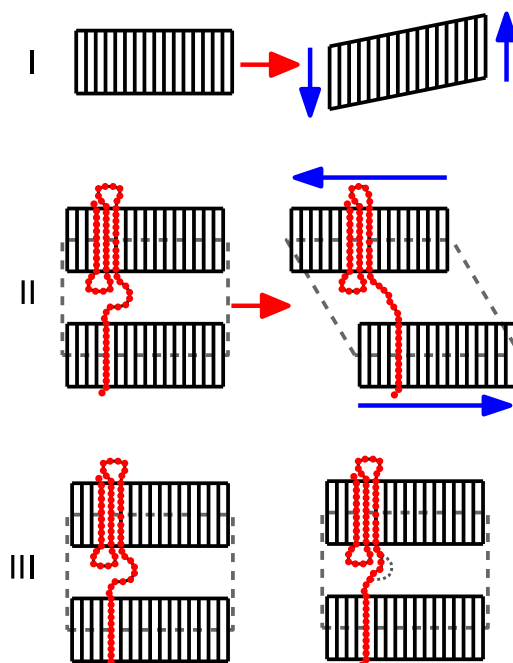


**Figure 3.11:** A schematic representation of the structure prior to deformation and after intra lamellar deformation or crystal slip (mechanism I), Inter-lamellar or  $\alpha_c$ -relaxation (mechanism II) and  $\beta$  or  $\alpha_a$ -relaxation (mechanism III).

deformation direction). This will hinder the diffuse crystal deformation and thus increase the resistance against yielding. The stress acting on the chain perpendicular to the lamellar stack can be decomposed in the following two parts: a component parallel to the chain and one perpendicular to the chain. The stress working parallel to the chain axis direction, i.e. the stress required for diffuse crystal deformation, is a factor  $\cos(40^\circ)$  lower than the stress applied perpendicular to the lamellar stack. Remarkably, if we apply this same factor to the yield stress determined with the  $\gamma$ -iPP parameters, at high temperatures, where only deformation mechanism I contributes to the mechanical response, it follows that the yield stress is roughly the same as the ones found for  $\alpha$ - and  $\beta$ -iPP. Instead, when comparing for example the yield stresses found at a strain rate of  $10^{-2} \text{ s}^{-1}$  and a temperature of  $110^\circ\text{C}$ , values of 27.8, 26.2 and 26.7 MPa are found for  $\alpha$ -,  $\beta$ - and  $\gamma$ -iPP respectively. This confirms the hypothesis that the mobility of the helix within the crystal determines the deformation kinetics, rather than the crystal structure on its own. Nevertheless, the packing of the chain within the lattice seems to have a major influence on the level of the yield stress.

Besides a comparison based on the parameters used in the Eyring equation, differences and similarities in the three deformation mechanisms can also be visualized by plotting the contributions separately. In Figure (3.13a,c,e) three distinct deformation mechanisms at room temperature are plotted for the  $\alpha$ -,  $\beta$ - and  $\gamma$ -crystals. From these figures it

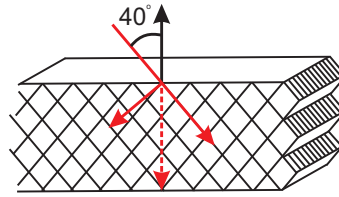


**Figure 3.12:** A schematic representation of iPP chains in  $\gamma$ -lamellae. The force applied perpendicular to the lamellar stack can be decomposed in components parallel to the chain.

follows immediately that the strong stress dependence of  $\gamma$ -iPP (at low temperatures or high strain rates) in comparison with  $\alpha$ - and  $\beta$ -iPP results from the inter-lamellar deformation mechanism and is therefore directly related to the constrained amorphous phase, see Figure (3.13c).

In order to compare the temperature dependence of each deformation mechanism similar plots are made and shown in Figure (3.13b,d,f). In the intra-lamellar deformation mechanism the  $\gamma$ -crystals display the strongest temperature dependence and the highest yield stress. Around a temperature of 120°C the descriptions coincide. Here, the  $\gamma$ - and  $\beta$ -crystals transform to the more stable monoclinic  $\alpha$ - form [37, 90] during deformation, and thus the model description does not hold at temperatures in this range. For the inter-lamellar deformation process it is found that the temperature dependence is the weakest for  $\gamma$ -iPP (smallest  $\Delta U$ ), however, if the effect of  $\dot{\epsilon}_{0,II}$  is taken into account it appears that the mobility is the lowest, which might be explained with a higher amount of constraints on the amorphous regions in the vicinity of the crystal lattices. Finally, the bulk amorphous contribution shows a temperature dependence that intersects at 0 K, which is expected when the activation energy and volume are equal, as can be deduced from eq. (3.7).

So far all the mechanical analyses are performed on samples that had aged at room temperature for at least one month. In the intrinsic material response, a relation exists between the (aged) rigid amorphous fraction and the amount of softening, or the yield drop. Softening resulting from the glassy part is two-fold: first of all the yield drop depends on the age of rigid amorphous phase and second, the amount or fraction of material in the rigid amorphous state also affects the softening. As a result there is a clear relation between the age of the iPP and the yield kinetics below the  $\alpha_c$  temperature. This is shown by Yue et al. [16] who investigated the effect of physical aging at room temperature. In their work it is suggested that aging results in a decrease of the activation volume. To our knowledge this effect has not been studied for  $\beta$ - or  $\gamma$ -iPP. In amorphous materials the rate constant is typically the only state dependent variable that is modified as a result of aging, although Senden et al. showed that in specific situations also the activation energy can increase with aging [114, 115]. Modifying the rate factor of deformation mechanisms II and III, where physical aging can be observed, is therefore the most straightforward way to incorporate aging in the Eyring based description.



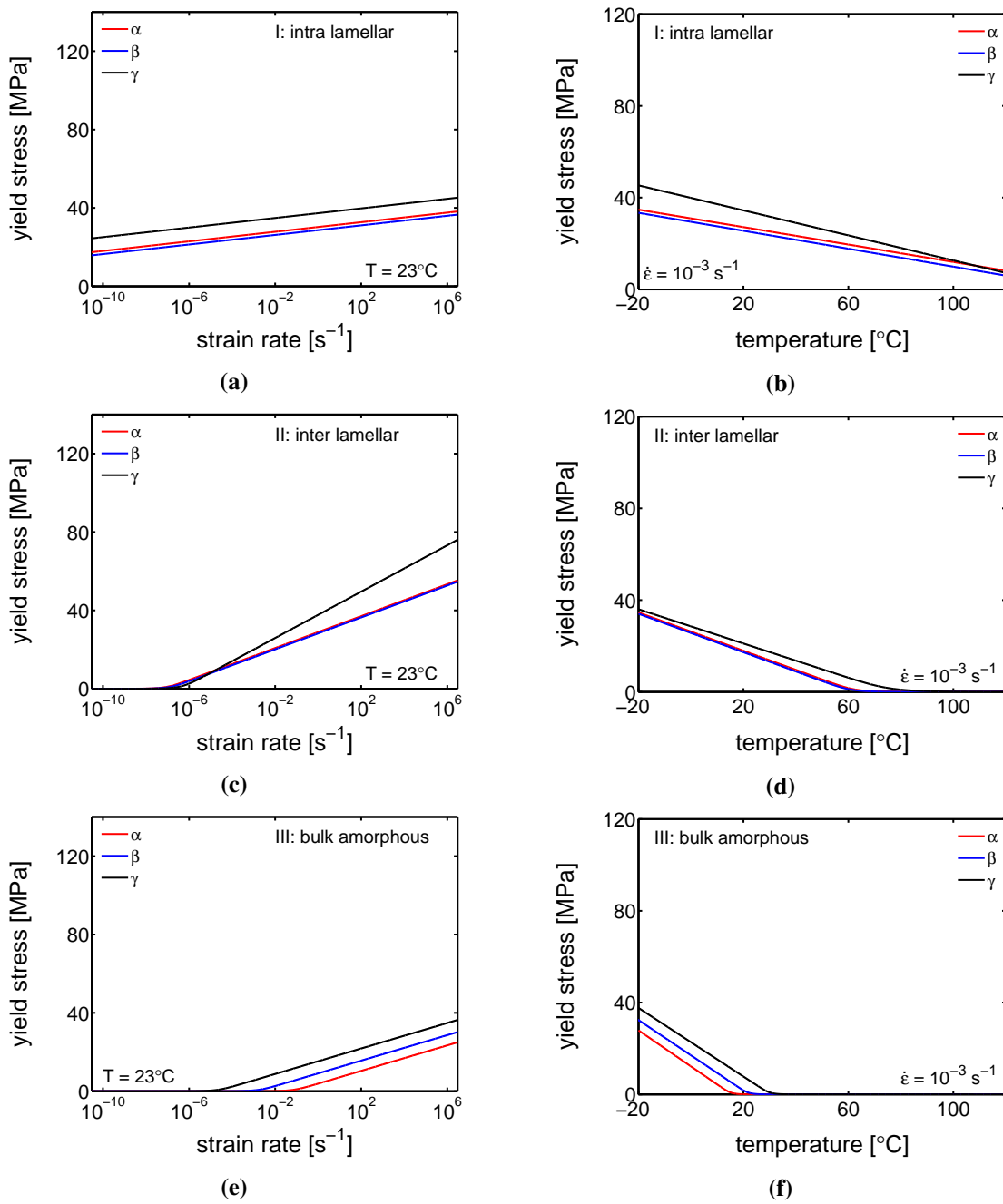


**Figure 3.13:** A comparison of the deformation mechanisms between the different crystallographic structures. a) and b) show the rate and temperature dependence of process I, c) and d) show these dependencies for deformation mechanism II and e) and f) show the same for mechanism III.

Because of the above mentioned effects, it makes sense to eliminate the contribution of aging and look at the mechanical properties of the rejuvenated iPP. In this study a thermal treatment is used to rejuvenate the rigid amorphous fractions. The samples were first heated to 85°C and kept there for 5 minutes to thermally rejuvenate, i.e. mobilize, the constrained amorphous phase. After this, the samples were quenched in ice-water and tested immediately after. This treatment leaves the crystals unaffected and therefore enables us to look at effects in the amorphous contributions only. The result of the uniaxial compression experiments performed at room temperature and a strain rate of  $10^{-3} \text{ s}^{-1}$  are shown in Figure (3.14).

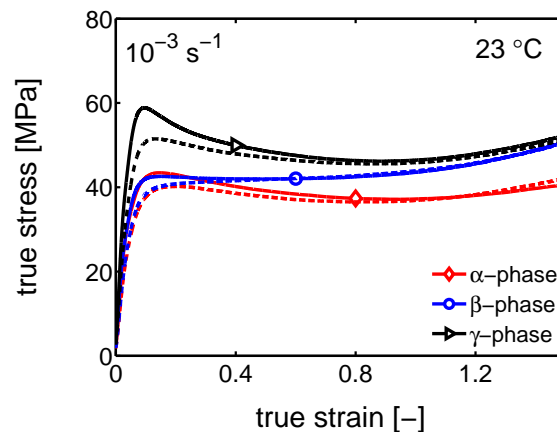


**Figure 3.14:** Intrinsic stress-strain response in uniaxial compression, taken at room temperature and a strain rate of  $10^{-3} \text{ s}^{-1}$ . The lines are the responses measured on the aged iPP and the dashed lines are measured on the rejuvenated iPP.

The effect of the rejuvenation treatment is particularly obvious for the  $\gamma$ -iPP, see Figure (3.14). The yield stress is much lower and the softening afterwards is less pronounced, hence the yield drop is much smaller. After softening, the hardening of the rejuvenated material coincides again with the hardening response of the aged iPP. This behavior is similar to that observed in amorphous polymers like polycarbonate and polystyrene [116]. The effect on the true stress-true strain of the  $\alpha$ - and  $\beta$ -iPP is much smaller. However, both show a decrease in yield stress and the softening is less strong. Subsequently the aged and rejuvenated material follow the same stress-strain response.

### Yield kinetics and rejuvenation

Since the yield behavior is clearly affected by the rejuvenation treatment this will also be reflected in the kinetics. In order to reveal the changes, experiments on rejuvenated samples are performed. Figure (3.15) shows the deformation kinetics of the aged material (open markers) together with the yield stress resulting from rejuvenated samples. New Eyring parameters values are determined for the yield data of process II, see Table (3.3), and the results are represented by the dashed lines in Figure (3.15). For the  $\gamma$ -iPP, the rate

dependence becomes much less strong. This difference of  $\gamma$ -iPP with respect to  $\alpha$ - and  $\beta$ -iPP can either be a result of the sample preparation procedure or it can be related to differences in aging kinetics. To model this, the rate constants of deformation mechanism II and III both have to be adapted.

When looking at the new parameters values (Table (3.3)) it indeed follows that with only a change in  $\epsilon_{0,II}$  and  $\epsilon_{0,III}$  the kinetics of the rejuvenated material at temperatures of 23°C and 50°C can be captured, as is illustrated in (3.15) for all crystal structures.

**Table 3.3:** List of parameter values for the rejuvenated samples

	$V_i^* [m^3]$	$\Delta U_i [J \cdot mol^{-1}]$	$\dot{\epsilon}_{0,i} [s^{-1}]$
<b><math>\alpha</math>-crystals</b>			
Mechanism <i>I</i>	$7.70 \cdot 10^{-27}$	$3.84 \cdot 10^5$	$2.0 \cdot 10^{43}$
Mechanism <i>II</i>	$2.31 \cdot 10^{-27}$	$1.95 \cdot 10^5$	$2.0 \cdot 10^{28}$
Mechanism <i>III</i>	$2.89 \cdot 10^{-27}$	$3.95 \cdot 10^5$	$1.0 \cdot 10^{69}$
<b><math>\beta</math>-crystals</b>			
Mechanism <i>I</i>	$7.70 \cdot 10^{-27}$	$3.84 \cdot 10^5$	$4.2 \cdot 10^{44}$
Mechanism <i>II</i>	$2.31 \cdot 10^{-27}$	$1.95 \cdot 10^5$	$1.0 \cdot 10^{28}$
Mechanism <i>III</i>	$2.89 \cdot 10^{-27}$	$3.95 \cdot 10^5$	$1.6 \cdot 10^{68}$
<b><math>\gamma</math>-crystals</b>			
Mechanism <i>I</i>	$7.70 \cdot 10^{-27}$	$5.30 \cdot 10^5$	$2.0 \cdot 10^{63}$
Mechanism <i>II</i>	$1.59 \cdot 10^{-27}$	$1.25 \cdot 10^5$	$5.5 \cdot 10^{16}$
Mechanism <i>III</i>	$2.89 \cdot 10^{-27}$	$3.95 \cdot 10^5$	$9.0 \cdot 10^{66}$

The temperature and rate dependence of the inter lamellar deformation mechanism for the rejuvenated samples is shown in Figure (3.16) and compared with that of the aged samples. As observed before, rejuvenation only leads to a shift in the rate and temperature at which the mechanisms become active. The decrease in yield stress seems to be inversely proportional to the amount of RAF.

## DMTA

Finally, the rejuvenation is examined with DMTA experiments. Again the behavior of rejuvenated material is compared with that of aged iPP, see Figure (3.15b,d,f). It immediately becomes clear that the biggest differences are observed in the temperature range of approximately 0°C to 75°C. This corresponds to the temperature window at which a distinction can be made between rigid and mobile amorphous domains, and is in good agreement with the work of Struik [33]. At lower temperatures, where the entire amorphous volume fraction is in a glassy state, and at higher temperatures, where the

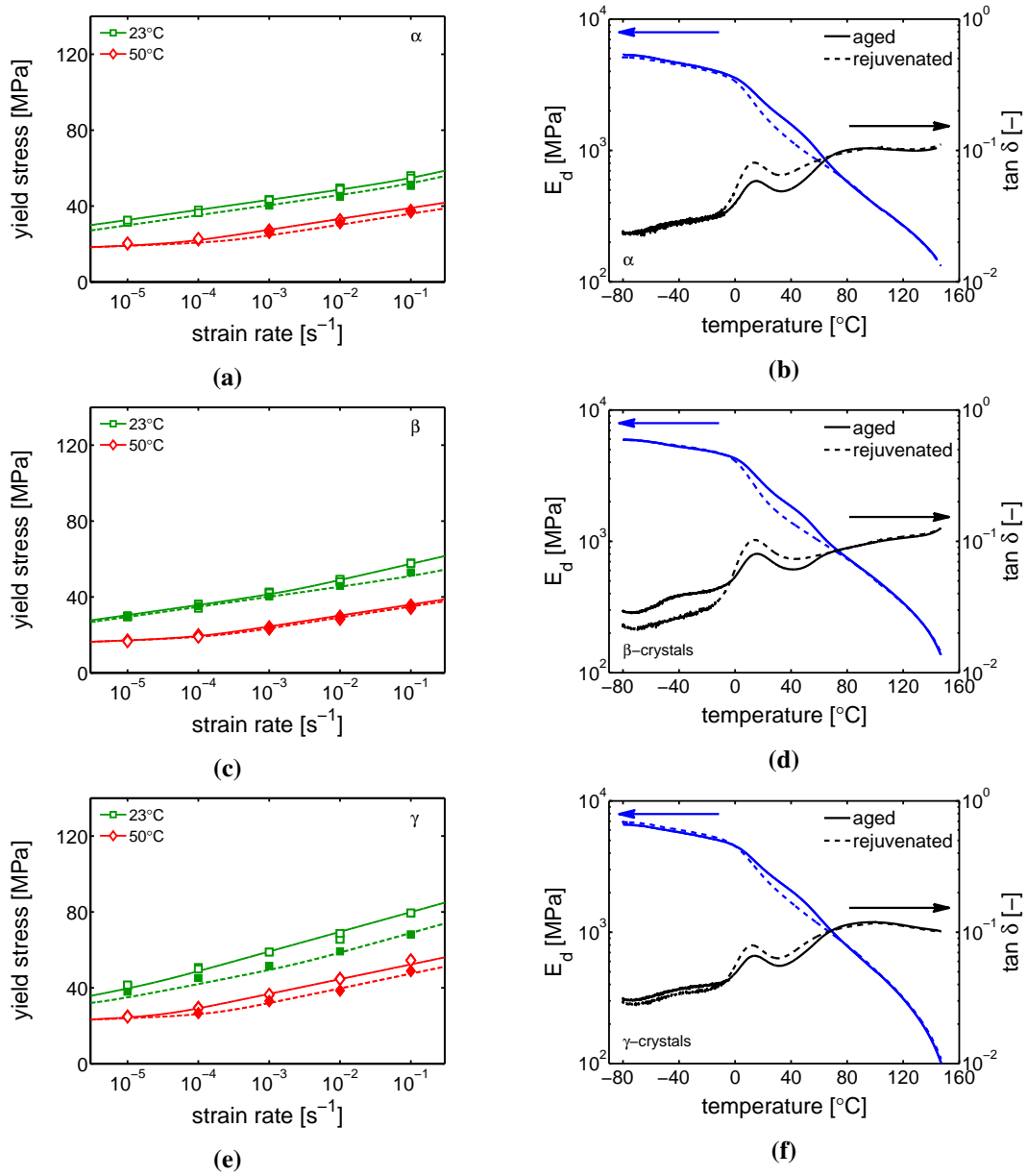


**Figure 3.15:** The yield kinetics of the iPP-polymorphs for a range of temperatures. Open markers represent the yield stress obtained from aged iPP and solid markers are measured on rejuvenated material. Solid and dashed lines are Eyring descriptions of the aged and rejuvenated iPP respectively, for a)  $\alpha$ -iPP, b)  $\beta$ -iPP and c)  $\gamma$ -iPP. The complex modulus and the  $\tan(\delta)$  of aged (solid lines) and rejuvenated (dashed lines) iPP containing a)  $\alpha$ , b)  $\beta$  and c)  $\gamma$ -crystals.

amorphous material is completely in the mobile state, the complex modulus is equal for aged and rejuvenated samples. The  $\tan(\delta)$  at low temperatures has decreased in the case of the  $\beta$ -iPP.

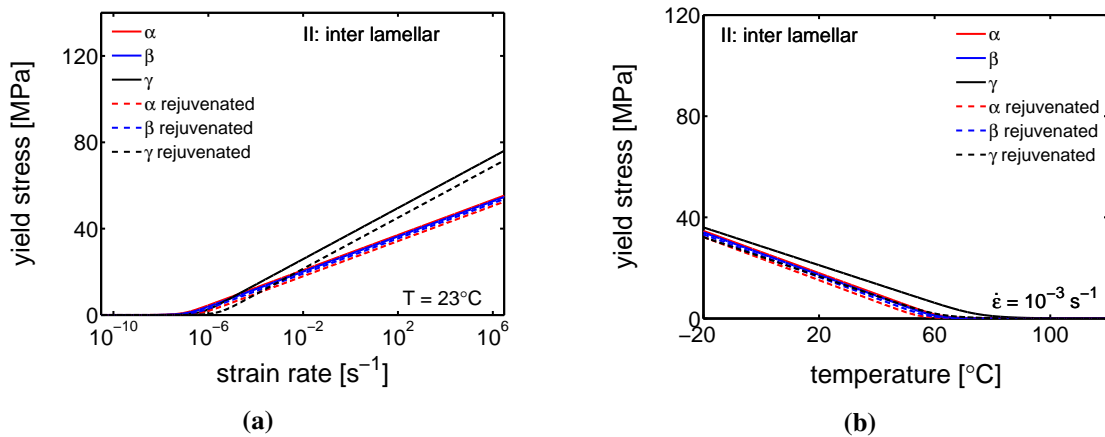


**Figure 3.16:** a) The rate dependence of the inter lamellar deformation mechanism, and b) the corresponding temperature dependence.

### 3.3.4 Failure kinetics

In creep experiments, in which a constant load is applied and the resulting strain is measured, three creep regimes can be distinguished. First, the primary creep regime can be identified during which the strain increases with a decreasing plastic strain-rate. Subsequently secondary creep will be observed. In this regime the plastic strain rate is steady and accumulation of plastic strain takes place. Finally, in the tertiary creep regime, acceleration of plastic strain rate takes place results in the occurrence of failure. A set of typical results measured on  $\alpha$ -iPP at room temperature, is shown in Figure (3.17a).

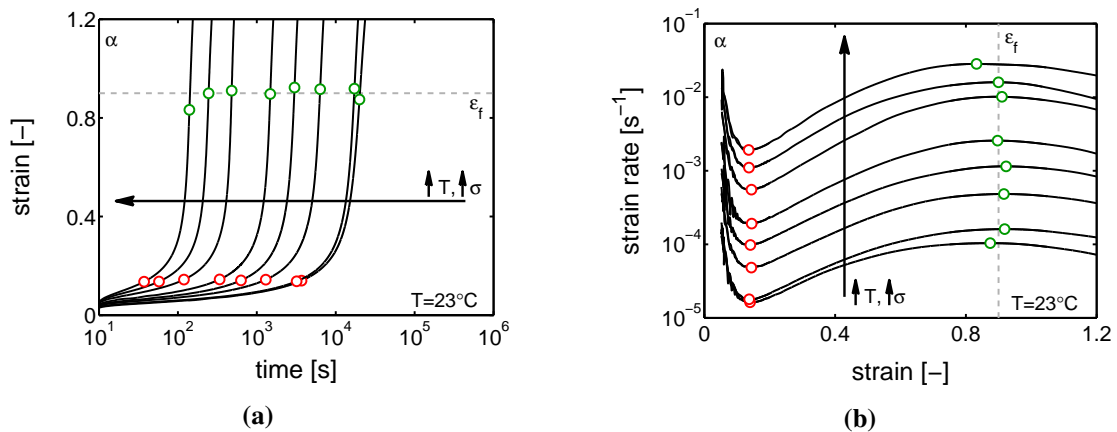


**Figure 3.17:** a) The strain as a function of time under constant loading conditions. Markers indicate the minimal (red) and maximal plastic flow rate (green) in the creep experiment. b) The accompanying Sherby-Dorn plot to illustrate the plastic flow rates for the set of creep experiments.

The lines represent the creep curves, the red symbols mark the minimum in the plastic strain rate and the green markers indicate the time of failure, corresponding to a maximum in the strain rate. The determination of these points is done with a Sherby-Dorn plot, given in Figure (3.17b). With increasing stress levels or temperatures, the accumulation of plastic strain is accelerated and thus failure takes place at shorter time scales. The strain at which the failure occurs,  $\epsilon_f$ , is always in the order of 0.9 [-].

In the work of Bauwens-Crowet et al. it is shown that creep in the secondary regime is identical to the plastic flow in the yield point [117]. Since the mode of failure in the creep experiments is similar to the mode of failure in the constant strain rate experiments, the same kinetics will be followed. To illustrate that this holds also for experiments performed in this study, the applied stress of the creep experiments is plotted as a function of the plastic flow rates obtained from the Sherby-Dorn plots, Figure (3.18). The Eyring description (gray lines), used with the parameters determined on the constant rate experiments and given in Table (3.2), coincides with the creep data.

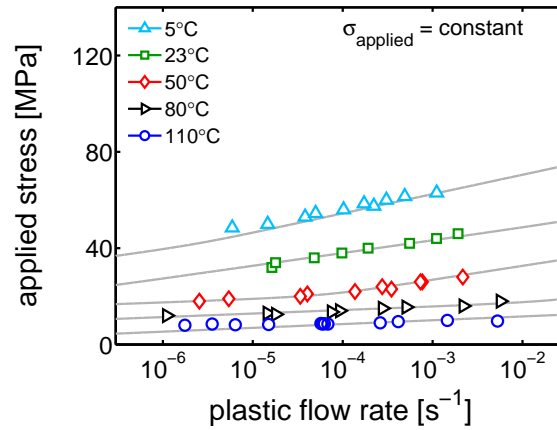


**Figure 3.18:** The applied stress of  $\alpha$ -iPP is plotted as a function of the plastic strain rate for different temperatures. Lines are model descriptions using the parameters given in Table (3.2) substituted into eq. (3.7).

In order to use the Eyring equation to describe and predict the time to failure under a constant load, one can use the concept of critical strain. This concept is based on the observation that the plastic flow rate as a function of the applied stress, multiplied with the time to failure, is constant:

$$ttf(\sigma) \cdot \dot{\epsilon}_{pl}(\sigma) = C \quad (3.8)$$

This relation also holds for the experiments performed here. This is validated with Figure (3.19a), which shows that the relation between the time to failure and the plastic flow rate is linear with a slope of -1 in a double logarithmic plot, i.e. confirming eq. (3.7).

This constant  $C$ , can be visualized in a plot where the plastic strain, accumulated as a

result of the applied stress, is plotted as a function of time (both on a linear scale), see Figure (3.19b). This clarifies that the constant  $C$  is considered here as a critical strain  $\epsilon_{cr}$ , which is different from the strain at failure  $\epsilon_f$ . Making use of the fact that  $\epsilon_{cr}$  is independent of the applied loading conditions (Figure (3.19b)) enables us to predict the time to failure according to:

$$ttf(\sigma, T) = \frac{\epsilon_{cr}}{\dot{\epsilon}_{pl}(\sigma, T)} \quad (3.9)$$

where  $\epsilon_{cr}$  follows from the creep experiments and  $\dot{\epsilon}_{pl}$  is the plastic strain rate. From this equation it directly follows that at a time to failure of  $1s$ ,  $\epsilon_{cr} = \dot{\epsilon}_{pl}$ , indicated with the dashed line in Figure (3.19a). For a given stress the plastic flow rate  $\dot{\epsilon}_{pl}$  follows directly from the Eyring equation, using the parameters given in Table (3.2).

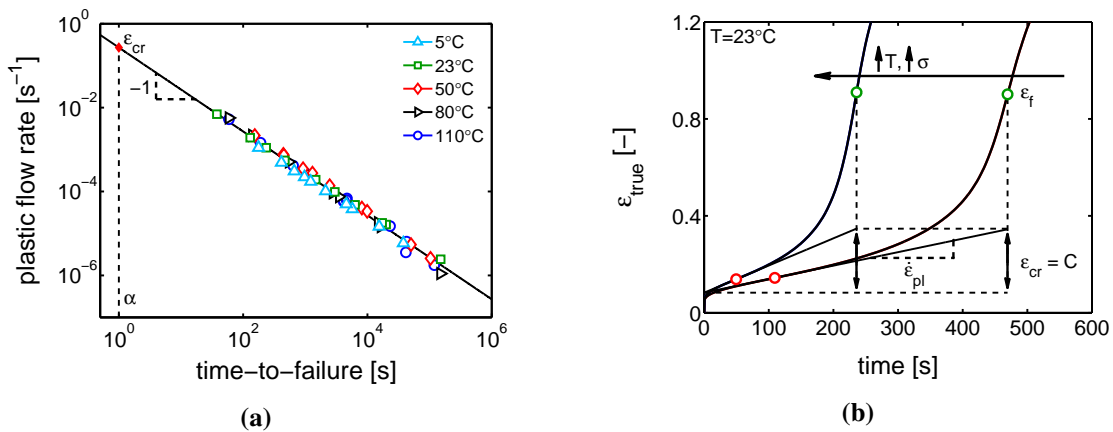


**Figure 3.19:** a) The plastic flow rate as a function of the time to failure on a logarithmic scale. The open markers represent the temperatures at which the creep experiments were performed and the filled marker is the critical strain. b) Creep curves of samples subjected to different loads to illustrate the effect of loading conditions. Furthermore, the definition of the critical strain and the strain at failure are indicated

Application of this concept is straightforward in the case of the  $\alpha$ - and  $\gamma$ -crystals. However, in the case of  $\beta$ -iPP, the Sherby-Dorn plots do not always display a minimum and/or maximum. Based on the creep experiments performed at lower temperatures, where there was a clear minimum and maximum, the plastic strain rate was determined at a true strain of 0.2 [-] and the time to failure at a true strain  $\epsilon_f$  of 0.4 [-]. The critical strain  $\epsilon_{cr}$  used to describe the creep data of all the crystallographic structures is 0.24 [-]. When applying eq. (3.9), the predictions shown in Figure (3.20) are obtained. The markers in these figures are the result of the creep experiments and the match proves the validity of the concept of critical strain. For all loads *and* temperatures, excellent agreement is found, except for the creep experiments performed at  $110^\circ C$ . For these experiments increasing deviations can be found upon longer times to failure. It is likely

that this deviation is caused by structural evolution (annealing), which increases the yield stress as a result of the applied temperature and stress level within the experimental time scale.

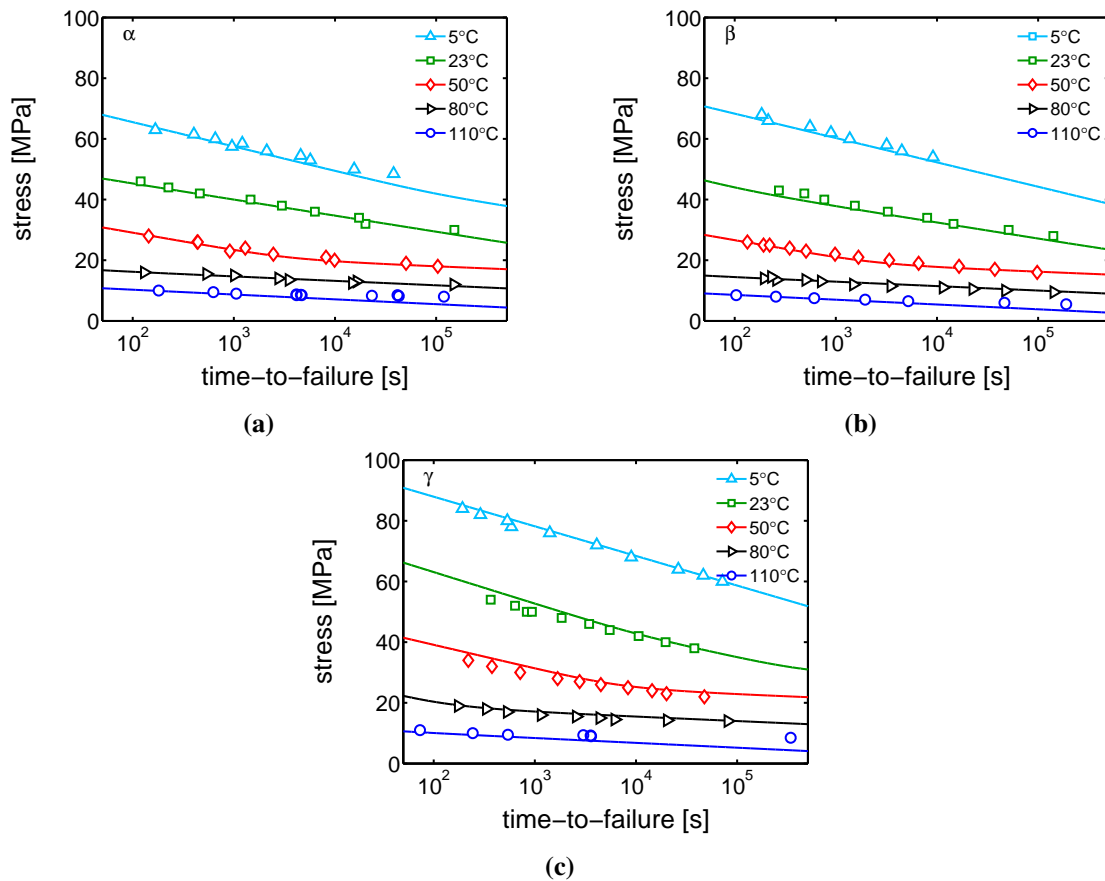


**Figure 3.20:** Time to failure as a function of the applied load for different temperatures of a)  $\alpha$ -iPP, b)  $\beta$ -iPP and c)  $\gamma$ -iPP. The lines are the predictions based on the concept of critical strain and the Eyring theory and the markers represent experimentally obtained creep data.

### 3.4 Conclusion

To study the performance of iPP-polymorphs different sample preparation procedures are used on an injection molding iPP grade. It is shown that these protocols result in samples containing almost solely the monoclinic  $\alpha$ -, the pseudo-hexagonal  $\beta$ - or the orthorhombic  $\gamma$ - crystal unit cell structure and therefore allow to study their mechanical response. A comparison of the intrinsic material response shows that:



- The  $\gamma$ -samples have the highest modulus and the  $\alpha$ -samples have the lowest. Although differences in crystallinity are small, it is assumed to partially cause the differences in the Young's modulus. The other contribution to the modulus follows from the part of the amorphous phase in the glassy state (RAF) and, therefore, is directly related to the constraints imposed by the crystals.
- The level of the yield stress turns out to be very similar for the  $\alpha$  and the  $\beta$ -crystals (for the whole range in temperature and strain rate), even though significant differences in lamellar thickness are found. The  $\gamma$ -crystals show a yield stress level which is clearly higher. It is therefore plausible that besides crystallinity (similar for all three samples) and lamellar thickness ( $\beta$  much higher than  $\alpha$ - and  $\gamma$ -iPP) the chain packing within the crystal lattice and the angle with respect to the lamellar normal, contributes to the magnitude of the yield stress. Moreover, the constraints of the amorphous chains in the vicinity of the crystals have significant influence on the yield stress and appear to be the strongest for  $\gamma$ -iPP.
- Softening after yielding is linked to the thermodynamic state of the rigid amorphous fraction and was the most pronounced for  $\gamma$ -crystals, whereas  $\beta$ -iPP showed no softening. This observation fits the hypothesis that  $\gamma$ -crystals impose the largest constraints on the amorphous phase and suggests that constraints imposed by  $\beta$ -crystals are relatively weak.
- Hardening of the  $\beta$ -samples was much stronger compared to the  $\alpha$  and  $\gamma$ -samples. In this work no direct factors or structural features were found that could be on the basis of this observation. However, it is expected that further research into the structural evolution upon deformation could explain the results.

The performance under various loading conditions of iPP, containing one of the polymorphs, is also investigated. It is remarkably found that the yield kinetics in the intra lamellar deformation regime (at high temperatures and/or low strain rates) are the same for all three samples in terms of activation volume. This could be an indication that the kinetics of this deformation mechanism are determined by the mobility of the 3/1 helix, rather than the crystal slip systems. The high activation energy of  $\gamma$ -iPP with respect to  $\alpha$ - and  $\beta$ -iPP is hypothetically explained by taking the angle of the chains with respect to the lamellar surface in  $\gamma$ -crystals into account.

In the inter lamellar deformation regime, which contributes to the kinetics if part of the amorphous fraction in the vicinity of the crystals experience a reduced mobility,  $\gamma$ -iPP has the highest resistance against yielding. Rejuvenation of the samples yields a decrease in the yield stress which is particularly strong in  $\gamma$ -iPP. This matches with the above mentioned findings with respect to softening, and illustrates that the constrained amorphous fraction is a very important factor affecting the yield stress (hence, the crystals remain unaffected by the rejuvenation treatment). The contribution of the bulk amorphous phase to the yield kinetics, observed at low temperatures, can be described with the same activation volume and energy for all three samples.

---

To predict the time to failure as a function of applied stress and temperature, the concept of critical strain is successfully used. It is shown that the same critical strain can be used for all three crystals. It is predicted that in the plasticity controlled failure regime the performance of  $\gamma$ -iPP is better than that of  $\alpha$ - and  $\beta$ -iPP. The predictions were validated with experimental results obtained from creep experiments and match very well. At high temperature and long testing times a deviation is found between the predictions and the experiments, probably caused by structural changes of the samples.



---

# Deformation-induced phase transitions in iPP polymorphs

---

## Chapter 4

### Abstract

This detailed study reveals the relation between structural evolution and the mechanical response of  $\alpha$ -,  $\beta$ - and  $\gamma$ -iPP. Uni-axial compression experiments, combined with in situ WAXD measurements, allowed for the identification of the evolution phenomena in terms of phase composition. Tensile experiments in combination with SAXS revealed orientation and voiding phenomena, as well as structural evolution in the thickness of the lamellae and amorphous layers. On the level of the crystallographic unit cell, the WAXD experiments provided insight in the early stages of deformation. Moreover, transitions in the crystal phases taking place in the larger deformation range and the orientation of crystal planes were monitored. At all stretching temperatures the crystallinity decreases upon deformation and, depending on the temperature, different new structures are formed. Stretching at low temperatures leads to crystal destruction and the formation of oriented mesophase, independent of the initial polymorph. At high temperatures, above  $T_{\alpha_c}$ , all polymorphs transform into oriented  $\alpha$ -iPP. Small quantities of the initial structures remain present in the material. The compression experiments, where localization phenomena are excluded, show that these transformations take place at similar strains for all polymorphs. For the post yield response the strain hardening modulus is decisive for the mechanical behavior, as well as for the orientation of lamellae and the evolution of void fraction and dimensions.  $\beta$ -iPP shows by far the most intense voiding in the entire experimental temperature range. The macroscopic localization behavior and strain at which the transition from disk like void shapes, oriented with the normal in tensile direction, into fibrillar structures takes place, is directly correlated with the strain hardening modulus.

---

Reproduced from: H.J.M. Caelers, E. Troisi, G.W.M. Peters, L.E. Govaert. Deformation-induced phase transitions in iPP polymorphs. *To be submitted to J. Mater. Sci.*

## 4.1 Introduction

Isotactic polypropylene (iPP) shows several crystal modifications (polymorphs) [7, 32]. Depending on chain architecture [10], additives [118] or the conditions experienced during processing [14] the formation of either one of them can be enhanced. The structures most often found are the monoclinic  $\alpha$ -, the pseudo-hexagonal  $\beta$ - [8, 85, 86], the orthorhombic  $\gamma$ - [10, 32, 35, 84] and the metastable meso-phase [87]. These crystals form a morphology in which the crystalline layers (lamellae) are alternated with amorphous layers. In a recent study the authors presented remarkable similarities in the yield and failure kinetics of the  $\alpha$ -,  $\beta$ - and  $\gamma$ -iPP, obtained from uni-axial compression experiments, even though the crystal structures are very different [119]. For the intrinsic material response (true stress versus true strain), however, some interesting differences were found, mainly in the post-yield behavior. It is well known that the softening and hardening of iPP displayed in the region after yielding, involves a number of structural modifications among which crystal destruction/melting, orientation of the surviving crystallites and the amorphous network, and recrystallization (possibly in other crystal-phases [92, 102, 103]). Furthermore, the typical alternating heterogeneous structure of a relatively soft amorphous domain and a stiff crystal part introduces stress and strain concentrations on a local scale [120]. In the case of uni-axial extension this gives rise to an additional phenomenon. Due to the negative hydrostatic pressure that develops while stretching, cavitation or voiding is initiated when the cavitation strength of the amorphous phase, which is lower than that of the crystals, is exceeded [121].

From an engineering point of view it is of great importance to understand the relation between the various (micro and meso scale) structural features of the material, and the behavior observed on a macroscopic scale and, therefore, this has been subject of several studies. The structural evolution of  $\alpha$ - [93, 102, 103, 122, 123],  $\beta$ - [89, 90, 101, 124, 124] and  $\gamma$ -iPP [36, 37, 92] was studied for several loading geometries. In general, cavitation is observed in case of uni-axial tensile deformation and it was found to affect yield stress and the properties at large strain tremendously.

Because of this strong coupling, Humbert et.al. investigated the initiation of voiding extensively [125], and concluded that, depending on molecular topology and the micro-structural parameters, cavitation can either proceed or follow the onset of plasticity. They related the type of cavitation, i.e. homogeneous or heterogeneous to a critical lamellar thickness  $L_{cc}$ . Below this thickness the critical shear stress for plastic crystal deformation is exceeded before cavitation takes place, while at higher thickness the critical stress for cavitation is exceeded before the crystals deform plastically. The effect of lamellar thickness on cavitation found by Wang et al. [126] can be explained with this framework. The influence of temperature was further investigated by Xiong et al. [127], who also modeled the cavitation/shear competition successfully [128].

In all these studies, the amorphous material plays a crucial role, for example, because it determines the critical cavitation stress. Starting from that perspective some studies were devoted to develop techniques to quantify the Young's modulus of the amorphous phase [129] and the strain hardening modulus from tensile experiments [130]. The

Young's modulus of the amorphous phase in the initial stages of deformation can be determined as shown by Xiong et al. [129], who used a procedure based on in-situ SAXS and WAXD tensile experiments. They found a decreasing Young's modulus of the amorphous network with increasing crystallinity and temperature. With respect to the strain hardening modulus it is concluded that at large strains the role of the network is dominant over the residual crystalline structures, particularly in the case of tensile deformation [26, 131]. In this perspective disentanglement induced cavitation at large strains, and void propagation via network relaxation were investigated as well [93, 123], and found to be able to reduce the strain hardening modulus to a large extent. Even in strongly oriented material whitening as a result of cavitation can still occur. Subsequent to voiding and the structure transformation into a fibrillated system, the amount of tie molecules is decisive for the final strength before fracture/failure takes place, as is shown by Ishikawa et al. [132].

Besides the structural features (nanometer scale) and the loading conditions discussed before, the relation between the crystal unit cell structure itself (Angstrom scale) and the cavitation process is investigated for  $\alpha$ - and  $\beta$ -iPP [133]. Using SEM techniques, they showed that  $\alpha$ -spherulites show micro-cracking in tensile loading. Cavitation takes place at the early stages of deformation and starts at the spherulite boundaries or in the equatorial region [133]. Contrary, the  $\beta$ -phase deforms plastically up to high deformations. Cavitation starts in the center of the spherulite and subsequently propagates to the equatorial regions [133]. Basic mechanisms like lamellar separation, plastic slip and crazing seem to be involved. Due to the cross-hatched structures of  $\alpha$ -iPP lamellae an increased stiffness is reported since crystalline domains are considered to form a connected physical network [133, 134]. The resistance against plastic flow is significantly less for  $\beta$ -iPP when compared to  $\alpha$ -iPP, even at deformation where the junctions of the cross hatched structures are destroyed. Therefore, intrinsic mechanical properties of crystals are more likely to be involved in plastic behavior than their micro-structural arrangement [102, 134, 135]. Due to reduced chain interactions and lower packing density in  $\beta$ -crystals, an enhanced chain mobility is obtained [134, 135]. An important limitation of the SEM observation [133], is that the assessed length scale is relatively large, especially compared to the data generated with X-ray techniques.

Despite the large number of studies in this field, a detailed comparison between  $\alpha$ -,  $\beta$ - and  $\gamma$ -iPP, tested in the same conditions, is still missing. The deformation and resulting phase transitions, onset of voiding, lamellar growth or destruction and the orientation are revealed in this work. Moreover, the relation of events taking place at the nano-, and micro-scale level with the macroscopically intrinsic mechanical response, is still unclear. Therefore, in this study in-situ WAXD and SAXS experiments are performed in combination with compression and tensile experiments. The compression experiments allow to investigate the phase transitions as a function of true stress and strain. Cavitation does not occur in compression tests due to a positive hydrostatic pressure. Due to the experimental restrictions, related to the compression setup blocking the diffracted X-ray, the maximal achievable compressive strain is restricted to a true strain of about 80%.

The tensile experiments allow to deform the material up to large strains and investigate voiding. The disadvantage is that it is difficult to relate the phase transitions to true strain. The combination of the two mechanical tests, together with a comparison of the different polymorphs deformed at the exact same conditions, offers a complete overall picture. This work provides insight on the sequence in which all these events, at the level of crystal structure ( $\text{\AA}$ -scale), lamellae (nm-scale) and voids ( $\mu\text{m}$ -scale), take place as a function of deformation and temperature. It deals with the structural changes occurring in uni-axial compression and extension of  $\alpha$ -,  $\beta$ - and  $\gamma$ -iPP. This detailed picture of what happens upon deformation allows us to explain the material behavior on a macroscopic scale in terms of micro-scale events. Since the amount of generated data is rather large, a small overview of how the results are presented is given first:

- First the mechanical response obtained from the tensile experiments is shown, together with the calculated true stress as a function of the true strain. The behavior is discussed and compared with the intrinsic material response measured in uni-axial compression.
- The structural evolution in terms of phase transitions, crystal plane orientation and slip, are revealed by WAXD experiments combined with uni-axial tensile tests. The crystal phase transitions are measured in compression experiments as well, allowing to compare these results with the ones obtained from tensile experiments (phase transitions), and couple it to true strain.
- The combination of SAXS experiments with uni-axial tensile tests provided insights on the onset of voiding, lamellar orientation and evolution of amorphous and lamellar thickness. Furthermore, a transition of initially disk like average void structure, to a fibrillar structure was found.

## 4.2 Experimental

### 4.2.1 Material and sample preparation

In this work, an isotactic polypropylene homo polymer was used (Sabic) with a weight averaged molar mass  $M_w$  of 320 kg/mole and a polydispersity index  $M_w/M_n$  of 5.4. Sheets of iPP material with a thickness of approximately 1mm, containing monoclinic  $\alpha$ -crystals, were prepared by compression molding. The granular material was placed in a mold and heated to 230°C, after which a pressure of about 5 MPa was applied stepwise. The material was kept under these conditions for 10 minutes to erase the thermo-mechanical history. Then, the solidification was induced by putting the mold in a cold press (25°C) for three minutes. The preparation of sheet material containing pseudo-hexagonal  $\beta$ -crystals was done following the same procedure but with a material containing 0.1 wt%  $\beta$ -specific nucleating agent (NJSTAR NU100, New Japan Chemical Group). To obtain the highest possible  $\beta$ -phase content, solidification was induced by cooling for 3 minutes in a press set at a temperature of 90°C, after which the sample was

cooled further in ambient conditions to room temperature. For the preparation of samples containing  $\gamma$ -crystals with an orthorhombic unit cell structure, a custom build hydrostatic compression tool is used [119]. The temperature and pressure history, applied during processing, is given in Figure (4.1). The preparation procedure is based on the work of Mezghani et al. [35]. First the temperature is increased to melt the iPP granulate. After erasing the thermo-mechanical history and the remaining air, a pressure of 180 MPa is applied. Subsequently the sample is slowly cooled to 150°C, which is sufficiently low to crystallize (The melting temperature increases approximately 30°C for a pressure increase of 100 MPa [41] and thus the undercooling increases with 30°C). Finally, when the crystallization process is completed, the sample is cooled further by blowing compressed air through the cooling channels. After reaching room temperature cylindrical sheets of approximately 1mm in thickness are taken out of the mold. All the iPP-sheets were stored at room temperature for two months before tensile experiments were performed. Thick plates of  $\alpha$ -,  $\beta$ - and  $\gamma$ -iPP were prepared following the same sample preparation procedure as described in [119].

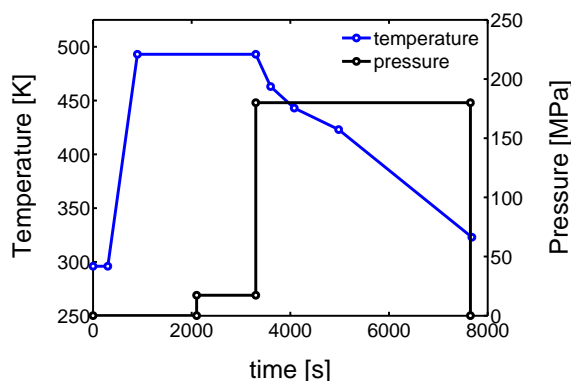


**Figure 4.1:** Schematic of the pressure-temperature protocol, used to prepare  $\gamma$ -iPP samples.

## 4.2.2 Mechanical testing

Two loading geometries were used for mechanical testing procedures, i.e. uni-axial compression and uni-axial tensile. Compression experiments are performed with a well defined constant true strain rate. In this way true stress as a function of the true strain can be related to structural changes. A special tool was developed to prevent the compression setup from blocking the diffracted intensity during in-situ X-ray measurements to the highest possible strain, see Figure (4.2).

The mechanical experiments were performed with a Zwick Z5.0 and the cylindrically shaped samples, with dimensions of  $\text{Ø}3 \times 3 \text{ mm}^2$ , were machined from the thick plates. With a custom built oven temperatures of 110°C were applied. After the application of a true strain of about 80%, the experimental setup starts to block the diffracted or scattered intensity. In order to study structural evolutions at higher strain, tensile experiments were



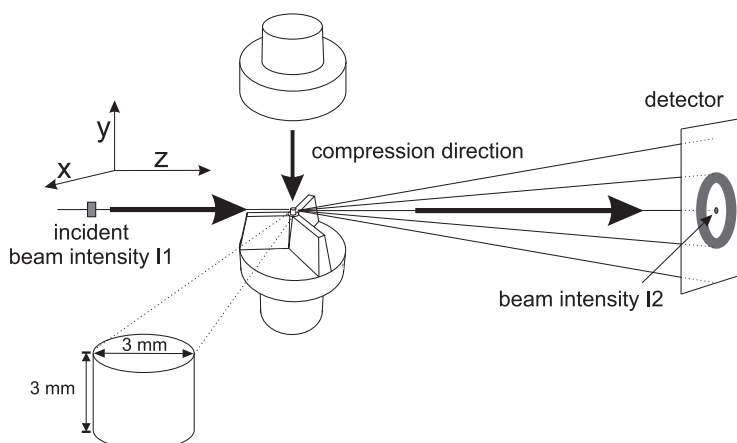


**Figure 4.2:** Schematic representation of the compression setup, combined with in-situ X-ray experiments.

performed. In this way, structural changes, even the ones taking place far beyond yielding, could be monitored. Also the onset and the evolution of the shape and dimensions of voids can be measured during tensile deformation. A disadvantage is that it is not possible to control the true strain rate. In tensile deformation the material deforms inhomogeneously after reaching the yield point. To force the tensile sample to neck in front of the beam, dumbbell shaped tensile bars were cut from the iPP-sheets, using a punch according to Figure (4.3). Another important drawback is that the local strain of the material in the beam area, related to the observed patterns, cannot be determined directly. However, an alternative approach will be explained in section 4.2.3. A Linkam TST 350 tensile stage is used to stretch the samples. Temperatures were chosen at 25, 50, 80 and 110°C respectively, while a stretching speed of 12  $\mu\text{m/s}$  was applied, being equivalent to an engineering strain rate of  $8 \cdot 10^{-4} \text{ s}^{-1}$ . The samples were stretched in horizontal direction, schematically illustrated in Figure (4.3). In this schematic, the incident beam intensity  $I_1$  and the intensity measured with the photo diode  $I_2$  are also indicated.

Stretching the  $\gamma$ -iPP samples as prepared, resulted in brittle failure at temperatures below the  $\alpha$ -transition. Obviously, this is not desired from an experimental point of view. Therefore, the ductility of the  $\gamma$ -iPP samples is improved with a thermal rejuvenation treatment just before the tensile experiment. This turned out to be a successful method to obtain the formation and growth of a stable neck. By keeping the sample for 300 seconds at a temperature of 85°C, the constrained amorphous domains in the vicinity of the crystals were rejuvenated, after which the samples were quenched to room temperature. The drop in the yield stress resulting from this treatment is sufficient to obtain ductile behavior [119, 136, 137].

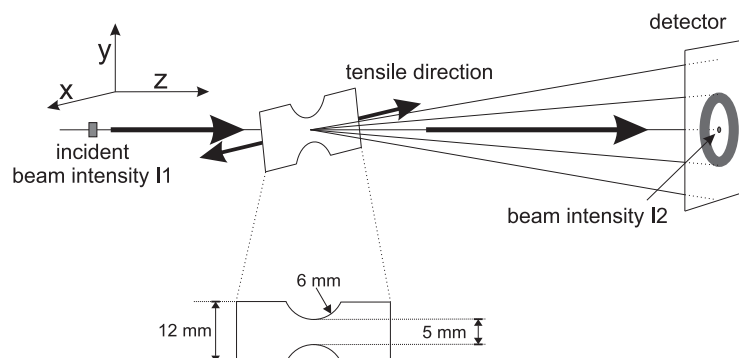


**Figure 4.3:** Schematic representation of the tensile setup, combined with in-situ X-ray experiments.

### 4.2.3 X-ray techniques and analysis

X-ray experiments were carried out at the Dutch-Belgian beamline BM26 (DUBBLE) in the European Synchrotron and Radiation Facility in Grenoble, France [47]. To monitor the structural evolution upon stretching at the level of the unit cell, lamellae and voids, the same set of experiments was repeated three times:

- The 2D WAXD patterns were recorded with a Frelon detector. This detector has a pixel size of  $97,65 \times 97,65 \mu\text{m}^2$  and was placed at approximately 140 mm from the sample. The acquisition time was 2.5 seconds.
- The 2D SAXS patterns were recorded with a Pilatus 1M detector. Simultaneously with these patterns, a Pilatus 3K was used to record WAXD patterns. From now on, we will refer to these patterns as 1D WAXD-patterns. The pixel size of the Pilatus 1M and 1K was  $172 \times 172 \mu\text{m}^2$ , with a sample to detector distance of approximately 2707 mm (for SAXS) and 283 mm (for WAXD). At this distance the Porod region is included in the SAXS data. Again the acquisition time was 2.5 seconds.
- Another set of 2D SAXS experiments were performed with a sample to detector distance of approximately 7258 mm, allowing to obtain scattering data at low  $q$ -values. Again these frames were acquired simultaneously with 1D WAXD patterns, recorded with the Pilatus 3K placed at a distance of approximately 183 mm, and an acquisition time of 2.5 seconds.
- During the compression experiments, in situ WAXD patterns were recorded using a Frelon detector. This detector is the same as the one used for the 2D WAXD experiments in tensile deformation, but was now placed at approximately 200 mm from the sample. In this case the acquisition time was 1 second.

The wavelength in all the experiments was  $\lambda = 1.033 \text{ \AA}$ . The size of the beamspot was approximately  $0.3 \times 1 \text{ mm}^2$ . The incident beam intensity  $I_1$  is measured using an ionization chamber and the transmitted beam intensity  $I_2$  is measured with a photo diode

### Data reduction

To subtract results from the X-ray experiments the data has to be normalized and corrected. In the case of the WAXD experiments a Frelon detector was used and as a result dark current  $I_{dc}$ , i.e. the signal recorded with a closed shutter, has to be subtracted. This is done on both the patterns recorded with ( $I_m$ ) and without the sample ( $I_{bkg}$ ). This correction is not needed for the patterns taken with a Pilatus detector because of the absence of readout noise and dark current. To correct for the air scattering the background  $I_{bkg}$  is subtracted. For proper subtraction  $I_{bkg}$  was first corrected for the ratio  $I_1/I_{1,bkg}$  between the incident beam intensity and the background. Next, a correction factor  $C = I_{1,bkg}/I_{2,bkg}$  is introduced to compensate for the fact that different devices were used to detect the incident beam intensity  $I_1$  and the intensity recorded by the photo diode in the beam stop  $I_2$ . The correction for the attenuation due to the presence of a sample is then  $C \cdot I_2/I_1$ . In the case of tensile experiments the sample thickness  $d_t$  decreases during the experiment and the transmission  $T$  is not constant. To correct for these contributions, eq. (4.1) and eq. (4.2) have to be used,

$$d_t = \mu \cdot \ln(I_{1,t}/(C \cdot I_{2,t})) \quad (4.1)$$

$$T = \frac{C \cdot I_2}{I_1} \quad (4.2)$$

where  $\mu$  is the absorption coefficient of the sample that can be determined from the intensity measured for the initial sample thickness  $d_0$ . Combining all the corrections results in [138]:

$$I_{cor} = \frac{\frac{(I_m - I_{dc})}{I_1} - C \cdot \frac{I_2}{I_1} \frac{I_1}{I_{1,bkg}} \frac{(I_{bkg} - I_{dc})}{I_{1,bkg}}}{T \cdot d_t} \quad (4.3)$$

### Phase composition

The crystallographic structures of iPP display a unique diffraction pattern, with intense scattering at angles that are related to specific crystal plane d-spacings by Bragg's law. In Figure (4.4) typical 2D diffraction patterns of isotropic  $\alpha$ -,  $\beta$ - and  $\gamma$ -iPP are shown.

The most clear diffractions of  $\alpha$ -iPP come from the crystal planes corresponding to d-spacings of 6.26Å (110), 5.24Å (040) 4.78Å (130) and 4.17Å/4.05Å (111)/(041). For the  $\gamma$ -iPP the 2D-pattern looks similar and the biggest difference can be observed from the third diffraction ring. The crystal planes and corresponding d-spacings are 6.39Å (111), 5.20Å (008) 4.38Å (117) and 4.17Å/4.05Å (202)/(026). For  $\beta$ -iPP only two important diffraction peaks can be observed at d-spacings of 5.50Å (300), 4.19Å (301) respectively.

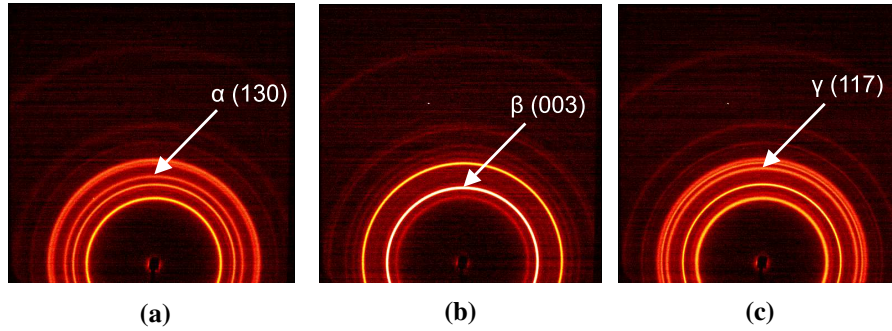


**Figure 4.4:** 2D WAXD patterns of iPP, characteristic for a)  $\alpha$ -iPP, b)  $\beta$ -iPP and c)  $\gamma$ -iPP. The diffraction peak unique for  $\alpha$ -iPP is the third clear one going from the center towards outside of the pattern. The same holds for  $\gamma$ -iPP, whereas the diffraction specific for  $\beta$ -iPP is the most clear one in the *beta* pattern. All characteristic peaks are indicated in the figure.

The arrows in Figure (4.4) indicate the characteristic  $\alpha$ -iPP reflection (Figure (4.4a)),  $\beta$ -iPP reflection (Figure (4.4b)) and  $\gamma$ -iPP reflection (Figure (4.4c)). When these structures orient, the intensity migrates azimuthally to specific angles where the diffracted intensity concentrates.

To obtain quantitative information about the phase composition upon stretching, the patterns are radially integrated over an azimuthal angle of  $180^\circ$ . Voigt functions are fitted to the integrated 1D patterns to quantify crystal fractions as a function of strain and temperature. In Figure 4.5a and 4.5b two typical examples of a deconvoluted signal of  $\gamma$ -iPP are shown. The first one, Figure 4.5a, is the sample at room temperature prior to deformation and the second one, Figure 4.5b, is the sample after deformation (last image in top row of Figure 4.15).

The dashed black line in this figure is the amorphous halo that was fitted to the pattern to determine the weight fraction of the crystallinity according to:

$$\chi_w = \frac{A_{tot} - A_a}{A_{tot}} \quad (4.4)$$

Where  $A_{tot}$  is the total diffracted intensity (integrated area) and  $A_a$  is the integrated area of the scaled amorphous halo (determined on quenched low tacticity iPP with negligible crystallinity). The dotted gray lines represent Voigt functions that were fitted on the diffraction peaks and used to determine the weight fraction of  $\alpha$ -,  $\beta$ -,  $\gamma$ - or meso-iPP according to:

$$\chi_i = \chi_w \cdot \left( \frac{A_i}{A_\alpha + A_\beta + A_\gamma + A_{meso}} \right) \quad (4.5)$$

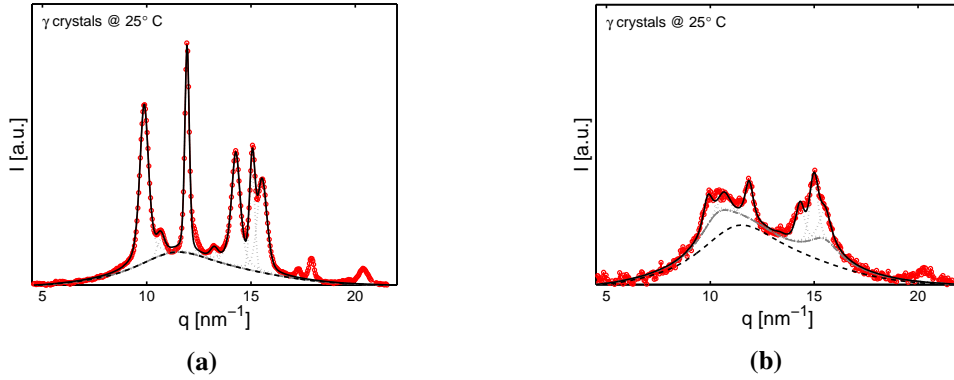


**Figure 4.5:** a) An example of a deconvoluted undeformed  $\gamma$ -iPP sample and b) a deformed  $\gamma$ -iPP sample, stretched at 25°C. The dashed black line is the amorphous halo, the dotted gray lines are the peak fittings, the solid gray line represents the mesophase and the solid black line is the sum of the fitted peaks. The red markers represent the radially integrated pattern obtained from the experiments.

Where  $A_\alpha$ ,  $A_\beta$  and  $A_\gamma$  are the surfaces corresponding to the characteristic  $\alpha$ -,  $\beta$ - and  $\gamma$ -reflections of the (110), (300) and (111) planes respectively.  $A_{meso}$  refers to the area of the two mesophase peaks. In Figure 4.5), the gray lines correspond to this latter phase and, together with the amorphous part (black dashed lines) and the crystal reflections (dotted gray lines), the total (black line) fits the measured patterns very well.

### Determination of $L_p$ , $L_c$ and $L_a$

Two different methods are used to obtain the long period, the lamellar thickness and the thickness of the amorphous layer. The first one is based on Bragg's law and follows from the integrated Lorentz corrected scattering (SAXS) intensity, given by:

$$I_1(q) = I(q)q^2 \quad (4.6)$$

where  $I$  is the intensity and  $q$  is the scattering vector. The long period then follows via

$$l_p = \frac{2\pi}{q_{I_1, max}} \quad (4.7)$$

with  $q_{I_1, max}$  the maximum of the Lorentz corrected intensity. Since the long period is constructed of an amorphous part and a crystalline part it is straightforward that the lamellar thickness  $l_c$  follows from

$$l_c = \frac{2\pi}{q_{I_1, max}} \chi \quad (4.8)$$

where  $\chi$  is the volume percentage of the crystallinity obtained from WAXD experiments, given by:

$$\chi = \frac{\frac{\chi_w}{\rho_c}}{\frac{\chi_w}{\rho_c} + \frac{1-\chi_w}{\rho_a}} \quad (4.9)$$

In this equation the mass fraction of crystals,  $\chi_w$ , follows from eq. (4.4). The amorphous layer thickness can then easily be obtained by subtraction of the lamellar thickness from the long period:

$$l_a = l_p - l_c \quad (4.10)$$

An alternative way to determine these quantities is via the 1D auto-correlation function  $\gamma_1(r)$  [52, 139]. For spherical symmetry this can be calculated with

$$\gamma_1(r) = \frac{1}{Q} \int_{q_0}^{q_\infty} I_1(q) \cos(qr) dq, \quad (4.11)$$

where  $r$  is the real space and  $Q$  is the scattering invariant defined by:

$$Q = \int_{q_0}^{q_\infty} I_1(q) dq, \quad (4.12)$$

To extrapolate the experimentally assessed range of the scattering vector, Debye-Bueche [140] and the Porod law [141] are used, respectively. The long period, amorphous layer thickness and lamellar thickness are then determined as described by Stein et al. [54]. The most important difference between the determination of these quantities via Bragg's law and the auto-correlation function is that the latter one gives higher values for the lamellar thickness, and thus lower values for the amorphous domain thickness. This originates from the interface between the two phases which is more dense than the bulk amorphous parts and therefore considered to be part of the lamellae in the approach using the autocorrelation function.

Lamellar quantities like the long period  $L_p$  can be determined from the scattering in either the meridional region, or the equatorial region, parallel and perpendicular to the tensile direction respectively (See Figure (4.6)):

This allows to distinct between these features in either the tensile direction (integration of the meridional region) or the transverse direction (integration of the equatorial region).

Obviously, this is only of interest at relatively low strains before lamellae start to break, voiding takes place or, depending on the temperature, the material recrystallizes.

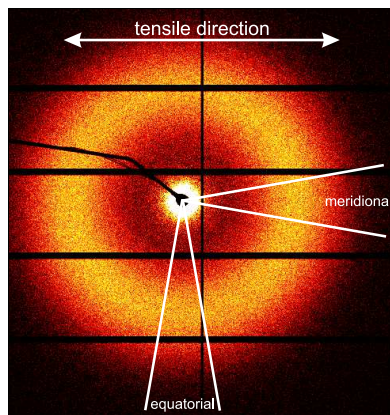


**Figure 4.6:** Regions used for radial integration of the SAXS patterns

### Determination of the strain

Due to the shape of the tensile samples and the inhomogeneous deformation after yielding, the true strain of the sample volume in front of the X-ray beam cannot be calculated directly from the applied engineering strain. However, the X-ray data can also be used to determine the draw ratio of the sample volume in front of the beam [142]. This allows us to obtain all structural parameters as a function of actual deformation. It should be noticed that, although we intended to create an uni-axial deformation, this was not guaranteed due to the initial sample shape, which was forced by the experimental conditions (i.e. the start of a neck in a known position where the beam is positioned), and the complex plastic deformation mechanisms accompanied with localization phenomena and crystal phase transitions. Moreover, the deformation mode (anything between uni-iaxial and planar) can change during the deformation path and these changes can be temperature, deformation rate, void formation and phase dependent. To deal with this complex situation we will analyze our experimental data by considering two limiting cases: pure uni-axial and pure planar deformation.

To determine the true strain, the draw ratio  $\lambda_l$  in the tensile direction, defined as

$$\lambda_l = \frac{l_t}{l_0} \quad (4.13)$$

should be determined first. Here  $l_0$  is the initial length of an arbitrary volume in front of the beam at  $t = 0$  and  $l_t$  is the length at time  $t$ . If we now assume incompressibility, we get:

$$l_0 w_0 d_0 = l_t w_t d_t \quad (4.14)$$

Combining this with eq. (4.13), and with the assumption of uni-axial deformation, i.e. the contraction in the tensile-, width- and thickness direction is equal, eq. (4.15) can be applied to obtain the actual draw ratio. This calculated ratio is resulting from the decrease of polymeric material in the beam area.

$$\lambda_{l,uni} = \frac{1}{\lambda_d^2} = \left(\frac{d_0}{d_t}\right)^2 \quad (4.15)$$

The sample thickness at time  $t$ , defined as  $d_t$ , can be straightforwardly calculated using eq. (4.1), and at time  $t = 0$  the initial thickness  $d_0$  follows from

$$d_0 = \mu \ln(I_{1,t=0} / (C \cdot I_{2,t=0})) \quad (4.16)$$

Substitution of eq. (4.1) and eq. (4.16) into eq. (4.15) allows us to determine the draw ratio on the local level of the beam spot, without determination of  $\mu$ . This ratio is determined on a homogenized volume since the beam dimensions are much larger than the spherulites and the lammellae. To calculate the draw ratio for plane strain conditions, eq. (4.17) is used.

$$\lambda_{l,pl} = \frac{1}{\lambda_d} = \left(\frac{d_0}{d_t}\right) \quad (4.17)$$

In this case, the draw ratio in tensile direction equals the draw ratio in thickness direction, but the sample width remains constant upon stretching. The true strain and true stress then follow via

$$\epsilon_{true,n} = \ln(\lambda_{l,n}) \quad (4.18)$$

and

$$\sigma_{true,n} = \sigma_{eng} \cdot \lambda_{l,n} \quad (4.19)$$

for both the assumptions of uni-axial deformation and plane strain conditions. The subscript  $n$  in this equation denotes either uni-axial deformation or plane strain conditions. The approach presented here, which is based on the intensity drop as a result of the sample presence, can be used if the following assumption holds:



$$I_1 = I_{trm} + I_{rfl} + I_{abs} + I_{sct} \approx I_{trm} + I_{abs} \quad (4.20)$$

where  $I_1$  is the incident beam intensity,  $I_{trm}$  is the transmitted intensity which is measured with the photo-diode,  $I_{rfl}$  is the reflected intensity,  $I_{abs}$  is the absorbed intensity and  $I_{sct}$  is the scattered intensity. However, if voids appear, large density differences are introduced and as a result the scattered part of the intensity is no longer negligible with respect to the transmitted part. Since the scattering from the voids takes place under a very small angle (due to the relatively large length scales involved), the intensity measured in the photo diode during the WAXD experiments is the sum of the scattering due to the voids, and the transmission. This means that for the WAXD experiments the transmitted intensity can be determined even if voids appear, and eq. (4.1) and eq. (4.16) can be applied. To obtain the strain for the SAXS experiments, where this is not the case, simultaneously recorded WAXD patterns (Pilatus 3K) were linked to the 2D-WAXD patterns via superposition, indicated with the rectangular section in Figure (4.7a). The white lines indicate the slice-shaped area used for radial integration. In Figure (4.7b), an example of the relation of the SAXS frames as a function of the WAXD frames is shown. The color represents the relative difference between the scaled integrated intensity as a function of the scattering vector  $q$  of the 2D- and the 1D WAXD patterns. The red markers highlight the minimum. With this coupling, determined for all sets of SAXS-, and their corresponding WAXD experiments, the evolution in sample thickness can be obtained.

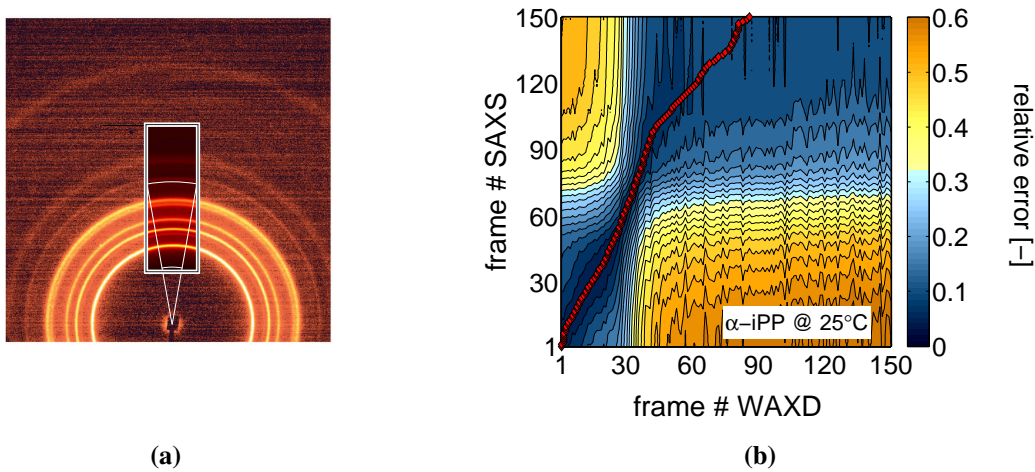


**Figure 4.7:** a) Example of a WAXD pattern measured with the Frelon detector. In the inset the WAXD pattern measured simultaneously with SAXS is put into the 2D WAXD pattern. b) An example of a figure used to find the minimal difference between the two WAXD patterns. Numbers on the axes indicate the frame number.

On a very local level, an estimate for the strain can be deduced from the changing distance between the crystal planes. Upon stretching, the evolving d-spacing can be used, similar

to Xiong et al. [129] according to:

$$\epsilon_{d-space} = \frac{d_{hkl} - d_{hkl,0}}{d_{hkl,0}} \quad (4.21)$$

to express the evolution in terms of a strain. In this equation  $d_{hkl}$  is the d-spacing of a specific plane  $hkl$  in time, and  $d_{hkl,0}$  is the spacing at time  $t = 0$ .

### Void fraction

Initially the scattering is caused by the crystals and amorphous phase, but upon deformation, voids appear, and the scattering resulting from these voids becomes dominant. This is accompanied by a strong increase in the scattering invariant due to the large difference in the density of the material and a void. For the calculation of the scattering invariant, cylindrical symmetry is assumed in the loading direction. The normalized scattering invariant is then given by [138]:

$$\frac{Q}{Q_0} = \frac{\int_{-\infty}^{\infty} \int_0^{\infty} I_{cor}(q_x, q_y) q_y dq_x dq_y}{\int_{-\infty}^{\infty} \int_0^{\infty} I_{cor,t=0}(q_x, q_y) q_y dq_x dq_y} \quad (4.22)$$

where  $q_y$  and  $q_x$  are the scattering vector in vertical and horizontal direction respectively.  $Q_0$  is the invariant at time  $t = 0$ , prior to deformation.

Under the assumption that we start from a situation without cavities, the void fraction can be calculated directly from the invariant according to [138]:

$$\phi_v = \left[ \frac{Q}{Q_0} - 1 \right] \cdot \left[ \frac{\chi \rho_c^2 + (1 - \chi) \rho_a^2}{\chi(1 - \chi)(\rho_c - \rho_a)^2} - 1 \right]^{-1} \quad (4.23)$$

with  $\rho_c$  the crystal density, given by

$$\rho_c = \frac{\chi_\alpha}{\chi} \cdot \rho_\alpha + \frac{\chi_\beta}{\chi} \cdot \rho_\beta + \frac{\chi_\gamma}{\chi} \cdot \rho_\gamma + \frac{\chi_{meso}}{\chi} \cdot \rho_{meso} \quad (4.24)$$

where  $\chi_i$  is the mass fraction of crystal phase  $i$ , with density  $\rho_i$  ( $i \sim \alpha, \beta, \gamma, meso$ ). The values used for the density of the specific crystal phases are given in Table (4.1), as well as the density of the amorphous phase. The fractions can be obtained from eq. (3.6).

**Table 4.1:** List of densities used in eq. (4.24)

	$\alpha$	$\beta$	$\gamma$	<i>meso</i>	<i>amorphous</i>
$\rho[\text{kg}/\text{m}^3]$	946	921	938	880	850

## 4.3 Results

Several strain and stress definitions are used in this study depending on the type of results presented. The engineering stress  $\sigma_e$  and strain  $\epsilon_{app}$  (also referred to as apparent macroscopic strain) are calculated with the initial gauge length and the initial cross sectional area. These are used when we intend to link structural transitions to the macroscopically observed tensile behavior. When we want to clarify transitions, the true stress  $\sigma_{true}$  and strain  $\epsilon_{true}$  are sometimes used. To obtain the strain hardening modulus we use  $\lambda^2 - 1/\lambda$  as a strain measure [136] and finally, for the strain determined at the local scale of the lamellae,  $\epsilon_l$  is used.

### 4.3.1 The mechanical response

#### Tensile tests (mechanical)

In Figure (4.8a), Figure (4.8c) and Figure (4.8e), the engineering stress as a function of macroscopic apparent strain is shown for tensile tests, performed on different iPP-polymorphs and at multiple temperatures. Initially, linear elastic behavior can be observed, but with increasing strain and stress the deformation becomes plastic, ultimately leading to yield. Temperature facilitates the mobility and, therefore, has a reducing effect on the resistance against yielding.

The two limiting cases of uni-axial extension and plane strain of  $\alpha$ -,  $\beta$ - and  $\gamma$ -iPP are shown in Figure (4.8b), Figure (4.8d) and Figure (4.8f). Up to yielding, where the deformation is close to homogeneous, the discrepancy between uniaxial and planar deformation is mainly observed in the initial elastic stiffness. After yielding a cross-over takes place and, depending on the amount of softening seen in the engineering stress, the uni-axial response increasingly deviates from the plane strain response. For  $\beta$ -iPP, with almost no softening, the difference is rather small.

Although in agreement with the findings presented by G'Sell et al. [143], the true stress-true strain results obtained in the tensile experiments are different from the ones from uni-axial compression, where softening is observed and the yield stress is much higher (see Figure (4.9a) and Figure (4.10a)). First of all, this discrepancy can result from the formation of cavities, that can develop due to positive hydrostatic stresses in the case of the tensile experiments. The cavities appear on a local level and cause macroscopic softening to (partially) disappear [144], even though locally the softening is maintained. This phenomenon is called sequential yielding and can start prior to macroscopic yield,

as will be shown in the following sections. Second, the stress and strain fields in a tensile experiments can become highly inhomogeneous after yield, and cause the sample to deform with a variable strain rate. As soon as the sample softens, locally the strain rate strongly increases. This has a reducing effect on the amount of softening observed in the mechanical response. Finally, the sample preparation procedure is slightly different for compression and tensile experiments, also having a minor effect.

### Compression tests (mechanical)

Since the amorphous network is crucial for the mechanical response at high strains [131], the strain hardening modulus  $G_r$  is determined from compression experiments. From tensile experiments it is not possible to find a qualitative value for the hardening modulus due to the difficulties discussed before. The compression experiments, on the other hand, are perfectly suitable for this goal since localization phenomena are excluded and a well defined constant true strain rate can be applied. Consequently, the intrinsic true stress and true strain can be obtained and the strain hardening modulus can straightforwardly be determined according to Haward [136]. In Figure (4.9b) a Gaussian plot, i.e. the true stress as a function of  $\lambda^2 - 1/\lambda$ , is shown, for  $\alpha$ -,  $\beta$ - and  $\gamma$ -iPP compressed at room temperature with a true strain rate of  $10^{-3} s^{-1}$ . The dashed lines are compression experiments performed under the same loading conditions, but on thermally rejuvenated samples as explained in our previous work [119]. Linear fits, determined in the hardening regime, are represented by the dotted lines. These slopes give an estimation for the strain hardening modulus  $G_r$ . It is clear that  $\beta$ -iPP has the highest strain hardening modulus (4.2 MPa) and  $\alpha$ -iPP the lowest (2.2 MPa). The strain hardening modulus of the  $\gamma$ -iPP is in between (3.5 MPa). Moreover, the thermal rejuvenation treatment does not affect the hardening, but reduces the softening significantly.

In our previous work [119] we showed that the contribution of the constrained amorphous phase to the effect of thermal rejuvenation on the yield stress, is almost similar for  $\alpha$ - and  $\beta$ -iPP, independent of the strain rate. This thermal rejuvenation treatment has no effect on the hardening modulus, see Figure (4.9b), but mainly leads to a reduction in the true stress-true strain response at strains around yielding. After yielding the thermally rejuvenated samples coincide again with the aged samples. This observation is in good agreement with the behavior typically observed in aged and, either thermally or mechanically, rejuvenated amorphous polymers [116].

Softening after yielding is a property of an amorphous glassy material. The degree of softening is a direct consequence of the amount of aging a sample has experienced, prior to the mechanical testing. In the case of iPP, at a temperature above the glass transition of the bulk material, and below the melting temperature of the crystals, softening is related to the constrained amorphous phase (which is considered to be in a glassy state). In the vicinity of the relatively immobile crystalline domains, the mobility of the amorphous material is strongly reduced. The extent of the constraints can depend on a number of morphological and crystallographic features. The strength of the secondary interactions in the crystal is related to the density, which is the lowest in case of  $\beta$ -iPP (see Table

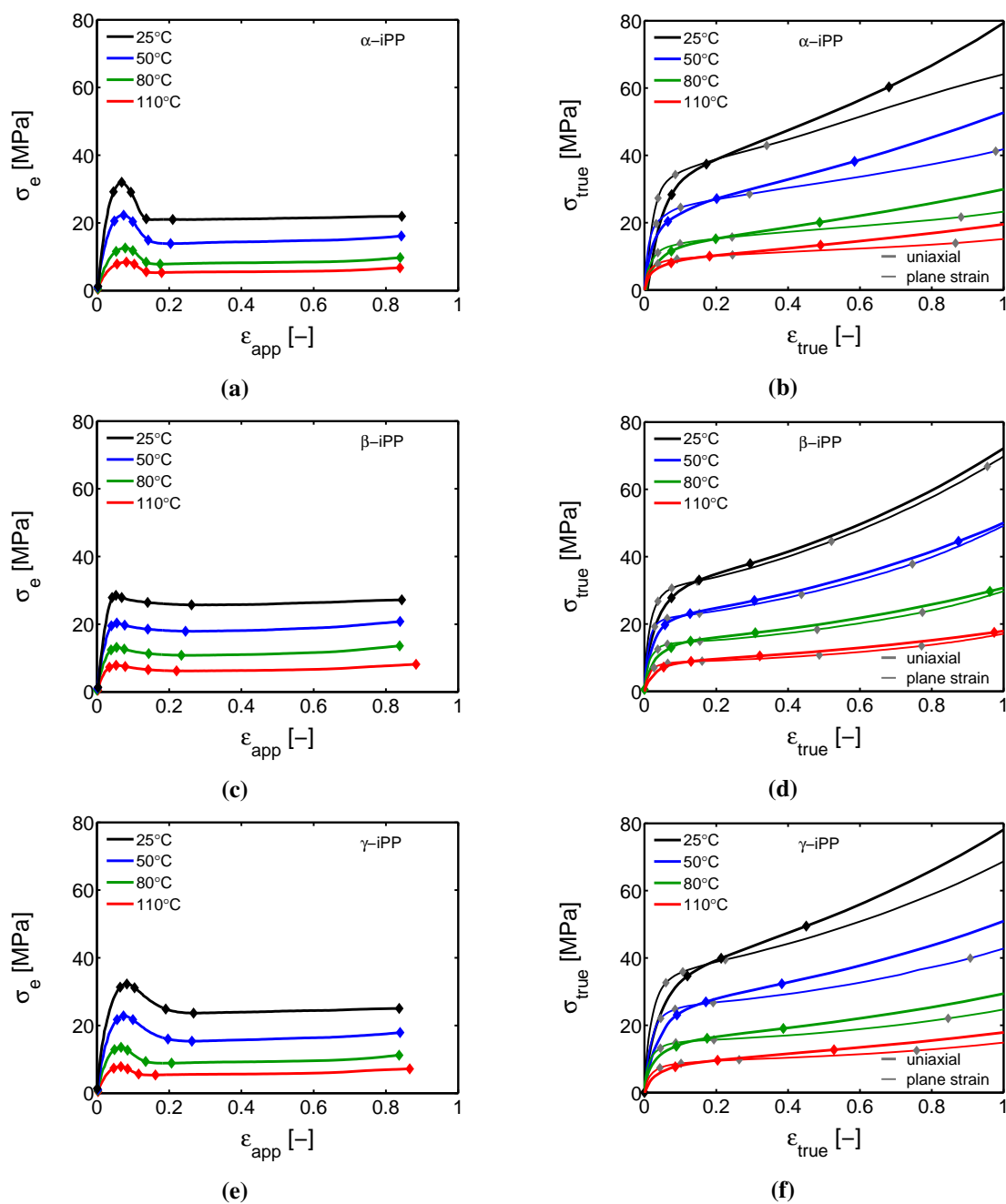


**Figure 4.8:** a),c) and e) The engineering stress as a function of the apparent strain for  $\alpha$ -,  $\beta$ - and  $\gamma$ -iPP tensile experiments respectively, stretched at different temperatures and a rate of 12  $\mu\text{m/s}$ . b),d) and f) The true stress as a function of true strain, corresponding to figure a),c) and e). The thick solid lines are calculated for the assumption of uniaxial deformation and the thin lines for plane strain. The markers in the figures correspond to the 2D WAXD and SAXS images, shown in the following sections.

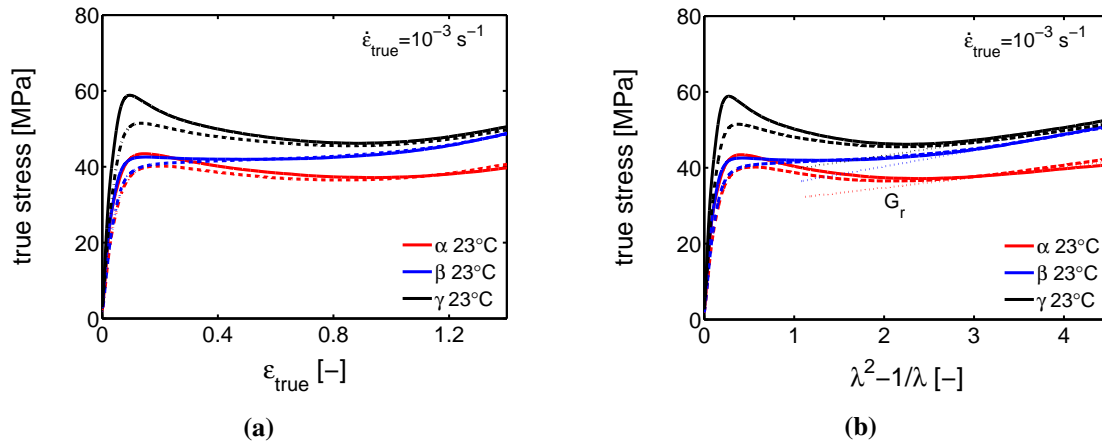


**Figure 4.9:** a) Gaussian plots for  $\alpha$ -,  $\beta$ - and  $\gamma$ -iPP. The results are obtained from uni-axial compression experiments at a strain rate of  $10^{-3}$  and a temperature of  $23^\circ\text{C}$  on samples with a dimension of  $\text{Ø}6 \times 6 \text{ mm}^2$  ( $\beta$ - and  $\gamma$ -iPP) or  $\text{Ø}3 \times 3 \text{ mm}^2$  ( $\alpha$ -iPP). The dashed lines are the true stress - true strain response obtained on the thermally rejuvenated samples. b) The corresponding Gaussian plots for  $\alpha$ -,  $\beta$ - and  $\gamma$ -iPP. The dotted lines represent the strain hardening moduli  $G_r$ .

(4.1)). The lamellar thickness and the density of crystal defects also affect the strength of the constraints. Furthermore, the crossed stacking of chains within the lamellae of  $\gamma$ -iPP is also positively contributing to the constraints. All these constraints are directly coupled to the properties of the crystal. With thermal rejuvenation softening partially disappears. Particularly in  $\gamma$ -iPP a large reduction in yield stress is found, but also in  $\alpha$ - and  $\beta$ -iPP a decrease is observed, indicating that the iPP contains constrained amorphous material in all three crystal phases. At  $110^\circ\text{C}$ , where the constrained amorphous material is mobile (above the  $\alpha_c$ -relaxation temperature), the  $\alpha$ - and the  $\gamma$ -iPP still show some remaining softening, see Figure (4.10). This means that as a result of deformation, the structural integrity further deteriorates after yielding. As can be observed from Figure 4.20 in sec. 4.3.2, this is not governed by a large reduction in crystallinity. Moreover, this reduction is very similar for the  $\beta$ -iPP. Based on these observations it could be hypothesized that the break-down of the cross hatched crystal network is responsible for the softening in  $\alpha$ - and  $\gamma$ -iPP, without destroying the crystals themselves, since these structures are typically present in these polymorphic forms [9, 32, 77]. In this perspective, the absence of these structures in the case of  $\beta$ -iPP could explain why the mechanical response displays no softening. The trends in the strain hardening moduli at  $110^\circ\text{C}$  are similar to that at  $25^\circ\text{C}$ . To summarize, from the mechanical behavior in uni-axial compression it is hypothesized that the intrinsic softening observed in polypropylene is an effect, mainly resulting from the constrained amorphous domains in the vicinity of the crystals. However, as follows from the compression experiments performed at  $110^\circ\text{C}$ , combined with the results of the WAXD experiments presented in sec. 4.3.2, suggests that the constraints implied by the cross-hatched structures, present in  $\alpha$ - and  $\gamma$ -iPP, also contribute to the softening.

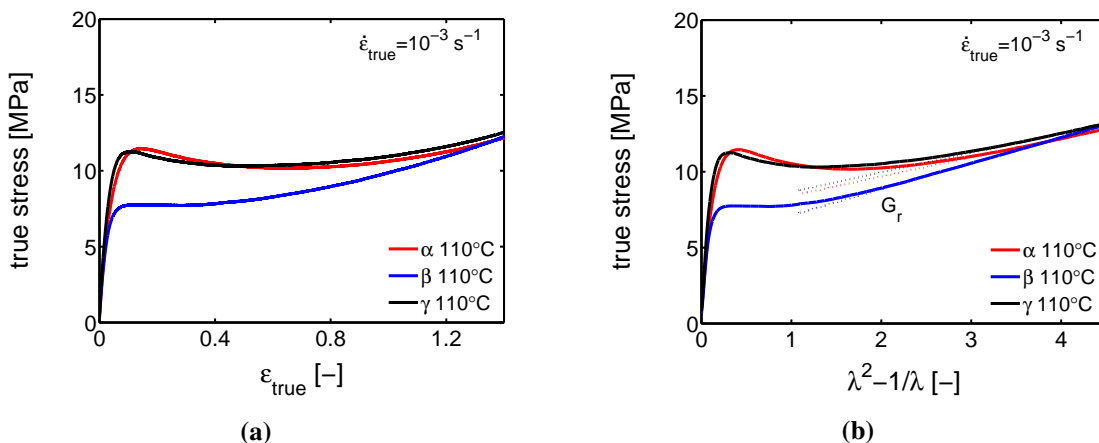


**Figure 4.10:** a) The solid lines are the true stress as a function of the true strain obtained from uniaxial compression experiments on  $\alpha$ -,  $\beta$ - and  $\gamma$ -iPP, measured at a strain rate of  $10^{-3}$  and a temperature of  $110^\circ\text{C}$  on samples with a dimension of  $\text{Ø}6 \times 6 \text{ mm}^2$  ( $\beta$ - and  $\gamma$ -iPP) or  $\text{Ø}3 \times 3 \text{ mm}^2$  ( $\alpha$ -iPP). b) The corresponding Gaussian plots for  $\alpha$ -,  $\beta$ - and  $\gamma$ -iPP. The dotted lines represent the strain hardening moduli  $G_r$ .

### 4.3.2 WAXD analysis

#### Tensile tests (WAXD)

Figure 4.11 shows the evolution of the  $\alpha$ -iPP crystal structure during tensile testing in terms of the normalized 2D WAXD patterns, as a function of strain for 4 different temperatures. Since most of the structural changes take place in the macroscopically observed softening regime, i.e. in a small apparent strain range, it is chosen to depict the changes as a function of uniaxial true strain for clarity reasons. The patterns depicted here correspond to the markers in Figure (4.8). Initially, before straining the sample, an isotropic diffraction pattern is observed which clearly shows the monoclinic  $\alpha$ -phase reflections. Upon straining the sample, the pattern becomes slightly elliptical, indicating that the d-spacings of the crystals in the polar regions are extended whereas the distances in the equatorial regions reduce. As a result of further straining, the reflections become less pronounced and the scattering intensity migrates to certain angles, indicating (strong) orientation. At high elongation at room temperature a transition from  $\alpha$ -iPP to oriented mesophase can be observed [145], whereas at high temperatures the isotropic  $\alpha$ -iPP transforms to a strongly oriented  $\alpha$  configuration.

This azimuthal orientation is investigated in more detail by integrating the (110) diffraction peak over an angle ranging from  $0$  to  $180^\circ$ . An angle of  $90^\circ$  represents the equator, while  $0$  and  $180^\circ$  are the polar regions. This integration was carried out for  $\alpha$ -iPP stretched at the lowest and the highest temperature, i.e. corresponding to the top and bottom row in Figure 4.11, and the results are given in Figure 4.12. Due to the strong orientation and the high intensity at an azimuth of  $90^\circ$  the minor effects at lower strains are unclear. In the inset an enlarged plot of this region is shown. The intensity transforms

from nearly isotropic in the initial stage of deformation to a slightly oriented state prior to yielding.

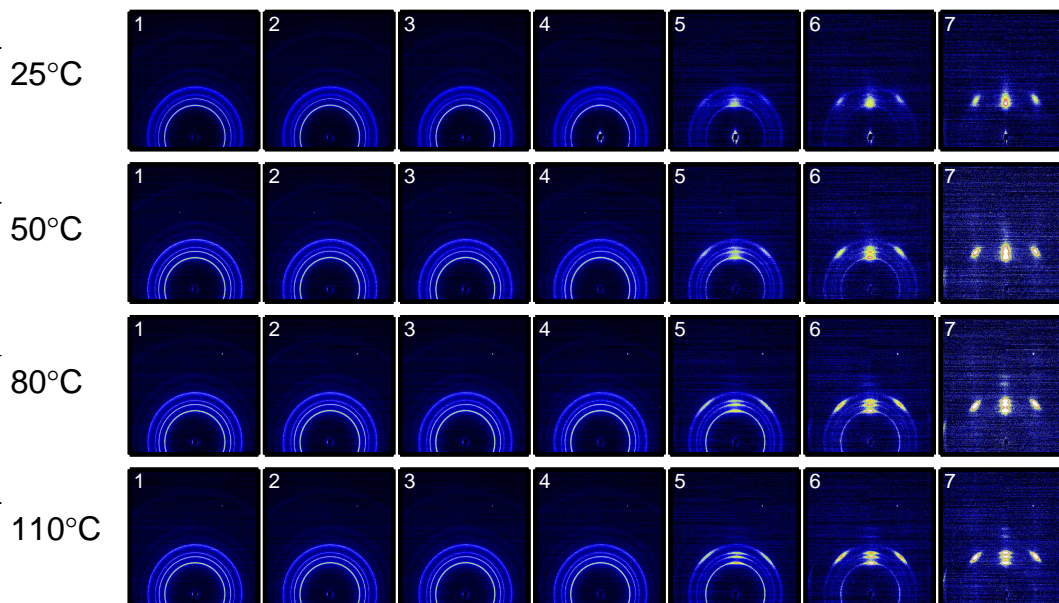


**Figure 4.11:** Normalized 2D WAXD patterns of  $\alpha$ -iPP stretched at temperatures of 25°C, 50°C, 80°C and 110°C from top to bottom. The true strains, determined with the assumption of fully uni-axial deformation, are given as well. The macroscopic strains at which the patterns are taken are indicated by the markers in Figure (4.8). The stretching direction is horizontal.

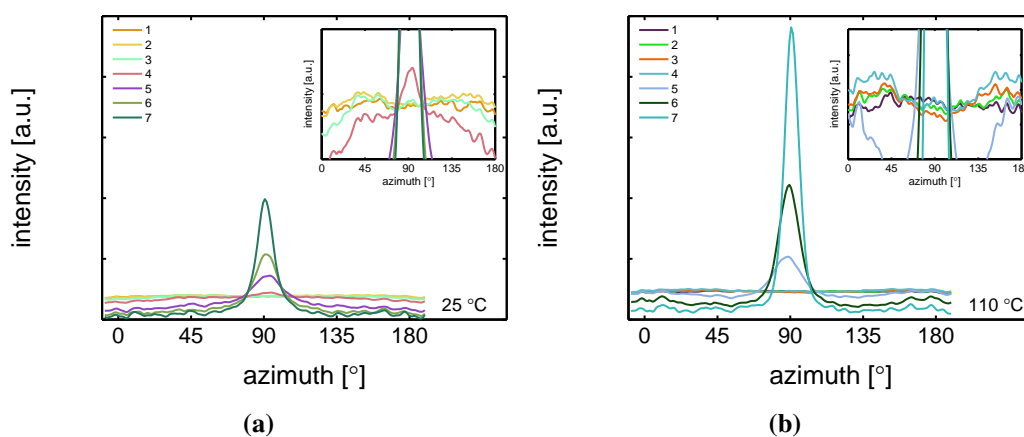


**Figure 4.12:** a) Azimuthal spread of the (110) diffraction of  $\alpha$ -iPP at various strains. a) uni-axial stretching 25°C and b) 110°C. The numbers in the legend correspond to the 2D patterns in Figure 4.11.



Straining the sample further leads to selective melting and recrystallization, and orientation of 'old crystals' into a strongly oriented mesophase at 25°C, and  $\alpha$ -phase at 110°C. The peak in the azimuthal integration, representative for these oriented structures shows up first in the yield point and evolves in the softening and hardening regions thereafter. Small intensity maxima at 10° and 170° degrees, observed in the material stretched at 110°C, indicate the survival or appearance of cross-hatched structures in the stretched sample.

A similar figure can be made for  $\beta$ -iPP, see Figure 4.13. In the initial stages of deformation the isotropic diffraction rings resulting from the pseudo-hexagonal  $\beta$ -phase structure become elliptical due to the (elastic) deformation. Contrary to  $\alpha$ -iPP at room temperature, the diffraction of the  $\beta$ -iPP crystals present in the initial isotropic crystal structure seems to be partially maintained during stretching. However, due to different localization behavior the uni-axial true strain belonging to the  $\beta$ -iPP images, is lower than the ones of  $\alpha$ -iPP. This makes a direct comparison complicated. Another part of the initial structure is destroyed and forms new oriented structures. At room temperature the diffracted intensity appears at positions typical for oriented mesophase. At elevated temperature and upon deformation, a transition from  $\beta$ -crystals to oriented and more stable  $\alpha$ -crystals takes place.

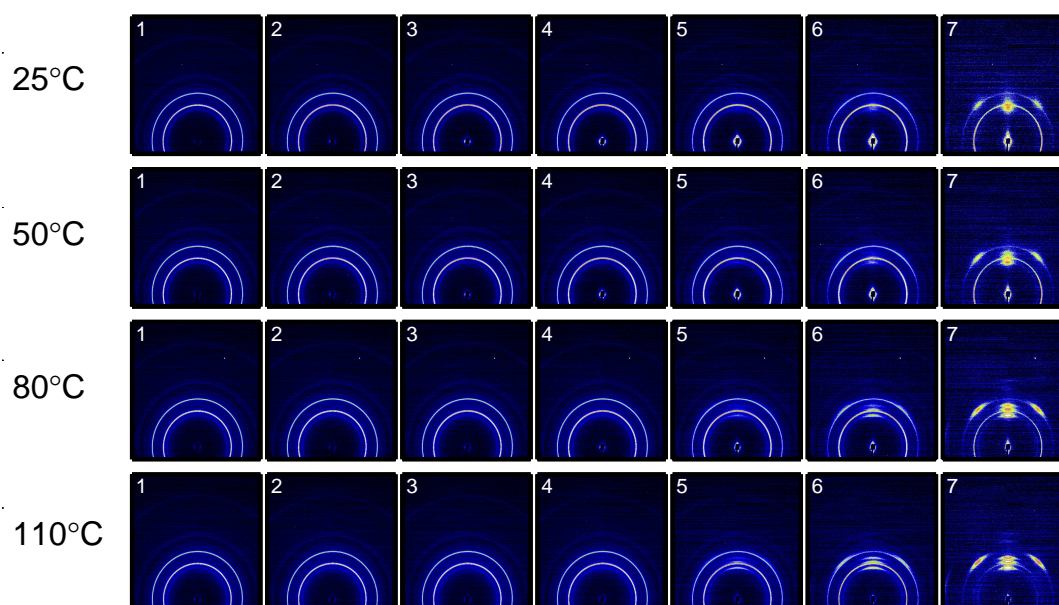


**Figure 4.13:** Normalized 2D-patterns of  $\beta$ -iPP stretched at temperatures of 25°C, 50°C, 80°C and 110°C from top to bottom. The true strains, determined with the assumption of fully uni-axial deformation, are given as well. The macroscopic strains at which the patterns are taken are indicated by the markers in Figure (4.8). The stretching direction is horizontal.

From an azimuthal integration over the (300) diffraction peak of  $\beta$ -iPP, deformed at 25°C and 110°C (Figure 4.14), it becomes clear that the amount of material involved in partial melting and/or orientation is much less (as a function of apparent macroscopic strain) as compared to  $\alpha$ -iPP. Only in the last few frames a clear decrease in the intensity at an azimuth of 0 and 180° is observed. The deformation of the initial structure to preferred orientations on the other hand, continues also after the yield point (frame 3). At room temperature, as well as at 110°C, the first evidence of recrystallization in a new oriented phase is found in frame 5, corresponding to deformation well beyond the macroscopic yield point.

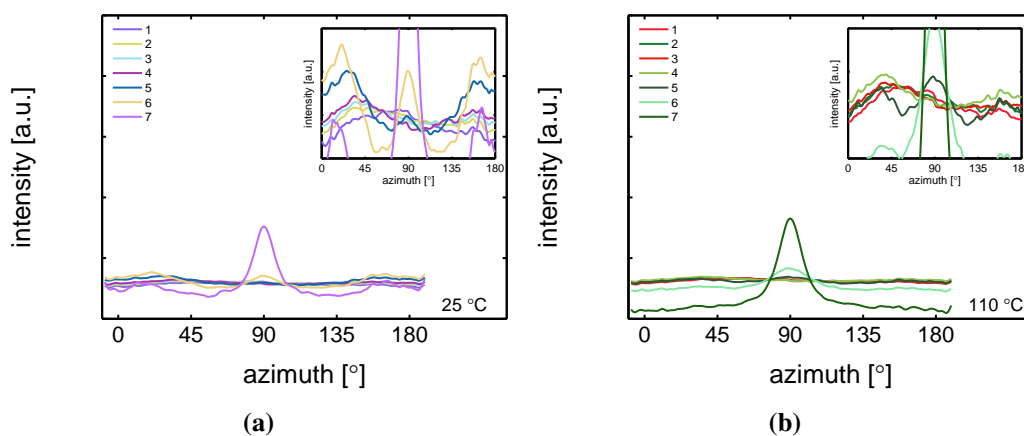


**Figure 4.14:** Azimuthal spread of the (300) diffraction of  $\beta$ -iPP at various strains. a) uni-axial stretching 25°C and b) 110°C. The numbers in the legend correspond to the 2D patterns in Figure 4.13.

The reflections of the orthorhombic  $\gamma$ -phase become very vague upon deformation at 25°C, and the scattering transforms into a pattern indicative for oriented mesophase, see Figure 4.15. Stretching at 50°C result is a similar response, however, besides mesophase some small amounts of oriented  $\alpha$ -iPP seems to be formed. Elongation at 80 and 100°C results in a transition of isotropic  $\gamma$ -iPP into strongly oriented  $\alpha$ -iPP. All these transitions take place after yielding. These 2D-patterns provide qualitative information about the orientation resulting from the stretching.

The azimuthal scan of the (111) peak and the evolution as a result of the deformation is given in Figure 4.16, for the  $\gamma$ -samples deformed at 25°C and 110°C. Interestingly, the intensity remains rather isotropic until the onset of the softening after yielding (frame 5-7). The absence of the off-axis orientation means that the  $\gamma$ -crystals do not allow for partial orientation of the initial crystallites. After yielding, when selective melting and recrystallization takes place, the intensity of the (111) peak in the polar regions starts to decrease and the newly formed structures appear at an azimuth of 90°.

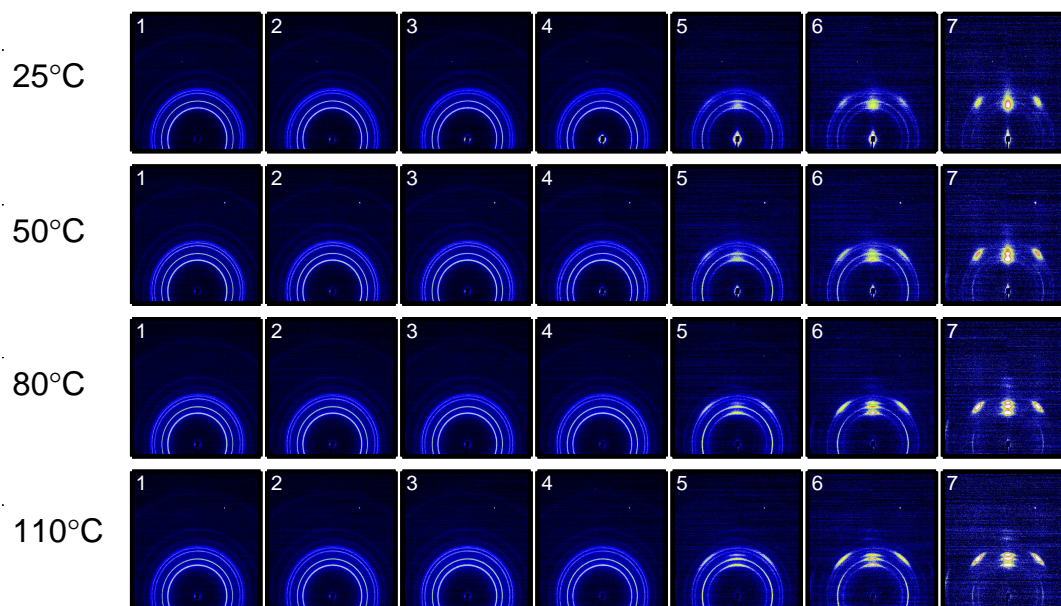


**Figure 4.15:** Normalized 2D-patterns of  $\gamma$ -iPP stretched at temperatures of 25°C, 50°C, 80°C and 110°C from top to bottom. The true strains, determined with the assumption of fully uni-axial deformation, are given as well. The macroscopic strains at which the patterns are taken are indicated by the markers in Figure (4.8). The stretching direction is horizontal.

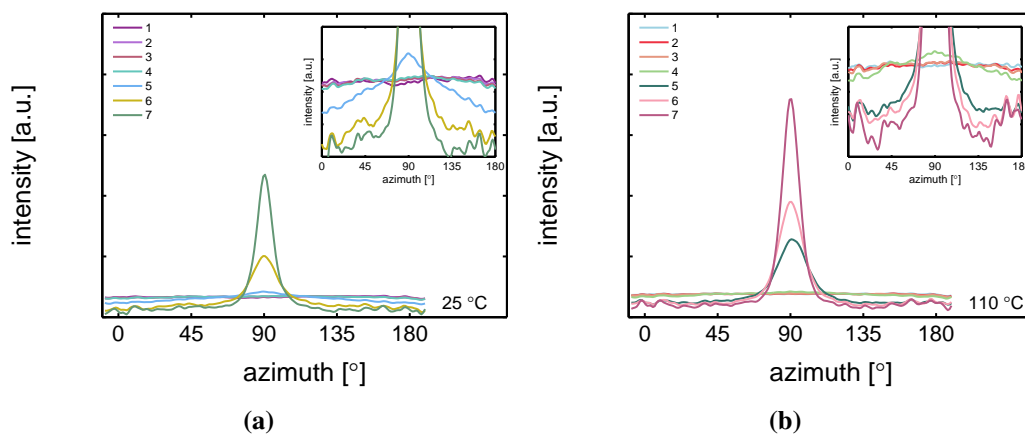


**Figure 4.16:** Azimuthal spread of the (111) diffraction of  $\gamma$ -iPP at various strains. a) uni-axial stretching 25°C and b) 110°C. The numbers in the legend correspond to the 2D patterns in Figure 4.15.

In Figure 4.17 the results of radial integration of the patterns measured on all crystal phases, stretched at testing temperatures of 25 and 110°C are plotted as a function of the scattering vector  $q$  and the true strain  $\epsilon_{true}$ . At 25°C the reflections of  $\alpha$ - and  $\gamma$ -iPP become less intense and broaden, particularly in the macroscopic softening region, corresponding to true strains of about 0.2 to 2 [-]. The  $\beta$ -crystals, on the other hand, seem to maintain their crystallographic structure, and the biggest change observed is broadening of the peaks. At 25°C and high strain,  $\alpha$ - and  $\gamma$ -iPP eventually transform into a 1D intensity typical for the mesophase. In the figures corresponding to elongation at 110°C it is evident that the  $\alpha$ -reflection seems to be maintained rather well, whereas for  $\beta$  and  $\gamma$ -iPP the characteristic reflections disappear, simultaneously with the appearance of the  $\alpha$ -reflection. The reflections remain sharp with well defined peaks up to high true strains.

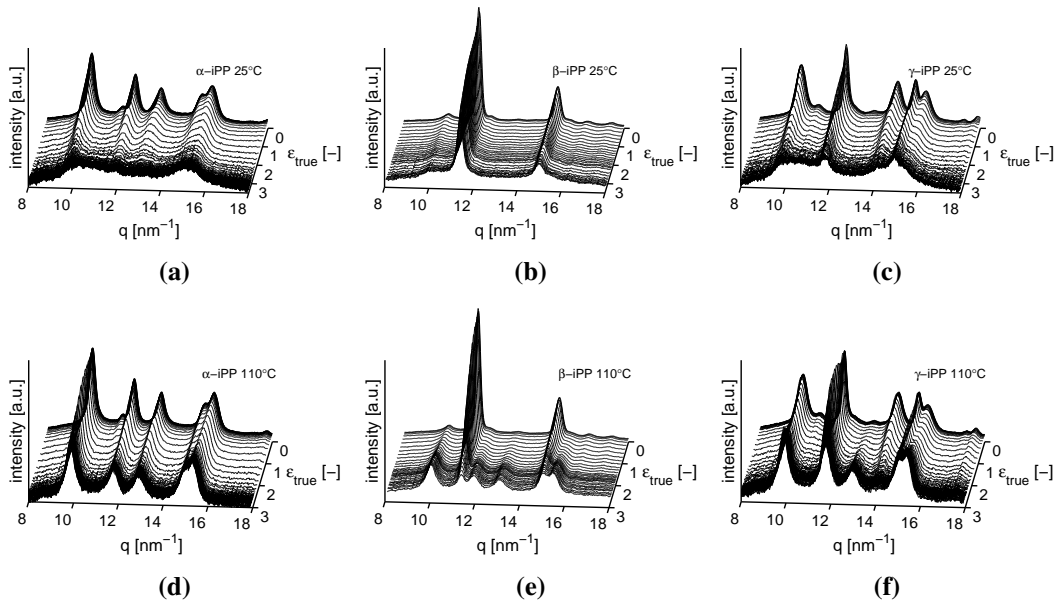


**Figure 4.17:** The integrated intensity as a function of the scattering vector  $q$ . From a) to c) we see the evolution of the crystallinity upon stretching at 25°C of the  $\alpha$ -,  $\beta$ - and  $\gamma$ -iPP respectively. The structural evolution is given as a function of the true strain.

The results of the approach, discussed in sec. 4.2.3, to quantify the crystal phase composition, are given in Figure 4.18. Here, together with the apparent macroscopic stress-strain response, the phase content of the samples deformed at 25°C and 110°C, is shown as function of the macroscopic strain. Results of tensile experiments performed at 50°C and 80°C can be found in the supporting information.

The difference in the structural evolution at room temperature of the  $\alpha$ -,  $\beta$ - and  $\gamma$ -samples that immediately draws the attention is the strong and drastic crystal destruction during the macroscopic softening for  $\alpha$ - and  $\gamma$ -iPP, which is contrasting to the slow and gradual changes in  $\beta$ -iPP. In  $\alpha$ -iPP, almost all the crystals that are initially present in the sample are being destroyed at low temperatures (25°C), and either transform to oriented

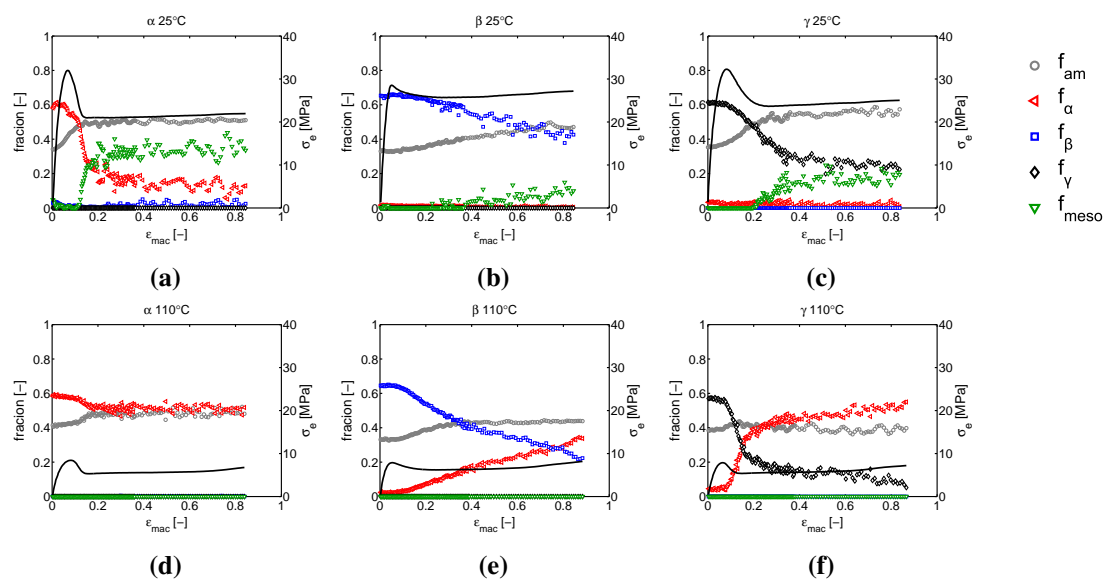


**Figure 4.18:** The crystal phase fractions obtained from the WAXD experiments. From a) to c) we see the evolution of the crystallinity and phase fractions upon stretching at 25°C. Figures d) to f) show the result of the tensile experiments performed at 110°C. From left to right we see  $\alpha$ -,  $\beta$ - and  $\gamma$ -iPP. The solid lines are the macroscopic engineering stress as a function of the apparent macroscopic strain.

mesophase or amorphous phase. At higher temperatures, the amount of newly formed mesophase is lower and ultimately, at a drawing temperature of 110°C reduces to zero. At the highest temperatures the  $\alpha$ -iPP fraction slightly changes, however, based on the results presented in Figure 4.12 it is known that the crystals partially melt and orient, and that the sample subsequently recrystallizes. The gradual transitions observed upon deformation of  $\beta$ -iPP are also observed at elevated temperatures. Where the transition at low temperatures is mainly from  $\beta$  to amorphous or mesophase, the recrystallization at elevated temperature gives  $\alpha$ -iPP. The overall crystallinity slightly decreases at all drawing temperatures. The  $\gamma$ -iPP transforms partially to  $\alpha$ -iPP already at a temperature of 50°C (see supporting information). With increasing temperature the fraction of  $\gamma$ -transforming to  $\alpha$ -phase increases, until a temperature of 110°C where this transition takes place exclusively. To summarize, at low temperatures all polymorphs are being partially destroyed and form amorphous material or oriented mesophase, while at high temperatures all polymorphs transform to oriented  $\alpha$ -iPP. In any case the crystallinity slightly decreases. The structural changes observed from X-ray and the coupling to the apparent macroscopic response are affected by geometric effects, rather than pure deformation, due to localization effects. Therefore, in sec. 4.3.2, these transitions are investigated by means of uni-axial compression.

For crystal phase transitions to take place, the chains within the crystal structures need to have a certain amount of mobility, induced by either the applied temperature or stress. From the results presented in Figure 4.18 it is clear that this mobility is mainly achieved



after the yield point. From that point on, the material is able to partially melt and form new oriented structures. The deformation at this stage is plastic. In order to determine the onset of plastic deformation in the crystal, the evolution of the d-spacing is used. The increasing distance between crystal planes in the polar regions of the diffraction pattern is reflected in the d-spacing and thus, the peak positions observed in the WAXD frames. In Figure 4.19, this evolution in d-spacing is depicted in terms of a strain obtained from eq. (4.21), and presented as a function of the macroscopically applied strain  $\epsilon_{app}$ .

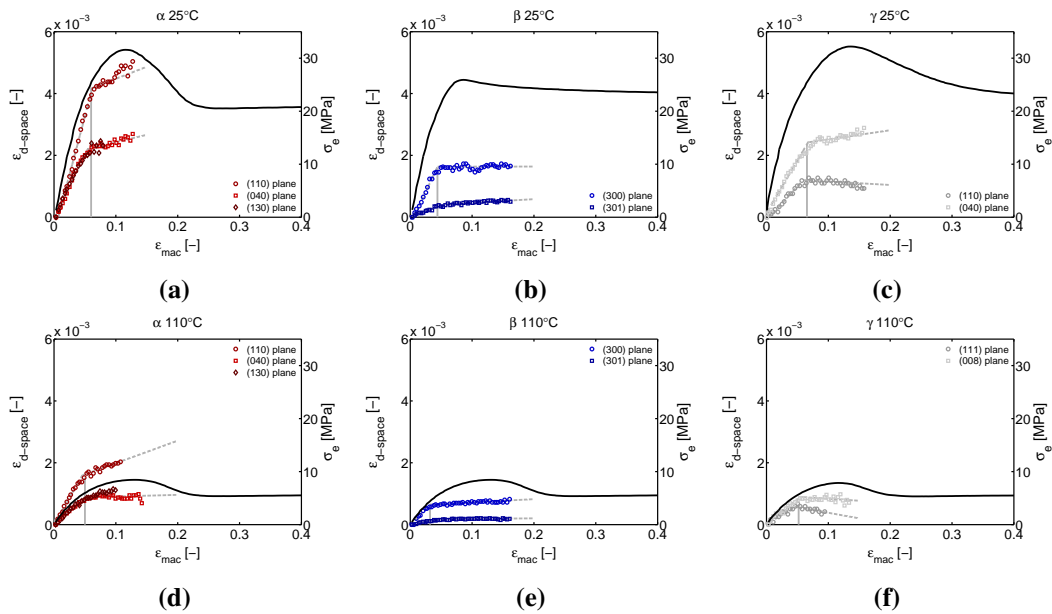


**Figure 4.19:** The increase of the distance between crystal planes of a) and d)  $\alpha$ -iPP, b) and e)  $\beta$ -iPP and c) and f)  $\gamma$ -iPP. The strain at which the distance between the crystal planes no longer increases following the initial slope is associated with the onset of the plastic deformation. Figures a), b) and c) are obtained from tensile tests performed at 25°C while d), e) and f) are taken at 110°C.

As expected for purely elastic behavior, a linear increase in the  $\epsilon_{d-space}$  is obtained first. Subsequently this increase levels off, indicating that the further increasing stress, transmitted on the crystals, no longer results in the same increase in d-spacing. This leveling off is clearly observed prior to yielding and can be interpreted as the onset of collective stress-induced  $\alpha$ -relaxation. Therefore, the onset of this deviation marks the beginning of crystal plasticity. In the case of  $\beta$ -iPP this transition takes place at low macroscopic strains compared to  $\alpha$ - and  $\gamma$ -iPP. The transition correlates to a combination of morphological features like density of the crystal on one hand, and lamellar thickness on the other hand. In  $\alpha$ - and  $\gamma$ -iPP, the crystals have a similar thickness (see sec. 4.3.3) and density (Table (4.1)). The crossed stacking of chains in the  $\gamma$ -iPP lamellae seems to slightly postpone plastic deformation as well. Note that prior to yielding this comparison can be made since the deformation is (close to) homogeneous.

### Compression tests (WAXD)

Since all the phase transitions are depicted as a function of the macroscopic tensile strain, the question rises how big the effect of localization phenomena are. To answer this, similar analysis are done on  $\alpha$ -,  $\beta$ - and  $\gamma$ -iPP deformed in uni-axial compression experiments at temperatures of 25°C and 110°C, where the applied true strain rate is constant and thus the true stress as a function of the true strain can be obtained, see Figure 4.20.

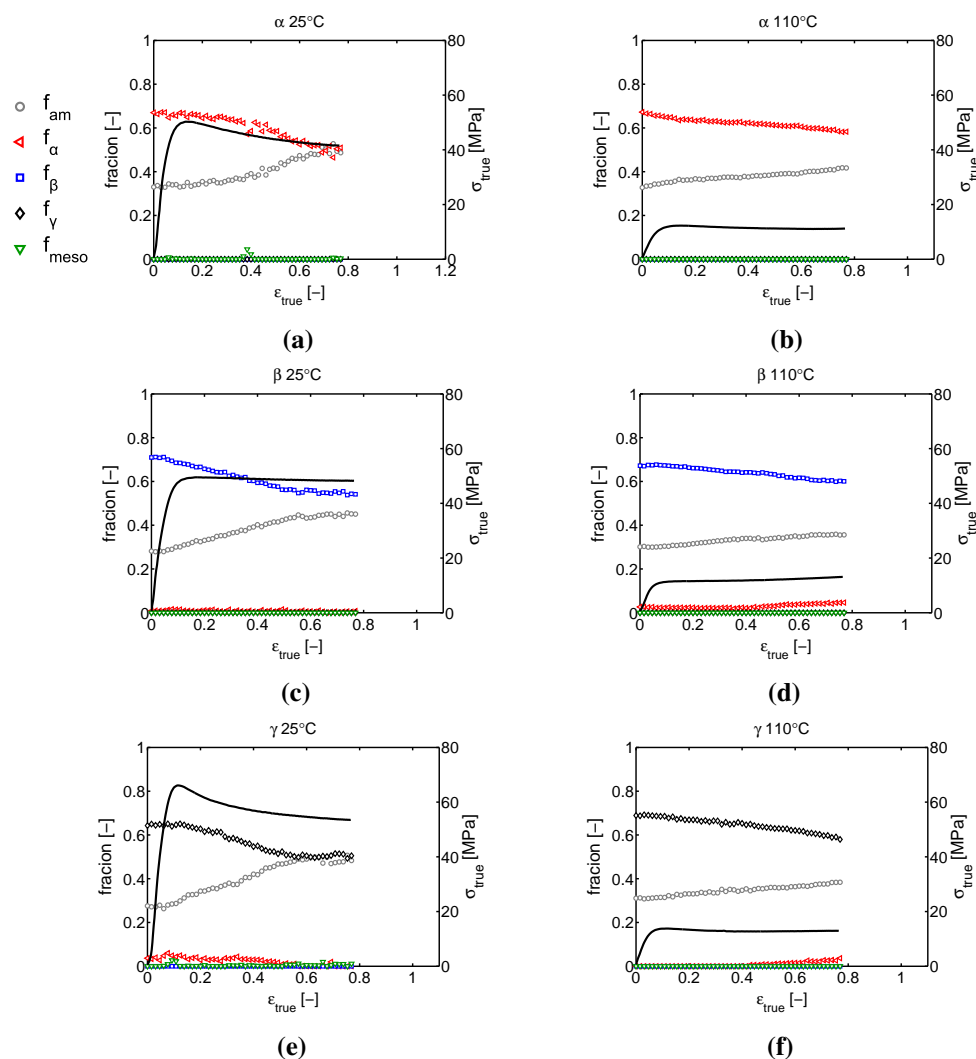


**Figure 4.20:** The crystal phase fractions obtained from the WAXD experiments. From top to bottom we see  $\alpha$ -,  $\beta$ - and  $\gamma$ -iPP. From left to right we see the evolution of the crystallinity and phase fractions upon compressing at 25°C and 110°C. The true stress as a function of the true strain obtained at a true strain rate of  $10^{-2} \text{ s}^{-1}$  is shown with the solid black lines.

The apparent conservation of the structural integrity of  $\beta$ -iPP upon deformation as observed from the tensile experiments (Figure 4.18) is purely a result of reduced localization compared to  $\alpha$ - and  $\gamma$ -iPP. In fact, during compression and at low temperatures it even seems as if the destruction of crystals already starts at relatively low strains, while for  $\alpha$ - and  $\gamma$ -iPP the crystallinity starts to decrease mainly after yielding. Furthermore, the compression experiments show no softening in  $\beta$ -iPP, independent of the temperature, whereas in the tensile experiments the  $\beta$ -iPP samples do show softening as a result of geometrical effects.

### 4.3.3 SAXS analysis

#### Tensile tests (SAXS)

To investigate the structural evolution at the nanometer length scale, SAXS data was taken for the same set of experimental conditions as for the WAXD experiments. In Figure 4.21, the results of the experiments conducted on  $\alpha$ -iPP are shown.

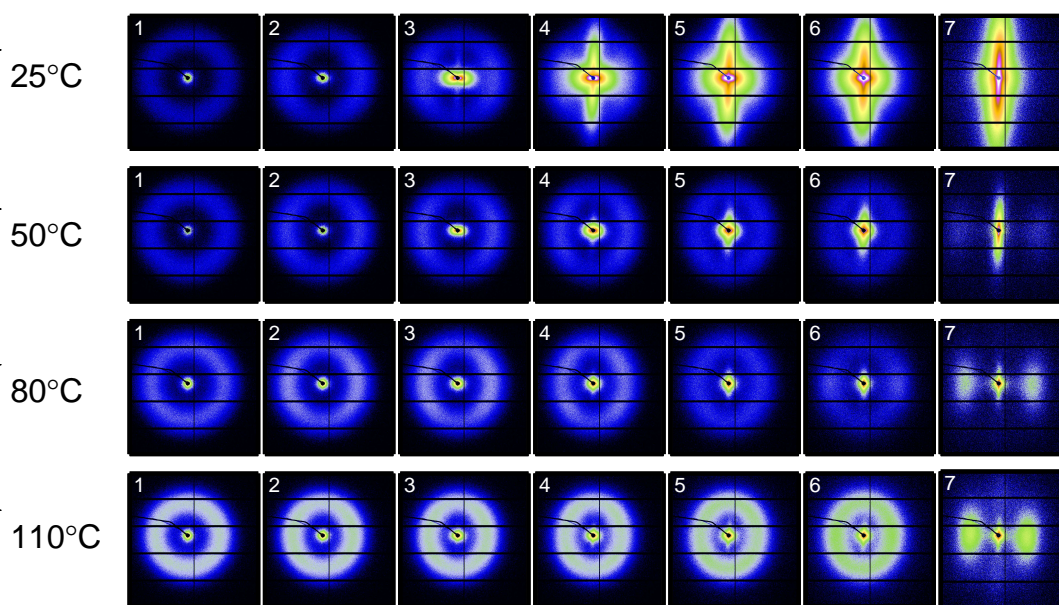


**Figure 4.21:** Normalized 2D SAXS patterns of  $\alpha$ -iPP stretched at temperatures of 25°C, 50°C, 80°C and 110°C from top to bottom. The true strains, determined with the assumption of fully uni-axial deformation, are given as well. The macroscopic strains at which the patterns are taken are indicated by the markers in Figure (4.8). The stretching direction is horizontal.

The intensity scattered from the lamellae increases with temperature, which can be explained by the difference in thermal expansion between the crystals and the amorphous domains that increases the density contrast. The undeformed samples, with randomly oriented lamellar stacks, give rise to a scattering circle with a homogeneous distribution.



Upon deformation, the sample transforms to a state in which the scattering of the lamellae concentrates in the polar regions. At 25°C voids are already present at the yield point (frame 3), evidenced by the clear lobes near the beam center. From the scattering pattern it becomes clear that the dimensions of the voids initially have the largest dimension in the direction perpendicular to the tensile direction. During strain softening and hardening this gradually evolves into the opposite; the largest dimensions of the voids are now parallel to the stretching direction. This observation is accompanied by a transition from high aspect ratio craze-like features to a highly voided state with shear deformation zones. This transition to micro-necking is related to the entanglement network as was shown by for example Kausch et al. [146] and Ishikawa et al. [132]. At high temperature no clear scattering as a result of voiding is observed at yield, however, close to the center some kind of non-cylindrical pattern is observed. This is an indication for the formation of voids, but with dimensions larger than the detectable length scales. Finally it is evident that lamellae of the newly formed crystals are strongly oriented with the so-called lamellar normal of the stacks parallel to the tensile direction.

To quantify the lamellar stack orientation upon stretching, azimuthal integrations are performed in a similar way as for the WAXD patterns. In Figure 4.22 the intensity along the azimuth is shown for the  $\alpha$ -sample stretched at room temperature. After yield, in frames 4 to 7, a strong intensity increase in the equatorial regions develops as a result of the transformation of the shape and the growth of fibrillar voids elongated in tensile direction. For this reason, only the first 3 or 4 frames are shown in the inset, i.e. depending on where voiding starts to affect the result. Although the last frame depicted in the insets already shows some features of voiding (development of a peak at 90°C), the main intensity distribution during the early stages of deformation is a direct result of the orientation of the lamellar stacks.

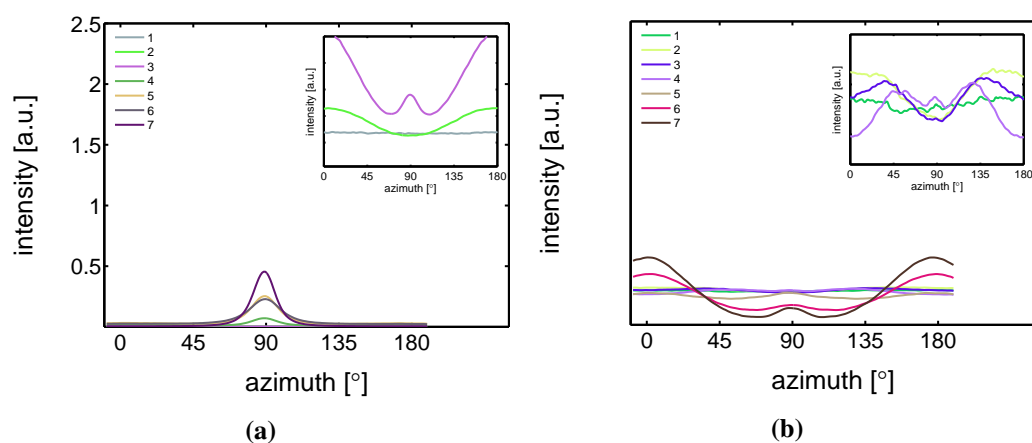


**Figure 4.22:** a) Azimuthal intensity of the lamellar scattering at various strains of  $\alpha$ -iPP. a) uniaxial stretching at 25°C and b) 110°C. The numbers in the legend correspond to the 2D patterns in Figure 4.21.

An important observation done at 110°C is that in the initial stages of deformation the intensity of the lamellae concentrates at angles of 45° and 135°. This phenomenon is often attributed to break-up in between lamellae [125, 147–149], following after cavitation. Here, the scattering patterns show no evidence of voids with a length scale similar to that of the lamellae. Combined with the absence of this preferential orientation in tests performed at room temperature, where there is voiding prior to yielding, it is therefore more likely that the material adopts this orientation because it is preferential for plastic deformation. At room temperature, where we are below  $T_{\alpha_c}$ , a different mechanism takes place which could indicate that the constrained amorphous network is strong enough with respect to the crystallites, to prevent the material to transform to this orientation.

The 2D SAXS patterns measured on  $\beta$ -iPP are shown in Figure 4.23. The scattering intensity close to the center is much stronger than that observed in the  $\alpha$ -samples, meaning that the samples exhibit much more voids in the domain of detectable void sizes. This holds for all temperatures. The process of voiding starts already in the early stages of deformation.

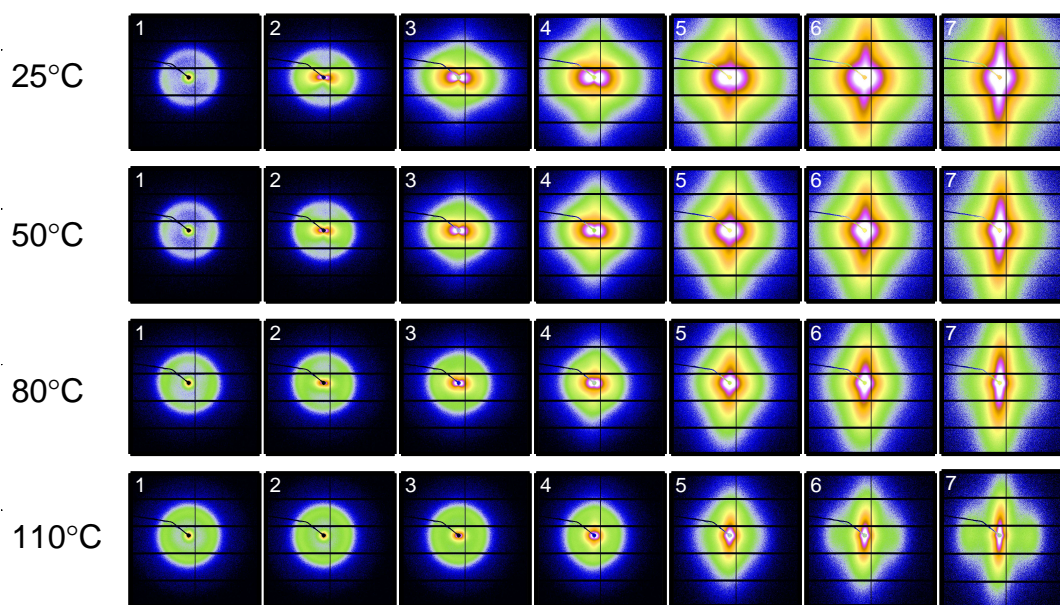


**Figure 4.23:** Normalized 2D SAXS patterns of  $\beta$ -iPP stretched at temperatures of 25°C, 50°C, 80°C and 110°C from top to bottom. The true strains, determined with the assumption of fully uni-axial deformation, are given as well. The macroscopic strains at which the patterns are taken are indicated by the markers in Figure (4.8). The stretching direction is horizontal.

The transition from cavities with the largest dimension perpendicular to the tensile direction to cavities with the largest dimension parallel to the tensile direction takes, compared to the  $\alpha$ -phase, place at higher strains and seems less clear/unfinished, even in the final stages of the stretching experiment. The scattering from the newly formed

crystals appears in the polar regions, indicating that the lamellar normals are oriented parallel to the tensile direction.

The intensities along the azimuths is shown in Figure 4.24. The tensile experiment is started from a state which is not completely isotropic. At 25°C the scattering of the voids affects the integrated intensity almost immediately. At 110°C cavitation is observed first in the third frame, corresponding to the yield point. Although a small anisotropy seems to be present from the beginning of the experiment there is no evidence for a tendency of the formation of a pattern with a orientation at + and -45°, which is different from  $\alpha$ -iPP. These observations are similar to the results found by Men et al., who worked on Poly(1-butene) [150], and claimed cavitation through lamellar breakup.

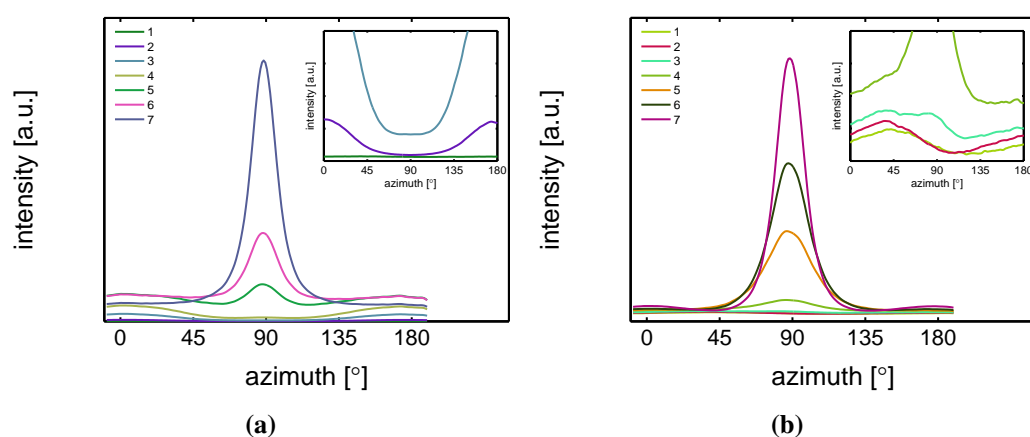


**Figure 4.24:** a) Azimuthal intensity of the lamellar scattering at various strains of  $\beta$ -iPP. a) uniaxial stretching at 25°C and b) 110°C. The numbers in the legend correspond to the 2D patterns in Figure 4.23.

Finally, Figure 4.25 contains the SAXS patterns taken from tensile experiments performed on  $\gamma$ -iPP. Based on the scattering intensity it is expected that the void fraction (within the detectable range) is in between that of  $\alpha$ - and  $\beta$ -iPP. The onset of voiding is clearly before yielding at low temperatures, and also at high temperatures there is some evidence since the scattering close to the center deviates from circular. At 110°C the scattering of the original lamellae becomes strongly elliptical, before the selective melting and recrystallization into oriented crystallites with the lamellar normal in tensile direction takes place. Similar to the  $\alpha$ - and  $\beta$ -iPP the dimensions of the voids are initially larger perpendicular to the tensile direction and transform to shapes that have the largest dimensions parallel to the drawing direction. This happens beyond yielding and takes place more gradual than in case of  $\alpha$ -iPP.

The intensity as a function of the azimuth is depicted in Figure 4.26 for the tests performed at 25°C and 110°C. The latter has a preferred orientation at angles of 45° and 135°, which indicates that also in  $\gamma$ -iPP the lamellar break-up or orientation takes place prior to yielding, similar to  $\alpha$ -iPP.

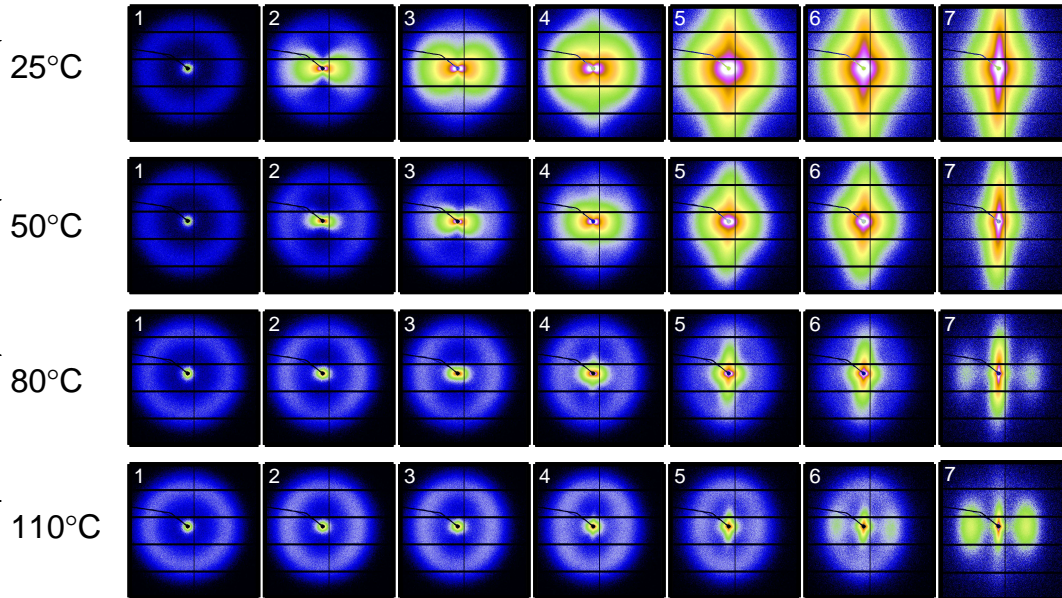


**Figure 4.25:** Normalized 2D SAXS patterns of  $\gamma$ -iPP stretched at temperatures of 25°C, 50°C, 80°C and 110°C from top to bottom. The true strains, determined with the assumption of fully uni-axial deformation, are given as well. The macroscopic strains at which the patterns are taken are indicated by the markers in Figure (4.8). The stretching direction is horizontal.

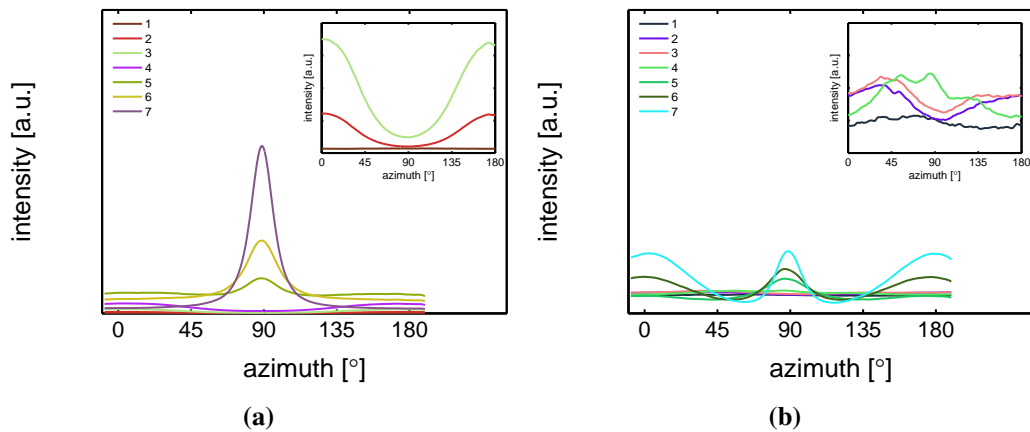


**Figure 4.26:** a) Azimuthal intensity of the lamellar scattering at various strains of  $\gamma$ -iPP. a) uni-axial stretching at 25°C and b) 110°C. The numbers in the legend correspond to the 2D patterns in Figure 4.25.

To quantify the void fraction, the 2D patterns are integrated according to eq. (4.22), which holds for the assumption of cylindrical symmetry, and by substitution of the result into eq. (4.23), the evolution of void fraction as a function of the strain is obtained. This

procedure was applied on the  $\alpha$ -,  $\beta$ - and  $\gamma$ -iPP for all the experimental conditions, and the result is shown in Figure 4.27. The increase of the void fraction becomes particularly clear at the strain where macroscopic yielding takes place. Based on the 2D images this can be linked to the transition of perpendicularly oriented voids towards voids parallel to the tensile direction, which coincides with a large increase in the scattering intensity. In the case of  $\alpha$ -iPP deformed at 25°C,  $\phi_v$  increases simultaneously with the macroscopic softening. This increase stops at the end of the softening after which the volume fraction decreases. Since a volume fraction is considered, two possible explanations can be given for this observation: 1) The voids grow (or coalesce) to larger dimensions and therefore are no longer in the detectable size domain. 2) Due to the extension of the voids and the resulting cylindrical dimensions, together with the fibrillar material morphology in between, the negative hydrostatic stresses reduce severely, causing the voids to collapse. This also leads to a reduction in volume.

When considering the  $\alpha$ -iPP elongated at high temperatures, no notable void fraction can be measured although the 2D-patterns clearly show the presence of voids, evidenced by the non-circular scattering close to the beam center. The intensity in these 2D images is given on a logarithmic scale, and thus, the early stage of void initiation immediately becomes clear. Apparently these effects are not strong enough to cause a scattered intensity increase, significantly large to be reflected in the void fraction. In the case of  $\beta$ -iPP the void fraction starts to increase at the yield point and continues to grow throughout the entire experiment. The two phenomena that cause the  $\phi_v$  in  $\alpha$ -iPP to decrease are not present in the  $\beta$ -sample. With increasing temperature, the volume percentage of voids decreases. At 25°C and 50°C, the  $\gamma$ -iPP shows an increase in the scattered intensity that is sufficiently large to be reflected in the void fraction. This starts to develop at the yield point, and continues to grow with increasing strain. However, after softening the void fraction reaches a plateau.

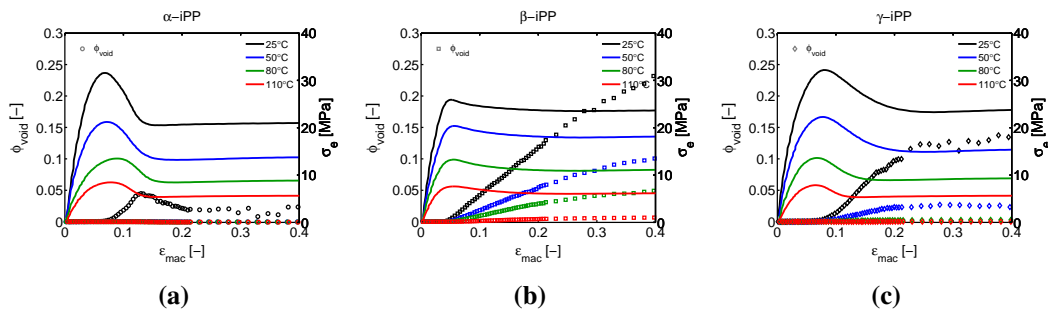


**Figure 4.27:** Void volume fraction as a function of the macroscopic strain for  $\alpha$ -iPP (a),  $\beta$ -iPP (b) and  $\gamma$ -iPP °C (c), elongated at 25, 50 80 and 110°C.



## Lamellar morphology

The crystal phase transformations are accompanied by changes in the lamellar morphology. For structural information on the lamellar thickness, the long period and the amorphous layer thickness, in both the tensile and transverse direction, the equatorial and meridional regions were integrated separately, see Figure (4.6). The integrated 1D intensity was Lorentz corrected and the methods described in section 4.2.3 were applied. In Figure 4.31 of the supporting information, the results are presented as a function of the macroscopic strain, in the range where the analysis could be applied, i.e. before crystals were destroyed too much. The most interesting observation is done while stretching  $\gamma$ -iPP at 110°C, see Figure 4.28. As expected, the lamellar thickness obtained using Bragg's law is lower than the ones obtained by using the auto-correlation function. In the latter case, the dense amorphous transition zones in the vicinity of the crystals add up to the crystal thickness. In that case, self evidently, the amorphous layers are thinner. In the elastic deformation regime, the long period in the equatorial region clearly increases. The evolution of the long period in the meridional region behaves opposite and even displays a decreasing trend. Based on the results obtained from Bragg's law, it follows that the amorphous regions increase in the initial stages of deformation, however, also the crystalline regions slightly thicken. After yielding, the associated destruction of  $\gamma$ -iPP and the transformation to  $\alpha$ -iPP, a sudden increase in long period is observed. This is dominated by the thickening of lamellae, that increase on average from approximately 8-9 nm, to 12-13 nm, see Figure 4.28. This strong increase is only observed in the  $\gamma$ -samples after yielding at high temperature, see supporting information.

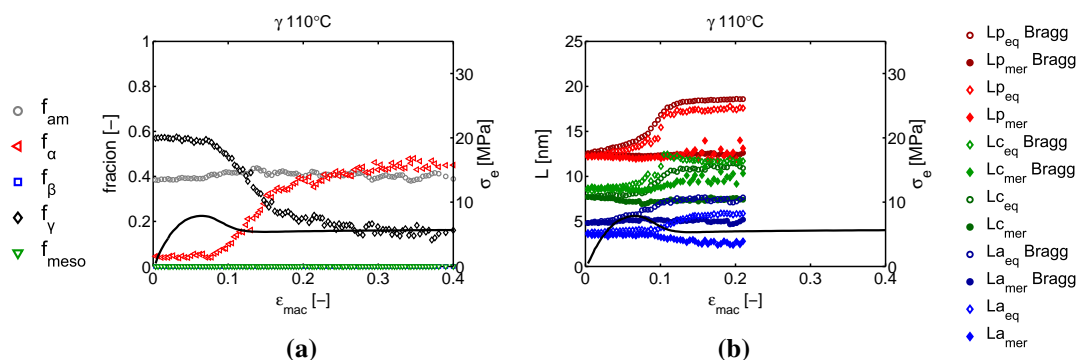


**Figure 4.28:** a) Crystal phases in  $\gamma$ -iPP upon stretching at 110°C, and b), The evolution of the long period, lamellar thickness, and amorphous layer thickness.

If we consider the  $\gamma$ -crystal lattice and compare it with the newly formed  $\alpha$ -lattice, the schematically depicted transformation in Figure 4.29 is obtained. This transition is investigated in detail, using WAXD experiments, by Auriemma et al. [92], who reported the transformation of  $\gamma$ -iPP (prepared in a low stereo regularity iPP) into  $\alpha$ -iPP upon stretching. Their findings and interpretations of the different mechanisms involved at the unit cell level, combined with the increase of the long period simultaneously with

the phase transition, suggest that the helical chain conformation is maintained during the transformation. During the destruction of  $\gamma$ -iPP at 110°C, the ternary helical chain conformation seems to be maintained, and directly incorporated in the newly formed  $\alpha$ -lattice. The observation of the increasing lamellar thickness could be worked out further, and offers a special way to obtain  $\alpha$ -iPP with large crystal thickness obtained from hot drawing of  $\gamma$ -iPP.

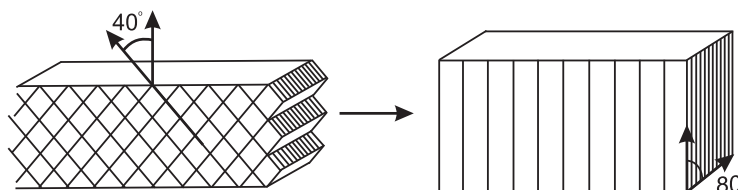


**Figure 4.29:** Suggested deformation of a  $\gamma$ -crystal with the orthorhombic unit cell structure at a temperature of 110°C. The newly formed lamellar crystal is comprised of a monoclinic alpha unit cell structure.

## 4.4 Discussion and conclusion

Tensile and compression experiments are combined with in-situ SAXS and WAXD measurements to reveal deformation induced structural evolution phenomena at multiple length scales for the three well known polymorphs of iPP. WAXD experiments are used to obtain information about phase transitions, selective melting and orientation of crystal planes. The orientation of lamellae, their thickness and the thickness of the intermediate amorphous layers, follow from the SAXS experiments, as well as the appearance and growth of voids. The findings, with respect to the structural evolution, are linked to the macroscopic intrinsic mechanical response.

Based on our previous work and the intrinsic behavior presented in sections 4.3.1 and 4.3.2 we hypothesize that the typically amorphous phenomenon of softening is mainly due to the constrained amorphous regions in the vicinity of the crystals, rather than deterioration of the crystals.

With respect to the crystallographic structures, the WAXD experiments revealed that at low temperatures all polymorphs undergo a (partial) phase transition to oriented mesophase or amorphous phase at large strains. At elevated temperature, the newly formed structure is predominantly the thermodynamically most stable oriented  $\alpha$  form. From the compression experiments it is found that the true strain at which these transitions take place is similar for all polymorphs and, therefore, not the cause for the different macroscopic behavior.

The crystallinity of all polymorphs decreases at similar true strain, independent of the loading conditions, whereas softening is mainly observed in  $\alpha$ - and  $\gamma$ -iPP. These are the crystalline forms with the highest density. The extent to which crystals constrain the

amorphous phase is dominated by density (secondary interactions) and lamellar thickness or crystal defects. Apparently, the higher density of  $\alpha$  and  $\gamma$ -iPP outweighs the influence of thicker lamellae in  $\beta$ -iPP. The crossed configuration of chains in  $\gamma$ -iPP lamellae seems to act as an additional constraint, whereby a rejuvenation treatment is needed in order to obtain the formation and growth of a stable neck in tensile deformation.

To obtain a rejuvenated constrained amorphous phase, mobility has to be created in constrained amorphous layers by either thermal treatments or mechanical deformation. The WAXD experiments show that the  $\beta$ -crystals deform at relatively low strains, clearly prior to yielding. This allows the constrained amorphous domains to gain mobility and soften. Since for  $\beta$ -iPP this happens far before yielding, it might partially explain the absence of softening.

Based on the observation of softening in  $\alpha$ - and  $\gamma$ -iPP at a testing temperature of 110°C, which is above the  $\alpha_c$ -relaxation temperature, it is hypothesized that this is a result of the cross-hatched structure. Break-down of these structures deteriorates the structural integrity, causing a reduction of the stress. In the absence of cross-hatched structures, as is the case for  $\beta$ -iPP, softening is not observed at this temperature.

The evolution of the lamellar orientation suggests that upon stretching  $\alpha$ - and  $\gamma$ -iPP behave different from  $\beta$ -iPP. In the latter one, the lamellae show no clear orientation while stretching at high temperatures. From the intrinsic behavior it is found that the strain hardening modulus is the highest in  $\beta$ -iPP. The crystal shear starts the earliest and also the onset of voiding, which is the most intense in  $\beta$ -iPP, is observed at the lowest strains. The observation that the crystal planes seem to slip before voiding starts, suggests that in  $\beta$ -iPP the critical shear stress is exceeded before the critical cavitation stress is reached.

The  $\gamma$ -iPP, with the crossed chain configuration in the crystal lattice, interestingly shows a strong increase in long period and lamellar thickness while stretching at high temperature. In the softening regime, where the  $\gamma$ -crystals transform to  $\alpha$ -crystals, the lamellar thickness in the equatorial regions increases to such an extent, that it is plausible to assume that the part of the chain originally incorporated in the crystal, maintains the ternary helical conformation during this transition.

The low strain hardening modulus of  $\alpha$ -iPP causes the initial disk-like voids to transform into an ellipsoid with a larger shape, oriented in the tensile direction, at relatively low apparent macroscopic strains, compared to the  $\gamma$ - and  $\beta$ -iPP, with the higher strain hardening modulus. In fact, for  $\beta$ - and  $\gamma$ -iPP this transition is still not completely fulfilled at large macroscopic strains.

Where the crystal structure and topology determine to a large extent the pre-yield behavior, and indirectly contribute to the level of the yield stress, the network is decisive in the post yield behavior (strain hardening). The constrained amorphous phase in the vicinity of the crystalline material is of vital importance for the softening observed after yielding and the strain hardening modulus determines when voids transform to other shapes.



## Supporting information

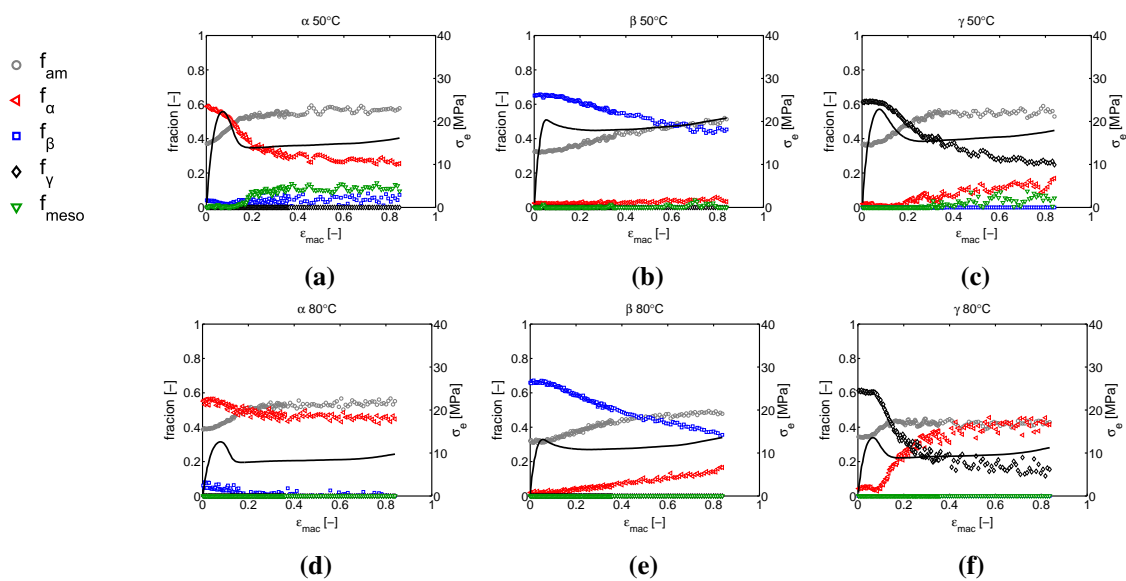


**Figure 4.30:** The crystal phase fractions obtained from the WAXD experiments. From a) to c) we see the evolution of the crystallinity and phase fractions upon stretching at 50°C. Figures d) to f) show the result of the tensile experiments performed at 80°C. From left to right we see  $\alpha$ ,  $\beta$  and  $\gamma$ -iPP.

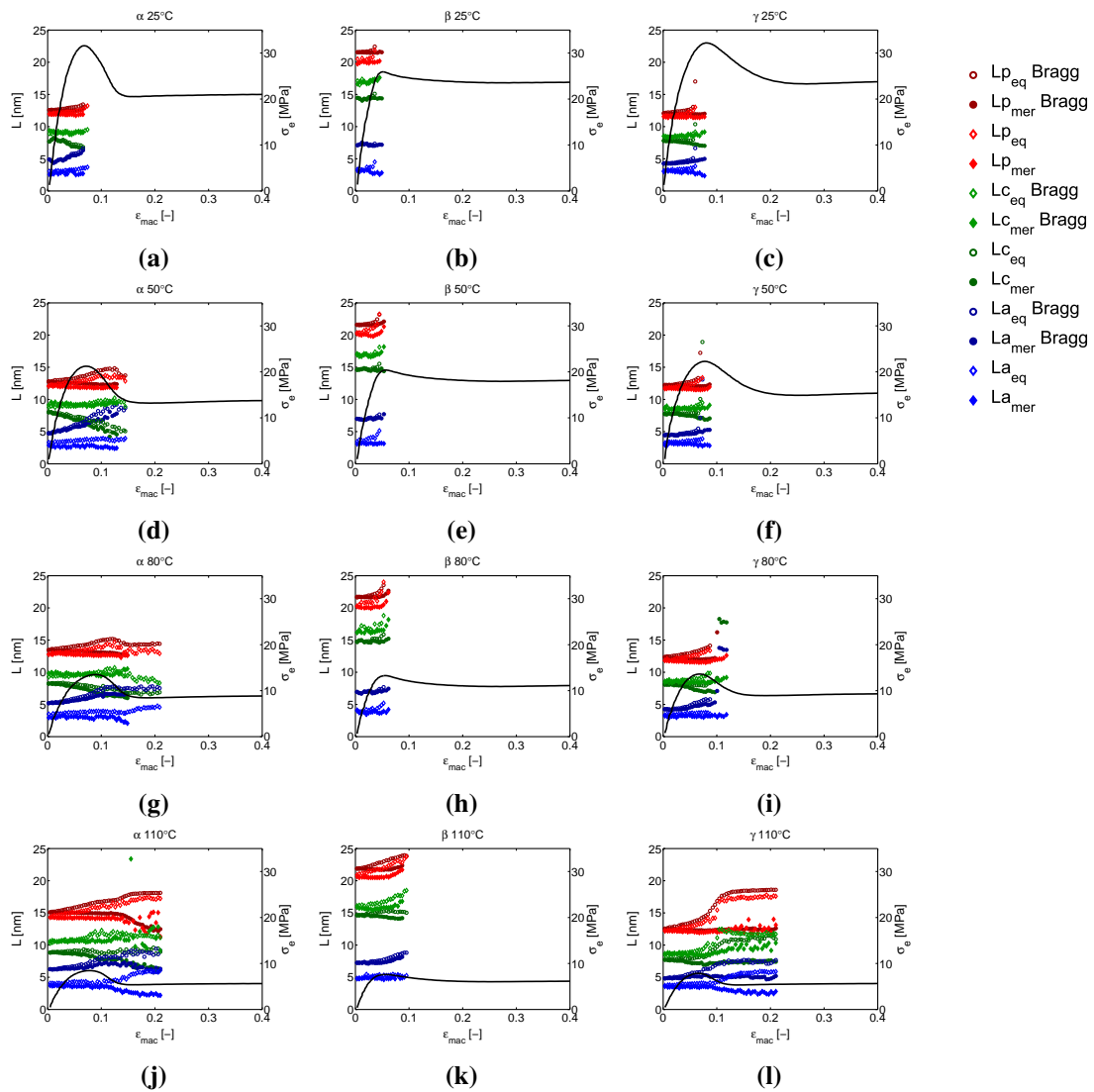


**Figure 4.31:** Long period, amorphous layer thickness and lamellar thickness determined via Bragg's law and the 1D autocorrelation function versus the macroscopic strain for  $\alpha$ -iPP (a,d,g,j),  $\beta$ -iPP (b,e,h,k) and  $\gamma$ -iPP (c,f,i,l), all elongated at 25, 50 80 and 110°C.



---

# Long term failure predictions in polypropylenes

---

## Chapter 5

### Abstract

Polymers display time-dependent behavior which ultimately leads to failure when loads are applied. To give guarantee for lifespans of 50 years and more, certification data is generated. Typically, to accelerate failure kinetics, elevated temperatures are used. As a consequence, the temperature range in which the experiments are performed covers regions above and below the  $\alpha$  relaxation temperature  $T_{\alpha_c}$ , where different molecular mechanisms govern failure. In a well-established testing procedure, ISO9080, time-temperature superposition (TTS) is used to estimate the time-to-failure as a function of the applied stress via linear regression in both the plasticity controlled failure regime and the slow crack growth controlled failure regime. This procedure lacks some important features making the applicability of TTS doubtful for materials like isotactic polypropylene (iPP) and iPP random cop-polymers (RACO's). Firstly, this approach makes no distinction between the different molecular mechanisms dominating the plasticity controlled failure in the different thermal regimes. Secondly, structural evolution, and consequently, the evolution of properties is not taken into account. In this study, the evolution of structure over time will be quantified, and the effect on mechanical properties in the plasticity and crack growth controlled failure regime will be discussed. It is shown that two distinct types of structural evolution both lead to an increasing yield stress. Moreover, it is discussed how these evolutions can corrupt the TTS procedure, and which precautions need to be considered when applying ISO9080. It is demonstrated that cyclic thermal conditions can have a significant effect on the life time at a specified load, particularly when fluctuating around  $T_{\alpha_c}$ . Finally, we show that the brittle failure is not a crack growth controlled mechanism, but rather a mechanism with dominant plasticity controlled characteristics.

---

Reproduced from: H.J.M. Caelers, N. Perillo, R.A.C. Deblieck, G.W.M. Peters, L.E. Govaert. Long term failure predictions in polypropylenes. *To be submitted.*

## 5.1 Introduction

Polymers are increasingly employed in load bearing applications, in which long term properties play an important role. For this reason, load bearing capacity and durability are important topics in current material research. One should be aware that when a load or a stress is applied on a polymer component, failure will always occur in time, even at stress levels far below the yield stress. In general, three different failure regimes can be recognized: I) plasticity controlled failure (ductile), II) fatigue crack growth controlled failure (brittle) and brittle fracture due to chemical degradation (III), see Figure (5.1) [2, 151].

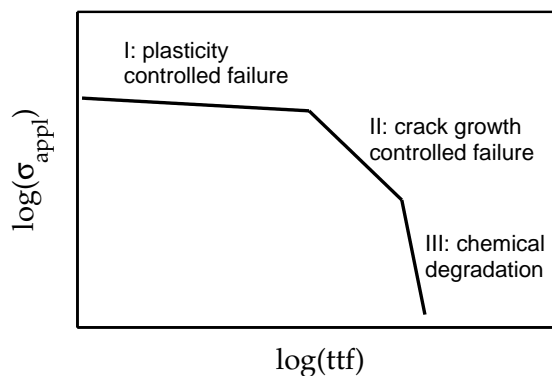


**Figure 5.1:** Schematic of time-to-failure response as a function of applied stress, typically observed in thermoplastics.

Depending on loading conditions like temperature and applied stress, either one of the three governs. Obviously, it is of major importance to be able to predict and ideally postpone the moment at which this occurs. This is a complicated task since all mechanisms have a different origin and, therefore, require a separate strategy. Chemical degradation for example leads to a reduction in molar mass, eventually causing the formation of many cracks. However, the development of additives has improved the thermal and chemical stability to such a degree that this failure mode is rarely observed [152]. Crack growth controlled failure on the other hand is observed regularly. This mode is characterized by the formation and stable growth of a crack throughout a product, and can be identified with creep or fatigue crack growth experiments, the latter one to accelerate time-to-failure [153]. The slope of this mechanism is clearly steeper than that of plasticity controlled ductile failure, and the change in slope marks the position of the so called "mechanical knee", i.e. the transition from ductile to brittle failure. Plasticity controlled failure originates from an accumulation of plastic strain, ultimately leading to large localized deformation, and can be accelerated with elevated temperatures [154]. A full characterization and the determination of the time-to-failure can be a time-consuming task.

To estimate and certify lifetimes of loaded polymer products subjected to specified loading conditions, standardized time-temperature superposition procedures are developed. An example of such a procedure is ISO9080 [155], which is used in industry for the prediction of pipe life-times up to time spans of 50 years. This method is developed for thermoplastics like PE and PVC, and is also frequently used for iPP. An example of such a certification result is shown in Figure (5.2) [156], where the procedure is applied on an iPP grade. The markers in this figure represent the results of pressurized pipe experiments.

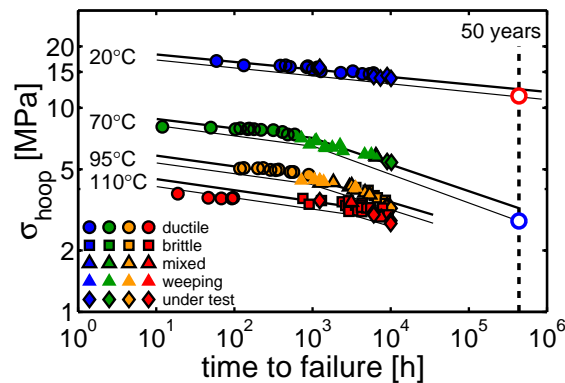


**Figure 5.2:** An example of certification data obtained from burst pressure experiments and a fit of the ISO9080 certification model.

From the results in Figure (5.1), the mechanical knee and the two failure mechanisms, i.e. plasticity- and crack growth controlled failure, can clearly be distinguished. Furthermore, different failure mechanisms are macroscopically observed. At relatively short time-to-failure the dominant failure mode is ductile, while at longer loading times a transition to brittle behavior is found. In the transition region a mixed failure mode might be observed, and occasionally weeping, i.e. leakage through percolated cavities, is observed. The lines in this figure denote the description using the 4-parameter model of ISO9080, and are based on time-temperature superposition:

$$\log_{10}(ttf) = C_1 + \left(\frac{C_2}{T}\right) + C_3 \cdot \log_{10}(\sigma_h) + \frac{C_4 \cdot \log_{10}(\sigma_h)}{T} + e \quad (5.1)$$

In this equation  $\sigma_h$  is the hoop stress and T is the temperature in °K. Failure, particularly in the plasticity controlled regime, is strongly accelerated by an increase in temperature. As a result of this strategy, the time required to do reliable life time predictions for life spans up to 50 years, reduces to about 1.5 years.

Unfortunately, however, the ISO9080 certification procedure lacks some important features that can not be neglected when considering polypropylenes. Firstly, it is well established that semi-crystalline polymers display more than one molecular deformation mechanism in the ductile failure regime, each having their own rate dependence. Above

the  $\alpha_c$  relaxation temperature, i.e. the temperature at which chains in the crystal experience sufficient mobility to display translational movement in and out of the lamellae, the intra lamellar deformation mechanism is responsible for the resistance against deformation, while below this temperature also the inter-lamellar mechanism contributes. This latter mechanism originates from a reduced mobility of the chains within the crystal. In ISO9080 two slopes are recognized, see Figure (5.1), but only one of them represents the plasticity controlled failure regime. This means that the parameters used for time temperature superposition are determined on different deformation mechanisms with contrasting stress and temperature dependence and, because of that, most certainly do not properly describe the actual kinetics.

Secondly, it is well-known that structural changes may take place in time, which largely affects the mechanical response. Temperature can significantly influence the type and rate of these structural changes and hence, controls the rate of change in properties. As a result the physical state of the material after prolonged loading at different stress and temperature will not be comparable [157, 158]. This implies that the TTS procedure builds on corrupted data. Self-evidently this can corrupt the long term predictions, for which samples are tested at various temperatures and for various times.

In this study it is aimed to estimate the importance of these missing components. This is investigated with an alternative model that takes into account both the shortcomings mentioned before. The two approaches, ISO9080 and Eyring, are based on a power law and an exponential respectively. Experiments are used to compare between the two approaches.

## 5.2 Experimental

### 5.2.1 Materials and sample preparation

In this study several polypropylenes are used to demonstrate that the phenomena discussed here are generic to this type of material. Besides three homo polymer injection molding grades with similar molecular weight and polydispersity, the group of materials also contains a random copolymer (extrusion grade) and a  $\beta$ -nucleated injection molding grade. The propylene granulate was kindly provided by Borealis and SABIC. An overview of these materials is given in Table (5.1).

### 5.2.2 Mechanical testing

A compression mold was used to obtain iPP sheets. First, the granulate was placed in between aluminum sheets (0.1mm) and brass plates (3mm). Subsequently the stack was placed in a hot press and heated to 220°C. After melting the material, a pressure of about 5 MPa was applied stepwise, and the sample was kept for 5-10 minutes at 220°C to erase thermo-mechanical history. Solidification was induced by placing the stack in a cold press at a temperature of 20°C, or 80°C in the case of iPP-4. A punch was used to obtain dog-

**Table 5.1:** Materials

<i>Material</i>	<i>Mw</i> [kg/mole]	<i>PDI</i>	<i>ethylene</i> [wt%]	<i>β – nucleant</i> [wt%]
<i>iPP – 1</i>	310	3.4	–	–
<i>iPP – 2</i>	365	5.4	–	–
<i>iPP – 3</i>	320	5.4	–	–
<i>iPP – 4</i>	710	4.4	3.3	–
<i>iPP – 5</i>	320	4.4	–	0.1
<i>iPP – 6</i>	740	4.4	–	–

bone shaped tensile bars (ISO 527 Type 1BA and ASTM D1708) out of the iPP plates. The tensile and creep experiments were conducted with a Zwick Z010 tensile machine, equipped with a Eurotherm temperature control and a 1kN load-cell. The dynamic loading experiments were performed on an Instron E1000, equipped with a Hielkema temperature control and a 1kN load cell

### 5.2.3 X-ray analysis

X-ray experiments were performed on sheet material with varying annealing history to determine the degree of crystallinity and the lamellar thickness. These scattering experiments were performed at the Dutch-Belgian (DUBBLE) beamline BM26 of the European Synchrotron and Radiation Facility in Grenoble (France) [47]. A Pilatus 1M detector with a pixel size of  $172 \times 172 \mu\text{m}^2$ , was used to obtain small-angle X-ray scattering (SAXS) patterns. The detector was placed at a distance of approximately 1420 mm from the sample. The wavelength  $\lambda$  was  $1.033\text{\AA}$  and the samples were exposed for 30 seconds. The background was subtracted from the SAXS data with the software package FIT2D.

The lamellar thickness and the thickness of the amorphous layer was obtained from the 1D correlation function, determined from the integrated Lorentz corrected scattering (SAXS) intensity, given by:

$$I_1(q) = I(q)q^2 \quad (5.2)$$

Here  $I$  is the intensity and  $q$  is the scattering vector. The 1D auto-correlation function  $\gamma_1(r)$  [52, 139] is, under the assumption of spherical symmetry, given by:

$$\gamma_1(r) = \frac{1}{Q} \int_{q_0}^{q_\infty} I_1(q) \cos(qr) dq, \quad (5.3)$$



where  $r$  is the real space and  $Q$  is the scattering invariant defined by:

$$Q = \int_{q_0}^{q_\infty} I_1(q) dq, \quad (5.4)$$

To extrapolate the experimentally assessable range of the scattering vector in the low  $q$ -range, Debye-Bueche [140] is used. At high  $q$ -values, the Porod law [141] is used for the extrapolation. The amorphous layer thickness  $L_a$  (because the crystallinity  $\chi$  is higher than 50%) and the long period  $L_p$  are subsequently determined as described by Stein et al. [54]. The lamellar thickness  $L_c$  is obtained from the difference between the two. The linear crystallinity is obtained according to:

$$\chi = \frac{L_c}{L_p} \quad (5.5)$$

## 5.2.4 Scanning electron microscopy

Tested samples of the creep experiments are used for scanning electron microscopy (SEM). The images are taken of the surface highlighted in the schematic representation shown in Figure (5.3). Samples were etched for 30 minutes with KMnO<sub>4</sub>. The instrument used in this study was a FEI Quanta 600 Scanning Electron Microscope. The images shown in this work were obtained by secondary electron mode, with a primary scanning beam of voltage of approximately 5 kV.

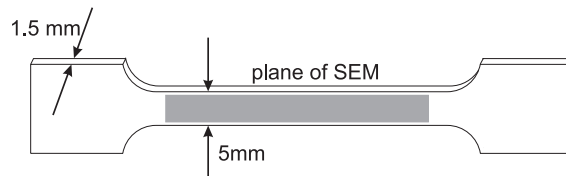


**Figure 5.3:** Schematic of the tensile bars used for the SEM study. The gray plane represents the surface used for SEM imaging.

## 5.3 Results and discussion

First, we elaborate on the structure of polypropylenes and the resulting yield kinetics. Then, the evolution of properties over time is investigated at different temperatures. This evolution is a result of evolving structural features that are discussed. Next, the mechanical knee and the failure phenomena involved will be revealed. Finally, the

consequence of these findings with respect to the ISO9080 certification procedure will be discussed.

### 5.3.1 Morphology and deformation kinetics of polypropylenes

Quiescently solidified high tacticity iPP contains spherulites in which crystalline and amorphous domains are alternately present. In the vicinity of the crystals the amorphous domains experience a reduced mobility due to the constraints implied by the crystalline lamellae. As a result, at certain temperatures, part of the amorphous phase can be considered to be in the glassy state (below  $T_{\alpha_c}$ ) whereas at the same temperature other amorphous regions, further away from the crystals, are still mobile. This effectively means that solid isotactic polypropylene is either a two-phase or a three-phase material, depending on the temperature.

When performing tensile tests it is found that the yield stress, defined as the maximum in the stress-strain response, increases upon increasing deformation rate and decreases with increasing temperature, see Figure (5.4a). The corresponding yield kinetics, i.e. the yield stress as a function of the applied strain rate measured at different temperatures, is shown in Figure (5.4b).

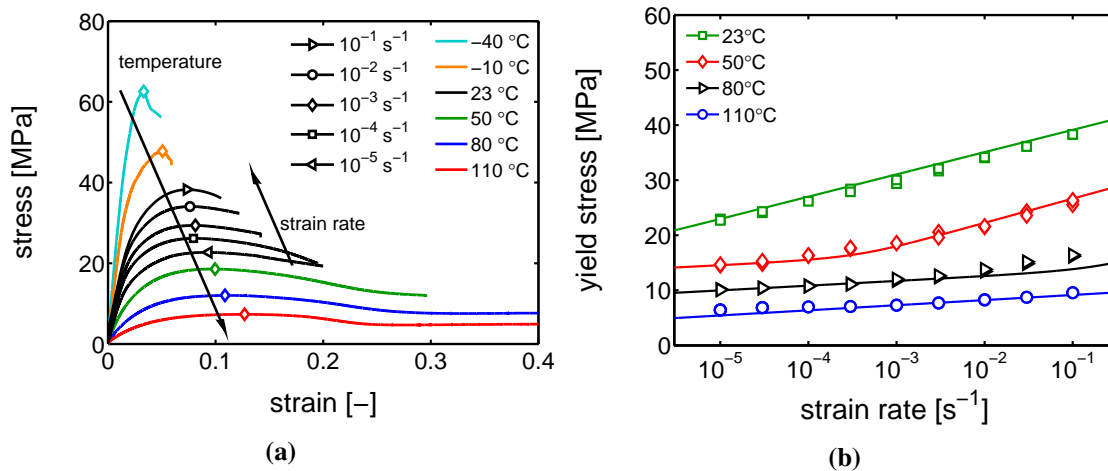


**Figure 5.4:** a) The macroscopic stress-strain response of iPP-3 at various strain rates and temperatures. Markers represent the yield stress, defined as the maximum in the tensile curve. The arrows indicate the effect of an increasing strain rate or temperature. b) Yield stresses as a function of strain rate obtained at various temperatures. Lines are fits obtained from the Eyring equation: eq. (5.6)

The heterogeneous micro-structure of the semi-crystalline material is reflected in the yield kinetics since it can immediately be observed that the rate dependence at elevated temperatures is less strong compared to the one at room temperature. The different slopes indicate two different molecular deformation mechanisms. Above the  $\alpha_c$  relaxation temperature a diffuse type of deformation is observed, originating from collective

diffusive mobility of the chains within the crystal, rendering the crystal "fluid-like" [113]. Here the amorphous domains are mobile and, therefore, the resistance against deformation is purely the result of the intra-lamellar deformation mechanism, schematically shown in Figure (5.5 I). Obviously, the amorphous phase acts as stress transmitter between the lamellae and is for that reason of vital importance

At lower temperature or higher strain rate, the thermal mobility is no longer sufficient to facilitate translational movement of chains throughout the crystal ( $\alpha$ -relaxation). As a consequence, constraints are imposed on the inter lamellar amorphous regions by the crystalline domains, and stress activation is required for  $\alpha_e$ -relaxation or chain slip, schematically depicted in Figure (5.5 II). At intermediate temperature, for example 50°C, a combination of the two can be observed where the flat slope merge into a steep one. A further expansion of the experimentally assessed temperature window would result in a third rate dependency [119].

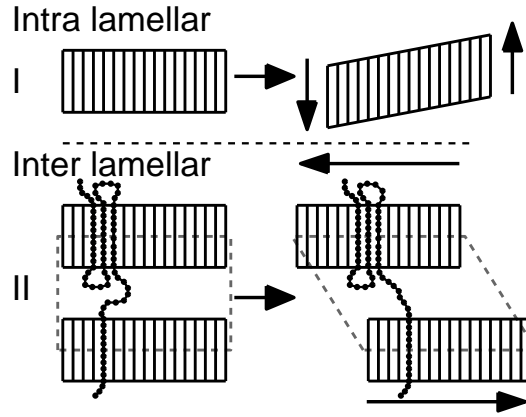


**Figure 5.5:** Schematic representation of the molecular deformation mechanisms in iPP. I) the intra-lamellar deformation mechanism encountered at high temperatures or low strain rate, and II), the inter lamellar deformation mechanism encountered at low temperature or high strain-rate.

The two clearly distinct deformation mechanisms require separate descriptions of the yield kinetics. A successful way to describe the yield kinetics is proposed by Ree and Eyring [106]. They modeled the yield stress in the two regimes, as a function of applied strain rate and temperature, with the modified Ree-Eyring equation, given by:

$$\sigma_{total} = \sum_{i=I,II} \sigma_i = \sum_{i=I,II} \frac{kT}{V_i^*} \sinh^{-1} \left( \frac{\dot{\epsilon}}{\dot{\epsilon}_{0,i} \exp(-\Delta U_i/RT)} \right) \quad (5.6)$$

where  $k$  is the Boltzmann constant,  $T$  is the temperature in  $[K]$ ,  $\dot{\epsilon}$  is the applied strain rate,  $V_i^*$  is the activation volume of deformation mechanism  $i$ ,  $\Delta U_i$  is the activation energy and  $\dot{\epsilon}_{0,i}$  is the rate constant.

### 5.3.2 Evolution of structure and properties

In the previous section it was shown that the different structural components each contribute to the mechanical response. An additional complexity is that these components are subject to change over time. These changes can be accelerated or erased by temperature. This emphasizes the importance of understanding the different processes involved, and the influence of the loading conditions on the final outcome of (certification) experiments.

The iPP constituents, crystalline and amorphous layers, can both display evolution. At low temperatures, ranging from approximately 10°C (well above the bulk amorphous  $T_g$ ) to  $T_{\alpha_c}$ , physical aging phenomena can take place in the constrained glassy layer, causing a reduction in the mobility. Hedesiu et al. investigated the effect of aging (shrinkage and densification) on mechanical properties as modulus and impact strength [58]. They found an increase of the modulus and a decrease of the impact strength. Both changes take place at a decreasing rate in time. As expected, the yield stress is affected over time in a similar way [57]. Furthermore, the ratio between crystal phase, mobile- and constrained amorphous fraction is related to processing which, therefore, affects the aging kinetics [95]. At lower temperature, the bulk amorphous material is out of equilibrium and in the glassy state as well, allowing for the same kind of evolution.

Above  $T_{\alpha_c}$  this phenomenon can not be observed because all amorphous domains are mobile [33, 159]. However, at these temperatures the second type of structural changes becomes more pronounced: secondary crystallization. The structural evolution manifests itself mainly in the crystalline domains. The crystallinity and lamellar thickness increase, and the defect density is expected to reduce. This results in a reduction of the chain mobility in the crystalline phase that obviously increases the resistance against deformation above  $T_{\alpha_c}$  (in the intra-lamellar deformation mechanism). The effect of the structural changes on the mechanical properties like the yield stress was investigated [17, 160] and a linear increase was found as a function of the logarithm of time.

These findings are summarized in Figure (5.6). The 2- and 3-phase systems are schematically presented in the top of Figure (5.6). The dark grey blocks in this figure represent the temperature window in which a specific phase, specified on the vertical axis, is present. The orange blocks mark the possibility of evolution of these phases. From now on, in this work we refer to yield stress evolution at low temperatures (see light grey block in Figure (5.7a) as physical aging, and to evolution of properties at high temperatures as annealing (dark grey block in Figure (5.7a)).

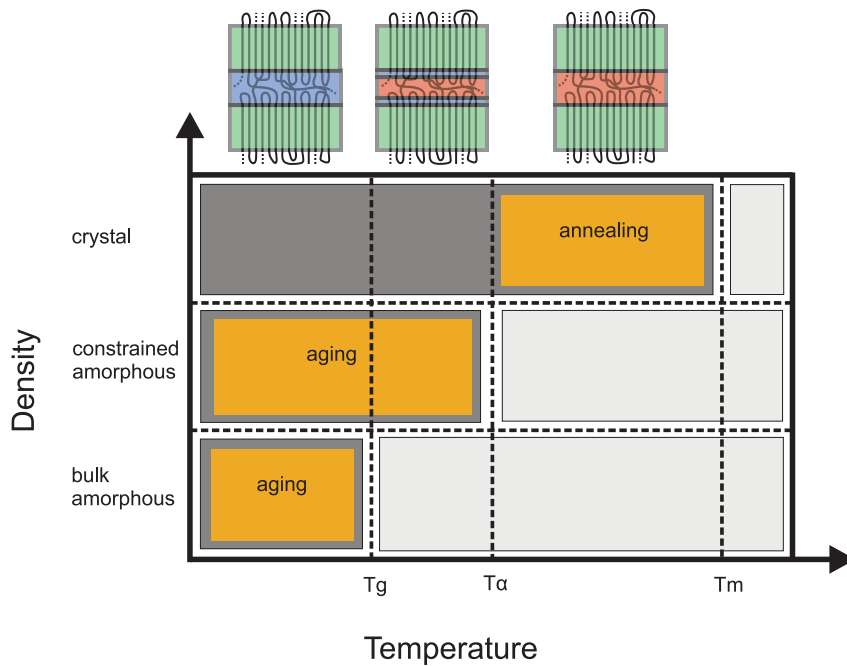


**Figure 5.6:** Graphical summary of the characteristics of polypropylenes. Schematics of the material, present in the specified temperature range are shown in the top of the figure. The dark grey rectangular blocks represent the temperature at which the phase, specified on the vertical axis, is present. The orange blocks mark the regimes where structural evolution can take place.

To investigate the yield stress evolution, the result of annealing and testing iPP-4 at several temperatures, is shown as a function of the logarithm of time, see Figure (5.7a). As expected, this treatment results in a linear increase of the yield stress, independent of the annealing temperature (which equals the test temperature). The rate of yield stress increase is plotted as a function of the annealing temperature in Figure (5.7b). The strongest yield stress increase is observed at the lowest annealing temperature, which is counter-intuitive. Another interesting observation is that there appears to be a jump in the slopes around the  $T_{\alpha_c}$ . This is a clear indication that the mechanisms behind the evolution of properties may be different below and above  $T_{\alpha_c}$ .

In an attempt to separate these two different types of evolution, a test case is developed: A set of iPP-4 samples, all prepared in the same way, was divided over two groups. One group of samples is annealed at a temperature below  $T_{\alpha_c}$ , 50°C, and the other group of samples is annealed above  $T_{\alpha_c}$ , at 110 °C. The yield stress of these samples is monitored over time by tensile tests performed at 50°C and 110°C respectively. The results are plotted in Figure (5.8). From Figure (5.8a) it follows that the annealing treatment at 50°C leads to a strong increase in the yield stress found at 50°C, however, at 110°C, no increase can be observed. This means that the evolution of properties resulting from annealing below  $T_{\alpha_c}$  is erased after the material is heated to testing temperatures above

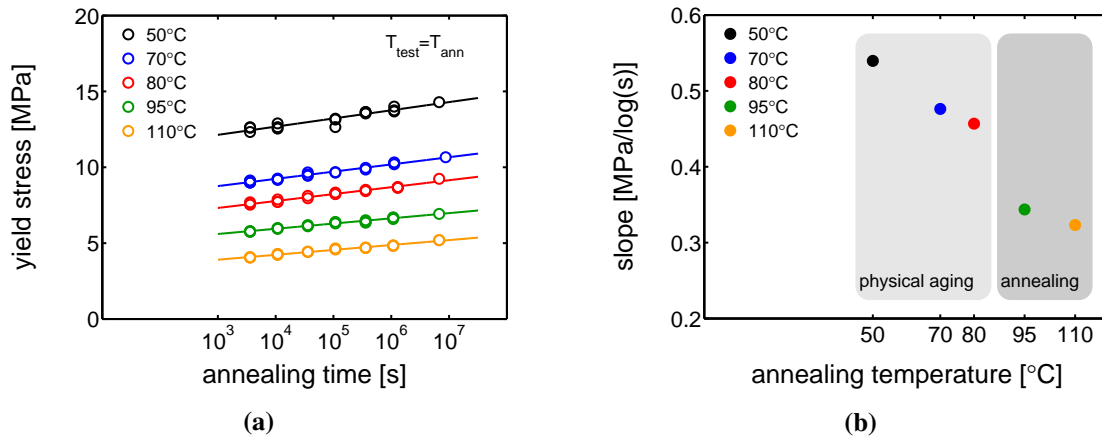


**Figure 5.7:** a) The evolution of the yield stress of iPP-4 over time, annealed and tested at several temperatures and: b) the slope of the yield stress increase as a function of the annealing (and testing) temperature. The light grey block indicates the temperature region below  $T_{\alpha_c}$  and the dark grey block to the region above  $T_{\alpha_c}$ , to which we refer from now on as physical aging and annealing respectively.

$T_{\alpha_c}$ . Contrary, the annealing treatment performed at 110°C leads to an increase of the yield stress found at 50°C, as well as at 110°C, see Figure (5.8b). The results presented in Figure (5.8a) reveal that physical aging only affects the properties below  $T_{\alpha_c}$ .

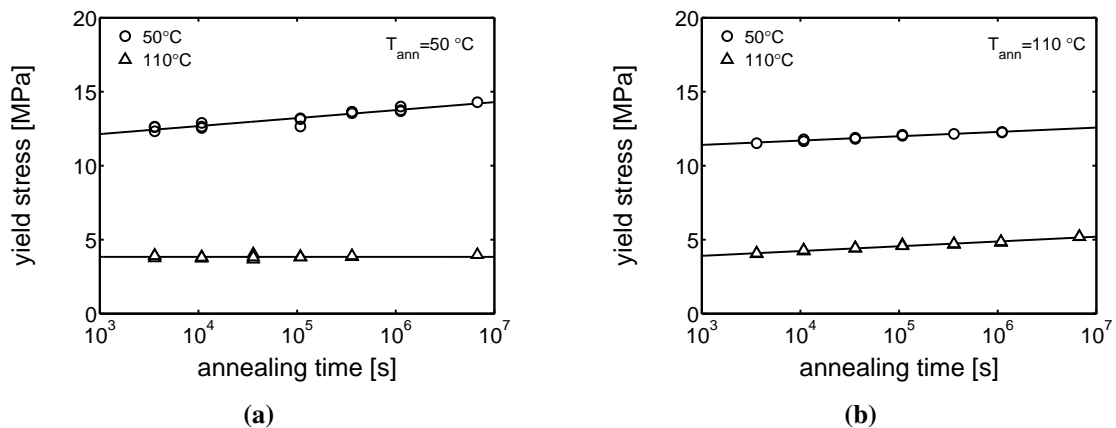


**Figure 5.8:** a) The effect of annealing iPP-4 at 50°C on the yield stress, measured at 50°C and 110°C, as a function of the annealing time. b) Similar results for an annealing treatment performed at 110°C.

To investigate the effect on the yield kinetics, the yield stresses measured directly after sample preparation are compared with the deformation kinetics after 1 month at room temperature, for iPP-1 and iPP-2 (see Figure (5.9)). Both show clear differences at room

temperature and small differences at 50°C. At 80°C and 110°C, the young and aged samples show the exact same yield stresses.

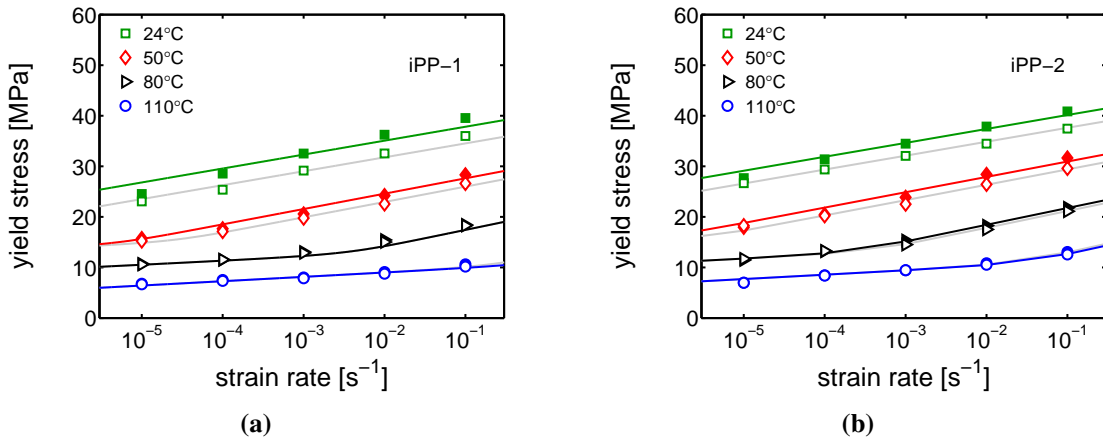


**Figure 5.9:** The evolution of the yield kinetics as a result of aging at room temperature. a) The evolution measured on iPP-1 and b), the results obtained for iPP-2. Open markers are obtained prior to aging and filled markers are from measured after aging.

In the ISO9080 certification procedure, these effects are typically avoided by storing the samples for several weeks at room temperature before testing. Of course, the state of the test specimens is, therefore, different from products that are used directly after processing, or in cyclic thermal (loading) conditions. In the last case the material is constantly going through  $T_{\alpha_c}$ , leading to large changes in yield stress [?, 119]. Self-evidently, this situation is totally different from the isothermal situation in certification tests.

The structural evolution, causing the change in properties in Figure (5.9) is investigated by means of X-ray. In Figure (5.10) the linear crystallinity  $\chi$ , determined via eq. (5.5), with  $L_p$  and  $L_c$  the long period and crystal thickness obtained from the 1D correlation function respectively, is plotted as a function of the aging time. The amorphous layer thickness  $L_a$  is determined from the difference between  $L_p$  and  $L_c$ . The 2 polymer grades both show a constant crystallinity (within the experimental spread) after storage at room temperature for 1 month. The long period and lamellar thickness both show a small increase, and the amorphous layer thickness remains constant. The increase in both cases is less than 1 nm. Due to the low mobility of the crystals at these temperatures, it is expected that the changes mainly take place in the interface of the constrained amorphous domains and the crystals, where the chains have segmental mobility.

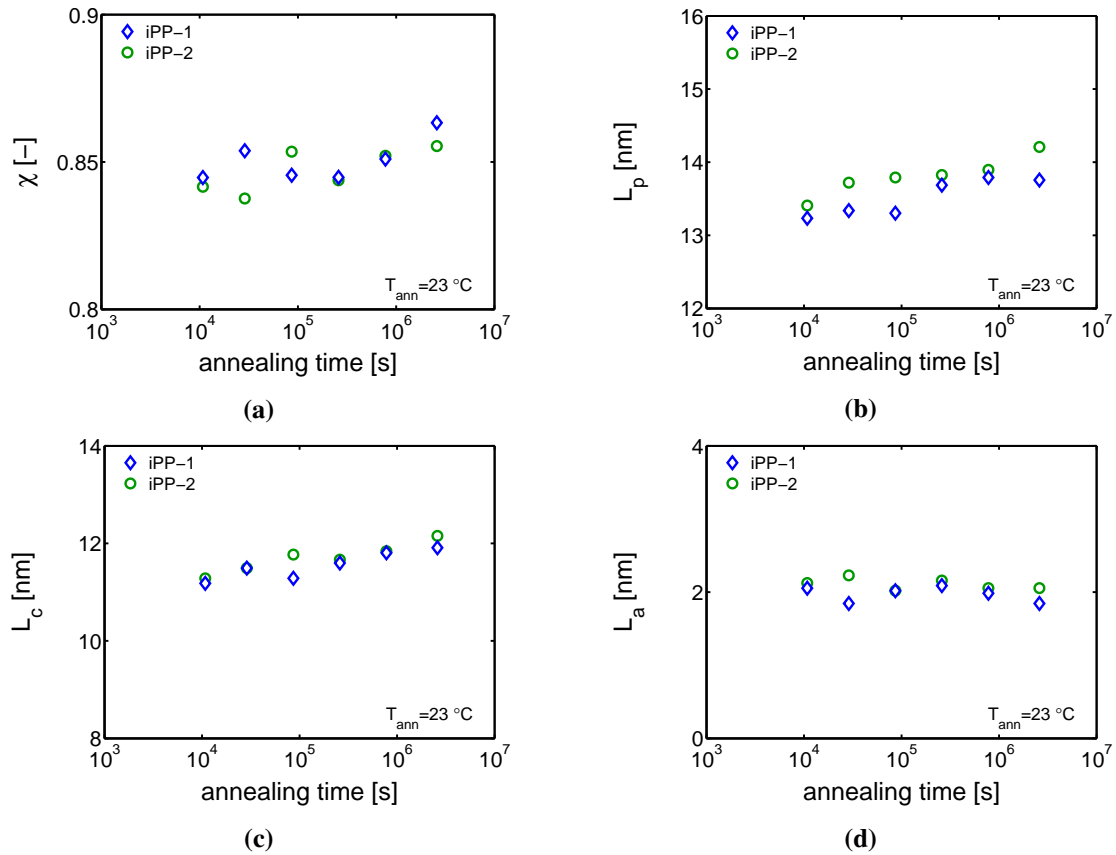


**Figure 5.10:** The evolution as a result of aging at room temperature of a) the linear crystallinity, b) the long period, c) the lamellar thickness and d) the amorphous layer thickness as a function of aging time.

The evolution of the (crystalline) structure above  $T_{\alpha_c}$  affects the properties at all test temperatures. However, when performing the experiments, only a limited amount of samples is subjected to high temperatures for a sufficiently long time to cause changes in the properties. This is illustrated with the Eyring fit shown in Figure (5.11), As can be seen, a rather good description of the yield kinetics can be obtained, however, at low temperatures and high strain rate the a mismatch between the Ree-Eyring fit and the experimentally obtained data can be observed. This may be an indication that in these conditions the bulk amorphous phase contribution to the yield kinetics, as was also observed before in compression experiments [119]. At high temperatures and long experimental timescales, the description clearly deviates from the measured yield stresses. As known from Figure (5.8b), this is most likely the result of annealing. A structural evolution, reflected in the yield kinetics at this temperature, has to originate from the crystalline domains, as can be seen from Figure (5.11). Awareness is required when experiments at  $110\text{ °C}$  are used for extrapolation at room temperature since it may corrupt the extrapolation. To put it simple: How relevant is the high temperature response for long



term predictions if the temperature also induces structural evolution that will not occur at room temperature?

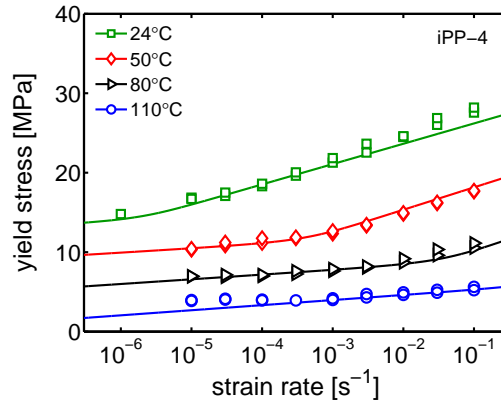


**Figure 5.11:** A fit of the Eyring model, eq. (5.6), on data measured on iPP-4. At 110 °C, a deviation between the model prediction and the experimentally obtained data can be observed.

Again, X-ray techniques are used to investigate the structural evolution, causing this increase in the yield stress. The results obtained from the 1D-correlation function are shown in Figure (5.12). Remarkably, the linear crystallinity remains constant upon annealing at 110°C for both iPP-4 and iPP-6. Similar to aging at room temperature, the long period and lamellar thickness show an increase, and the amorphous layer thickness remains constant. Although the maximum annealing time at 110°C is an order of magnitude lower than the one at room temperature, the increase in lamellar thickness is much stronger (more than 2 nm). At 110 °C,  $\alpha$ -relaxation can take place and the amorphous phase is relatively mobile. Apparently, this allows for accelerated lamellar growth in comparison with the evolution monitored at room temperature. Although iPP-4 and iPP-6 are different from the grades used to investigate the effect of aging at room temperature, the observed behavior is general for different molecular weights and comonomer contents.

Based on X-ray and in terms of the deformation mechanisms presented in sec. 5.3.1, one could remark that the low temperature treatment affects the inter-lamellar  $\alpha_c$  relaxation mechanism, whereas the high temperature treatment works on the intra-lamellar deformation mechanism. This latter one is assigned to secondary crystallization, i.e. lamellar perfecting and lamellar growth. The intra-lamellar deformation mechanism is strongly connected to the constrained amorphous domains, considered to be in a low mobility or glassy state below the  $\alpha_c$  temperature.

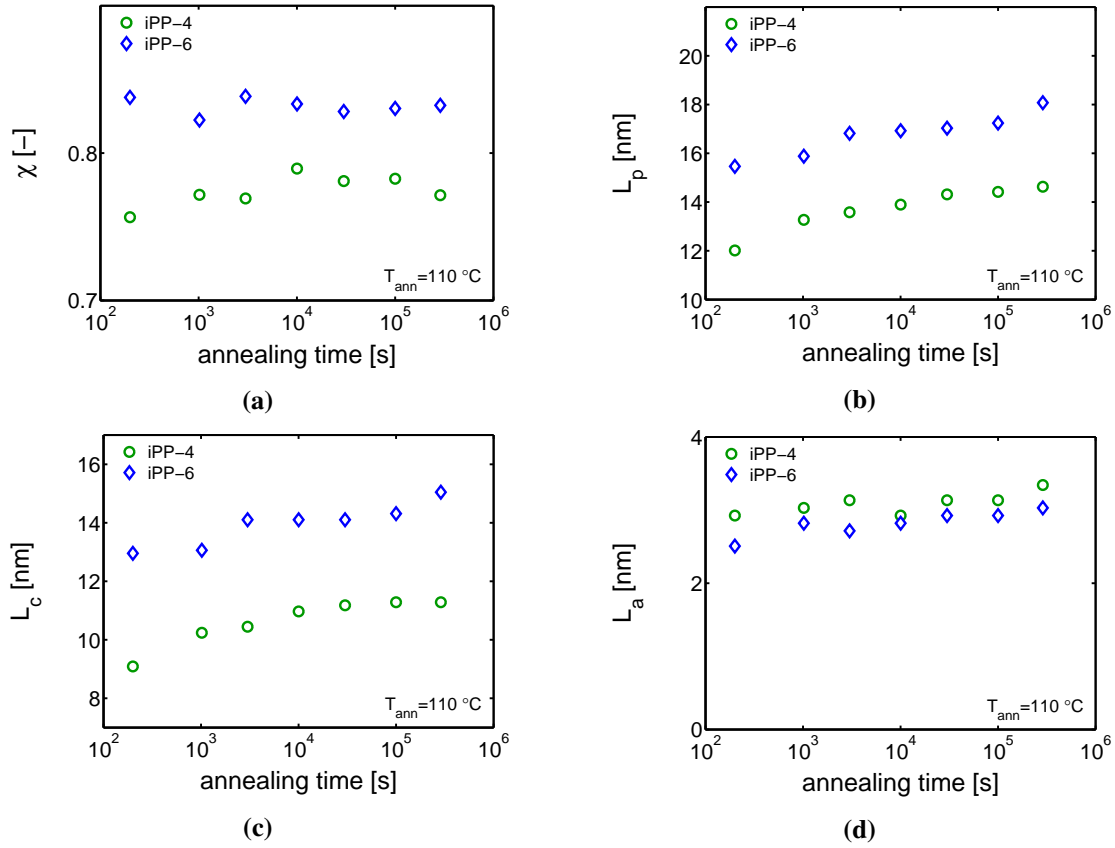


**Figure 5.12:** The evolution as a result of aging at 110 °C of a) the linear crystallinity, b) the long period, c) the lamellar thickness and d) the amorphous layer thickness as a function of aging time.

### 5.3.3 Life-time predictions

To predict the time-to-failure as a function of loading conditions with the modified Reo-Eyring equation, eq. (5.6), the concept of critical strain is used. In this approach, the yield kinetics determined with constant rate experiments at variable temperatures, are employed to estimate the rate of accumulation of plastic deformation. The concept is based on the observation that the time-to-failure multiplied with the plastic flow rate in the secondary creep regime is constant:

$$ttf(\sigma) \cdot \dot{\epsilon}_{pl}(\sigma) = C \quad (5.7)$$

The constant in this equation is interpreted as a critical strain  $\epsilon_{cr}$  that can be determined from a single creep test. A combination of eq. (5.6) and eq. (5.7) can then be used to predict the time-to-failure, since the steady state reached at the yield point is identical to the steady state reached in secondary creep [117]. From eq. (5.7) it follows that

the application of a high load results in a short time-to failure and vice versa, which means that in order to measure the failure time at a relatively low stress a large time is required; note that the time is on a logarithmic scale. Self-evidently, the two distinct molecular mechanisms revealed in the deformation kinetics are also observed in the stress dependence of the time-to-failure. In ISO9080, this distinction is not made, although the time-temperature-superposition is fitted on data collected in both regimes. A careful look at the ductile failure data presented in Figure (5.1), shows that the data at high temperature does not match the fittings. Indeed, this leads to poor descriptions and may corrupt the validity of the time-to-failure predictions. Furthermore, it makes the procedure sensitive for the time-to-failure regime in which the certification data is collected.

To validate the life-time predictions based on the concept of critical strain, creep experiments are performed. Typical results of these experiments are shown in Figure (5.13a), where creep curves of experiments performed at room temperature are shown. Obviously, for increasing loads the time-to-failure decreases. After the application of the load (10 seconds) the different creep regimes can clearly be distinguished. Primary creep follows directly after loading the sample, followed by steady secondary creep. After the specimen accumulated a certain amount of plastic strain it enters the tertiary creep regime, followed by failure. These curves can be used to obtain so-called Sherby-Dorn plots, see Figure (5.13b) [161], in which the plastic flow rate is plotted as a function of the strain. The minimum in these plots represents the steady plastic flow rate  $\dot{\epsilon}_{pl}$ , used in eq. (5.7).

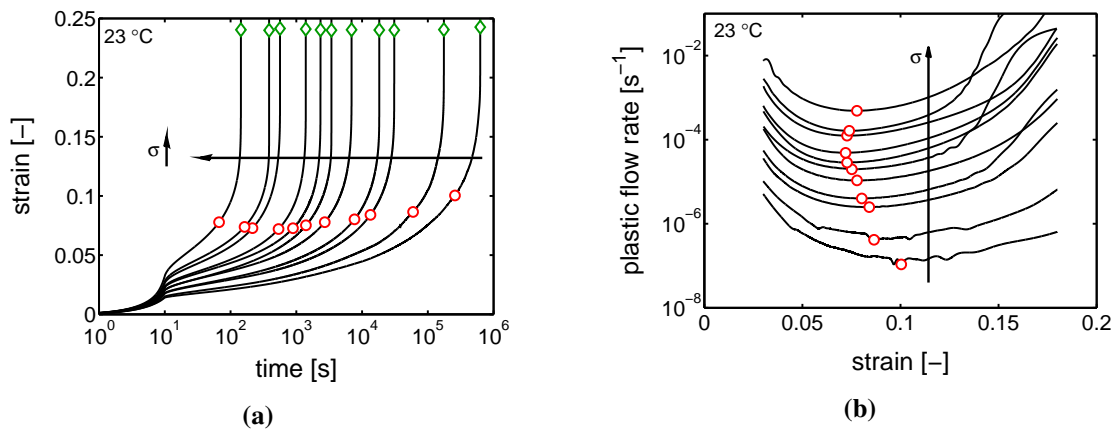


**Figure 5.13:** a) An example of a typical creep response obtained from creep experiments performed on iPP-3 at various stress levels and a temperature of 23°C. b) The corresponding Sherby-Dorn plots.

The plastic flow rates, obtained from the creep curves of samples subjected to various loads at temperatures of 23°C, 50°C, 80°C and 110°C, are plotted as a function of the corresponding time-to-failure, see Figure (5.14a). To meet the requirements to fulfill the concept of critical strain, the data have to follow a linear relation with a slope of -1, on a double logarithmic plot. However, two problems may occur. Firstly, the concept of critical strain only applies when all Eyring parameters remain constant. Due to annealing

and the corresponding evolution of structure and properties in the long experiments, this requirement cannot be fulfilled. An increasing lamellar thickness, as observed in Figure (5.12), directly translates to a decreasing rate constant  $\dot{\epsilon}_0$  [98]. This can be incorporated in the model by making  $\dot{\epsilon}_0(t)$ , but requires much more experiments [162, 163]. Additionally, as can be seen from Figure (5.14a), some data-points deviate from the relation crucial for the application of the concept of critical strain. Here, failure occurs sooner than expected. These are specifically the experiments that show brittle failure on a macroscopic scale. When plotting the applied stress as a function of the time-to-failure, depicted in Figure (5.14b), the samples that fail brittle, are found at high temperatures (80°C and 110°C) and (relatively) large time-to-failure.

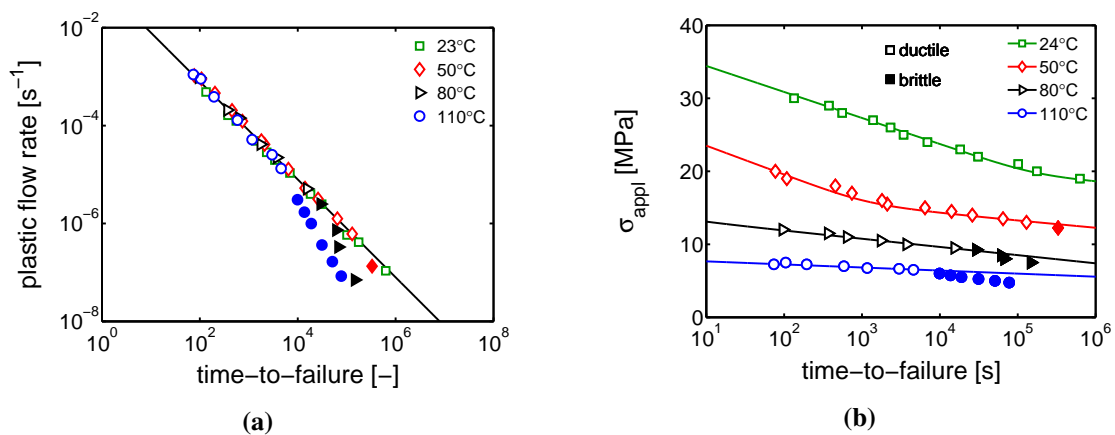


**Figure 5.14:** a) The plastic flow rate of iPP-3, obtained from Sherby-Dorn plots, corresponding to creep experiments performed at various temperatures and stresses plotted as a function of the time-to-failure. b) The corresponding plot of the failure kinetics. Open markers represent the samples that displayed ductile macroscopic failure. Closed markers represent samples that failed brittle and the lines are guides to the eye.

Based on the deformation kinetics, it is clear that a transition from one failure mechanism to another takes place. This corresponds to the change in failure mode, observed in the certification data, see Figure (5.2), where at large time scales a regime is entered in which brittle failure, mixed failure and weeping coexist. The transition from ductile failure towards brittle failure, i.e. the 'mechanical knee', is interpreted as the transition from a plasticity controlled mechanism to crack growth controlled failure. Due to material inhomogeneities, stress or strain concentrations develop, eventually leading to the formation of a cavity. This cavity can grow over time until a sample or product fails. Therefore, the time-to-failure in the case of fatigue crack growth, depends on the crack propagation rate. Experimental studies have shown that this rate can be significantly accelerated by the application of cyclic loading conditions. In cyclic loading conditions, the maximum load, the minimum load, the amplitude and the frequency can be varied. Here, the load maximum is plotted. The frequency is chosen at 1 [Hz] and the minimal

load level is chosen at one tenth of the load maximum (load ratio  $R=0.1$ ). Static and dynamic loading conditions are visualized in Figure (5.15a). Application of static or cyclic loading conditions affects plasticity controlled failure and crack growth controlled failure in a different way. Plasticity controlled failure is the result of an accumulation of a critical amount of plastic strain, which is directly proportional to the integral of the applied stress as a function of time. Therefore, when defined as in Figure (5.15a), in plasticity controlled failure it always takes longer to accumulate the critical amount of plastic strain in the case of cyclic loading. In contrast, due to an increased crack propagation rate as a result of cyclic loading, the crack growth controlled failure mechanism shifts towards lower time-to-failure. As a result, additionally to static loading, cyclic loading can be used to distinguish between the different mechanisms and, moreover, to accelerate crack growth [3].

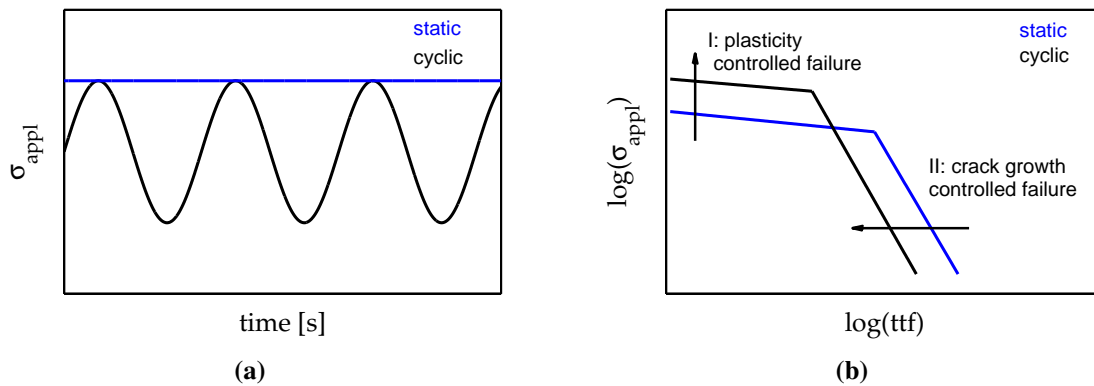


**Figure 5.15:** a) Schematic representation of static and cyclic loading conditions and b) the expected behavior resulting from these loading conditions.

In Figure (5.16) a comparison is made between the time-to-failure obtained from static and cyclic experiments, performed at various stress and a temperature of  $80^{\circ}\text{C}$ . The stresses plotted for cyclic loading correspond to the maximum stress. Remarkably, the brittle failure is not accelerated by cyclic loading. In fact, it is even postponed to longer failure times, similar to failure in the plasticity controlled failure regime. This is an interesting observation from which it can be concluded that the failure mechanism in the brittle regime is not crack growth, but rather a plasticity controlled phenomenon. An optical investigation of failed samples (iPP-2) displays a kind of behavior that is general for the iPP tested in this study at high temperature, where the brittle failure is observed. A selection of tensile specimens, used for the creep experiments performed at  $80^{\circ}\text{C}$  and tested at different stress levels, is depicted in Figure (5.17). In this picture, from right to left, failed samples are shown after being loaded at stresses ranging from 7 to 13 MPa respectively (with steps of 1 MPa). Interestingly, the amount of whitening observed in the samples initially increases with the life time, and thus decreasing level of applied stress. Subsequently, after the transition from ductile to brittle failure the opposite trend is observed, and the amount of whitening decreases with increasing life-

time. The dimensions of the crazes become so large at low stress levels, that they are macroscopically observable.

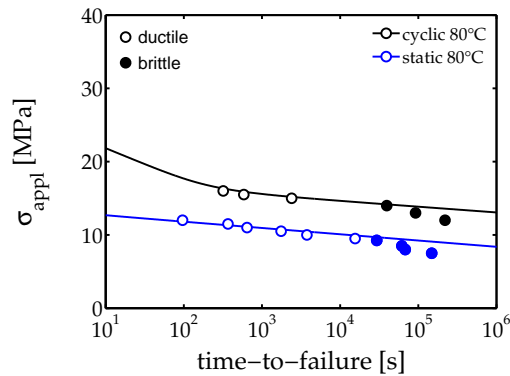


**Figure 5.16:** Experimentally obtained time-to-failure measured on iPP-3 at a temperature of 80°C. Open markers represent the samples that displayed ductile macroscopic failure. Closed markers represent samples that failed brittle.

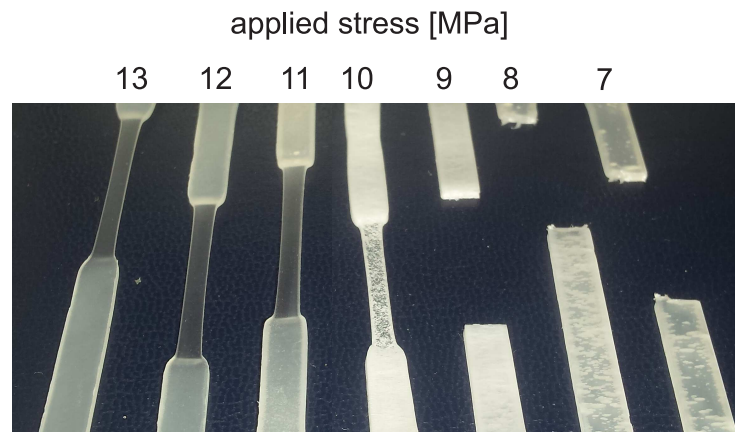


**Figure 5.17:** A picture of failed iPP-2 samples after creep experiments performed at 80°C.

To obtain a better insight in the phenomena taking place in the whitened regions, SEM images were taken on samples (iPP-3) subjected to dynamic creep loads with a maximum stress level of 13 and 14 MPa at a temperature of 80°C. The SEM pictures, shown in Figure (5.18), allow for visual inspection of the crazes. The dynamic creep loading direction was horizontal. All the SEM images of the iPP samples, loaded at 80°C with a cyclic load maximum of 13 and 14 MPa, reveal multiple crazing. From Figure (5.18a), it becomes clear that a large amount of craze like entities is formed perpendicular to the loading direction. Further magnification, Figure (5.18b) to Figure (5.18d), shows that the crazes are full of load bearing fibrillar structures. These fibrils have diameters

in the order of  $1\ \mu\text{m}$ , which is orders of magnitude larger than crazing observed in other materials, e.g. in polystyrene, where the fibrils are typically 2-3 nm. In the latter case the fibrils consist of 5-10 chains that, upon deformation, disentangle or break up due to chain scission. For polypropylene on the other hand, it is demonstrated in Figure (5.18e) and Figure (5.18f), that the fibrillar structures remain stable and able to carry load for a long time. After large plastic deformation fibers break up, initiating a crack. An interesting observation is that the crack propagates straight through the spherulites. Eventually, these cracks become fatal and cause failure of the sample.

The time to form a craze, that grows substantially large and then initiates the formation of a pre-crack, is much larger than the time required for the pre-crack to become critical. Therefore, this macroscopically brittle process is regarded to be plasticity controlled, similar to the macroscopically ductile mechanisms. After all, the formation of crazes and the fibrillar structures is a plastic phenomenon, rather different for crack without load bearing capacity. The kinetics, on the other hand, differ from the plastic events observed for ductile failure.

This observations presented above rigorously changes the interpretation of the mechanical behavior, since it does not represent a transition from plasticity controlled failure to crack growth controlled failure, but rather a transition from one plastic phenomenon to the other. The brittle failure mechanism is governed by the appearance and coalescence or growth of crazes, causing the most intense whitening of the sample around the ductile-to-brittle transition. In this transition region, a mixed failure mechanism is observed. Weeping, observed around the ductile-brittle transition in pressurized pipe testing, could be a result of the formation of cavities or craze-like structures that subsequently grow and coalesce. Ultimately, these cavities could percolate, resulting in weeping pipes.

### 5.3.4 Lifetime improvement

Micro structural features that affect the yield kinetics are known to have a similar influence on the life-time in the plasticity controlled failure regime. An increase in crystallinity and lamellar thickness, or a decrease in the defect density, results in a higher yield stress. This increased yield stress is directly reflected in the time-to-failure. Since it is also found that the mechanical response after the so-called mechanical knee shows plasticity controlled characteristics, it is interesting to study if the position can be affected by changes in morphology. Typically, for crack growth controlled failure, a different route has to be followed to improve the performance. Often this involves the chemical architecture of the iPP-chain. For example, the usage of random copolymers or polymers with a high molecular weight is common in load bearing applications like pipes. These adjustments, however, negatively affect the performance in the plasticity controlled failure regime. Here, two morphological features with a known effect on plasticity controlled failure are investigated, to see if, and how they affect the performance of iPP, particularly after the mechanical knee.

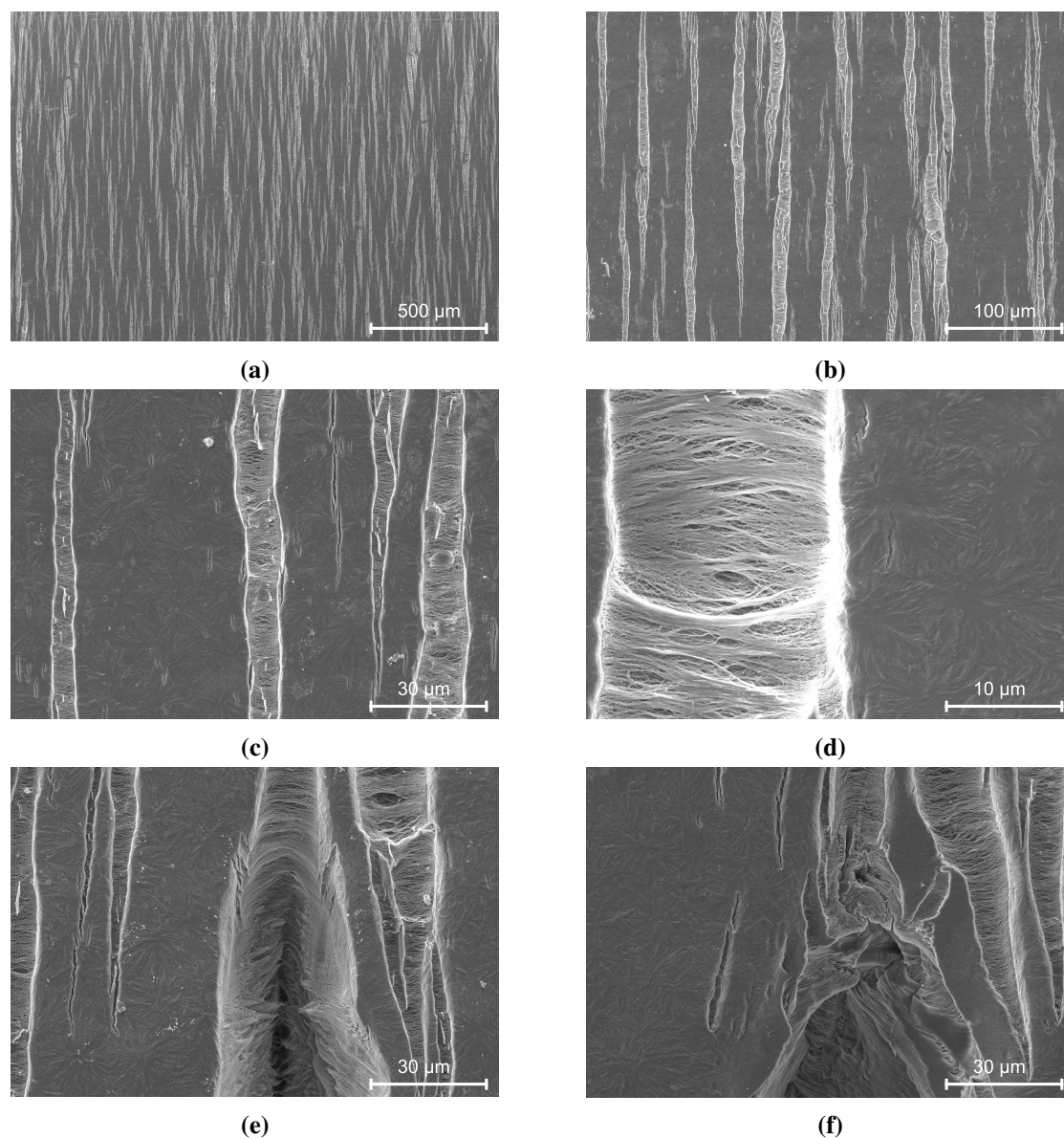


**Figure 5.18:** SEM images of the surface of tensile bars (Figure (5.3)), subjected to dynamic creep loads. The loading direction was horizontal. The images a) to d) show the whitened regions at different magnifications. e) and f) show failure phenomena.

### The effect of annealing

The primary goal is to find the position of the mechanical knee, and to monitor the stress dependence before, and after this transition point. At a testing temperature of 80°C, the change in behavior is the most clearly noticeable. An iPP-sample (iPP-2) quenched in a compression molding machine set at 20°C, is used as a reference material. Two more sets of test specimens were prepared for the creep tests: 1 group of tensile samples is prepared



by annealing for 15 minutes at 120°C, and another set of samples is created by annealing the 'as prepared samples' for 2 days at a temperature of 120°C. The applied stress levels and the corresponding time-to-failure are plotted in Figure (5.19). The lines in this plot are guides to the eye and mark the level of the plasticity controlled failure. The open markers indicate ductile failure and the crosses represent brittle samples. As expected, in the ductile failure regime at a given failure time, the allowed applied stress level is the highest for the sample that has been annealed the longest. The position of the mechanical knee, however, is found at the smallest timespan for the most heavily annealed sample. The samples that failed brittle seem to follow the same trend, and demonstrates similar kinetics after the transition.

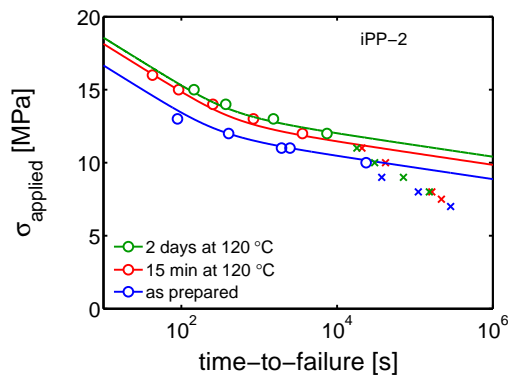


**Figure 5.19:** The time-to-failure, measured on samples after different annealing treatments, for macroscopically ductile failure (open markers) and brittle failure (crosses), observed in creep experiments performed at 80°C.

The structural features that dominate the resistance against the accumulation of plastic strain, and thus plasticity controlled failure, do not seem to affect the brittle response since in that regime the behavior of the different specimens overlaps. The apparent absence of a dependence on crystal features could be explained by the fact that the brittle failure mechanism originates from the amorphous layers. These layers are hardly affected by the applied annealing treatments.

## Polymorphism

The rich polymorphism, displayed by iPP, triggers the investigation of the position of the mechanical knee for the different polymorphs, and the behavior afterwards. In Figure (5.20), the creep data of  $\alpha$  (left),  $\beta$  (middle) and  $\gamma$ -iPP (right) is shown. The lines in these figures are obtained from the Eyring equation, eq. (5.6), and the concept of critical strain: eq. (5.7). The transition from ductile (open markers) towards brittle failure (filled markers) is observed at the shortest timespans for  $\gamma$ -iPP (at 80°C and 110°C), followed by  $\alpha$ -iPP (at 50°C, 80°C and 110°C). Remarkably, in the experimentally assessed time scales,  $\beta$ -iPP displays this transition at larger times, and only at 110°C.

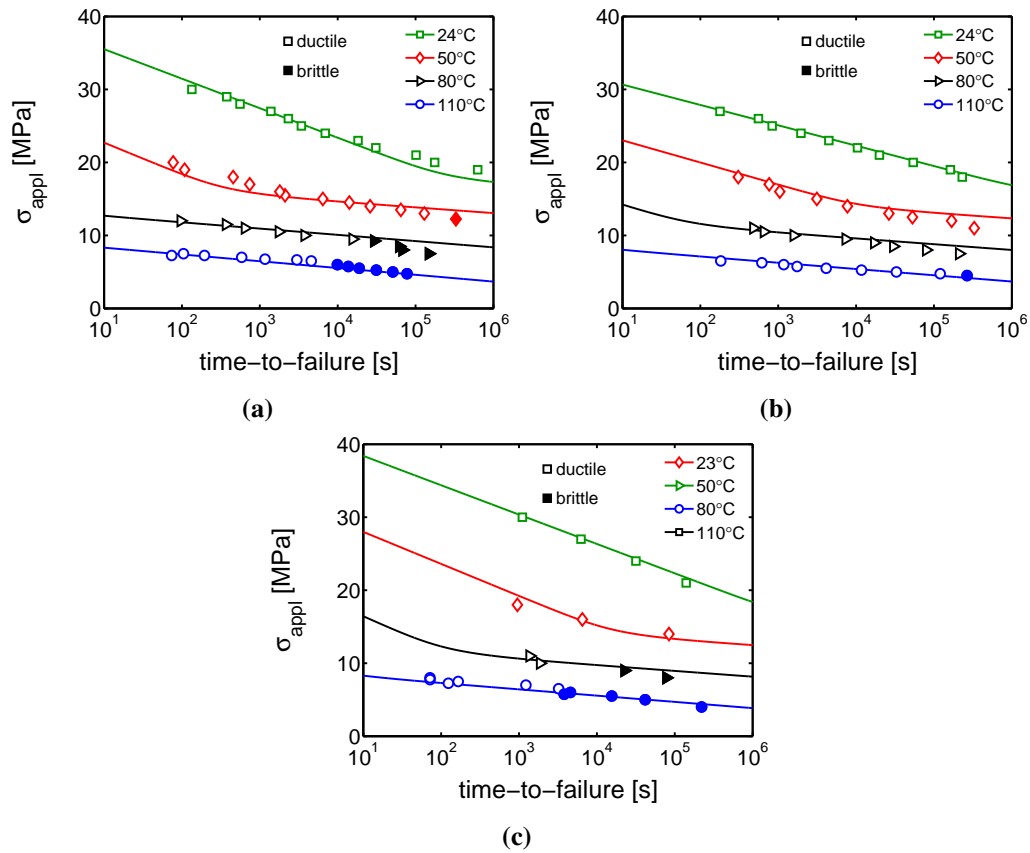


**Figure 5.20:** Time-to-failure obtained from creep experiments on a)  $\alpha$ -iPP, b)  $\beta$ -iPP and c)  $\gamma$ -iPP (all iPP-3). Open markers represent ductile failure and closed markers are used to plot brittle failure. The lines are obtained from the Eyring model: eq. (5.6).

The creep results measured at 80°C and 110°C are plotted in one graph, see Figure (5.21), to quantitatively compare the level of brittle failure of the different polymorphs. In this figure, the lines are guides to the eye. The applied stress level, corresponding to a time-to-failure of for example 1000 [s], is clearly the highest for  $\gamma$ -iPP, as is expected from literature [119]. The postponed transition in the case of the  $\beta$ -polymorph causes a cross-over in the time-to failure. This means that at relatively low stress levels the  $\beta$ -iPP suddenly performs better than the  $\alpha$ - and  $\gamma$ -iPP, which is exactly the opposite from the plasticity controlled failure observed before the mechanical knee (when comparing  $\alpha$  and  $\beta$ -iPP).

From the results presented in sec. 5.3.4, it is concluded that the brittle failure mechanism most probably originates from the amorphous network, because it is not affected by the annealing treatments. When comparing different polymorphs, however, a remarkable improvement is encountered in the case of  $\beta$ -iPP. This polymorph shows almost no softening, and strong hardening, whereas both  $\alpha$ - and  $\gamma$ -iPP show softening at all temperatures [119]. The combination of little softening and pronounced strain hardening

allow delocalization of the stress. These specific properties could hinder the formation of craze-like entities, depicted in Figure. (5.17) [164]. If this is indeed the explanation for the improved performance of  $\beta$ -iPP, it would strongly change the search for a strategy to improve long term properties.

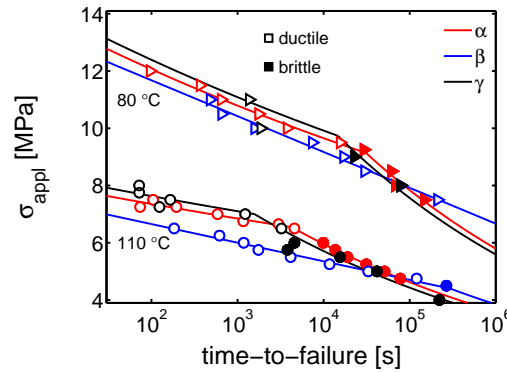


**Figure 5.21:** A comparison of the time-to-failure measured on  $\alpha$ -iPP,  $\beta$ -iPP and  $\gamma$ -iPP respectively, at temperatures of 80°C and 110°C (all iPP-3). The lines are guides to the eye.

## 5.4 Conclusion

To study the effect of structural evolution on the performance of polypropylenes, several materials are selected and tested at various conditions. The effect of structural evolution is different for ductile and brittle failure. Therefore, they will be treated separately, after which the consequences for certification procedures like ISO9080 are discussed.

In the case of ductile failure, an evolution of structure and properties is found over the entire temperature window. Independent of the annealing and testing temperature (if chosen equal), a linear increase of the yield stress as a function of the logarithm of time is found. However, the molecular processes that dominate the kinetics at low temperature (below  $T_{\alpha_c}$ ), or at high temperature (above  $T_{\alpha_c}$ ), appear to be very different. An important finding is, therefore, that a distinction has to be made between the evolution of structure and properties in both regimes. Evolution below  $T_{\alpha_c}$  is controlled by aging of the constrained amorphous phase. The influence of aging on the yield stress disappears in experiments performed above  $T_{\alpha_c}$ , independent of the aging time. This means that the evolution of the structure is torn down by the temperature increase. Below  $T_{\alpha_c}$ , a linear increase is observed as a function of the logarithm of annealing time. In contrast, structural evolution above  $T_{\alpha_c}$ , referred to as annealing, causes structural changes that affect the yield stress in both temperature regimes. In both cases an increase in lamellar thickness is found over time. After 1 month at room temperature the lamellae grew approximately 0.5 nm in thickness. This increase is expected to mainly take place on

the crystal-amorphous interfaces. Annealing for 4 days at 110°C resulted in an increase of approximately 2 nm. In ISO9080 only one single time-temperature superposition is used to describe the failure times measured at various temperatures, i.e. in a temperature window where clearly two different molecular processes contribute to the failure kinetics. Obviously, this superposition does not capture the proper material behavior, which frustrates lifetime predictions. Annealing below  $T_{\alpha_c}$  the material displays physical aging, while above  $T_{\alpha_c}$  progressive annealing takes place. These are distinct processes that govern evolution at different temperatures, meaning that the observed behavior is incomparable.

To investigate the brittle failure mode occurring at high temperature, static and cyclic loading conditions are used. Remarkably, it was found that cyclic loading conditions postpone the moment of failure when compared to static loading, in the case that  $\sigma_{max}$  was chosen equal to the static stress ( $\sigma_{max}=10\sigma_{min}=\sigma_{static}$ ). These characteristics indicate that the brittle failure mechanism is plasticity controlled, rather than crack growth controlled. In the SEM images multiple crazing is observed. Within these crazes stable fibrils, able to carry loads, are found with a diameter of approximately 1  $\mu m$ . Failure is initiated when these fibrils break and the crazes form pre-cracks. The time required to form crazes that grow and become pre-cracks is much larger than the time required for the pre-crack to become critical. This means that the plasticity dominates this failure mechanism, and explains the mechanically obtained results. In an attempt to extend the lifetime, a comparison between different annealing treatments is made. It was found that the brittle failure overlaps for all thermal histories. The mechanical knee moves towards lower failure-times, but this is purely caused by a vertical shift of the time-to failure in the ductile regime. Moreover, a comparison between the different polymorphs shows that  $\beta$ -iPP clearly performs better in the brittle failure regime, which is the opposite of the performance in the ductile failure regime. Based on these findings, together with the difference in intrinsic material response, it is suggested that the failure mechanism originates from the amorphous network. The differences in lamellar thickness do not influence the brittle failure, whereas the different polymorphs that each display their own strain softening and hardening behavior, do affect the lifespan in this regime. Therefore, product improvement should mainly be achieved by focusing at the structural features that determine the strain softening and more important, the strain hardening of iPP, rather than the level of the yield stress only.

In conclusion it can be stated that the highest caution is required for the application of certification procedures such as ISO9080. One should be aware of erroneous interpretations of the certification data, due to structural evolution prior to, and during product lifetime. The brittle failure mechanism, although seemingly crack growth controlled, displays plastic characteristics. Consequently, the focus for improvement of product-performance has to be reconsidered.



---

# Conclusions and Recommendations

---

## 6.1 Conclusions

This research is devoted to gain deeper understanding of the relation between structure and mechanical properties of isotactic polypropylene. The main focus was on the influence of polymorphism on the intrinsic material response and the yield and failure kinetics. Furthermore, the evolution of structure and properties as a function of deformation and temperature over time, are investigated extensively. Knowledge of these relations ultimately has to allow for predictions of mechanical performance based on the processing conditions. However, due to the complexity of this problem, a simplified but feasible processing-structure-property pathway, is developed as a proof of principle.

The main conclusions of this work are:

*The prediction of mechanical performance of isotactic polypropylene on the basis of processing conditions*

- A non-isothermal crystallization model is combined with the 1D heat balance and the Lauritzen Hoffman equation to calculate the lamellar thickness distribution that forms in a compression molded plate for two different iPP grades. The only grade specific parameters were the nucleation density, the maximum growth rate of the  $\alpha$ -crystals and the surface free energy. The combination of this model framework with these equations allows for a good prediction of the processing dependent morphology in terms of lamellar thickness.
- The empirical relation between the yield kinetics and the lamellar thickness, observed by van Erp et al. after a systematic application of different cooling rates, and the extensive investigation of the corresponding yield kinetics, enables the prediction of a temperature and strain rate dependent yield stress. From the lamellar thickness, the only morphology dependent parameter in the yield kinetics, the rate constant, can be determined. The yield stress predictions are in good agreement with the experimentally obtained ones.

- Making the connection between processing, the resulting morphology and the mechanical properties is feasible for a simplified case. By varying a few parameters only, good results are obtained for different iPP grades. The approach offers a promising pathway for the prediction of properties of more complicated mixed structures in geometrically complex products.

#### *Deformation and failure kinetics of iPP-polymorphs*

- The comparison of the mechanical response of samples containing solely one of the iPP-polymorphs, prepared from the same grade, revealed large differences in the intrinsic material behavior.  $\gamma$ -iPP samples show the most pronounced softening whereas this is almost not observed in  $\beta$ -iPP. The strain hardening, however, is by far the strongest in  $\beta$ -iPP samples, while  $\alpha$ - and  $\gamma$ -iPP only show a limited amount of strain hardening.
- Remarkably, despite having completely different unit cell structures the yield kinetics in the intra-lamellar deformation regime, i.e. at high temperatures or low strain rates, is identical for all three polymorphs in terms of activation volume. This could be an indication that the deformation and failure kinetics in this regime are dominated by the mobility of the helical chain conformation in the crystal lattice, rather than the crystal slip systems. The high activation energy of  $\gamma$ -iPP with respect to  $\alpha$ - and  $\beta$ -iPP is hypothetically explained by the crossed chain configuration in the  $\gamma$ -lamellae.
- It is demonstrated that softening is related to the thermodynamic state of the constrained amorphous domains. With thermal rejuvenation treatments the yield stress and softening can be significantly reduced, whereas the hardening remains unaffected. The effects are particularly large in  $\gamma$ -iPP.

#### *Deformation induced phase transitions in iPP-polymorphs*

- The softening observed in the intrinsic material behavior of the iPP-polymorphs is not related to deformation induced melting of crystals. From in-situ compression experiments, combined with advanced X-ray techniques, a similar decreasing trend of the crystallinity level is found in all iPP-polymorphs at the same strain levels. The large differences observed in the softening can, therefore, not be explained by deterioration of the crystalline domains.
- Upon tensile deformation at low temperatures (below  $T_\alpha$ ), all polymorphs partially transform to oriented mesophase and amorphous phase. This transformation is observed mainly in the strain hardening regime. At high temperatures (above  $T_\alpha$ ), all polymorphs display a transition into oriented  $\alpha$ -phase at high strains. In the case of  $\gamma$ -iPP this transition is accompanied by a sudden increase of the

lamellar thickness, suggesting that throughout the process of crystal destruction and recrystallization, the chain segments incorporated in the crystal maintain their helical conformation.

- The  $\beta$ -iPP samples show the most intense voiding at all tensile test temperatures. The volume fraction of voids in the detectable length scale of in-situ SAXS experiments, i.e. up to approximately 80 nm, is the highest, and increases throughout the entire tensile experiment.

#### *Long term failure predictions in polypropylenes*

- Standardized certification procedures like ISO9080 do not correctly capture the deformation kinetics of iPP and, therefore, the reliability of the time-temperature superposition procedure is doubtful. The power-law, determined mainly on the data measured at room temperature, is not representative for the behavior observed at elevated temperatures. This leads to corrupted extrapolations.
- At any temperature, applied in certification procedures, iPP displays evolution of structure and properties which cannot be neglected when estimating life times. This evolution can be divided into two main subgroups: 1) Evolution below  $T_{\alpha_c}$  and 2) Evolution above  $T_{\alpha_c}$ . Above  $T_{\alpha_c}$ , the crystalline lamellar thickness increases significantly, causing an increase in the yield stress at all testing temperatures. Contrary, below  $T_{\alpha_c}$ , only a small increase is observed in lamellar thickness, which is thought to originate from the interface layers. Only the yield stress measured below  $T_{\alpha_c}$  is affected by this kind of structural evolution, and exposure to temperatures higher than  $T_{\alpha_c}$  erases the aging phenomena.
- The brittle failure observed in certification data displays plasticity controlled characteristics. For fatigue crack growth controlled failure, the application of cyclic loads should lead to accelerated failure, but instead, postponed failure is observed, typical for plasticity controlled failure. Macroscopically brittle failure is initiated when fibrils in the crazes break and form pre-cracks. The time to form these crazes, which can grow and transform into pre-cracks, is much larger than the time required for the pre-crack to become critical, explaining the plasticity controlled type of behavior.
- The brittle failure mechanism cannot be postponed by tuning structural features like an increased lamellar thickness. Processing and annealing have a limited effect, and brittle response always overlaps. However, different polymorphs display distinct behavior.  $\beta$ -iPP overrules the performance of  $\alpha$  and  $\gamma$ -iPP at high temperature and large time-to-failure. This could be a consequence of the minimal strain softening and the pronounced strain hardening observed in  $\beta$ -iPP with respect to  $\alpha$ - and  $\gamma$ -iPP.



## 6.2 Recommendations

In this thesis the relation between structure and properties, for different iPP-polymorphs, has been investigated. This led in some cases to unexpected findings for which, based on assumptions, explanations were given. Some interesting experiments or extended research that could provide more solid evidence for these assumptions are discussed here. Furthermore, some missing steps to achieve the ultimate goal of predicting performance on the basis of processing conditions, will be raised.

The main recommendations of this work are:

- The successful pathway to predict the mechanical properties of iPP on the basis of the processing conditions, demonstrated on  $\alpha$ -iPP (see **Chapter 2**), has to be extended to the other polymorphs. To do this, the state parameter in the Eyring equation, i.e. the rate constant, needs to be linked to the lamellar thickness. The most straightforward way to do this is by the preparation of Eyring plots, measured on samples with different lamellar thickness as a result of variable applied cooling rates. Furthermore, the influence of the hydrostatic pressure needs to be incorporated, allowing for yield stress predictions, irrespective of the loading geometry.
- Since in injection molded products always a mixture of isotropic domains and highly anisotropic oriented crystalline regions is formed, the effect of orientation on the yield stress has to be quantified for all crystal phases, similar to the work of van Erp et al. [19] on  $\alpha$ -iPP. The crystallization model developed by Roozmond et al. [14] could be used to provide the processing conditions required to obtain oriented  $\beta$  and  $\gamma$ -iPP. Implementation of the gained knowledge on the behavior of multiphase and oriented iPP allows for the prediction of mechanical properties of injection molded products.
- As is shown particularly in **Chapters 3 and 5**, the evolution of structure significantly affects the mechanical behavior. The deformation and failure kinetics evolve in time, resulting in corrupted product life-time estimations. To properly predict life times, these evolutions need to be captured in kinetic models, being able to describe the mechanical properties as a function of the state or mobility they are in.
- In **Chapter 4** it is hypothesized that the cross hatched structures present in  $\alpha$ - and  $\gamma$ -iPP could cause the softening observed in the intrinsic material response above  $T_{\alpha,c}$ . An interesting investigation would be to see whether this is the case or not. Compression experiments on  $\alpha$ -iPP, prepared according to a specifically chosen temperature and pressure history [77], resulting in  $\alpha$ -iPP without cross-hatched structures, allow for experimental evidence of this hypothesis.

- The pronounced hardening observed in the intrinsic material behavior of  $\beta$ -iPP (**Chapter 3** and **4**), is thought to partially be an explanation for the improved performance observed in the brittle failure regime (Chapter 5). A possible explanation for the pronounced hardening is the strongly accelerated crystallization kinetics as a result of the  $\beta$ -specific nucleation agent, used to obtain  $\beta$ -iPP. If this is indeed the case, it would be of great interest to see whether or not the strain hardening can be further improved by instantaneous crystallization, resulting from a sudden pressure increase applied on the polymer melt (and therewith the accompanying increase of the under-cooling). If these samples indeed show stronger strain hardening, they should also be tested in tensile creep experiments to reveal the relation between hardening and the brittle plasticity dominated failure behavior. This approach could offer a good route towards enhanced (long term) properties via structure tuning.
- The results in **Chapter 5** do not exclude the possibility of aging and rejuvenation as a result of a temperature dependent increase of the amount of Reneker defects [165]. The observed evolution phenomena at low temperature are often considered to be caused by physical aging of the constrained amorphous phase. However, the findings presented in the structural evolution observed in X-ray experiments indicate that an explanation in terms of Reneker defects can also be a possibility. Therefore, it is interesting to investigate this hypothesis further. If the latter explanation is true, physical aging would yield a change in  $T_{\alpha_c}$  (towards higher T upon aging). However, due to the shape of the DMTA curves it is difficult to determine the real peak position and, consequently, other techniques like NMR should be considered.



# References

- [1] A. Chudnovsky, Z. Zhou, H. Zhang, and K. Sehanobish. Lifetime assessment of engineering thermoplastics. *International Journal of Engineering Science*, 59:108–139, 2012.
- [2] R.W. Lang, A. Stern, and G. Doerner. Applicability and limitations of current lifetime prediction models for thermoplastics pipes under internal pressure. *Angewandte Makromolekulare Chemie*, 247:131–145, 1997.
- [3] M.J.W. Kanters, T. Kurokawa, and L.E. Govaert. Competition between plasticity-controlled and crack-growth controlled failure in static and cyclic fatigue of thermoplastic polymer systems. *Polymer Testing*, 50:101–110, 2016.
- [4] M.J.W. Kanters, K. Remerie, and L.E. Govaert. A new protocol for accelerated screening of long-term plasticity-controlled failure of polyethylene pipe grades. *Polymer Engineering and Science*, 56(6):676–688, 2016.
- [5] B.A.G. Schrauwen, L.C.A. van Breemen, A.B. Spoelstra, L.E. Govaert, G.W.M. Peters, and H.E.H. Meijer. Structure, deformation, and failure of flow-oriented semicrystalline polymers. *Macromolecules*, 37(23):8618–8633, 2004.
- [6] J.-W. Housmans, M. Gahleitner, G.W.M. Peters, and H.E.H. Meijer. Structure-property relations in molded, nucleated isotactic polypropylene. *Polymer*, 50(10):2304–2319, 2009.
- [7] S. Brückner, S.V. Meille, V. Petraccone, and B. Pirozzi. Polymorphism in isotactic polypropylene. *Progress in Polymer Science*, 16(2-3):361–404, 1991.
- [8] S.V. Meille, D.R. Ferro, S. Brückner, A.J. Lovinger, and F.J. Padden. Structure of  $\beta$ -isotactic polypropylene: A long-standing structural puzzle. *Macromolecules*, 27(9):2615–2622, 1994.
- [9] K. Mezghani and P.J. Phillips. The  $\gamma$ -phase of high molecular weight isotactic polypropylene. ii: The morphology of the  $\gamma$ -form crystallized at 200 mpa. *Polymer*, 38(23):5725–5733, 1997.
- [10] C. De Rosa, F. Auriemma, A. Di Capua, L. Resconi, S. Guidotti, I. Camurati, I.E. Nifant'ev, and I.P. Laishevstev. Structure-property correlations in polypropylene from metallocene catalysts: Stereodeficient, regioregular isotactic polypropylene. *Journal of the American Chemical Society*, 126(51):17040–17049, 2004.
- [11] C. De Rosa, F. Auriemma, O.R. de Ballesteros, L. Resconi, and I. Camurati. Crystallization behavior of isotactic propylene–ethylene and propylene–butene copolymers: Effect of comonomers versus stereodeficient on crystallization properties of isotactic polypropylene. *Macromolecules*, 40(18):6600–6616, 2007.
- [12] R.G. Alamo, M.-H. Kim, M.J. Galante, J.R. Isasi, and L. Mandelkern. Structural and kinetic factors governing the formation of the  $\gamma$  polymorph of isotactic polypropylene. *Macromolecules*, 32(12):4050–4064, 1999.
- [13] A Turner-Jones. Development of the  $\gamma$ -crystal form in random copolymers of propylene and their analysis by dsc and x-ray methods. *Polymer*, 12(8):487 – 508, 1971.
- [14] P.C. Roozmond, T.B. Van Erp, and G.W.M. Peters. Flow-induced crystallization of isotactic polypropylene: Modeling formation of multiple crystal phases and morphologies. *Polymer*, 89:69–80, 2016.
- [15] P.C. Roozmond, M. van Drongelen, and G.W.M. Peters. Modeling flow-induced crystallization. *Advances in Polymer Science*, 277:243–294, 2017.

- [16] C.Y. Yue and W.F. Msuya. Changes in yield in polypropylene of different morphology caused by physical ageing. *Journal of Materials Science Letters*, 9(8):985–988, 1990.
- [17] W.J. O’Kane, R.J. Young, and A.J. Ryan. The effect of annealing on the structure and properties of isotactic polypropylene films. *Journal of Macromolecular Science, Part B*, 34(4):427–458, 1995.
- [18] F. Auremma, O. Ruiz De Ballesteros, C. De Rosa, and C. Invigorito. Tailoring the mechanical properties of isotactic polypropylene by blending samples with different stereoregularity. *Macromolecules*, 44(15):6026–6038, 2011.
- [19] T.B. Van Erp, C.T. Reynolds, T. Peijs, J.A.W. Van Dommelen, and L.E. Govaert. Prediction of yield and long-term failure of oriented polypropylene: Kinetics and anisotropy. *Journal of Polymer Science, Part B: Polymer Physics*, 47(20):2026–2035, 2009.
- [20] T.B. Van Erp, D. Cavallo, G.W.M. Peters, and L.E. Govaert. Rate-, temperature-, and structure-dependent yield kinetics of isotactic polypropylene. *Journal of Polymer Science, Part B: Polymer Physics*, 50(20):1438–1451, 2012.
- [21] T.B. Van Erp, L.E. Govaert, and G.W.M. Peters. Mechanical performance of injection-molded poly(propylene): Characterization and modeling. *Macromolecular Materials and Engineering*, 298(3):348–358, 2013.
- [22] J.J. Janimak and G.C. Stevens. Inter-relationships between tie-molecule concentrations, molecular characteristics and mechanical properties in metallocene catalysed medium density polyethylenes. *Journal of Materials Science*, 36(8):1879–1884, 2001.
- [23] A. Lustiger and R.L. Markham. Importance of tie molecules in preventing polyethylene fracture under long-term loading conditions. *Polymer*, 24(12):1647–1654, 1983.
- [24] J.C. Halpin and J.L. Kardos. Moduli of crystalline polymers employing composite theory. *Journal of Applied Physics*, 43(5):2235–2241, 1972.
- [25] M. Elmajdoubi and T. Vu-Khanh. Effect of cooling rate on fracture behavior of polypropylene. *Theoretical and Applied Fracture Mechanics*, 39(2):117–126, 2003.
- [26] B.A.G. Schrauwen, R.P.M. Janssen, L.E. Govaert, and H.E.H. Meijer. Intrinsic deformation behavior of semicrystalline polymers. *Macromolecules*, 37(16):6069–6078, 2004.
- [27] R. Popli and L. Mandelkern. Influence of structural and morphological factors on the mechanical properties of the polyethylenes. *Journal of Polymer Science, Part B: Polymer Physics*, 25(3):441–483, 1987.
- [28] J.M. Peterson. Thermal initiation of screw dislocations in polymer crystal platelets. *Journal of Applied Physics*, 37(11):4047–4050, 1966.
- [29] R.J. Young. Screw dislocation model for yield in polyethylene. *Materials Forum*, 11:210–216, 1988.
- [30] N.W.J. Brooks and M. Mukhtar. Temperature and stem length dependence of the yield stress of polyethylene. *Polymer*, 41(4):1475–1480, 2000.
- [31] T. Kazmierczak, A. Galeski, and A.S. Argon. Plastic deformation of polyethylene crystals as a function of crystal thickness and compression rate. *Polymer*, 46(21):8926–8936, 2005.
- [32] B. Lotz, J.C. Wittmann, and A.J. Lovinger. Structure and morphology of poly(propylenes): A molecular analysis. *Polymer*, 37(22):4979–4992, 1996.
- [33] L.C.E. Struik. The mechanical behaviour and physical ageing of semicrystalline polymers: 2. *Polymer*, 28(9):1534–1542, 1987.
- [34] P.B. Bowden and R.J. Young. Deformation mechanisms in crystalline polymers. *Journal of Materials Science*, 9(12):2034–2051, 1974.
- [35] K. Mezghani and P.J. Phillips. The  $\gamma$ -phase of high molecular weight isotactic polypropylene: Iii. the equilibrium melting point and the phase diagram. *Polymer*, 39(16):3735–3744, 1998.
- [36] E. Lezak, Z. Bartczak, and A. Galeski. Plastic deformation behavior of  $\gamma$ -phase isotactic polypropylene in plane-strain compression at room temperature. *Polymer*, 47(26):8562–8574, 2006.
- [37] E. Lezak, Z. Bartczak, and A. Galeski. Plastic deformation of the  $\gamma$  phase in isotactic polypropylene in plane-strain compression. *Macromolecules*, 39(14):4811–4819, 2006.

- [38] P.C. Roozmond, M. Van Drongelen, Z. Ma, A.B. Spoelstra, D. Hermida-Merino, and G.W.M. Peters. Self-regulation in flow-induced structure formation of polypropylene. *Macromolecular Rapid Communications*, 36(4):385–390, 2015.
- [39] C. Angelloz, R. Fulchiron, A. Douillard, B. Chabert, R. Fillit, A. Vautrin, and L. David. Crystallization of isotactic polypropylene under high pressure ( $\gamma$  phase). *Macromolecules*, 33(11):4138–4145, 2000.
- [40] S. Piccarolo. Morphological changes in isotactic polypropylene as a function of cooling rate. *Journal of Macromolecular Science - Physics*, B31(4):501–511, 1992.
- [41] M. Van Drongelen, T.B. Van Erp, and G.W.M. Peters. Quantification of non-isothermal, multi-phase crystallization of isotactic polypropylene: The influence of cooling rate and pressure. *Polymer*, 53(21):4758–4769, 2012.
- [42] J.I. Lauritzen Jr. and J.D. Hoffman. Extension of theory of growth of chain-folded polymer crystals to large undercoolings. *Journal of Applied Physics*, 44(10):4340–4352, 1973.
- [43] V. La Carrubba, S. Piccarolo, and V. Brucato. Crystallization kinetics of ipp: Influence of operating conditions and molecular parameters. *Journal of Applied Polymer Science*, 104(2):1358–1367, 2007.
- [44] G. Lamberti. Isotactic polypropylene crystallization: Analysis and modeling. *European Polymer Journal*, 47(5):1097–1112, 2011.
- [45] T.B. Van Erp, P.C. Roozmond, and G.W.M. Peters. Flow-enhanced crystallization kinetics of ipp during cooling at elevated pressure: Characterization, validation, and development. *Macromolecular Theory and Simulations*, 22(5):309–318, 2013.
- [46] F.J.M.F. Custódio, R.J.A. Steenbakkens, P.D. Anderson, G.W.M. Peters, and H.E.H. Meijer. Model development and validation of crystallization behavior in injection molding prototype flows. *Macromolecular Theory and Simulations*, 18(9):469–494, 2009.
- [47] W. Bras, I.P. Dolbnya, D. Detollenaere, R. Van Tol, M. Malfois, G.N. Greaves, A.J. Ryan, and E. Heeley. Recent experiments on a combined small-angle/wide-angle x-ray scattering beam line at the esrf. *Journal of Applied Crystallography*, 36(3 I):791–794, 2003.
- [48] M. van Drongelen, P.C. Roozmond, E.M. Troisi, A.K. Doufas, and G.W.M. Peters. Characterization of the primary and secondary crystallization kinetics of a linear low-density polyethylene in quiescent- and flow-conditions. *Polymer*, 76:254 – 270, 2015.
- [49] J.R. Isasi, L. Mandelkern, M.J. Galante, and R.G. Alamo. The degree of crystallinity of monoclinic isotactic poly(propylene). *Journal of Polymer Science, Part B: Polymer Physics*, 37(4):323–334, 1999.
- [50] D. Delaunay, P. Le Bot, R. Fulchiron, J.F. Luye, and G. Regnier. Nature of contact between polymer and mold in injection molding. part i: influence of a non-perfect thermal contact. *Polymer Engineering and Science*, 40(7):1682–1691, 2000.
- [51] G.R. Strobl and M. Schneider. Direct evaluation of the electron density correlation function of partially crystalline polymers. *Journal of polymer science. Part A-2, Polymer physics*, 18(6):1343–1359, 1980.
- [52] W. Ruland. The evaluation of the small-angle scattering of lamellar two-phase systems by means of interface distribution functions. *Colloid and Polymer Science Kolloid Zeitschrift & Zeitschrift für Polymere*, 255(5):417–427, 1977.
- [53] N. Stribeck and W. Ruland. Determination of the interface distribution function of lamellar two-phase systems. *Journal of Applied Crystallography*, 11(5):535–539, 1978.
- [54] J.T. Koberstein, B. Morra, and R.S. Stein. The determination of diffuse-boundary thicknesses of polymers by small-angle X-ray scattering. *Journal of Applied Crystallography*, 13(1):34–45, 1980.
- [55] B.S. Hsiao and R.K. Verma. A novel approach to extract morphological variables in crystalline polymers from time-resolved synchrotron saxs data. *Journal of Synchrotron Radiation*, 5(1):23–29, 1998.

- [56] C. Santa Cruz, N. Stribeck, H.G. Zachmann, and F.J. Baltá Calleja. Novel aspects in the structure of poly(ethylene terephthalate) as revealed by means of small-angle x-ray scattering. *Macromolecules*, 24(22):5980–5990, 1991.
- [57] M. Kristiansen, T. Tervoort, P. Smith, and H. Goossens. Mechanical properties of sorbitol-clarified isotactic polypropylene: Influence of additive concentration on polymer structure and yield behavior. *Macromolecules*, 38(25):10461–10465, 2005.
- [58] C. Hedesiu, D.E. Demco, R. Kleppinger, G.V. Poel, K. Remerie, V.M. Litvinov, B. Blümich, and R. Steenbakkens. Aging effects on the phase composition and chain mobility of isotactic poly(propylene). *Macromolecular Materials and Engineering*, 293(10):847–857, 2008.
- [59] R. Le Goff, G. Poutot, D. Delaunay, R. Fulchiron, and E. Koscher. Study and modeling of heat transfer during the solidification of semi-crystalline polymers. *International Journal of Heat and Mass Transfer*, 48(25-26):5417–5430, 2005.
- [60] S.Z.D. Cheng, J.J. Janimak, A. Zhang, and E.T. Hsieh. Isotacticity effect on crystallization and melting in polypropylene fractions: 1. crystalline structures and thermodynamic property changes. *Polymer*, 32(4):648 – 655, 1991.
- [61] Y. Lu, Y. Wang, Z. Jiang, and Y. Men. Molecular weight dependency of surface free energy of native and stabilized crystallites in isotactic polypropylene. *ACS Macro Letters*, 3(11):1101–1105, 2014.
- [62] A. Gradys, P. Sajkiewicz, A.A. Minakov, S. Adamovsky, C. Schick, T. Hashimoto, and K. Saijo. Crystallization of polypropylene at various cooling rates. *Materials Science and Engineering A*, 413-414:442–446, 2005.
- [63] A.N. Kolmogoroff. On the statistic theory of metal crystallization (in russian). *Izvestiia Akademii Nauk SSSR Ser Math*, 1:335–339, 1937.
- [64] M. Avrami. Kinetics of phase change. i: General theory. *The Journal of Chemical Physics*, 7(12):1103–1112, 1939.
- [65] M. Avrami. Kinetics of phase change. ii transformation-time relations for random distribution of nuclei. *The Journal of Chemical Physics*, 8(2):212–224, 1940.
- [66] W. Schneider, A. Köppel, and J. Berger. Non - isothermal crystallization of polymers. *International Polymer Processing*, II(3-4):151–154, 1988.
- [67] A. Sedighiamiri, L.E. Govaert, M.J.W. Kanters, and J.A.W. Van Dommelen. Micromechanics of semicrystalline polymers: Yield kinetics and long-term failure. *Journal of Polymer Science, Part B: Polymer Physics*, 50(24):1664–1679, 2012.
- [68] R.H. Boyd. Relaxation processes in crystalline polymers: molecular interpretation - a review. *Polymer*, 26(8):1123–1133, 1985.
- [69] D.C. Bassett. On the role of the hexagonal phase in the crystallization of polyethylene. *Advances in Polymer Science*, 180:1–16, 2005.
- [70] J.D. Hoffman and R.L. Miller. Kinetics of crystallization from the melt and chain folding in polyethylene fractions revisited: Theory and experiment. *Polymer*, 38(13):3151–3212, 1997.
- [71] M. Iijima and G. Strobl. Isothermal crystallization and melting of isotactic polypropylene analyzed by time- and temperature-dependent small-angle x-ray scattering experiments. *Macromolecules*, 33(14):5204–5214, 2000.
- [72] C. Devoy and L. Mandelkern. Effect of molecular weight on the radial growth rates of polymer spherulites. *Journal of Polymer Science Part A-2: Polymer Physics*, 7(11):1883–1894, 1969.
- [73] K. Yamada, M. Hikosaka, A. Toda, S. Yamazaki, and K. Tagashira. Molecular weight dependence of equilibrium melting temperature and lamellar thickening of isotactic polypropylene with high tacticity. *Journal of Macromolecular Science - Physics*, 42 B(3-4 SPEC.):733–752, 2003.
- [74] G. Strobl. Colloquium: Laws controlling crystallization and melting in bulk polymers. *Reviews of Modern Physics*, 81(3):1287–1300, 2009.
- [75] A. Wlochowicz and M. Eder. Distribution of lamella thicknesses in isothermally crystallized polypropylene and polyethylene by differential scanning calorimetry. *Polymer*, 25(9):1268–1270, 1984.

- [76] J. Xu, S. Srinivas, H. Marand, and P. Agarwal. Equilibrium melting temperature and undercooling dependence of the spherulitic growth rate of isotactic polypropylene. *Macromolecules*, 31(23):8230–8242, 1998.
- [77] K. Yamada, S. Matsumoto, K. Tagashira, and M. Hikosaka. Isotacticity dependence of spherulitic morphology of isotactic polypropylene. *Polymer*, 39(22):5327–5333, 1998.
- [78] M. Kristiansen, M. Werner, T. Tervoort, P. Smith, M. Blumenhofer, and H.-W. Schmidt. The binary system isotactic polypropylene/bis(3,4-dimethylbenzylidene)sorbitol: Phase behavior, nucleation, and optical properties. *Macromolecules*, 36(14):5150–5156, 2003.
- [79] Z. Horváth, A. Menyhárd, P. Doshev, M. Gahleitner, G. Vörös, J. Varga, and B. Pukánszky. Effect of the molecular structure of the polymer and nucleation on the optical properties of polypropylene homo- and copolymers. *ACS Applied Materials and Interfaces*, 6(10):7456–7463, 2014.
- [80] F. Luo, K. Wang, N. Ning, C. Geng, H. Deng, F. Chen, Q. Fu, Y. Qian, and D. Zheng. Dependence of mechanical properties on  $\beta$ -form content and crystalline morphology for  $\beta$ -nucleated isotactic polypropylene. *Polymers for Advanced Technologies*, 22(12):2044–2054, 2011.
- [81] K.-H. Nitta, Y.-W. Shin, H. Hashiguchi, S. Tanimoto, and M. Terano. Morphology and mechanical properties in the binary blends of isotactic polypropylene and novel propylene-co-olefin random copolymers with isotactic propylene sequence 1. ethylene-propylene copolymers. *Polymer*, 46(3):965–975, 2005.
- [82] C. De Rosa and F. Auriemma. Single site metallorganic polymerization catalysis as a method to probe the properties of polyolefins. *Polymer Chemistry*, 2(10):2155–2168, 2011.
- [83] M. Naffakh, Z. Martín, N. Fanegas, C. Marco, M.A. Gómez, and I. Jiménez. Influence of inorganic fullerene-like ws2 nanoparticles on the thermal behavior of isotactic polypropylene. *Journal of Polymer Science, Part B: Polymer Physics*, 45(16):2309–2321, 2007.
- [84] S. Valdo Meille and S. Brückner. Non-parallel chains in crystalline  $\gamma$ -isotactic polypropylene. *Nature*, 340(6233):455–457, 1989.
- [85] J. Varga and J. Karger-Kocsis. Rules of supermolecular structure formation in sheared isotactic polypropylene melts. *Journal of Polymer Science, Part B: Polymer Physics*, 34(4):657–670, 1996.
- [86] J. Varga, I. Mudra, and G.W. Ehrenstein. Highly active thermally stable  $\beta$ -nucleating agents for isotactic polypropylene. *Journal of Applied Polymer Science*, 74(10):2357–2368, 1999.
- [87] C. De Rosa, F. Auriemma, R. Di Girolamo, O.R. De Ballesteros, M. Pepe, O. Tarallo, and A. Malafrente. Morphology and mechanical properties of the mesomorphic form of isotactic polypropylene in stereodeficient polypropylene. *Macromolecules*, 46(13):5202–5214, 2013.
- [88] D. Cavallo, F. Azzurri, R. Floris, G.C. Alfonso, L. Balzano, and G.W. Peters. Continuous cooling curves diagrams of propene/ethylene random copolymers. the role of ethylene counts in mesophase development. *Macromolecules*, 43(6):2890–2896, 2010.
- [89] E. Lezak, Z. Bartczak, and A. Galeski. Plastic deformation behavior of  $\beta$ -phase isotactic polypropylene in plane-strain compression at room temperature. *Polymer*, 47(26):8562–8574, 2006.
- [90] E. Lezak and Z. Bartczak. Plastic deformation behavior of  $\beta$ -isotactic phase isotactic polypropylene in plane-strain compression at elevated temperatures. *Journal of Polymer Science, Part B: Polymer Physics*, 46(1):92–108, 2008.
- [91] W. Xu, D.C. Martin, and E.M. Arruda. Finite strain response, microstructural evolution and  $\beta \rightarrow \alpha$  phase transformation of crystalline isotactic polypropylene. *Polymer*, 46(2):455–470, 2005.
- [92] F. Auriemma and C. De Rosa. Stretching isotactic polypropylene: From "cross- $\beta$ " to crosshatches, from  $\gamma$  form to  $\alpha$  form. *Macromolecules*, 39(22):7635–7647, 2006.
- [93] B. Na, R. Lv, and W. Xu. Effect of network relaxation on void propagation and failure in isotactic polypropylene at large strain. *Journal of Applied Polymer Science*, 113(6):4092–4099, 2009.
- [94] R. Thomann, H. Semke, R.-D. Maier, Y. Thomann, J. Scherble, R. Mülhaupt, and J. Kressler. Influence of stereoirregularities on the formation of the  $\gamma$ -phase in isotactic polypropylene. *Polymer*, 42(10):4597–4603, 2001.



- [95] Q. Zia, D. Mileva, and R. Androsch. Rigid amorphous fraction in isotactic polypropylene. *Macromolecules*, 41(21):8095–8102, 2008.
- [96] O. Policianová, J. Hodan, J. Brus, and J. Kotek. Origin of toughness in  $\beta$ -polypropylene: The effect of molecular mobility in the amorphous phase. *Polymer*, 60:107–114, 2015.
- [97] M.P.F. Pepels, L.E. Govaert, and R. Duchateau. Influence of the main-chain configuration on the mechanical properties of linear aliphatic polyesters. *Macromolecules*, 48(16):5845–5854, 2015.
- [98] H.J.M. Caelers, L.E. Govaert, and G.W.M. Peters. The prediction of mechanical performance of isotactic polypropylene on the basis of processing conditions. *Polymer*, 83:116–128, 2016.
- [99] R. Thomann, C. Wang, J. Kressler, and R. Mülhaupt. On the  $\gamma$ -phase of isotactic polypropylene. *Macromolecules*, 29(26):8425–8434, 1996.
- [100] P. Zhang, X. Liu, and Y. Li. Influence of  $\beta$ -nucleating agent on the mechanics and crystallization characteristics of polypropylene. *Materials Science and Engineering A*, 434(1-2):310–313, 2006.
- [101] C. Zhang, G. Liu, Y. Song, Y. Zhao, and D. Wang. Structural evolution of  $\beta$  - ipp during uniaxial stretching studied by in-situ waxes and saxs. *Polymer*, 55(26):6915–6923, 2015.
- [102] Z. Ma, C. Shao, X. Wang, B. Zhao, X. Li, H. An, T. Yan, Z. Li, and L. Li. Critical stress for drawing-induced  $\alpha$  crystal-mesophase transition in isotactic polypropylene. *Polymer*, 50(12):2706–2715, 2009.
- [103] F. Zuo, J.K. Keum, X. Chen, B.S. Hsiao, H. Chen, S.-Y. Lai, R. Wevers, and J. Li. The role of interlamellar chain entanglement in deformation-induced structure changes during uniaxial stretching of isotactic polypropylene. *Polymer*, 48(23):6867–6880, 2007.
- [104] C. Bauwens-Crowet, J.C. Bauwens, and G. Homès. Tensile yield-stress behavior of glassy polymers. *Journal of Polymer Science Part A-2: Polymer Physics*, 7(4):735–742, 1969.
- [105] J.A. Roetling. Yield stress behaviour of isotactic polypropylene. *Polymer*, 7(7):303–306, 1966.
- [106] Taikyue Ree and Henry Eyring. Theory of non-newtonian flow. i. solid plastic system. *Journal of Applied Physics*, 26(7):793–800, 1955.
- [107] R.W. Truss, P.L. Clarke, R.A. Duckett, and I.M. Ward. The dependence of yield behavior on temperature, pressure, and strain rate for linear polyethylenes of different molecular weight and morphology. *Journal of polymer science. Part A-2, Polymer physics*, 22(2):191–209, 1984.
- [108] L.E. Govaert, P.J. De Vries, P.J. Fennis, W.F. Nijenhuis, and J.P. Keustermans. Influence of strain rate, temperature and humidity on the tensile yield behaviour of aliphatic polyketone. *Polymer*, 41(5):1959–1962, 2000.
- [109] M.I. Okereke, C.P. Buckley, and C.R. Siviour. Compression of polypropylene across a wide range of strain rates. *Mechanics of Time-Dependent Materials*, 16(4):361–379, 2012.
- [110] K. Schmidt-Rohr and H.W. Spiess. Chain diffusion between crystalline and amorphous regions in polyethylene detected by 2d exchange 13c nmr. *Macromolecules*, 24(19):5288–5293, 1991.
- [111] G. Attalla, I.B. Guanella, and R.E. Cohen. Effect of morphology on stress relaxation of polypropylene. *Polymer Engineering & Science*, 23(16):883–887, 1983.
- [112] T. Ariyama, Y. Mori, and K. Kaneko. Tensile properties and stress relaxation of polypropylene at elevated temperatures. *Polymer Engineering and Science*, 37(1):81–90, 1997.
- [113] W.-G. Hn and K. Schmidt-Rohr. Polymer ultradrawability: The crucial role of  $\alpha$ -relaxation chain mobility in the crystallites. *Acta Polymerica*, 50(8):271–285, 1999.
- [114] L.E. Govaert, T.A.P. Engels, E.T.J. Klompen, G.W.M. Peters, and H.E.H. Meijer. Processing-induced properties in glassy polymers: Development of the yield stress in pc. *International Polymer Processing*, 20(2):170–177, 2005.
- [115] D.J.A. Senden, J.A.W. Van Dommelen, and L.E. Govaert. Physical aging and deformation kinetics of polycarbonate. *Journal of Polymer Science, Part B: Polymer Physics*, 50(22):1589–1596, 2012.
- [116] H.E.H. Meijer and L.E. Govaert. Mechanical performance of polymer systems: The relation between structure and properties. *Progress in Polymer Science (Oxford)*, 30(8-9):915–938, 2005.

- [117] C. Bauwens-Crowet, J.-M. Ots, and J.-C. Bauwens. The strain-rate and temperature dependence of yield of polycarbonate in tension, tensile creep and impact tests. *Journal of Materials Science*, 9(7):1197–1201, 1974.
- [118] J. Varga.  $\beta$ -modification of isotactic polypropylene: Preparation, structure, processing, properties, and application. *Journal of Macromolecular Science - Physics*, 41 B(4-6):1121–1171, 2002.
- [119] H.J.M. Caelers, E. Parodi, D. Cavallo, G.W.M. Peters, and L.E. Govaert. Deformation and failure kinetics of ipp polymorphs. *Journal of Polymer Science, Part B: Polymer Physics*, 55(9):729–747, 2017.
- [120] B. Xiong, O. Lame, J.-M. Chenal, C. Rochas, R. Seguela, and G. Vigier. In-situ saxs study of the mesoscale deformation of polyethylene in the pre-yield strain domain: Influence of microstructure and temperature. *Polymer*, 55(5):1223–1227, 2014.
- [121] A. Pawlak, A. Galeski, and A. Rozanski. Cavitation during deformation of semicrystalline polymers. *Progress in Polymer Science*, 39(5):921–958, 2014.
- [122] S. Ran, X. Zong, D. Fang, B.S. Hsiao, B. Chu, and R.A. Phillips. Structural and morphological studies of isotactic polypropylene fibers during heat/draw deformation by in-situ synchrotron saxs/waxd. *Macromolecules*, 34(8):2569–2578, 2001.
- [123] Y. Lu, Y. Wang, R. Chen, J. Zhao, Z. Jiang, and Y. Men. Cavitation in isotactic polypropylene at large strains during tensile deformation at elevated temperatures. *Macromolecules*, 48(16):5799–5806, 2015.
- [124] C. Jia, X. Liao, J. Zhu, Z. An, Q. Zhang, Q. Yang, and G. Li. Creep-resistant behavior of  $\beta$ -polypropylene with different crystalline morphologies. *RSC Advances*, 6(37):30986–30997, 2016.
- [125] S. Humbert, O. Lame, J.M. Chenal, C. Rochas, and G. Vigier. New insight on initiation of cavitation in semicrystalline polymers: In-situ saxs measurements. *Macromolecules*, 43(17):7212–7221, 2010.
- [126] Y. Wang, Z. Jiang, L. Fu, Y. Lu, and Y. Men. Lamellar thickness and stretching temperature dependency of cavitation in semicrystalline polymers. *PLoS ONE*, 9(5), 2014.
- [127] B. Xiong, O. Lame, J.-M. Chenal, C. Rochas, R. Seguela, and G. Vigier. Temperature-microstructure mapping of the initiation of the plastic deformation processes in polyethylene via in situ waxes and saxs. *Macromolecules*, 48(15):5267–5275, 2015.
- [128] B. Xiong, O. Lame, J.M. Chenal, C. Rochas, R. Seguela, and G. Vigier. In-situ saxs study and modeling of the cavitation/crystal-shear competition in semi-crystalline polymers: Influence of temperature and microstructure in polyethylene. *Polymer*, 54(20):5408–5418, 2013.
- [129] B. Xiong, O. Lame, J.-M. Chenal, C. Rochas, R. Seguela, and G. Vigier. Amorphous phase modulus and micro-macro scale relationship in polyethylene via in situ saxs and waxes. *Macromolecules*, 48(7):2149–2160, 2015.
- [130] S. Humbert, O. Lame, and G. Vigier. Polyethylene yielding behaviour: What is behind the correlation between yield stress and crystallinity? *Polymer*, 50(15):3755–3761, 2009.
- [131] Y. Men, J. Rieger, and G. Strobl. Role of the entangled amorphous network in tensile deformation of semicrystalline polymers. *Physical Review Letters*, 91(9):955021–955024, 2003.
- [132] M. Ishikawa, K. Ushui, Y. Kondo, K. Hatada, and S. Gima. Effect of tie molecules on the craze strength of polypropylene. *Polymer*, 37(24):5375–5379, 1996.
- [133] M. Aboulfaraj, C. G'Sell, B. Ulrich, and A. Dahoun. In situ observation of the plastic deformation of polypropylene spherulites under uniaxial tension and simple shear in the scanning electron microscope. *Polymer*, 36(4):731–742, 1995.
- [134] T. Labour, C. Gauthier, R. Séguéla, G. Vigier, Y. Bomal, and G. Orange. Influence of the  $\beta$  crystalline phase on the mechanical properties of unfilled and caco3-filled polypropylene. i. structural and mechanical characterisation. *Polymer*, 42(16):7127–7135, 2001.
- [135] T. Labour, G. Vigier, R. Séguéla, C. Gauthier, G. Orange, and Y. Bomal. Influence of the  $\beta$ -crystalline phase on the mechanical properties of unfilled and calcium carbonate-filled polypropylene: Ductile cracking and impact behavior. *Journal of Polymer Science, Part B: Polymer Physics*, 40(1):31–42, 2002.

- [136] R.N. Haward. Strain hardening of thermoplastics. *Macromolecules*, 26(22):5860–5869, 1993.
- [137] H.G.H. Van Melick, L.E. Govaert, and H.E.H. Meijer. Localisation phenomena in glassy polymers: Influence of thermal and mechanical history. *Polymer*, 44(12):3579–3591, 2003.
- [138] H. Zhang, A.K. Scholz, J. De Crevoisier, F. Vion-Loisel, G. Besnard, A. Hexemer, H.R. Brown, E.J. Kramer, and C. Creton. Nanocavitation in carbon black filled styrene-butadiene rubber under tension detected by real time small angle x-ray scattering. *Macromolecules*, 45(3):1529–1543, 2012.
- [139] C.G. Vonk and G. Kortleve. X-ray small-angle scattering of bulk polyethylene - ii. analyses of the scattering curve. *Kolloid-Zeitschrift & Zeitschrift für Polymere*, 220(1):19–24, 1967.
- [140] P. Debye and A.M. Bueche. Scattering by an inhomogeneous solid. *Journal of Applied Physics*, 20(6):518–525, 1949.
- [141] G. Porod. Die röntgenkleinwinkelstreuung von dichtgepackten kolloiden systemen - i. teil. *Kolloid-Zeitschrift*, 124(2):83–114, 1951.
- [142] B.J.P. Jansen, S. Rastogi, H.E.H. Meijer, and P.J. Lemstra. Rubber-modified glassy amorphous polymers prepared via chemically induced phase separation. 2. mode of microscopic deformation studied by in-situ small-angle x-ray scattering during tensile deformation. *Macromolecules*, 34(12):4007–4018, 2001.
- [143] C. G'Sell and J.J. Jonas. Yield and transient effects during the plastic deformation of solid polymers. *Journal of Materials Science*, 16(7):1956–1974, 1981.
- [144] R.J.M. Smit, W.A.M. Brekelmans, and H.E.H. Meijer. Prediction of the large-strain mechanical response of heterogeneous polymer systems: Local and global deformation behaviour of a representative volume element of voided polycarbonate. *Journal of the Mechanics and Physics of Solids*, 47(2):201–221, 1999.
- [145] M. von Compostella, A. Coen, and F. Bertinotti. Fasern und filme aus isotaktischem polypropylen. *Angewandte Chemie*, 74(16):618–624, 1962.
- [146] C.J.G. Plummer and H.-H. Kausch. Micronecking in thin films of isotactic polypropylene. *Macromolecular Chemistry and Physics*, 197(6):2047–2063, 1996.
- [147] M.F. Butler, A.M. Donald, and A.J. Ryan. Time resolved simultaneous small- and wide-angle x-ray scattering during polyethylene deformation - ii. cold drawing of linear polyethylene. *Polymer*, 39(1):39–52, 1998.
- [148] A. Pawlak. Cavitation during tensile deformation of high-density polyethylene. *Polymer*, 48(5):1397–1409, 2007.
- [149] A. Pawlak and A. Galeski. Plastic deformation of crystalline polymers: The role of cavitation and crystal plasticity. *Macromolecules*, 38(23):9688–9697, 2005.
- [150] Y. Men, J. Rieger, and J. Homeyer. Synchrotron ultrasmall-angle x-ray scattering studies on tensile deformation of poly(1-butene). *Macromolecules*, 37(25):9481–9488, 2004.
- [151] U.W. Gedde, J. Viebke, H. Leijström, and M. Ifwarson. Long-term properties of hot-water polyolefin pipes-a review. *Polymer Engineering & Science*, 34(24):1773–1787, 1994.
- [152] I. Hussain, S.H. Hamid, and J.H. Khan. Polyvinyl chloride pipe degradation studies in natural environments. *Journal of Vinyl and Additive Technology*, 1(3):137–141, 1995.
- [153] A. Gray, J.N. Mallinson, and J.B. Price. Fracture behaviour of polyethylene pipes. *Plastics and Rubber Processing and Applications*, 1(1):51–53, 1981.
- [154] J.M. Crissman and G.B. McKenna. Relating creep and creep rupture in pmma using a reduced variable approach. *Journal of Polymer Science Part B: Polymer Physics*, 25(8):1667–1677, 1987.
- [155] "iso 9080, plastic piping and ducting systems - determination of the long-term hydrostatic strength of thermoplastic materials in pipe form by extrapolation". 2003.
- [156] "Exova Case Results". <http://polymer.exova.com/wp-content/uploads/2014/09/Case-308.pdf>. Retrieved: 28-4-2016.
- [157] L.C.E. Struik. Mechanical behaviour and physical ageing of semi-crystalline polymers: 3. prediction of long term creep from short time tests. *Polymer*, 30(5):799–814, 1989.

- 
- [158] P.E. Tomlins and B.E. Read. Creep and physical ageing of polypropylene: A comparison of models. *Polymer*, 39(2):355–367, 1998.
- [159] L.C.E. Struik. The mechanical and physical ageing of semicrystalline polymers: 1. *Polymer*, 28(9):1521–1533, 1987.
- [160] W.J. O’Kane and R.J. Young. The role of dislocations in the yield of polypropylene. *Journal of Materials Science Letters*, 14(6):433–435, 1995.
- [161] O.D. Sherby and J.E. Dorn. Anelastic creep of polymethyl methacrylate. *Journal of the Mechanics and Physics of Solids*, 6(2):145–162, 1958.
- [162] E.T.J. Klompen, T.A.P. Engels, L.C.A. Van Breemen, P.J.G. Schreurs, L.E. Govaert, and H.E.H. Meijer. Quantitative prediction of long-term failure of polycarbonate. *Macromolecules*, 38(16):7009–7017, 2005.
- [163] H.A. Visser, T.C. Bor, M. Wolters, J.G.F. Wismans, and L.E. Govaert. Lifetime assessment of load-bearing polymer glasses: The influence of physical ageing. *Macromolecular Materials and Engineering*, 295(12):1066–1081, 2010.
- [164] R.A.C. Deblieck, D.J.M. Van Beek, K. Remerie, and I.M. Ward. Failure mechanisms in polyolefines: The role of crazing, shear yielding and the entanglement network. *Polymer*, 52(14):2979–2990, 2011.
- [165] D.H. Reneker and B. Fanconi. Effects of defects on the longitudinal acoustic mode of n-alkane chains. *Journal of Applied Physics*, 46(10):4144–4147, 1975.



# Samenvatting

Isotactisch polypropreen (iPP) is een goedkoop semi-kristallijn polymeer, dat makkelijk te verwerken is en een brede variëteit aan eigenschappen heeft. Hierdoor wordt het in vele verschillende toepassingen gebruikt. De producten worden typisch vervaardigd door middel van processen zoals spuitgieten en extrusie. Onafhankelijk van de gebruikte techniek zijn de tijdens het productieproces opgelegde condities zoals temperatuur, koelsnelheid, druk en stroming, van doorslaggevend belang voor de morfologie die gevormd wordt tijdens het stollen. De gevormde structuren op zowel de micro als de nanoschaal bepalen in grote mate de mechanische eigenschappen, waaronder de vloeikinetiek. Daarnaast ontstaan onder bepaalde belastingcondities holtes in het materiaal, die op hun beurt ook invloed uitoefenen op het mechanisch materiaal gedrag. Op de nanometerschaal is de dikte van de kristallijne gebieden van belang, terwijl op de Å-lengteschaal de kristallografische eenheids cell de eigenschappen domineert.

Het doel van dit project is om bij te dragen aan een methodologie die het mogelijk maakt om de mechanische eigenschappen van polymere producten direct te evalueren op basis van morfologische eigenschappen, voortkomend uit simulaties van het fabricageproces. In het specifieke geval van isotactisch polypropreen komt de complexiteit van dit probleem voort uit het rijke polymorfisme, en de variëteit aan morfologieën, die het materiaal kan vertonen. Daarnaast kunnen de morfologie en de bijbehorende mechanische eigenschappen sterk afhangen van de positie binnen het product.

Om de aanpak te demonstreren is eerst een versimpeld maar uitvoerbaar probleem gedefinieerd. Hierin wordt slechts een enkele kristalfase beschouwd, de monokliene  $\alpha$ -fase, waarna de invloed van een variabele thermische geschiedenis is onderzocht. De hieruit resulterende heterogene morfologie is voorspeld met een kristallisatiemodel, ontwikkeld binnen de Polymeer Technologie groep. Structurele eigenschappen, zoals de lokale distributie van de kristal dikte volgen uit het model, en zijn daarna gebruikt om de vloeikinetiek te voorspellen. Een vergelijking met de experimenteel verkregen resultaten laat goede overeenkomst zien, waarmee gedemonstreerd is dat deze aanpak werkt.

Omdat het probleem zo complex is zijn vervolgens deelproblemen gedefinieerd, die los van elkaar systematisch zijn onderzocht. Een zorgvuldige selectie van de verwerkingscondities faciliteert het onderzoek van proefstukken die slechts een enkel type kristalstructuur bevatten. Hierdoor kunnen de individuele vloe- en faalkinetieken

blootgelegd worden. Het mechanische gedrag van deze verschillende polymorfen is vervolgens succesvol gemodelleerd, en de voorspelde faaltijden als functie van de belastingscondities zijn experimenteel gevalideerd voor zowel  $\alpha$ -,  $\beta$ - en  $\gamma$ -iPP. Hoewel de structuren van de bijbehorende eenheids cellen volledig verschillend zijn, zijn er enkele opmerkelijke overeenkomsten gevonden. De kinetiek die geobserveerd is boven de  $\alpha_c$ -relaxatie temperatuur is hetzelfde voor alle polymorfen. Boven deze temperatuur kunnen de deels in bewegingsvrijheid beperkte amorf domeinen, die dicht bij de kristallen bevinden, thermisch verjongd worden.

Vervolgens is ook de evolutie van de structuur, zoals die plaatsvindt tijdens mechanisch belasten, uitgebreid onderzocht. Dit is hoofdzakelijk gedaan door röntgen experimenten uit te voeren gelijktijdig met het deformatieproces (bij de European Synchrotron and Radiation Facility (ESRF) in Grenoble) als gevolg van uniaxiale rek- en drukproeven. De veranderingen in de structuur die plaatsvinden in  $\alpha$ -,  $\beta$ - en  $\gamma$ -iPP zijn daarmee aan het licht gebracht. Evolutie in de zin van fase overgangen, kristalliniteits afname en lamel dikte verandering, als ook het ontstaan van caviteiten, is gekoppeld aan het intrinsieke materiaal gedrag, verkregen met behulp van de mechanische experimenten. Bij alle verstrekkingstemperaturen neemt de kristalliniteit af als gevolg van deformatie en, afhankelijk van de temperatuur, worden verschillende nieuwe structuren gevormd. Verstrekken op lage temperaturen leidt tot de afbraak van kristallen en de formatie van georiënteerde mesofase, onafhankelijk van de initiële kristal structuur. Op hoge temperaturen, boven de  $T_{\alpha_c}$ , transformeren alle polymorfen in georiënteerd  $\alpha$ -iPP. Kleine hoeveelheden van de initiële structuur blijven behouden in het materiaal. De compressie experimenten, waar lokalisatie fenomenen zijn uitgesloten, laten bovendien zien dat deze transformaties plaatsvinden op vergelijkbare rekken voor alle onderzochte kristal structuren. De vorming van caviteiten wordt duidelijk waargenomen voordat het materiaal vloeit, en is het meest intens in het geval van  $\beta$ -iPP.

De verkregen kennis van het morfologie afhankelijke intrinsieke materiaalgedrag, de vloeï- en faalkinetiek, en de structuurontwikkeling als gevolg van deformatie zijn gebruikt om een gestandaardiseerde certificatie procedure voor polymere producten te onderzoeken. Tijdsafhankelijk gedrag, dat typisch is voor dit soort materialen, voedt de behoefte aan certificatie data van bepaalde producten die worden onderworpen aan belastingen. Een veelgebruikte methode om in deze behoefte te voorzien, in dit specifieke geval voor het voorspellen van de levensduur van kunststof buizen, is gedefinieerd in ISO9080. Hierin wordt gebruik gemaakt van tijd-temperatuur-superpositie. Er worden echter ook enkele belangrijke eigenschappen over het hoofd gezien, zoals de aanwezigheid van verschillende deformatie mechanismen en de evolutie van structuur en eigenschappen. De tekortkomingen van de certificeringsprocedure laten zien dat een goede en betrouwbare levensduurvoorspelling een uitbreiding van de methode vereist. Twee verschillende types van structuur evolutie die plaats kunnen vinden in toepassingen (zoals kunststof buizen) zijn onthuld, en de verraderlijke effecten die dit op de levensduurvoorspellingen heeft worden bediscussieerd. Bovendien is aangetoond

dat het brosse faalmechanisme verkeerd wordt geïnterpreteerd. In werkelijkheid is dit mechanisme plasticiteits gedomineerd en volgt het slechts een andere kinetiek. Dit biedt nieuwe inzichten in de structuur-eigenschappen relatie in iPP, en verandert de route die gevolgd moet worden om de (mechanische) eigenschappen te verbeteren aan de hand van het beïnvloeden van de structuur.





# Dankwoord

Graag wil ik iedereen bedanken die heeft bijgedragen aan het tot stand komen van dit proefschrift. Als eerste wil ik beginnen bij mijn twee promotoren, Gerrit Peters en Leon Govaert, voor hun motiverende aanpak en hun kritische blik. De fijne sfeer waarin ik mijn promotieonderzoek heb mogen doen is denk ik voor een groot deel aan hen te danken. Ondanks de verschillen in hun karakter, en de daaruit voortvloeiende aanpak van problemen, denk ik dat de combinatie van deze twee begeleiders een ideale mix was. Gerrit, jouw vermogen om de meest gecompliceerde problemen te versimpelen tot oplosbare deelproblemen heeft mij erg geholpen. Verder heb je mij in ieder geval bij proberen te brengen om niet teveel om zaken heen te draaien. Samen met jouw uiterst brede interesse heeft dit ervoor gezorgd dat ik altijd graag even binnen viel. Leon, jouw nadruk op consistentie bij het verklaren van de experimentele observaties heeft veel houvast geboden. Wanneer mijn gedachten de vrije loop namen bij het zoeken naar hypothesen stuurde je er altijd op aan dat ik eerst eens vanuit het bestaande plaatje naar verklaringen op zoek ging. Uiteindelijk heeft dat sterk geholpen bij de begripvorming. Ook wil ik Patrick bedanken voor de promotieplek binnen de polymerengroep.

Verder wil ik ook SABIC bedanken voor de financiering van dit project. In het bijzonder wil ik Rieky, Klaas, Mark, Rudy en Ralf noemen. De buitengewoon prettige samenwerking en de talloze waardevolle constructieve discussies over de interpretatie van de resultaten, de (keuze van de) materialen en de SEM plaatjes, hebben ervoor gezorgd dat ik iedere keer weer uitkeek naar de volgende voortgangsbespreking. Ik heb genoten van de collaboratie en ben dankbaar voor de kans die jullie me hebben gegeven.

In almost all the chapters of this thesis, data obtained from experimental work carried out at the European Synchrotron and Radiation Facility, Grenoble, is used. Therefore, the synchrotron has been of indispensable value for this research. The valuable discussions with Daniel, Giuseppe and Wim, and their support with the X-ray experiments and data analysis, is highly appreciated.

Zonder de hulp en technische ondersteuning van voornamelijk Lucien en Sjef, was het nooit mogelijk geweest om het experimentele deel van dit proefschrift uit te voeren. Hun praktische oplossingen bij de experimentele problemen waren van onschatbare waarde. Verder ben ik ook dank verschuldigd aan Marc van Maris, die heeft geholpen met verschillende experimenten, maar vooral ook voor de vele interessante gesprekken tijdens

de lunch op woensdag. Ans en Marleen wil ik bedanken voor hun hulp bij de het regelen van de dagelijkse zaken. Furthermore, I would like to thank all my (former) office mates, colleagues (either from mechanical engineering or chemical engineering) and all the students who contributed to this thesis. Answering my numerous questions, often questions just to start a conversation or a discussion, required a lot of patience. Besides helping me to solve all kind of work related issues using their expertise, they are also thanked for the fact that the last four years were valuable from a social point of view. The trip to Rome, the "polymerenoverleg" the fair in Weert and all kind of other occasional events were nice, and will hopefully continue to take place.

Natuurlijk ben ik ook dank verschuldigd aan de vrienden van buiten de TU, die voor de broodnodige afwisseling hebben gezorgd. Na weekenden heb ik mezelf soms af moeten vragen waar ik voor het weekend ook alweer mee bezig was. Het heeft erg geholpen om af en toe wat afstand te kunnen nemen en daarna weer met een frisse blik verder te gaan. Als laatste wil ik mijn familie bedanken voor de onvoorwaardelijke steun tijdens mijn promotie, maar zeker ook tijdens de studie die daaraan voorafging. Loes, Lon en Hai, zonder jullie vertrouwen was ik niet tot dit resultaat kunnen komen.

# Curriculum Vitae

Harm Caelers was born on the 3th of May 1989 in Venray, the Netherlands. He graduated from the pre-university education in 2007 at the Bouwens van de Boije college in Panningen, the Netherlands. Hereafter he studied Mechanical Engineering at the Eindhoven University of Technology in Eindhoven, the Netherlands. In February 2013 he received his Master's degree with great appreciation, on the thesis entitled "The prediction of mechanical properties of isotactic polypropylene on the basis of processing conditions". This work was performed in the Polymer Technology group chaired by prof.dr.ir. H.E.H. Meijer, under the supervision of prof.dr.ir. L.E. Govaert and prof.dr.ir. G.W.M. Peters. As part of his master track he performed an internship at Océ, Venlo, the Netherlands, under supervision of dr.ir. L. Saes.

After completion of his Master's degree he took a position in the Polymer Technology group as a PhD student under the supervision of prof.dr.ir. L.E. Govaert and prof.dr.ir. G.W.M. Peters. The current research project entitled 'Structure Tuning for Enhanced Properties of isotactic Polypropylene', is supported by SABIC.

During his PhD he successfully completed the postgraduate course Register Polymer Science of the National Dutch Research School PTN (Polymeer Technologie Nederland) and is given the title of Registered Polymer Scientist. The course consists of the following modules: A - Polymer Chemistry, B - Polymer Physics, C - Polymer Properties, D&E - Rheology and Processing. He also attended the 14th European School on Rheology at the University of Leuven during the summer of 2013.



# List of Publications

This thesis has resulted in the following publications:

- H. J. M. Caelers, E. Parodi, D. Cavallo, G. W. M. Peters, L. E. Govaert. Deformation and Failure Kinetics of iPP Polymorphs . *J. Polym. Sci. Part B: Polym. Phys.*, 55(9), 729–747 (2017).
- H. J. M. Caelers, L. E. Govaert, G. W. M. Peters. The prediction of mechanical performance of isotactic polypropylene on the basis of processing conditions. *Polymer (United Kingdom)*, 83, 116–128 (2016).
- H. J. M. Caelers, E. M. Troisi, G. W. M. Peters, L. E. Govaert. Deformation induced phase transitions in iPP polymorphs. *To be submitted to J. of Mater. Sci.*.
- H. J. M. Caelers, N. Perillo, R.A.C. Deblieck, G. W. M. Peters, L. E. Govaert. Long term failure predictions in polypropylenes. *To be submitted*.

Additionally, the author contributed to a number of publications outside the scope of this thesis:

- E. M. Troisi, M. Van Drongelen, H.J.M. Caelers, G. Portale, G. W. M. Peters. Structure evolution during film blowing: An experimental study using in-situ small angle X-ray scattering . *European Polymer Journal*, 74, 190–208 (2016).
- D. Cavallo, M. J. W. Kanters, H. J. M. Caelers, G. Portale, L. E. Govaert. Kinetics of the polymorphic transition in isotactic poly(1-butene) under uniaxial extension. New insights from designed mechanical histories. *Macromolecules*, 47(9), 3033–3040 (2014).
- E. M. Troisi, H. J. M. Caelers, G. W. M. Peters. Full characterization of multi-phase, multi-morphological kinetics in flow-induced crystallization of iPP at elevated pressure *Accepted in Macromolecules*.

